McGill University

Neutrino Charm Production

and a

Limit to Neutrino Oscillations

by

Ph.D. Thesis

David Charles Bailey

Abstract

The production of charmed particles and a limit to tau lepton production have been measured using a hybrid emulsion spectrometer in the Fermilab wide-band neutrino beam.

The relative cross section for charged current charmed particle production is $\sigma(\nu\to\mu^-c)/\sigma(\nu\to\mu^-)=6.5\pm^{1.9}_{1.8}\%$, and the energy dependence of the cross section and the kinematic distributions of the charm events are given. One event with charm pair production was observed. A limit of $\sigma(\nu\to\mu c\bar{c})/\sigma(\nu\to\mu c)<0.06$ (90%C.L.) is set to the ratio of charged current pair and single charm production. The relative rates of D^o, D^+, F^+, and Λ_c^+ production have been measured - the fraction of D mesons is $69\pm^{8}_{10}\%$. Momentum, transverse momentum, Feynman X, and fragmentation (Z) distributions are presented. The mean Z for charmed hadrons is $0.59\pm0.03(\pm0.03)$.

No tau leptons were observed, and an upper limit to the ν_μ-τ coupling of 0.0063 (90%C.L.) is set. For ν_μ-ν_τ oscillations this implies $|m^2_{\nu_\mu}-m^2_{\nu_\tau}|<3.0$ eV^2 for maximum mixing.

Sommaire

Nous avons mesuré la production du charme et établi une borne supérieure de la production des leptons tau en utilisant une combinaison spectromètre-émulsion hybride dans le faisceau à bande large de neutrinos au Fermilab.

La section efficace de production du charme par courant chargé est $\sigma(\nu \to \mu^- c)/\sigma(\nu \to \mu^-) = 6,5 \pm^{1,9}_{1,8}\%$. Nous présentons aussi la dépendance énergétique de celle-ci ainsi que les distributions cinématiques des événements charmés. Un événement exhibant la production d'une paire charmée fut observé. Nous établissons la borne supérieure $\sigma(\nu \to \mu c\bar{c})/\sigma(\nu \to \mu c) < 6\%$ (90% de confiance) du rapport production par courant chargé de paires charmées sur production unique du charme. Les taux de production de D^o, D^+, F^+ et Λ_c^+ ont été mesurés. Nous présentons les distributions d'impulsions, d'impulsions transversales, de la variable de Feynman et de la variable de fragmentation.

Aucun lepton tau ne fut observé. Nous établissons une borne supérieure du couplage ν_μ-τ de 0,63%. Ceci implique $|m^2_{\nu_\mu} - m^2_{\nu_\tau}| < 3,0\ eV^2$ pour un mélange maximal dans les oscillations $\nu_\mu \to \nu_\tau$.

Acknowledgements

This thesis presents and analyses data obtained by Experiment 531 at the Fermi National Accelerator Laboratory in Batavia, Illinois. Few modern experiments in high energy physics would be possible without the work of many, many people, and this experiment is no exception.

I must acknowledge the implicit contributions of all the members of the E-531 collaboration (Appendix I). In particular, I thank my advisor, John Trischuk, for his years of patience; I thank Sergio Conetti for showing me how physics should be done; I thank Ron Sidwell for his sage advice; I thank Steve Errede for his electric enthusiasm; and I thank Dale Pitman for her help, her inspiration, and her friendship.

I also must acknowledge the great amount of work done by the technical and support staff at McGill and the other institutions involved in the collaboration. As well, I am fully aware of my debt to the entire community, physicists and non-physicists, who make Fermilab work.

I would like to thank Marc Turcotte for his assistance with the abstract, and Robert Nowac for drawing most of the figures.

Table of Contents

Introduction

In less than a decade, high energy physics has gone from revelation to dogma. Today there is a standard, if incomplete, view of the fundamental constituents of matter and their interactions. Most physicists believe that the fundamental constituents are quarks and leptons, and these interact via electroweak forces described by the theory of Quantum Flavourdynamics (QFD), and via the strong interaction described by Quantum Chromodynamics (QCD). Only gravity, described at the macroscopic level by General Relativity, is not yet described at a microscopic level.

The development of this standard picture has been much guided by the discovery and study of new quarks and leptons. The 1974 discovery [1] of the J/Ψ particle was the catalyst that lead to the common acceptance of QFD. The J/Ψ was the first obvious manifestation of a new quark, predicted by QFD [2], carrying a new quantum number - charm. In 1975 a new lepton, the tau (τ), was discovered [3] and in 1977 another new quark, the beauty quark, was found [4].

Among the most obvious characteristics shared by the new particles were their short lifetimes. The expected lifetimes of the tau lepton and the weakly decaying charmed particles were $\lesssim 10^{-13}$ seconds, much shorter than the lifetimes ($\gtrsim 10^{-10}$ s) of previously known weakly decaying particles.

The experiment described in this work, Fermilab experiment E-531, was one of the first experiments to successfully measure the lifetimes of the charmed particles [5-13]. The experiment had a high resolution nuclear emulsion target (in which decays as short as a few micrometers or as long as several centimeters could be seen) followed by a multipurpose multiparticle spectrometer (which measured the momentum, energy, and identity of particles emerging from the emulsion). The experiment was capable of finding, reconstructing, and identifying short-lived particle decays with lifetimes in the range 10^{-15} to 10^{-11} seconds.

This thesis presents E-531 data on the production of short-lived particles by neutrinos: charm production rates and characteristics, limits to beauty production, and limits to tau production and ν_μ-ν_τ oscillation have been measured. E-531 is unique among neutrino experiments in its ability to observe with high efficiency, and almost no background, the weak production and decay of charmed particles. E-531 is the first experiment to measure the total charm production cross sections, the relative production rates of different charmed particles, and the detailed kinematic distributions of the charmed particles.

Except for a few charmed particle decays observed in other neutrino-emulsion experiments [14], all previous information on charmed particle and tau lepton production by neutrinos has come from bubble chambers or counter experiments with massive targets. Examples of charmed particle decays have been reconstructed in bubble chambers [15], and mass peaks for several charmed particle decay modes have been detected [16], but bubble chambers have too coarse a spatial resolution to find more than an occasional visible decay [17]. As a result, most studies have only indirectly detected charm by observing strange particles [18] or leptons [19] presumed to come from the decay of charmed particles. Similarly, limits to tau lepton production have been set indirectly by searching for electrons from semileptonic tau decays.

When a particle decays weakly, it often decays semileptonically with either an electron or a muon among its decay products. If the decaying particle comes from a charged current muon neutrino interaction, this secondary decay lepton will be in addition to the primary muon produced by the neutrino. The production of a short-lived particle can be inferred from the secondary lepton. Heavy liquid bubble chambers are used to look for the electrons from semi-electronic decays of the new particles, and counter and bubble chamber experiments look for the muon from semi-muonic decays. Also, since charmed quarks usually decay into strange quarks, measuring strange particle production rates in bubble chambers is another way of indirectly detecting charm.

Much has been learned about neutrino charm production from such

experiments, but there are limits to the sensitivity of indirect measurements. For example, only neutral, not charged, strange particles are easily identified in bubble chambers, and there is a large background from strange particles that do not come from charm decays. An inherent difficulty for dilepton experiments is that the average charm semileptonic branching ratio, which depends on the relative rates of production of the different charmed particles, may vary with the reaction (charged or neutral current, single or associated production), the beam (ν or $\bar{\nu}$), and the kinematic parameters (E_ν,x,Z,...). It is also difficult to infer the properties of the charmed particles from their decay leptons. (e.g. The charm fragmentation function is determined with more precision by E-531 with $\sim$40 measured charmed particles, than by a dimuon experiment with >10000 dimuon events [20].)

In general, this experiment (E-531) can better measure the characteristics of the charmed particles, while dimuon experiments can, with their great statistical power (many events), better measure the characteristics (E_ν, x, y, Q^2, W) of the neutrino interactions. These dimuon measurements do, however, require certain assumptions about the charm dimuon production process, and the direct measurements from E-531 are an important complement to the dimuon results.

This thesis is organized along fairly traditional lines. The theoretical framework and basic background for the experiment are presented in Chapter 1, the apparatus and techniques of the experiment are described in Chapter 2, and methods of analysis are discussed in Chapter 3. Finally, the results of the experiment are presented in the last two chapters: the characteristics of charm production in Chapter 4, and limits to tau production and neutrino oscillations in Chapter 5. There are, of course, deviations from this plan in (what I hope are) the interests of clarity and context. To avoid confusion because of the wide range of results, some details of theory or analysis are deferred to the appropriate discussion of results.

CHAPTER 1: Theory and Basics

1.1 The Standard Model

There now exists a possible framework for a microscopic understanding of the physical universe. This "standard model" classifies, and tries to synthesize, the basic constituents and forces of nature.

It is believed that the fundamental constituents of matter are quarks and leptons [21]. These fermions interact via a strong interaction mediated by vector bosons called gluons, and via an electroweak interaction mediated by the photon and three intermediate vector bosons: the W^+, W^-, and Z^o (Table 1-1). Only gravity, so very much weaker than the strong and electroweak forces, is not yet included in this microscopic description.

Quarks and leptons are distinguished by the strong charge (known as colour): quarks have colour charge and leptons do not. There are now believed to be at least 6 types each of quarks and leptons; more quarks and leptons may exist, but are, as yet, unnecessary and unobserved. Table 1-2 lists the quarks and leptons. The leptons exist as independent particles, but quarks are only seen as components of hadronic particles. Free quarks (not part of a multiquark hadron) have not been seen, and may not exist.

1.1.1 The Strong Interaction - Quantum Chromodynamics (QCD)

The strong interaction is thought to be described by a non-Abelian SU(3) gauge theory: Quantum Chromodynamics (QCD) [22]. The SU(3) charge is called "colour", and the interactions are mediated by 8 massless vector gauge bosons called gluons. Any flavour of quark has 3 possible colour states (red, green, or blue), and the gluons are a colour-anticolour SU(3) octet. (There are not 9 gluons because QCD has no

Table 1-1: The gauge bosons of the standard model.

	Boson	Electric charge	Mass	
gluons[a]	G	0	0	
electroweak bosons	$W^{\pm}$	±1	83±3 GeV/c^2	[63]
	Z^o	0	94±2 GeV/c^2	
	γ (photon)	0	0	

(a) Gluons come in 8 colour-anticolour combinations.

Table 1-2: The fundamental fermions. The t quark and ν_τ lepton have not yet been discovered, but their existence is assumed. Each flavour of quark comes in 3 colours. It is possible that all neutrino masses are identically zero.

	Flavour	Electric charge	Mass (MeV/c^2)
Quarks	u (up)	+2/3	~300[b] (~5)[c]
	d (down)	-1/3	~300[b] (~10)[c]
	s (strange)	-1/3	~500[b] (~200)[c]
	c (charm)	+2/3	~1500[b] (~1300)[c]
	b (beauty)	-1/3	~4700
	t (truth)	+2/3	>18000
Leptons	ν_e (electron neutrino)	0	<0.000046[d]
	e (electron)	-1	0.511
	ν_μ (muon neutrino)	0	<0.52
	μ (muon)	-1	106
	ν_τ (tau neutrino)	0	<250
	τ (tau)	-1	1784

(b) constituent mass: This is approximately that portion of the mass of a hadron (e.g. the proton) the quark contributes.

(c) current mass: This is the effective mass of the quark in its interactions with other quarks and leptons [64].

(d) A lower limit of 0.000014 is also reported [30]; see [65].

SU(3) colour singlet interaction.) Except for effects due to the different quark masses, quantum chromodynamic interactions are flavour independent. Figure 1-1 shows some lowest order interactions.

Although quarks and gluons come in colours, all observed physical particles are colourless. Thus the simplest particles made up of quarks are 3 quark (qqq) states and quark-antiquark ($q\bar{q}$) pairs [23]. A red quark, blue quark, and green quark together form a white (colourless) particle, and a quark and antiquark combine colour and anticolour for no colour. The qqq states are "baryons", and the $q\bar{q}$ states are "mesons". Figure 1-2 shows the lowest mass flavour multiplets of mesons and baryons made up of u, d, s, and c quarks; Table 1-3 lists properties of a number of mesons and baryons. "Exotic" quark combinations (e.g. $qqqq\bar{q}$) may exist, and "glueballs" (made up only of gluons) should exist and may have been observed [24].

The allowable interactions of hadrons can be viewed simply in terms of discrete quark and gluon interactions. For example, Figure 1-3 shows the strong decay $D^{*+} \rightarrow D^{+} \pi^{o}$, and the weak decay $D^{o} \rightarrow K^{-}\pi^{+}\pi^{o}$. (In QCD interactions many, many gluons are exchanged, but here only the minimum number necessary to conserve colour are shown; often no gluons are shown in diagrams of weak interactions or decays.)

1.1.2 Quantum Flavourdynamics (QFD)

Electromagnetic and weak interactions are together described by a non-Abelian SU(2)xU(1) gauge theory: Quantum Flavourdynamics (QFD) [25]. The SU(2) charge is the weak-isospin (T) component T_3, and the U(1) charge of a weak-isospin multiplet is its average electric charge. The electroweak forces are mediated by 3 massive intermediate vector bosons, the W^{+}, W^{-}, and Z^{o}, and by the (massless) photon(γ).

Under the charged current (Figure 1-4) the quarks and leptons are grouped into left-handed weak-isospin doublets (T=1/2) and right-handed singlets (T=0).

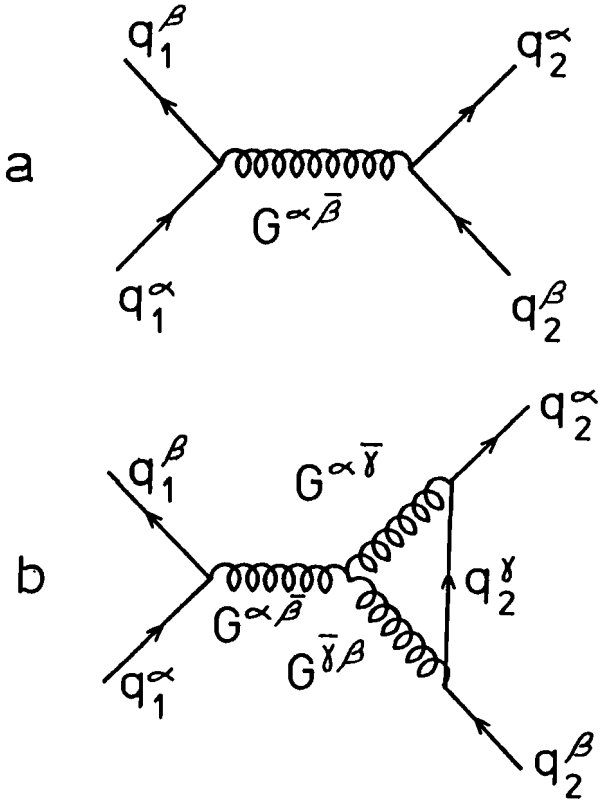

Figure 1-1: (a) The lowest order QCD interaction between two quarks and (b) a 3-gluon interaction. α, β, and γ are colour indices.

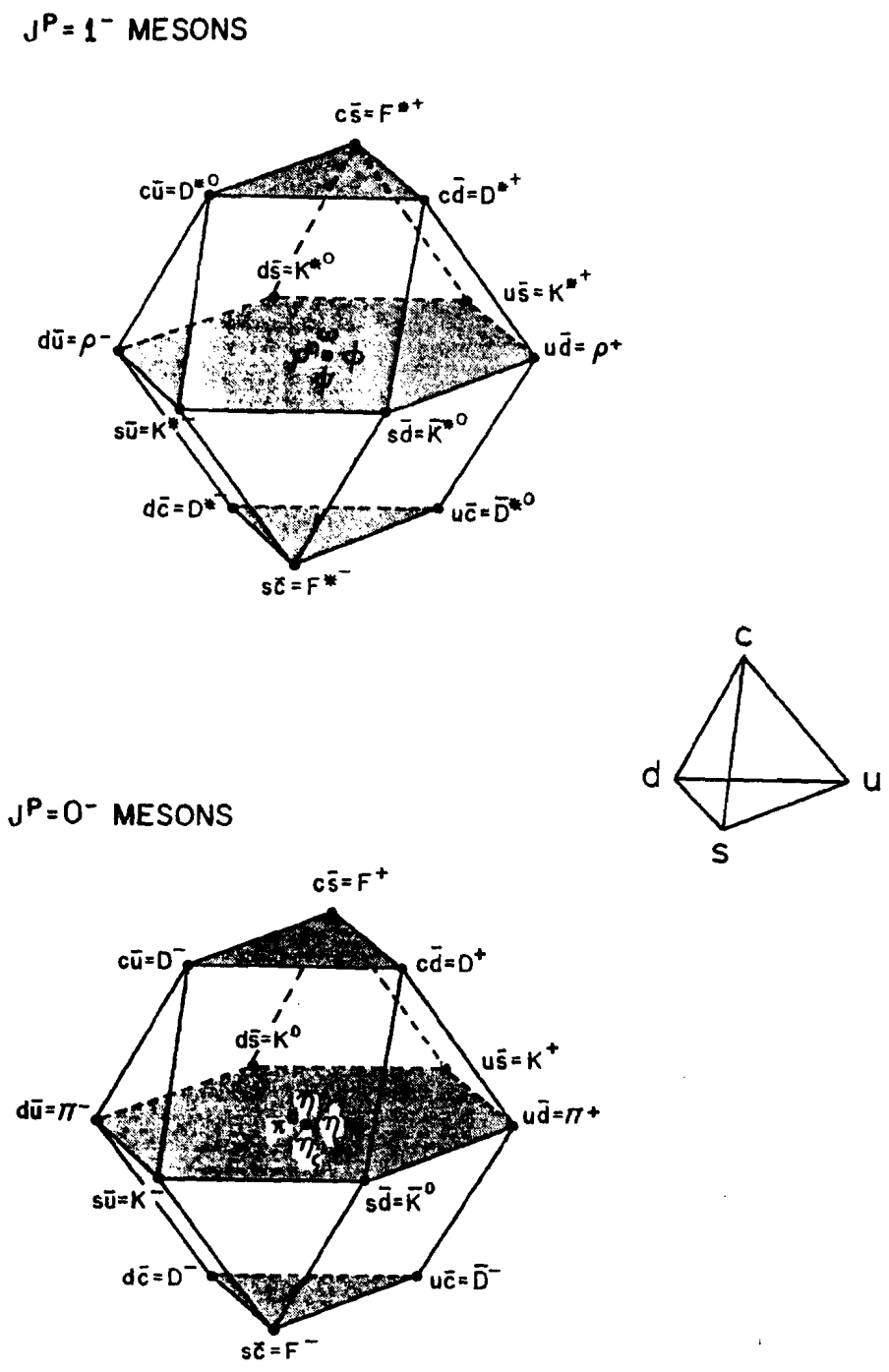

Figure 1-2: Lowest SU(4) multiplets of hadrons made from up (u), down (d), strange (s), and charm (c) quarks.

$J^P = \frac{1}{2}^+$ BARYONS

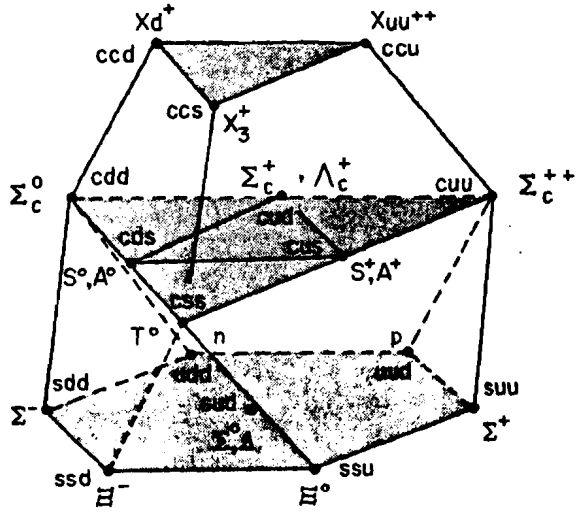

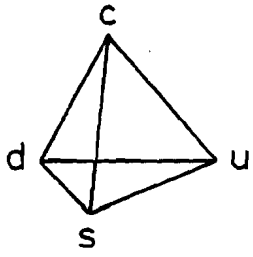

$J^P = \frac{3}{2}^+$ BARYONS

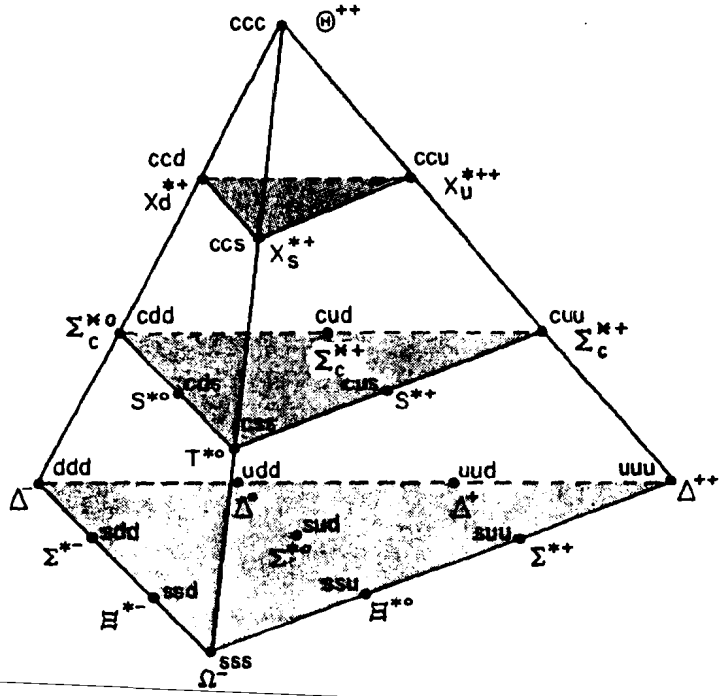

Table 1-3: Characteristics of some hadrons [65].

Particle	Valence Quarks	J^P	Mass (MeV/c^2)	Lifetime (seconds)	($c\tau$)
π^+	$u\bar{d}$	0^-	139.6	2.603×10^{-8}	(7.8m)
π^o	$u\bar{u}+d\bar{d}$	0^-	135.0	0.83×10^{-16}	(2.5μm)
K^-	$\bar{u}s$	0^-	493.7	1.237×10^{-8}	(3.7m)
K^o_S	$\bar{d}s+d\bar{s}$	0^-	497.7	0.892×10^{-10}	(2.7cm)
K^o_L	$\bar{d}s+d\bar{s}$	0^-	497.7	5.18×10^{-8}	(15.5m)
p	uud	$\frac{1}{2}^+$	938.3	$\gtrsim10^{38}$	
n	udd	$\frac{1}{2}^+$	939.6	925	(28Tm)
Λ^o	uds	$\frac{1}{2}^+$	1116	2.632×10^{-10}	(7.9cm)
Σ^+	uus	$\frac{1}{2}^+$	1189	0.800×10^{-10}	(2.4cm)
Σ^0	uds	$\frac{1}{2}^+$	1192	5.8×10^{-20}	(1.7nm)
Σ^-	dds	$\frac{1}{2}^+$	1197	1.482×10^{-10}	(4.4cm)
D^o	$c\bar{u}$	0^-	1865	$2.3\pm^{0.8}_{0.5}\times10^{-13}$*	(0.1mm)
D^+	$c\bar{d}$	0^-	1869	$11.5\pm^{7.5}_{3.5}\times10^{-13}$*	(0.3mm)
F^+	$c\bar{s}$	0^-	2020	$1.9\pm^{1.3}_{0.7}\times10^{-13}$*	(0.1mm)
Λ^+_c	cud	$\frac{1}{2}^+$	2282	$2.3\pm^{1.0}_{0.6}\times10^{-13}$*	(0.1mm)
D^{*o}	$c\bar{u}$	1^-	2007	strong decay	
D^{*+}	$c\bar{d}$	1^-	2010	strong decay	

The properties of the charmed particles are reviewed in Ref. [66].

* E-531 value [11,13], for lifetime (for world average see [65,67])

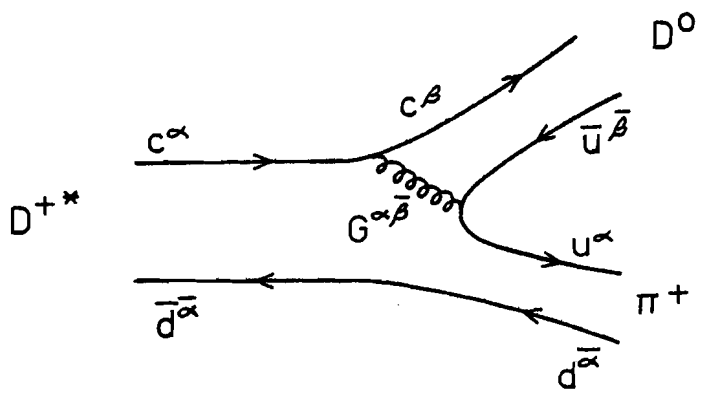

Figure 1-3a: $D^{*0} \rightarrow D^0 \pi^0$ strong decay (lowest order).

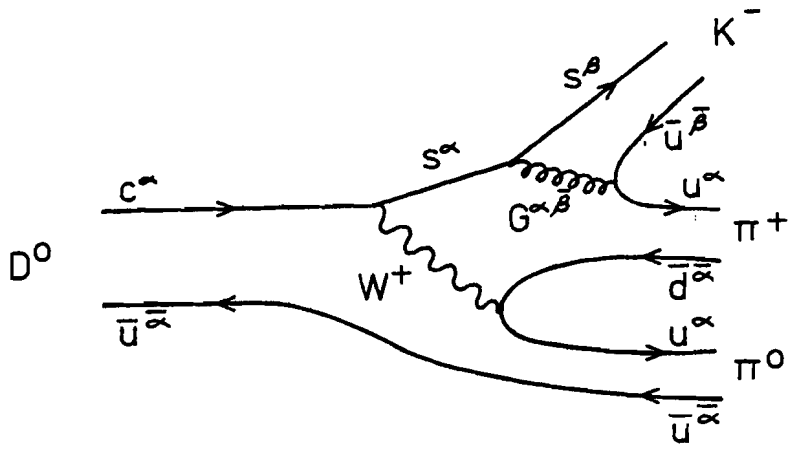

Figure 1-3b: $D^0 \rightarrow K^- \pi^+ \pi^0$ weak decay (lowest order).

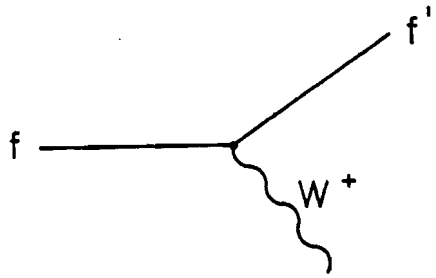

Figure 1-4: The lowest order diagram for the charged weak current. The W couples f to f', where ff' are either leptons ($\nu_e e^-$, $\nu_\mu \mu^-$, $\nu_\tau \tau^-$, ...) or quarks (ud', cs', tb', ...).

$$T_3 = +\tfrac{1}{2} \quad \begin{pmatrix} u \\ d' \end{pmatrix}_L \quad \begin{pmatrix} c \\ s' \end{pmatrix}_L \quad \begin{pmatrix} t \\ b' \end{pmatrix}_L \qquad T=0 \quad (u)_R,(d)_R,(s)_R,(c)_R,(b)_R,(t)_R$$

$$T_3 = -\tfrac{1}{2}$$

$$T_3 = +\tfrac{1}{2} \quad \begin{pmatrix} \nu_e \\ e^- \end{pmatrix}_L \quad \begin{pmatrix} \nu_\mu \\ \mu^- \end{pmatrix}_L \quad \begin{pmatrix} \nu_\tau \\ \tau^- \end{pmatrix}_L \qquad T=0 \quad (e^-)_R,(\mu^-)_R,(\tau^-)_R$$

$$T_3 = -\tfrac{1}{2}$$

No right-handed neutrinos have been observed; the absence of ν_R implies a zero Dirac mass for the neutrinos. The d',s',b' are quark weak eigenstates that are dominated by the quark mass eigenstates d,s,b. The mass eigenstates (states of definite mass) and weak eigenstates (states of definite flavour) do not necessarily coincide, i.e. $d \neq d'$, $s \neq s'$, $b \neq b'$, and ν_e,ν_μ,ν_τ may be combinations of neutrino mass eigenstates ν_1,ν_2,ν_3; u,c,t and e^-,μ^-,τ^- are (by definition) both mass eigenstates and weak eigenstates.

The charged weak current is

$$J^c_\alpha = (\bar{u}\ \bar{c}\ \bar{t})\gamma_\alpha \frac{(1-\gamma_5)}{2}\begin{pmatrix} d' \\ s' \\ b' \end{pmatrix} + (\bar{\nu}_e\ \bar{\nu}_\mu\ \bar{\nu}_\tau)\gamma_\alpha \frac{(1-\gamma_5)}{2}\begin{pmatrix} e^- \\ \mu^- \\ \tau^- \end{pmatrix}$$

or, in terms of the mass eigenstates,

$$J^c_\alpha = (\bar{u}\ \bar{c}\ \bar{t})\gamma_\alpha \frac{(1-\gamma_5)}{2} U_q \begin{pmatrix} d \\ s \\ b \end{pmatrix} + (\bar{\nu}_1\ \bar{\nu}_2\ \bar{\nu}_3)\gamma_\alpha \frac{(1-\gamma_5)}{2} U_\ell \begin{pmatrix} e^- \\ \mu^- \\ \tau^- \end{pmatrix}$$

where U_q and U_ℓ are unitary 3x3 matrices:

$$U_q\ (\equiv U_{quark}) = \begin{pmatrix} U_{ud} & U_{us} & U_{ub} \\ U_{cd} & U_{cs} & U_{cb} \\ U_{td} & U_{ts} & U_{tb} \end{pmatrix}$$

and

$$U_\ell\ (\equiv U_{lepton} = U_{i\alpha}) = \begin{pmatrix} U_{1e} & U_{1\mu} & U_{1\tau} \\ U_{2e} & U_{2\mu} & U_{2\tau} \\ U_{3e} & U_{3\mu} & U_{3\tau} \end{pmatrix}$$

These matrices each have only 4 independent components.

U_q is commonly written in the Kobayashi-Maskawa [26] form

$$U = \begin{pmatrix} c_1 & -s_1c_3 & -s_1s_3 \\ s_1c_2 & c_1c_2c_3-s_2s_3e^{-i\delta} & c_1c_2s_3+s_2c_3e^{-i\delta} \\ s_1s_2 & c_1s_2c_3+c_2s_3e^{-i\delta} & c_1s_2s_3-c_2c_3e^{-i\delta} \end{pmatrix}$$

$c_j=\cos\theta_j$ and $s_j=\sin\theta_j$ (j=1,2,3), where the θ_j are the generalized Cabbibo mixing angles and δ is a complex (CP violating) phase. For quarks, the angle θ_1 controls the relative strength of u↔d transitions, θ_2 controls the relative rates of d↔c and d↔t, and θ_3 controls the relative rates for u↔s and u↔b.

The amplitude for a charged current $f_i \leftrightarrow f_j$ transition at low q^2 ($|q| \ll M_W \approx 80$ GeV, f_i and f_j are either quarks or leptons) is determined by the effective charged weak Lagrangian

$$4\frac{G_F}{\sqrt{2}} J^{c\alpha} J_\alpha^{c\dagger} \quad ,$$

and so the rate for the transition is proportional to

$$G_F^2 |U_{f_i f_j}|^2 \quad ,$$

if the fermion masses and strong interactions are ignored. The strength of the weak interaction is given by the weak coupling constant G_F^2.

In many situations, transitions between only two quark or lepton generations are considered. For 2 generations there is only 1 independent mixing parameter and we can write U_ℓ or U_q in the Cabibbo form [27]

$$U_{(2\text{ generations})} = \begin{pmatrix} \cos\theta & \sin\theta \\ -\sin\theta & \cos\theta \end{pmatrix}$$

Measuring the amount of mixing among both quarks and leptons is clearly of fundamental interest. Current experimental constraints on U_{quark} are shown in Table 1-4, and a representative, but not unique,

Table 1-4: Experimental constraints to quark mixings.

(1) $\|U_{ud}\| = 0.9737 \pm 0.0025$	from the muon lifetime and nuclear β decay [68]
(2) $\|U_{us}\| = 0.219 \pm 0.011$	from hyperon and kaon β decays [68]
(3) $\|U_{cd}\| = 0.24 \pm 0.03$	from charm interpretation of neutrino dimuon data [20]
(4) $\|U_{cs}\| = 0.66 \pm 0.33$	from D^+ lifetime and D semileptonic B.R. compared with theory [69]
$\|U_{cs}\| > 0.81$	from charm interpretation of neutrino dimuon data [70]
(5) $\|U_{cb}\| \gg \|U_{ub}\|$	from indirect studies of B meson decays [71]

From the above limits and unitarity [28,70]:

$|U_{ub}| = 0.06 \pm 0.06$
$|U_{cb}| < 0.54$
$|U_{td}| < 0.12$
$|U_{ts}| < 0.55$
$|U_{tb}| > 0.83$ *

In terms of the Kobayashi-Maskawa angles:

$\|\sin\theta_1\| = 0.228 \pm 0.011$	[28]
$\|\cos\theta_2\| = 1.05 \pm 0.14$	[20]
$\|\sin\theta_3\| = 0.28 \pm {}^{0.21}_{0.28}$	[68,72] **
$\|\sin\delta\| \gtrsim 10^{-3}$	[68] ***

* This lower limit is only for three quark generations; there is no lower limit if there are quarks heavier than the t quark.

** There is also a lower limit, based on the upper limit to the beauty lifetime [73], that depends on the value of θ_2.

*** The limit to δ, based on CP violating kaon decays, depends on the values of θ_2 and θ_3.

matrix [28] consistent with the known constraints is

$$U_q = \begin{pmatrix} 0.97 & 0.22 & 0.068 \\ -0.22 & 0.85-0.00066i & 0.48+0.0021i \\ -0.046 & 0.48+0.0032i & -0.88-0.0010i \end{pmatrix}$$

For leptons, there is no compelling evidence [29] that U_{lepton} is not simply the identity matrix; i.e. the mass and weak eigenstates may be the same. Also, if the neutrino masses are all equal, then the mass eigenstates are degenerate and can simply be defined to be the weak eigenstates. Except for one unconfirmed result [30], the experimentally measured neutrino masses are all consistent with zero (see Table 1-2).

If the neutrino masses are not all the same, then the observable effects of lepton mixing will depend on both the amount of mixing and the size of the mass differences. For reasons of computational and illustrational simplicity, the experimental constraints on U_ℓ are usually displayed in the two neutrino (Cabibbo-like) approximation. Figure 1-5 shows the current experimental limits to neutrino mixings. These limits are not too strict in comparison to the prejudice of Grand Unified Theories that lepton mixing should be comparable to quark mixing [31], i.e. $\sin^2(2\theta)$ $(\approx|U_{i\alpha}|^2) \sim 0.01-0.1$.

All these limits are from searches for changes in neutrino weak eigenstates. If $\nu_e,\nu_\mu,\nu_\tau,\ldots$ do mix, then the neutrinos should oscillate between the weak eigenstates in an manner analogous to the mixing of K^o and $\bar{K}^o$. For example, a neutrino produced as a ν_μ weak eigenstate would propagate in time as a mixture of different mass eigenstates and could change (oscillate) into a ν_τ weak eigenstate.

1.2 Lifetimes of Weakly Decaying Particles

The decay of a charged lepton is very simply described as the emission of a virtual W boson that materializes as a fermion-antifermion pair (see Figure 1-6). If the masses and interactions of decay

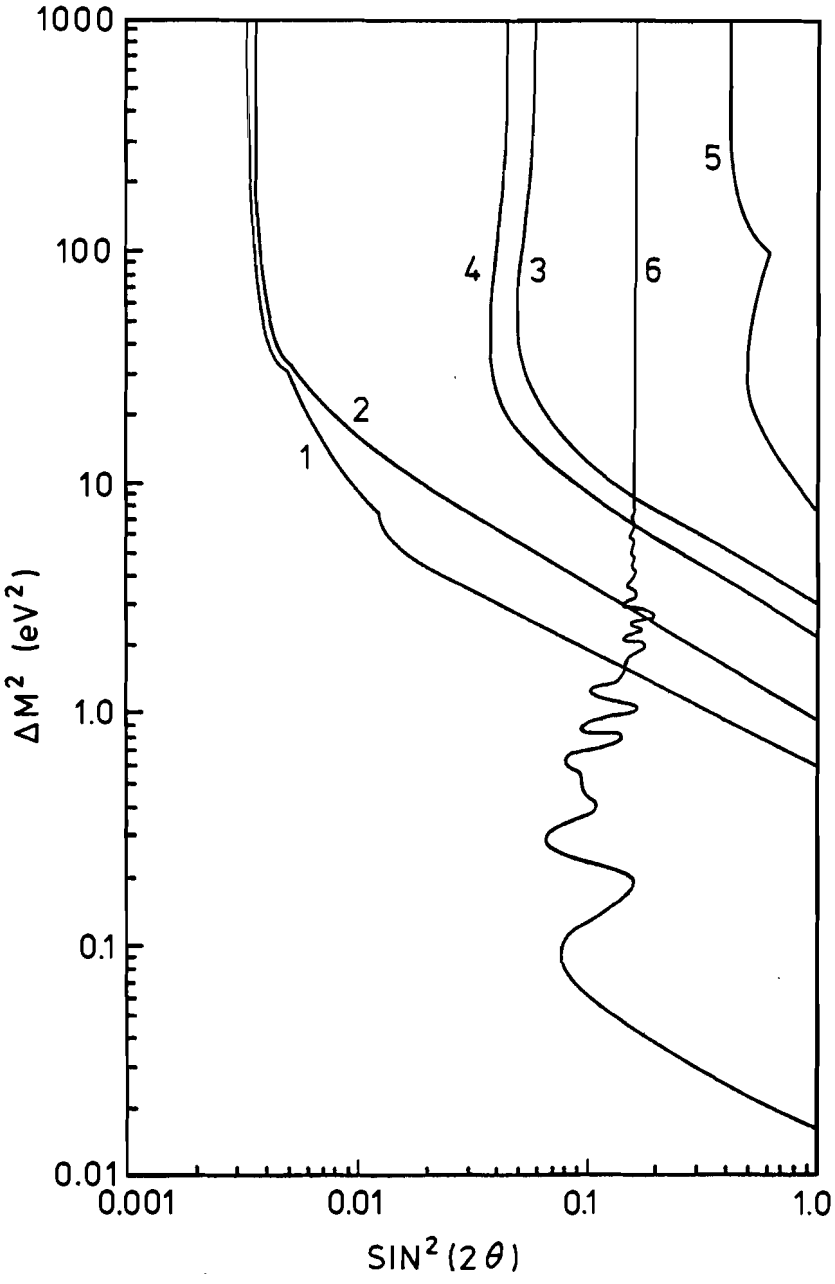

Figure 1-5: World limits (90% C.L.) to neutrino mixings.

1. ν_μ-ν_e [32,33,34,35,36]
2. $\bar{\nu}_\mu$-$\bar{\nu}_e$ [32]
3. ν_μ-ν_τ [33,34,35]
4. $\bar{\nu}_\mu$-$\bar{\nu}_\tau$ [37]
5. ν_e-ν_x [33,34,38]
6. $\bar{\nu}_e$-$\bar{\nu}_x$ [39]

θ is the two component mixing angle in the 2 generation approximation; $\sin^2 2\theta \approx |U_{i\alpha}|^2$ for small mixings.

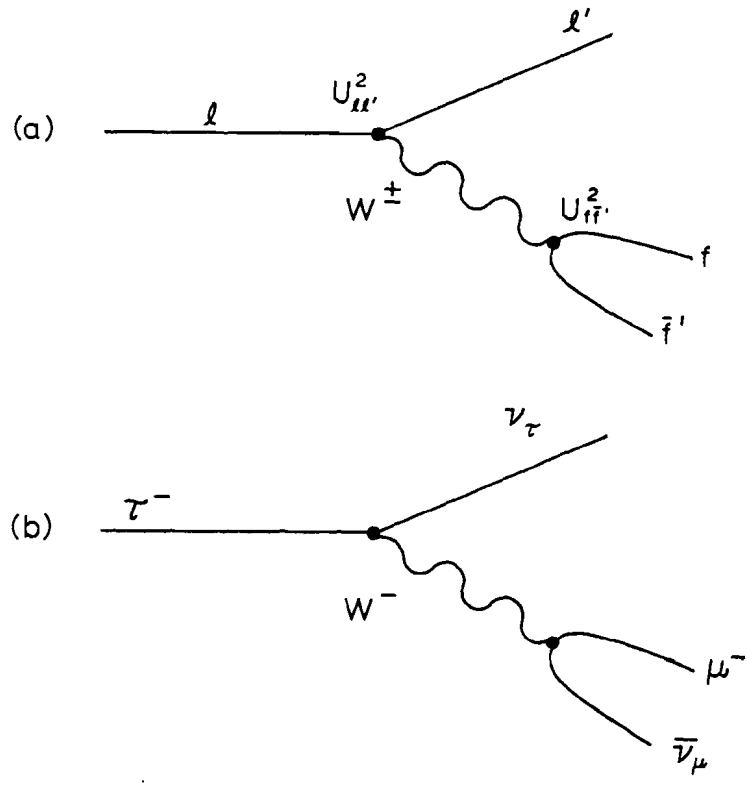

Figure 1-6: Charged current decay of leptons (lowest order). The lepton and ff' vertices have strengths proportional to $|U_{\ell\ell'}|^2$ and $|U_{ff'}|^2$. The fermion-antifermion pair $f\bar{f}'$ are a coupled quark-antiquark ($q\bar{q}$) or lepton-antilepton ($\ell\bar{\ell}'$) pair. A specific decay ($\tau^- \to \mu^- \nu_\tau \bar{\nu}_\mu$) is shown in (b); instead of the $\mu^-\bar{\nu}_\mu$ pair, the other possible $f\bar{f}'$ pairs are $e^-\bar{\nu}_e$ and $\bar{u}s$ or $\bar{u}s$ in 3 colour-anticolour combinations.

secondaries are neglected (except for energy conservation mass thresholds), then the decay lifetime is

$$\tau_\ell = \frac{192\pi^3}{NG_F^2 m_\ell^5}\left[\sum_i |U_{i\ell}|^2\right]^{-1}$$

where N is the number of fundamental fermion pairs (ff') the lepton can decay into (as allowed by energy, charge, and lepton numbers conservation). N=0 for the electron - there are no lighter charged fermions it can decay into; N=1 for the muon - it can only decay into $e\nu\bar{\nu}$, it cannot decay into quarks because the lightest hadron, the pion, is heavier than the muon; and N=5 for the τ - it can decay into either of the 2 lighter charged leptons or any of 3 colours of quarks. The electron is stable, the measured muon lifetime can be used to give us the value of G_F^2,

$$G_F^2 = \frac{192\pi^3}{m_\mu^5}\frac{1}{\tau_\mu} ,$$

and the expected tau lifetime is

$$\tau_\tau = \frac{1}{5}\left(\frac{m_\mu}{m_\tau}\right)^5 \tau_\mu\left[\sum_i |U_{i\tau}|^2\right]^{-1}$$

The sum over "i" is over all neutrinos that are not more massive than the tau. If the tau couples only to such light neutrinos then the sum is equal to 1, and the tau lifetime would be 3.2×10^{-13} seconds. The factor of 1/5 in the above equation is altered by the effects of the masses of the secondary particles and their interactions. A more accurate estimate of the lifetime uses the measured tau semi-electronic branching ratio (0.17 ± 0.01 [40] instead of "1/5") to predict a lifetime $\tau_\tau \cong 2.8\times10^{-13}$s. Published measurements of the tau lifetime are $(4.6\pm1.9)\times10^{-13}$s and $(4.9\pm2.0)\times10^{-13}$s [41].

Unlike leptons, quarks do not decay as free particles, but the "naive" model for quark decays is exactly in analogy with lepton decays. For example, the expected lifetimes of the charm and beauty quarks are

$$\tau_{charm} = \frac{1}{5}\left(\frac{m_\mu}{m_c}\right)^5 \tau_\mu \left[\,|U_{cd}|^2+|U_{cs}|^2\right]^{-1} \sim 5\times10^{-13}\,s$$

$$\tau_{beauty} = \frac{1}{6}\left(\frac{m_\mu}{m_b}\right)^5 \tau_\mu \left[\,|U_{cb}|^2+|U_{ub}|^2\right]^{-1} \sim 10^{-14}\,s$$

Of course, it is particles containing the quarks which are seen to decay, not free quarks, and so the naive model is incomplete. The actual hadron lifetimes differ from the naive quark lifetimes because the masses and interactions of the parent and secondary quarks can have large effects on decay rates. These effects are very important for the decays of light hadrons made of u, d, and s quarks. The measurements of the charmed particle lifetimes made by this experiment [5-13] provide important information on the secondary effects in charmed hadron decays.

1.3 Kinematics of Neutrino-Nucleus Interactions [42]

The interaction of a lepton (L) with a nucleon (N) producing a lepton (L') plus hadrons (H)

$$L + N \rightarrow L' + H \qquad \text{(see Figure 1-7)}$$

is kinematically described as

$$k + p \rightarrow k' + p'$$

where k, p, k', and p' are the four-momenta of the incident lepton, the target nucleon, the outgoing lepton, and the final hadronic system. The four-momentum transfer of the interaction is

$$q \equiv k-k' = p-p'$$

From the 4 four-momenta we define 3 independent Lorentz invariant scalars

$$Q^2 \equiv -q\cdot q$$
$$W^2 \equiv p'\cdot p'$$
$$\nu \equiv (p\cdot q)/M_N \qquad (M_N = \text{nucleon mass})$$

and 2 independent dimensionless scaling variables

$$x \equiv \frac{-q\cdot q}{2p\cdot q} \qquad y \equiv \frac{q\cdot p}{k\cdot p} \qquad (0< x,y <1)\ .$$

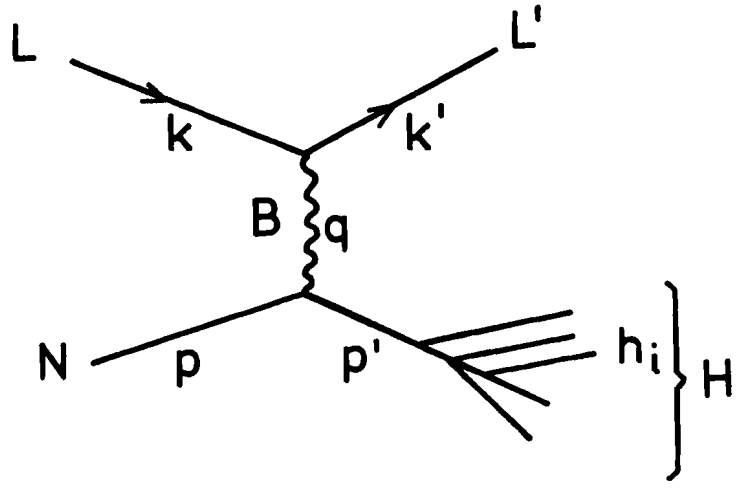

Figure 1-7: Interaction of a lepton (L) with a nucleon (N), mediated by a vector boson (B), resulting in a lepton (L') and hadrons (H). (k, k', q, p, and p' are four-momenta; h_i is the four-momentum of a specific hadron in the hadronic system.)

Q is the mass of the exchanged virtual boson, W is the mass of the produced hadronic system, x is the fraction of the nucleon's momentum struck, and y is a measure of the inelasticity of the interaction (y=0 for elastic scattering).

In particular, in the laboratory frame (the rest frame of the target nucleon) for charged current muon neutrino interactions

$$\nu_\mu + N \rightarrow \mu^- + X$$

the kinematic variables are:

$$k = (E_\nu, \vec{P}_\nu)$$
$$p = (M_N, \vec{0}) \qquad [\vec{0}=(0,0,0)]$$
$$k' = (E_\mu, \vec{P}_\mu)$$
$$p' = (E_H, \vec{P}_H)$$

$$Q^2 = 2E_\nu E_\mu - 2P_\nu P_\mu \cos\theta - m_\nu^2 - m_\mu^2$$
$$\nu = E_\nu - E_\mu \quad (= E_H - M_N)$$
$$W^2 = -Q^2 + 2M_N\nu + M_N^2$$

and

$$x = \frac{Q^2}{2M_N\nu} \qquad\qquad y = \frac{\nu}{E_\nu} = \frac{E_\nu - E_\mu}{E_\nu}$$

The E's and P's are laboratory energies and three-momenta, θ is the ν-μ laboratory scattering angle, and m_ν and m_μ are the neutrino and muon masses. In this frame ν is the difference between the intial hadron energy, M_N, and the final hadron energy, E_H.

The hadronic system consists of one or more hadrons. The kinematic properties of a particular hadron, relative to the total hadronic system, are described by the hadron's energy fraction, transverse momentum, and Feynman X.

For the i^{th} hadron with four-momentum

$$h_i = (E_i, \vec{P}_i) \ ,$$

we define the Lorentz scalar

$$Z = \frac{h_i \cdot p}{q \cdot p} \ .$$

In the lab frame, Z is the fraction of the total hadronic energy carried by the hadron in question:

$$Z = \frac{E_i}{\nu} \qquad \text{(in lab frame).}$$

Feynman X, X_F, is defined in the centre-of-momentum (C.O.M.) frame of the hadronic system to be

$$X_F = \frac{P^*_{\parallel}}{P^*_{\parallel max}} \quad .$$

$P^*_{\parallel}$ is the component of the hadron's momentum (in the C.O.M. frame) parallel to $\vec{P}_H$ (lab), and $P^*_{\parallel max}$ is the maximum C.O.M. momentum the hadron could have consistent with conservation laws (e.g. charge, baryon number). In general,

$$P^{*2}_{\parallel max} = [W^4+m_h^4+m_r^4-2W^2m_h^2-2m_h^2m_r^2-2m_r^2W^2]/(2W)^2$$

where m_h is the mass of the hadron and m_r is the mass of the lightest possible particle(s) recoiling against the hadron. (For inclusive-nucleus neutrino reactions ($\nu N \to h_i X$, X is anything), I use $m_r=0$ if the hadron, h, is a baryon (e.g. a proton or a Λ_c^+), and $m_r=M_N$ if h is a meson (e.g. a pion or a D^o).) X_F is not defined for elastic and quasi-elastic scattering where the hadronic system consists of only one particle.

The transverse momentum of a hadron is defined relative to the direction of the total hadronic system. $P_\perp$ is the component of the hadron's momentum perpendicular to $\vec{P}_H$, and P_{out} is the momentum of the hadron out of the plane defined by $\vec{P}_\nu$ and $\vec{P}_\mu$. If the target nucleon is at rest, then $\vec{P}_\nu$, $\vec{P}_\mu$, and $\vec{P}_H$ must all lie in the same plane (See Figure 1-8). For a complex nuclear target, such as nuclear emulsion, this is still a good approximation, but the target nucleons have some motion due to Fermi momentum ($\lesssim$250 MeV/c [43]) within the nucleus, so $\vec{P}_\nu$, $\vec{P}_\mu$, $\vec{P}_H$ no longer lie exactly in the same plane. If hadrons are produced isotropically about $\vec{P}_H$ (i.e. $P_{out} = P_\perp \sin\theta$, where θ is a uniformly distributed angle), then the mean value of P_{out} is $\langle P_{out}\rangle = \frac{2}{\pi}\langle P_\perp\rangle$, and $\langle P^2_{out}\rangle = \frac{1}{2}\langle P^2_\perp\rangle$.

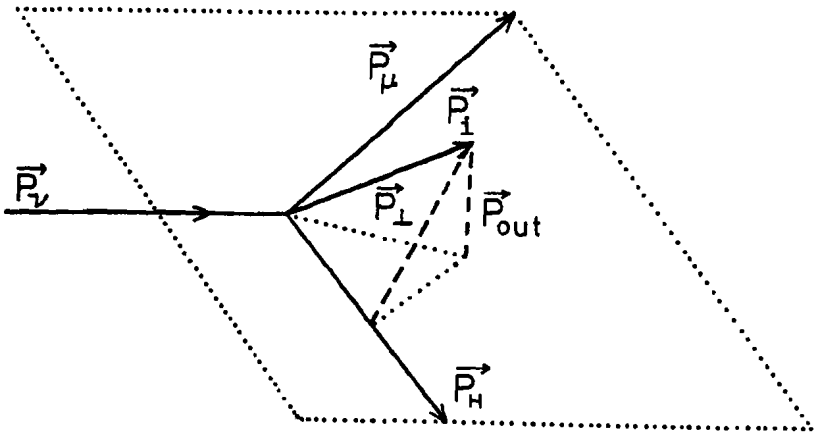

Figure 1-8: Definition of $P_\perp$ and P_{out} for a nucleon target at rest. $\vec{P}_\nu$, $\vec{P}_\mu$, and $\vec{P}_H$ lie in the same plane, i.e. $\hat{P}_\nu \times \hat{P}_\mu = \hat{P}_\nu \times \hat{P}_H$ ("^" indicates unit direction vector).

$$P_\perp \equiv |\vec{P}_i - (\vec{P}_i \cdot \hat{P}_H)\hat{P}_H|$$

$$P_{out} \equiv \vec{P}_i \cdot \hat{P}_\nu \times \hat{P}_\mu = \vec{P}_\perp \cdot \hat{P}_\nu \times \hat{P}_\mu$$

The above formulation has used charged current muon neutrino interactions as a specific example, but the definitions can be generally applied to any charged current interaction,

$$\nu_\ell + N \to \ell^- + X \quad ,$$

or neutral current interaction,

$$\nu_\ell + N \to \nu_\ell + X \quad .$$

ν_ℓ and ℓ^- are a neutrino and charged lepton of any flavour, ℓ=e,μ,τ,....

1.4 Neutrino Cross Sections and Structure Functions

The inclusive cross section for charged current neutrino interactions has the general form

$$\frac{d^2\sigma^{\nu(\bar{\nu})}}{dxdy} = \frac{G^2 M_N E_\nu}{\pi} \left\{B(x,y,Q^2) + \frac{m_\ell y}{4E_\nu M_N} A(x,y,Q^2)\right\} \qquad \{1.4a\}$$

where m_ℓ is the mass of the outgoing charged lepton,

$$B(x,y,Q^2) = (1-y-\frac{M_N}{2E_\nu}xy)F_2^{\nu(\bar{\nu})} + xy^2F_1^{\nu(\bar{\nu})} \mp (y-\tfrac{1}{2}y^2)xF_3^{\nu(\bar{\nu})} \qquad \{1.4b\},$$

and

$$A(x,y,Q^2) = \frac{m_\ell^2 y}{4E_\nu M_N}\Big[2F_1^{\nu(\bar{\nu})} - \Big(\frac{M_N}{yE_\nu}+\frac{2xM_N^2}{m_\ell^2}\Big)F_2^{\nu(\bar{\nu})} \pm F_3^{\nu(\bar{\nu})} + \Big(2x+\frac{m_\ell^2}{yE_\nu M_N}\Big)F_4^{\nu(\bar{\nu})} - \frac{2}{y}F_5^{\nu(\bar{\nu})} + F_6^{\nu(\bar{\nu})}\Big] \qquad \{1.4c\}.$$

The neutrino mass is assumed to be small ($m_\nu << m_\ell, M$), and so terms proportional to m_ν have been neglected.

The $F_i(=F_i(x,Q^2)$, i=1,6) are the 6 nucleon structure functions. (Note: F_3 is chosen to be a negative quantity.) The 6 structure functions can be reduced to 2 by symmetry arguments and the assumption that the neutrino interacts with spin $\frac{1}{2}$ partons within the nucleon:

$F_6(x,Q^2) = 0$	required by time reversal invariance
$F_4(x,Q^2) = 0$	required by asymptotic chiral symmetry
$2xF_1(x,Q^2) = F_2(x,Q^2)$	Callan-Cross relation - depends on the elementary fields (quarks and leptons) having spin 1/2

$$F_5(x,Q^2) = 2F_1(x,Q^2) \quad \text{from } 2xF_1(x,Q^2)=F_2(x,Q^2) \text{ and kinematical constraints}$$

$$= F_2(x,Q^2)/x$$

In the Bjorken limit of $Q^2\to\infty$ with fixed x, the F_i are functions of x only.

In the standard quark-parton model the structure functions of a nucleon are given by

$$F_2^{\nu}(x,Q^2) = 2x(d(x)+\bar{u}(x)+s(x)+\bar{c}(x)+....)$$

$$F_2^{\bar{\nu}}(x,Q^2) = 2x(u(x)+\bar{d}(x)+c(x)+\bar{s}(x)+....)$$

$$F_3^{\nu}(x,Q^2) = -2(d(x)-\bar{u}(x)+s(x)-\bar{c}(x)+....)$$

$$F_3^{\bar{\nu}}(x,Q^2) = -2(u(x)-\bar{d}(x)+c(x)-\bar{s}(x)+....)$$

and

$$q(x) = u(x)+d(x)+s(x)+c(x)+...$$

$$\bar{q}(x) = \bar{u}(x)+\bar{d}(x)+\bar{s}(x)+\bar{c}(x)+...$$

where q(x) and $\bar{q}(x)$ are the quark and antiquark content of the nucleon for some Q^2, i.e. q(x)dx is the number of quarks in the target nucleon with momentum fraction x in the range x to x+dx. (Note: q(x) and $\bar{q}(x)$ are not independent of Q^2, they could be written as $q(x,Q^2)$.) u, d, s, and c refer to up, down, strange, and charm quarks.

Most of the quark momentum in a nucleon is carried by the three valence quarks (uud in a proton, udd in a neutron), but ocean quarks (virtual $q\bar{q}$ pairs) also carry some momentum. Thus the u(x) and d(x) distributions are sums of valence and ocean contributions, while $\bar{q}(x)$ and $s(x)+c(x)+...$ are pure ocean contributions. (Note that ocean quarks are always $q\bar{q}$ pairs, so $s(x)=\bar{s}(x)$, $c(x)=\bar{c}(x)$, and the ocean content of u and d quarks is equal to $\bar{u}(x)$ and $\bar{d}(x)$.) The ocean distributions are concentrated at small x, each ocean quark carrying little momentum, but

the total ocean momentum is about 1/4 of the total quark momentum [44] (this fraction decreases at lower energies [45]). The ocean should contain almost equal numbers of light quarks, but the strange quark mass is large enough to reduce s(x) somewhat, i.e. $\overline{U}\approx\overline{D}\gtrsim\overline{S}$, where $\overline{U}\equiv\int x\bar{u}(x)dx$, $\overline{D}\equiv\int x\bar{d}(x)dx$ and $\overline{S}(\equiv\int x\bar{s}(x)dx$. Because of the large charm quark mass, the total charm content of the nucleon is expected to be very small, and that of heavier quarks (e.g. beauty) even smaller. In addition to quarks, nucleons also contain gluons, and these gluons carry slightly more than half of the total nucleon momentum: the fraction of the total momentum carried by the quarks is $Q+\overline{Q}(\equiv\int x[q(x)+\bar{q}(x)]dx)=0.45\pm0.02$ [46].

In the free quark-parton model limit

$$B(x,y,Q^2) = \left[(1-y-\frac{M_N}{2E_\nu}xy)+\frac{1}{2}y^2\right]F_2^{\nu(\bar{\nu})} \mp (y-\frac{1}{2}y^2)xF_3^{\nu(\bar{\nu})} \qquad \{1.4d\},$$

and

$$A(x,y,Q^2) = \frac{m_\ell^2 y}{4E_\nu M_N}\left[\left(\frac{1}{x}-\left(\frac{M_N}{yE_\nu}+\frac{2xM_N^2}{m_\ell^2}+\frac{2}{xy}\right)F_2^{\nu(\bar{\nu})} \pm F_3^{\nu(\bar{\nu})}\right]\right. \qquad \{1.4e\}.$$

If the produced lepton is a muon or electron ($(m_\ell^2/E_\nu M_N)\ll1$), then $A(x,y,Q^2)$ can be ignored and the high energy ($E_\nu\gg M_N$) deep inelastic charged current neutrino interaction cross sections are

$$\frac{d\sigma^\nu}{dxdy} = \frac{G^2M_NE_\nu}{\pi}\,2x\left[(d(x)+s(x)+\ldots)+(\bar{u}(x)+\bar{c}(x)+\ldots)(1-y)^2\right] \qquad \{1.4f\}$$

and for antineutrinos

$$\frac{d\sigma^{\bar{\nu}}}{dxdy} = \frac{G^2M_NE_{\bar{\nu}}}{\pi}\,2x\left[(\bar{d}(x)+\bar{s}(x)+\ldots)+(u(x)+c(x)+\ldots)(1-y)^2\right] \qquad \{1.4g\}.$$

(Note: These cross sections are written with explicit flavour quark structure functions: they do not follow the common convention of defining u(x) and d(x) in terms of the proton.)

1.5 Charm Production by Neutrinos

There are many conceivable ways for neutrino interactions to produce charmed particles. Charm could be produced in charged or neutral current interactions, charm could be produced from valence or ocean quarks, from weak boson diffraction, or from gluon fragmentation, charm could be produced by pair or single production, and charm could be produced directly or indirectly. Many possible charm production processes are shown in Figures 1-9 to 1-13.

1.5.1 Deep Inelastic Charged Current Charm Production

The dominant mechanism for neutrino charm production at Fermilab energies is expected to be direct deep inelastic charged current production of a single charmed quark from a down or strange quark. Neutrinos can produce a charm quark from a valence down quark (Figure 1-9a) or from a strange ocean quark (Figure 1-9b); similarly, antineutrinos can produce anti-charm from anti-strange ocean quarks. (There are no valence antiquarks, so there is no antineutrino production process corresponding to Fig. 1-9a.) Charm and anti-charm production from ocean down quarks also occurs, but this is only a small part of the total rate, and is subsumed in d(x) in calculating the production cross section.

Deep inelastic charm production is simply a specific part of the deep inelastic neutrino cross section discussed in Sec. 1.4. The charged weak current couples d, s, and b quarks to the charm quark, so the rate for charm production depends on the d, s, and b quark content of the nucleon target and on the weak couplings of these quarks to the charmed quark. Neutrino interactions will produce charm, and antineutrino interactions will produce anti-charm. For massless quarks, the production cross section follows from Eqns. 1.4f,g and from the charged current weak couplings. For neutrinos,

$$\frac{d\sigma(\nu_\mu N\to Xc\mu^-)}{dxdy} = \frac{G^2 M_N E_\nu}{\pi} 2x\left[\,|U_{cd}|^2 d(x)+|U_{cs}|^2 s(x)+|U_{cb}|^2 b(x)\right] \qquad \{1.5a\}$$

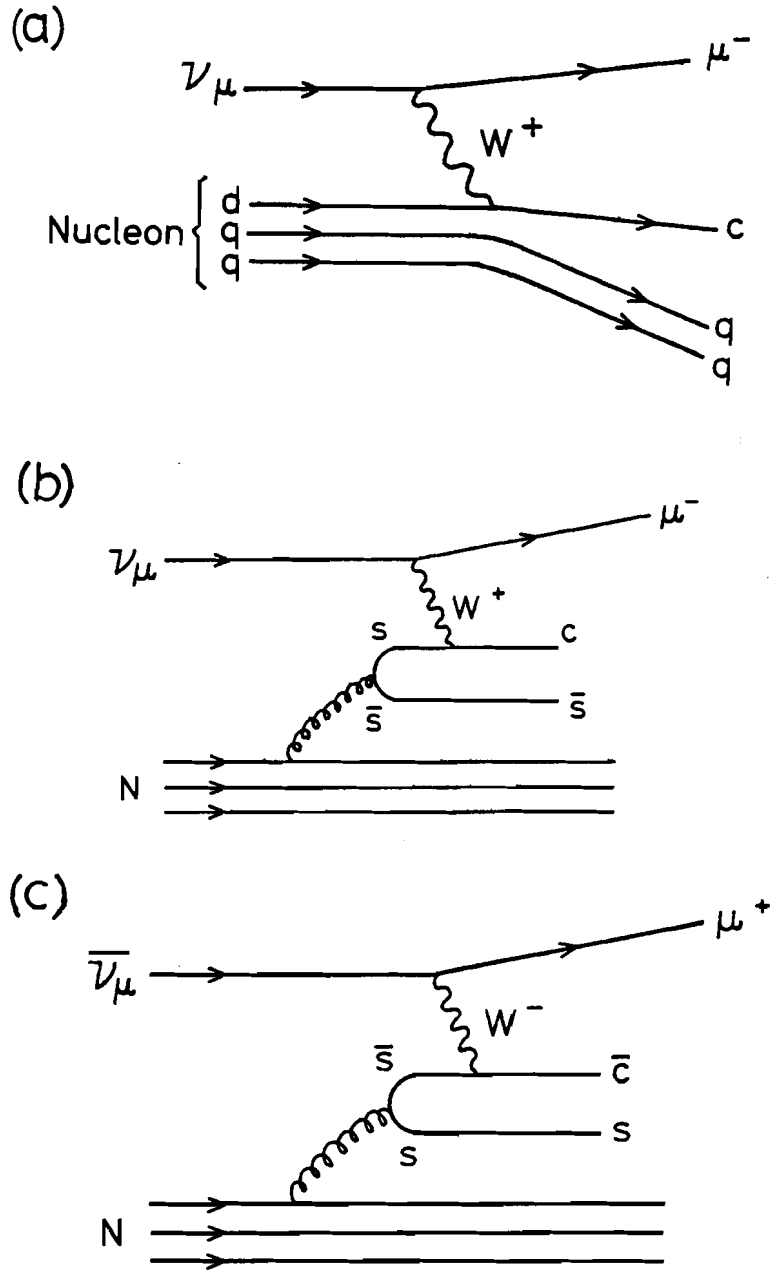

Figure 1-9: Charged current charm production by neutrinos:

(a) from valence d quarks ($\nu_\mu d \to \mu^- c$)

$$\frac{d\sigma}{dxdy} \propto d(x)|U_{cd}|^2$$

(b) from ocean s quarks ($\nu_\mu s \to \mu^- c$)

$$\frac{d\sigma}{dxdy} \propto s(x)|U_{cs}|^2$$

(c) from ocean $\bar{s}$ quarks ($\bar{\nu}_\mu s \to \mu^+ \bar{c}$)

$$\frac{d\sigma}{dxdy} \propto \bar{s}(x)|U_{cs}|^2$$

and for antineutrinos

$$\frac{d\sigma(\bar{\nu}_\mu N\to Xc\mu^+)}{dxdy} = \frac{G^2 M_N E_\nu}{\pi} 2x\left[\,|U_{cd}|^2\bar{d}(x)+|U_{cs}|^2\bar{s}(x)+|U_{cb}|^2\bar{b}(x)\right] \qquad \{1.5b\}$$

The contribution to charm production from beauty quarks must be infinitesimal (b(x) is tiny because of the large b mass) and can be ignored.

The mass of the charm quark is too large to be ignored at Fermilab energies, so the above formulae must be modified to include the effect of a non-zero mass for the (final) produced quark. In the quark-parton model, massive quarks require the structure functions to scale in ξ instead of x, where ξ is the slow rescaling variable [47]. If the masses of the target nucleon and (initial) struck quark are ignored and $Q^2 \ll \nu^2$, then for charm quark production:

$$\xi = \frac{Q^2+m_c^2}{2M_N\nu} = x+\frac{m_c^2}{2M_N\nu}$$

(ξ reduces to x for $\nu\to\infty$.) The charm production cross sections are now given by

$$\frac{d\sigma(\nu_\mu N\to Xc\mu^-)}{dxdy} = \frac{G^2 M_N E_\nu}{\pi}\left(1-y+\frac{xy}{\xi}\right)2\xi\left[\,|U_{cd}|^2 d(x)+|U_{cs}|^2 s(x)\right]$$

and for antineutrinos

$$\frac{d\sigma(\bar{\nu}_\mu N\to Xc\mu^+)}{dxdy} = \frac{G^2 M_N E_\nu}{\pi}\left(1-y+\frac{xy}{\xi}\right)2\xi\left[\,|U_{cd}|^2\bar{d}(x)+|U_{cs}|^2\bar{s}(x)\right]$$

(These formulae are derived by replacing $F_i(x,Q^2)$ by $F_i(\xi,Q^2)$ in Eqns. 1.4a,b,c and then following through the steps leading to Eqns. 1.5a&b.) Total charm production cross sections can be calculated from these formulae with x, y, and E_ν constrained by the kinematic threshold requirement that the total hadronic mass W exceed the minimum mass neccessary to produce a charmed hadron. (For detailed calculations of charm production cross sections, see references 48, 49, and 50.)

Some general features of deep inelastic charm production are:

(1) The production rate from strange quarks is comparable to the production rate from down quarks. (There are far fewer s than d quarks in a nucleon, but the s to c coupling is about 20 times larger than the d to c coupling. Neutrino charm production is, as yet, the only feasible method for studying the strange quark content of nucleons. The ratio of s to d quarks in an isoscalar target is 0.065±0.01, calculated from the charm production results of a high statistics dimuon experiment [51])

(2) The x distribution of anti-charm production by antineutrinos is proportional to $\bar{s}(x)$, and the difference between antineutrino anti-charm production and neutrino charm production is proportional to d(x).

(3) The intrinsic y distribution will be almost flat ($d\sigma/dy \approx$ constant) for both neutrino charm production and antineutrino anti-charm production.

1.5.2 "Elastic" Processes

Single charmed particles can be directly produced by "elastic" processes as well as by (messy) deep inelastic neutrino interactions. In such cases the charmed particle is produced by an interaction involving the whole target nucleon and the charmed particle carries almost all of the energy of the virtual intermediate vector boson. Elastic production occurs with low Q^2, in comparison to the large momentum transfers of deep inelastic scattering. Quasi-elastic baryon production and elastic diffractive vector meson production are two processes expected to contribute to neutrino charm production.

In charged current quasi-elastic charmed baryon production, one of the d quarks in the target nucleon is changed to a c quark and the target nucleon transformed into a charmed baryon. No other hadrons are produced. Figure 1-10 shows Λ_c^+ production from neutrons and $\Sigma_c^{++(*)}$ production from protons.

Quasi-elastic scattering of neutrinos is reasonably well understood, and quasi-elastic production of light baryons (e.g. Δ^{++}) accounts for as

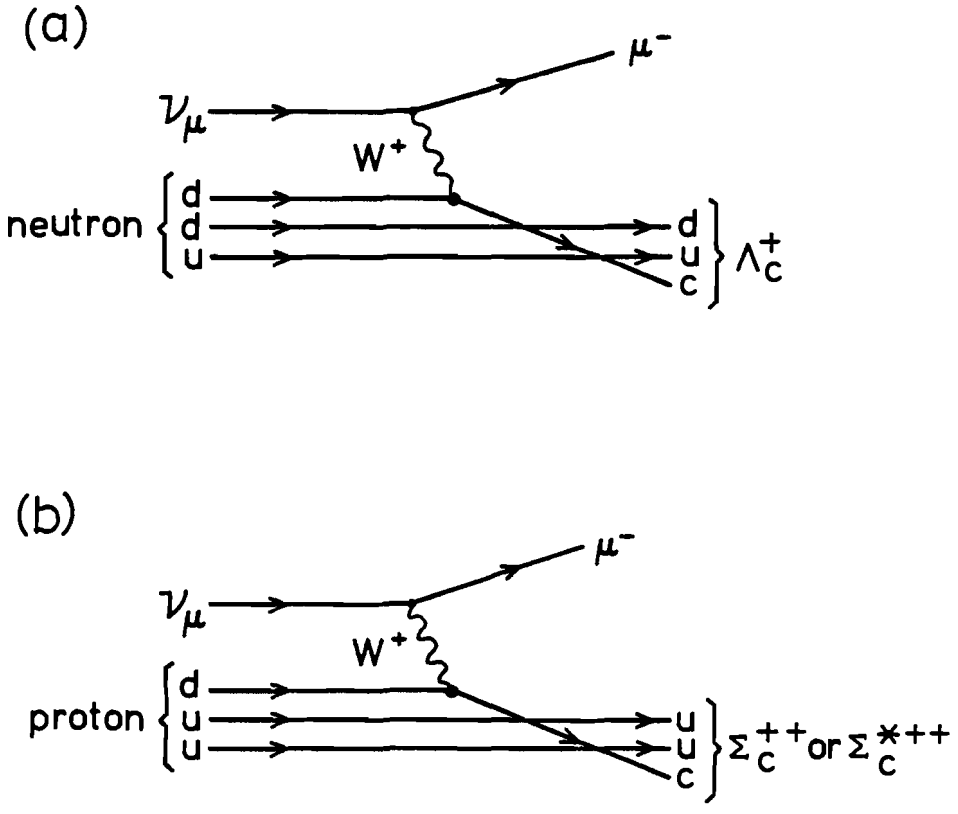

Figure 1-10: Quasi-elastic charmed baryon production.
(a) $\nu_\mu n \rightarrow \mu^- \Lambda_c^+$
(b) $\nu_\mu p \rightarrow \mu^- (\Sigma_c^{++}$ or $\Sigma_c^{*++})$

much as 5% of the total charged current cross section in current wide-band neutrino beams [52]. The cross section for a given process (e.g. $\nu_\mu p \to \mu^- \Delta^{++}$ or $\nu_\mu n \to \mu^- \Lambda_c^+$) is constant well above threshold ($\sigma(\nu p)_{\text{quasi-elastic}} \sim 1 \times 10^{-38} \text{cm}^2/\text{nucleon}$). Most of the total quasi-elastic charmed baryon production cross section should be due to Λ_c^+, Σ_c^{++}, and Σ_c^{++*} production, but higher mass baryons (L=1,2,... orbital excitations) will be also produced. Predictions for the total quasi-elastic charm cross section range from 2 to 50 $\times 10^{-40}$ cm^2, with an expected average Q^2 of 0.8 to 1.9 GeV^2 [53]. The predictions vary because of different assumptions about the form factors of the baryons (The quasi-elastic production rate depends on the overlap between the wave functions of the initial target nucleon and final charmed baryon.) The total quasi-elastic charmed baryon production cross section times the branching ratio into modes containing a Λ^o or $p\bar{K}^o$ system has been measured to be $\sigma \cdot B = (14.3 \pm 7.4) \times 10^{-40} \text{cm}^2$ for νn reactions and $\sigma \cdot B < 3.3 \times 10^{-40} \text{cm}^2$ for νp interactions [54].

Just as the photon can diffractively produce a vector meson, the other intermediate vector bosons (W^+, W^-, Z^o) should diffractively produce vector and axial-vector mesons [55]. Diffractive production is characterized by the strong coupling of the vector boson to the target nucleus; this can be visualized as the vector boson forming a virtual quark-antiquark pair that couples via gluons to the target. Elastic diffractive production of F^{*+} ($c\bar{s}$) and D^{*+} ($c\bar{d}$) charmed vector mesons would be expected in charged current neutrino interactions, with F^{*+} production (Figure 1-11) being favoured over D^{*+} production because $|U_{cs}|^2 \approx 20 |U_{cd}|^2$.

1.5.3 Other Rare Processes

Figures 1-12 and 1-13 show other possible charm production processes.

A charm quark will be produced in any interaction of a neutrino with

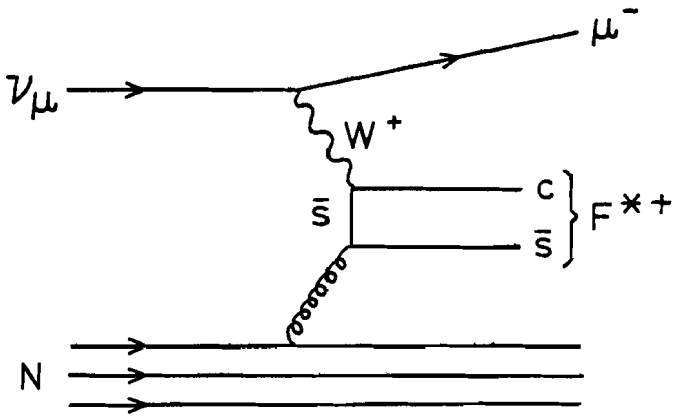

Figure 1-11: Charged current elastic diffractive production of an F^{*+}.

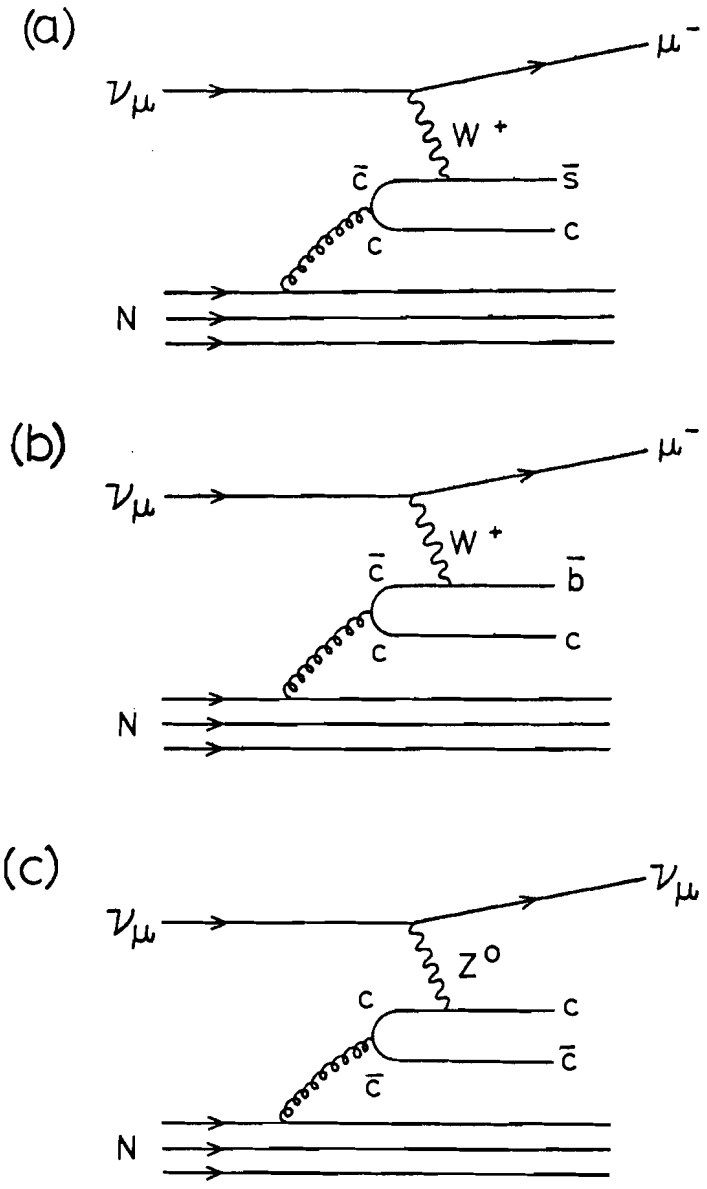

Figure 1-12: Neutrino interactions with ocean charm quarks:

(a) $\nu_\mu c\bar{c} \to \mu^- c\bar{s}$ $\quad \frac{d\sigma}{dxdy} \propto c(x)(1-y)^2 |U_{cs}|^2$

(b) $\nu_\mu c\bar{c} \to \mu^- c\bar{b}$ $\quad \frac{d\sigma}{dxdy} \propto c(x)(1-y)^2 |U_{cb}|^2$

(c) $\nu_\mu c\bar{c} \to \nu_\mu c\bar{c}$

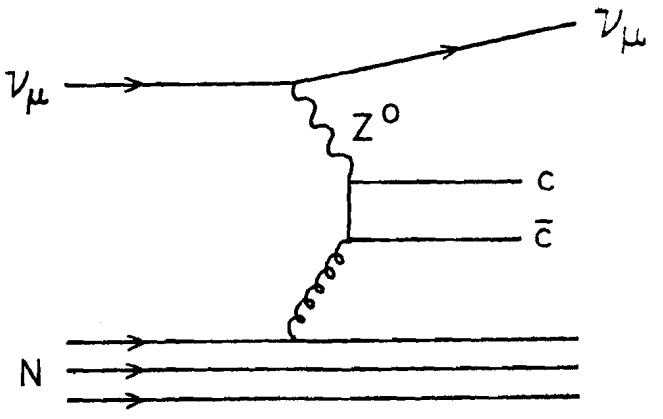

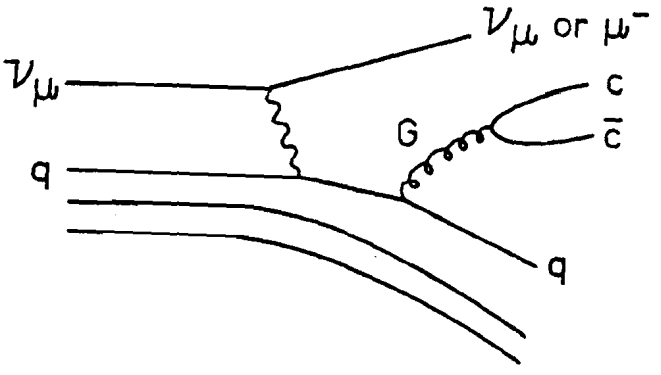

Figure 1-13: Other $c\bar{c}$ charm pair production processes.
(a) Diffractive neutral current production
(b) Gluon bremsstrahlung in charged or neutral current interactions

ocean charm quarks. As shown in Figure 1-12, ocean charm quarks would contribute to (a) charged current single charm production, (b) charged current beauty production, and (c) neutral current $c\bar{c}$ charm pair production. The charm ocean is, however, kinematically suppressed [56] and experimental measurements indicate $C \equiv \int xc(x) < \frac{1}{2}\%$ [57]. Reactions (b) and (c) are also kinematically suppressed by the large masses of any $c\bar{c}$ or $c\bar{b}$ system. Reactions (a) and (b) have a $(1-y)^2$ dependence instead of the flat y dependence of charm production from d or s quarks, and these reactions also are noteworthy because the charm quark is produced as a target fragment - it is not the struck quark.

Other processes that can produce $c\bar{c}$ charm pairs are shown in Figure 1-13. One elastic diffractive $c\bar{c}$ production process, $\nu N \rightarrow \nu \Psi X$, has been observed at a rate of $\sim 1 \times 10^{-4}$ of the total neutrino interaction cross section [58]. Gluon bremsstrahlung is closely related to the mechanisms by which charm is produced in hadronic interactions. The gluon is more likely to fragment into light quarks ($u\bar{u}$, $d\bar{d}$, or $s\bar{s}$), but $c\bar{c}$ production is possible in energetic enough interactions.

As in charm production, beauty production has much potential interest. The two most obvious beauty production processes are $\bar{b}$ production from $\bar{c}$ quarks (Fig. 1-12b) and b production from u quarks (Figure 1-14). Both of these processes are, unfortunately, likely to be very rare (because $\bar{c}(x)$ and $|U_{ub}|^2$ are tiny).

1.6 Quark Fragmentation and Particle Production

When a charmed quark is produced in an interaction, it is not observed as a lone quark, instead it manifests itself as one or more hadrons. The process by which a quark produces physical hadrons is known as the "fragmentation" of the quark into hadrons. As illustrated in Figure 1-15, the fragmentation process is a complex strong interaction of quarks and gluons. This process is, in principle, independent of how the quark was originally produced. Quark fragmentation is of fundamental

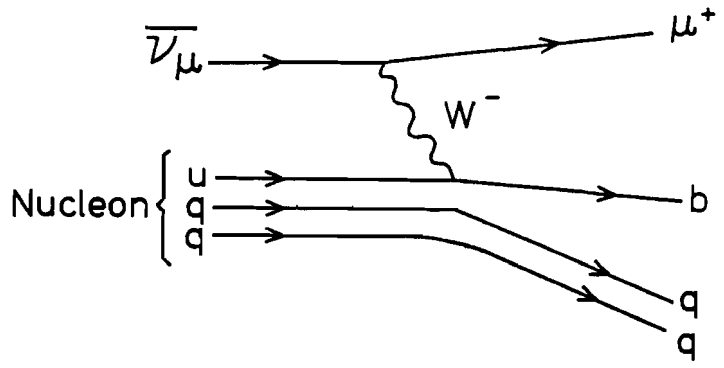

Figure 1-14: Beauty production from valence u quarks in antineutrino interactions; $\frac{d\sigma}{dxdy} \propto u(x)(1-y)^2 |U_{ub}|^2$.

interest for what it can tell us about the strong interaction, and it is also of practical interest because it is difficult to test our understanding of quarks if we do not know how the quarks change into the hadrons we see.

1.6.1 Fragmentation Functions

When a quark fragments into hadrons, each of the hadrons carries some fraction of the original quark's momentum. The fragmentation variable Z is the fraction of the original quark's momentum carried by a hadron. In charged current neutrino interactions, the quark of interest is the quark that couples to the $W^{\pm}$, and the Lorentz invariant definition of Z is given in Sec. 1.3.

"Fragmentation functions" are the distributions of hadrons in terms of the fragmentation variable Z. It is possible to define many fragmentation functions, for example:

(a)	$D_h(Z)$	-	the distribution in Z of all hadrons
(b)	$D_+(Z)$	-	positive hadrons
(c)	$D_{\pi^+}(Z)$	-	positive pions
(d)	$D_o(Z)$	-	the hadron carrying the original quark
(e)	$D_n(Z)$	-	all hadrons not carrying the original quark
(f)	$D_c(Z)$	-	all charmed hadrons

For normal charged current single charm production, $D_o(Z)$ and $D_c(Z)$ are obviously equivalent since the charm quark is also the original struck quark.

It should be noted that, since a quark never exists in isolation, the fragmentation process cannot be totally independent of the quark's environment. In Figure 1-15, not only is the struck quark fragmenting, but the diquark (the qq pair left over from the target nucleon) is also "fragmenting" into observable hadrons. There is no sharp boundary between the current (struck quark) and target (diquark) fragmentation regions. In

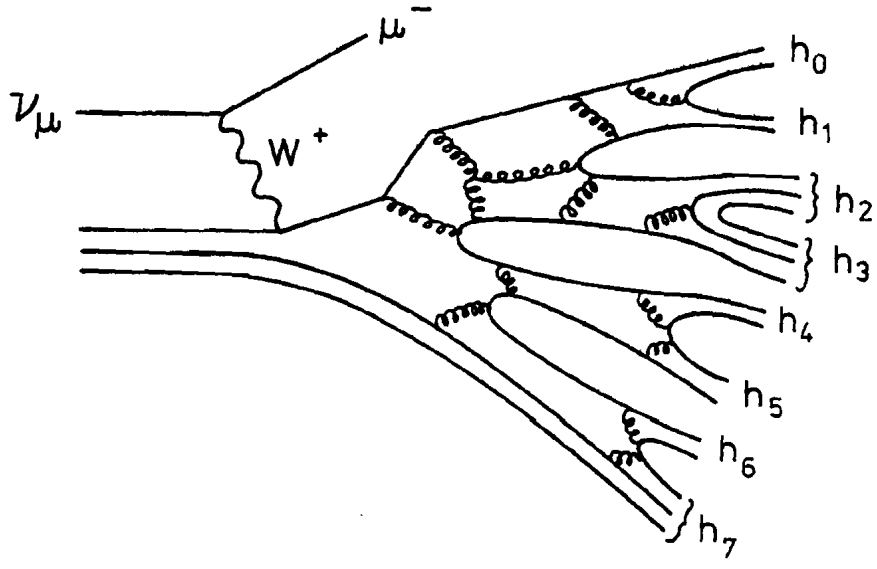

Figure 1-15: A charged current neutrino interaction followed by the fragmentation of the struck quark into hadrons. h_o is the hadron containing the original quark; h_1-h_5 are other hadrons produced by the fragmenation process. h_6 and h_7 are a meson and baryon from the fragmentation of the spectator diquark from the target nucleon.

Fig. 1-15, hadron h_6 could be considered as a mixture of target and current fragment.

Of experimental note: it is usually not possible to tell whether hadrons come directly from the fragmentation process, or indirectly from the decay of resonance particles. For example, hadron h_0 could be a $\rho'(1600)$, which later decays to 4 pions. The 4 pions would be seen, but it would not be known that these pions come from a decay, not directly from quark fragmentation.

1.6.2 Specific Charmed Hadron Production Rates

When a quark fragments into hadrons, the types of physical hadrons produced reflect the characteristics of the fragmentation process. Although the total charmed particle production rate is determined by the total charm quark production rate, the relative production rates of different charmed hadrons are, in general, determined by the fragmentation process. These relative production rates are thus an important part of any description of charm quark fragmentation.

1.6.3 Charge Independence and Spin Statistics

In the simplest model for charm fragmentation it is assumed that there are no dynamical effects in the matrix elements for the production of specific charmed particles. Thus the relative rates for production of different members of an isospin multiplet can be calculated using simple spin counting statistics. For example, D^* charmed (vector) mesons have spin 1 and hence 3 spin states, while D (scalar) mesons have spin 0 and only 1 spin state, so the ratio of D^*:D production would be expected to be 3:1. If u and d quarks are equally produced in the fragmentation process, then the rates of charged and neutral D mesons would be expected to be equal, and the total rates of D and D^* production would be in the ratios of $D^{*+}:D^+:D^{*o}:D^o=3:1:3:1$. Similar arguments would lead us to

expect production ratios for charmed-strange mesons and non-strange charmed baryons of $F^{*+}:F^{+}=3:1$ and $\Sigma_c^{*++}:\Sigma_c^{*+}:\Sigma_c^{*o}:\Sigma_c^{+}:\Sigma_c^{+}:\Sigma_c^{o}:\Lambda_c^{+}=2:2:2:1:1:1:1$. (These ratios are only for production from fragmenting quarks, not for the elastic processes which may account for a large fraction of the total F^{*+} and charmed baryon production rates.)

The simplest spin statistics arguments may not be completely correct. It has been observed that vector meson production is suppressed in light quark fragmentation and the ratio of vector to pseudoscalar meson production (e.g. $\rho:\pi$) is about 1:1 [59]. Vector meson production may be less suppressed for heavier quarks [60], but it is possible that the $D^*:D$ and $F^{*+}:F^{+}$ ratios will be less than 3:1.

1.6.4 Strange Charmed Particles

The fragmentation of a quark into hadrons is a strong (QCD) process that is intrinsically flavour independent. If the strange quark were as light as the up and down quarks, the u:d:s quark production ratio would be 1:1:1 in the fragmentation process, and so 1/3 of all charmed mesons would be strange charmed mesons, and 5/9 of all charmed baryons would contain at least one strange quark. The strange quark is, however, not as light as the up and down quarks, and so the production of strange quarks in the fragmentation process is kinematically suppressed.

For non-charmed hadrons, the ratio of strange to non-strange particles produced is typically 0.1 to 0.2 [61], indicating that about 10% to 20% of the quark-antiquark pairs produced in the fragmentation process are strange quarks [62]. The fraction of strange quarks in the fragmentation process should be essentially independent of the flavour of the fragmenting quark, so it might be expected that 10% to 20% of charmed hadrons produced by fragmentation would be strange charmed hadrons. In the case of special production processes, the strange charmed particle production fractions may range from zero for quasi-elastic baryon production (there are no strange valence quarks in nucleons) to ~90% for W^{+} elastic diffractive vector meson production (Sec. 1.5.2).

1.7 Feynman X and Transverse Momentum

Figure 1-16 represents a charged current neutrino interaction in the rest frame of the final state hadronic system - the (virtual) W^+ is incident from the left and it interacts with one of the quarks contained in the target nucleon. Were it not for the strong interaction, the struck quark would simply be turned around by the interaction and the remaining diquark fragment would continue on to the left. The struck quark moves off in the "forward" or "current" direction - referring to the weak current carried by the W^+ - and the target fragment continues on in the "backward" or "target" direction. In this simple "billiard ball" parton model without strong interactions, the quarks have no relative transverse momentum ($P_\perp$) except for that due to their motion within the nucleon.

Feynman X is the longtitudinal C.O.M. momentum of a particle divided by the maximum possible C.O.M. momentum the particle could have. In the simple parton model, the struck quark is produced at $X_F=+1$ and the diquark target fragment is at $X_F=-1$. In the lab frame the target fragment is left sitting where it was and the struck quark carries off the energy of the W^+. The struck quark is at Z=1.

In the real world, with strong interactions and no free quarks, the physical hadrons observed present a more complicated picture. The struck quark and target diquark both fragment into observable hadrons. This is a strong interaction process and quarks in both current and target regions can strongly interact with each other. Studying the $P_\perp$, X_F, and Z of the observed hadrons may provide information on the strong interaction and its effect on the simple picture of the weak interactions.

Studying the production of charmed particles provides a unique probe because the struck quark is "tagged", i.e. the charm quark is the struck quark. The charm quark is a heavy quark, so studying charm production will also provide information on the effects of quark masses on the quark production and fragmentation processes.

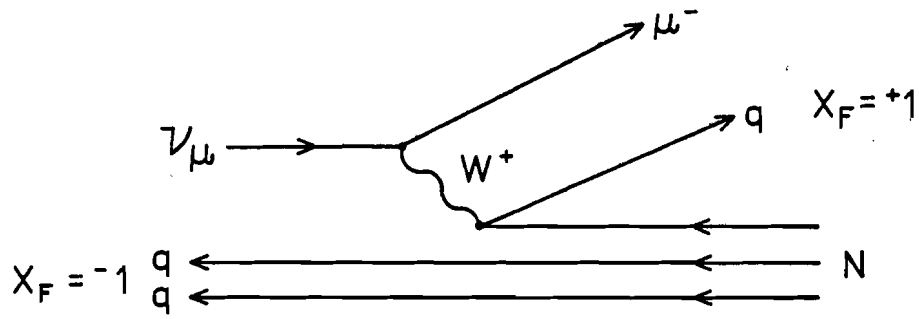

Figure 1-16: A neutrino interaction in the hadronic system rest frame.

CHAPTER 2: The Experiment

This experiment was designed to observe and identify charmed particles, and to measure their lifetimes and other properties. The experimental technique followed from these objectives.

A nuclear emulsion target was used because the expected lifetime of charm was such that charmed particles would travel only a few hundreds of micrometers before decaying - nuclear emulsion is the only standard detector with a fine enough resolution to easily see such decays. Nuclear emulsion also has two properties that determined the choice of the particle beam used to produce the charmed particles: (1) Any charged particle leaves a permanent track, and (2) it can take a long time to find an interaction in emulsion. Thus a neutral beam (no tracks) with a large charm production cross section (most charm decays per found event) was desired: a neutrino beam. (Neutrinos are neutral, and neutrino dilepton data [74] suggested that charmed particles were produced in as many as 10% of high energy charged current neutrino interactions.) In order to help find the events in the emulsion, a high resolution downstream detector was used to predict the location of neutrino interactions and secondary tracks in the emulsion. This detector was also a multiparticle magnetic spectrometer and calorimeter: it measured the momentum, energy, and identity of secondary particles, so the momentum and identity of any charmed particles could be determined.

The experiment, known as "E-531", was performed at the Fermi National Accelerator Laboratory (Fermilab) in Batavia, Illinois.

2.1 The Neutrino Beam

The proton synchrotron at Fermilab (Figure 2-1) [75] is capable of producing primary proton beams with energies up to 500 GeV. This experiment was situated in the N0 secondary beam line and used a broad band (no momentum selection, maximum intensity) neutrino beam.

The primary proton beam is produced by a 4-stage accelerating process. From an ionized hydrogen gas source, protons are accelerated to a kinetic energy of 750 keV in a Cockcroft-Walton electrostatic accelerator, to 200 MeV in a 175 m long linear accelerator, to 8 GeV in an alternating gradient booster synchrotron, and to full energy in the 2 km diameter proton synchrotron (the "main ring"). The protons are then extracted and split three ways to the Meson, Proton, and Neutrino experimental areas. The external beam is produced in bursts ("spills") of up to 3×10^{13} protons repeated with a typical cycle time of 7 to 11 seconds. During the data run of this experiment, the primary proton energy was 350 GeV.

To produce the neutrino beam, $1\text{-}2 \times 10^{13}$ protons in a ~1 ms duration fast spill are transported to a 27 cm (~1 interaction length) beryllium oxide target (Figure 2-2). Proton interactions in the target produce pions and kaons which pass through a magnetic horn [76] downstream of the target. During the spill a pulsed current of 80 kA flows through the horn in the direction of the beam. Charged particles from the target produced at angles greater than 1.8 mr (with respect to the beam direction) pass through the horn itself (~0.1 interaction length thick) and are then bent by the horn's magnetic field. Positive particles are bent towards the beam (focussed - with a 0.17 GeV/c transverse momentum kick), and negative particles are bent away from the beam (defocussed). Particles at angles less than 1.3 mr pass straight through the horn's central hole and are neither focussed nor defocussed; particles between 1.3 and 1.8 mr pass through the narrow horn collar and are unaffected by the magnetic field, but about half of these interact in the aluminium. After the horn, the secondary particles (and unabsorbed primary protons) enter a 410 m long, 0.9 m diameter decay pipe. About 10% of the charged

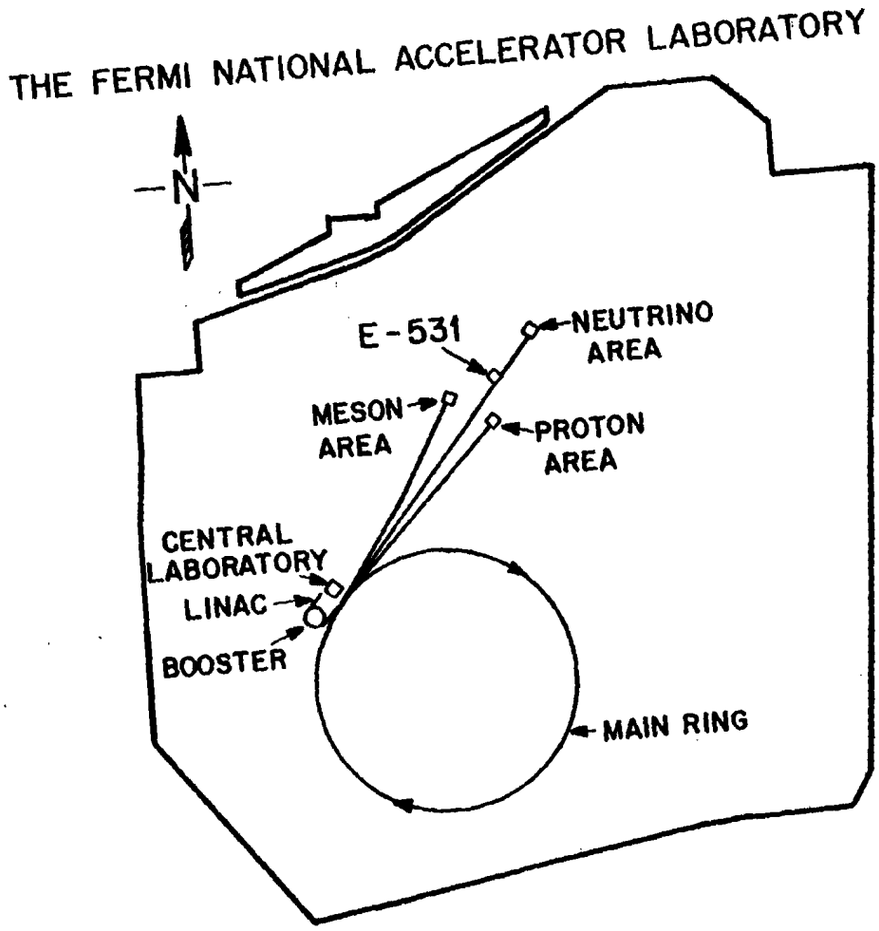

Figure 2-1: Fermilab.

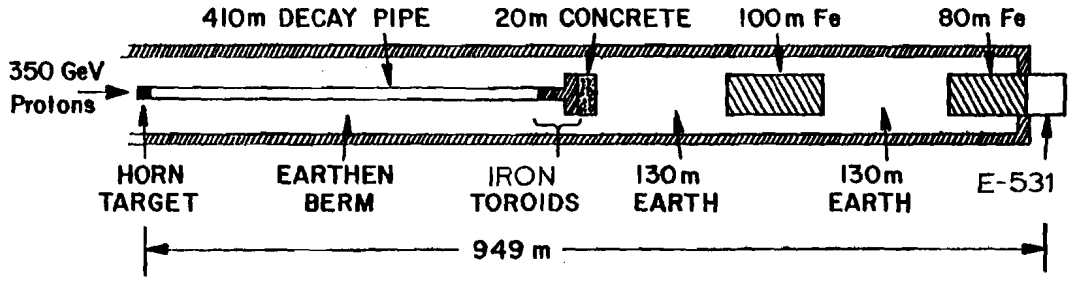

Figure 2-2a: NO neutrino beamline at Fermilab.

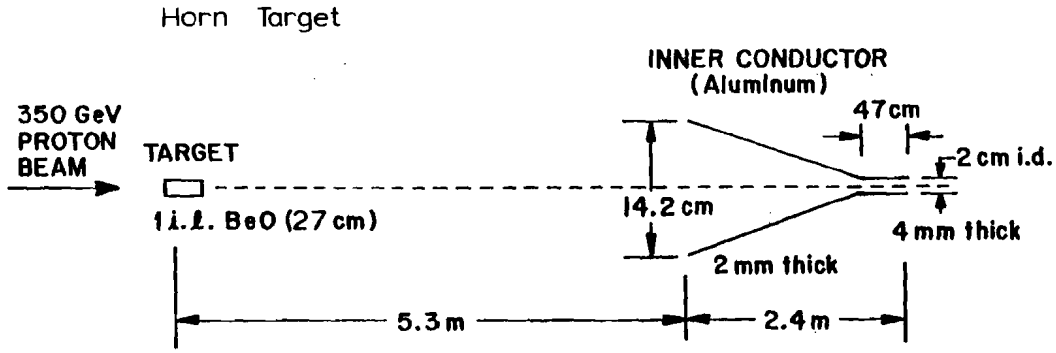

Operating Conditions:

I = 80 kA

Δp_T = 0.17 GeV/c

Figure 2-2b: Proton target and single horn for production of wide-band neutrino beam.

pions and 30% of the kaons decay in this decay region, and the remaining hadrons are absorbed in concrete at the end of the pipe. Most muons, but not all, are absorbed in the steel, concrete, and earth shield (berm) between the end of the decay pipe and E-531. For part of our data run, muons were also deflected away from the neutrino beam by magnetized iron toroids.

The neutrino beam consists primarily of muon neutrinos from the decays:

$$\pi^+ \rightarrow \mu^+\nu_\mu \qquad \text{B.R.} \cong 100\%$$
$$K^+ \rightarrow \mu^+\nu_\mu \qquad \text{B.R.} = 63.5\%$$

The beam also contains antineutrinos from negative mesons not sufficiently defocussed by the horn, and a very small number of electron neutrinos from the decays:

$$K^\pm \rightarrow \pi^o e^\pm \nu_e(\bar{\nu}_e) \qquad \text{B.R.} = 4.8\%$$
$$K^o_L \rightarrow \pi^\mp e^\pm \nu_e(\bar{\nu}_e) \qquad \text{B.R.} = 38.8\%$$

The predicted fluxes of neutrinos at the location of E-531 are shown in Figure 2-3. The residual muon flux at the experiment was typically $300/m^2/(10^{13}$ protons on target).

2.2 Veto Array

The veto array was used to reject spurious neutrino triggers caused by charged particles entering the detector from upstream. The experiment's data acquisition system (Sec. 2.11) could only read full data from one trigger per spill, so any fake neutrino trigger would prevent the recording of any subsequent neutrino trigger in the same spill. The many muons passing through the experiment would have caused many fake neutrino triggers if they had not been detected and rejected.

The veto array was a wall of 7 scintillation counters covering an area 178cm(x) by 175cm(y) 1.3 m upstream of the emulsion target (see Figure 2-4). The timing of the trigger logic coincidences was carefully set up so that charged particles emitted backwards from a real neutrino interaction in the target could not veto the event. The veto wall was 98%

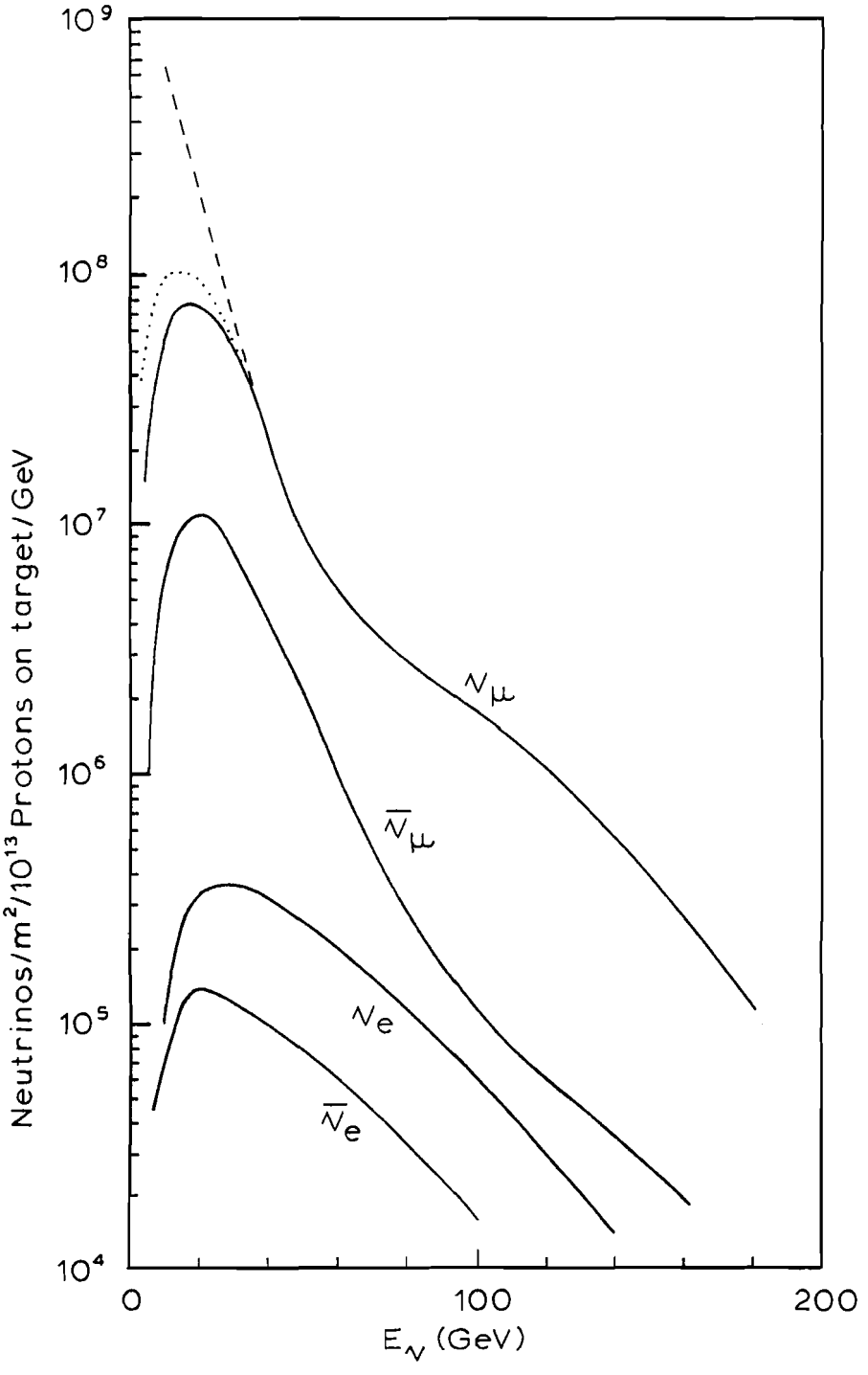

Figure 2-3: Predicted neutrino fluxes through E-531 target. The unbroken curves are Monte Carlo predictions, the dashed line is a flux extrapolated from E-545 bubble chamber data, and the dotted line is a flux consistent with the observed E-531 rates (See Sec. 3.1).

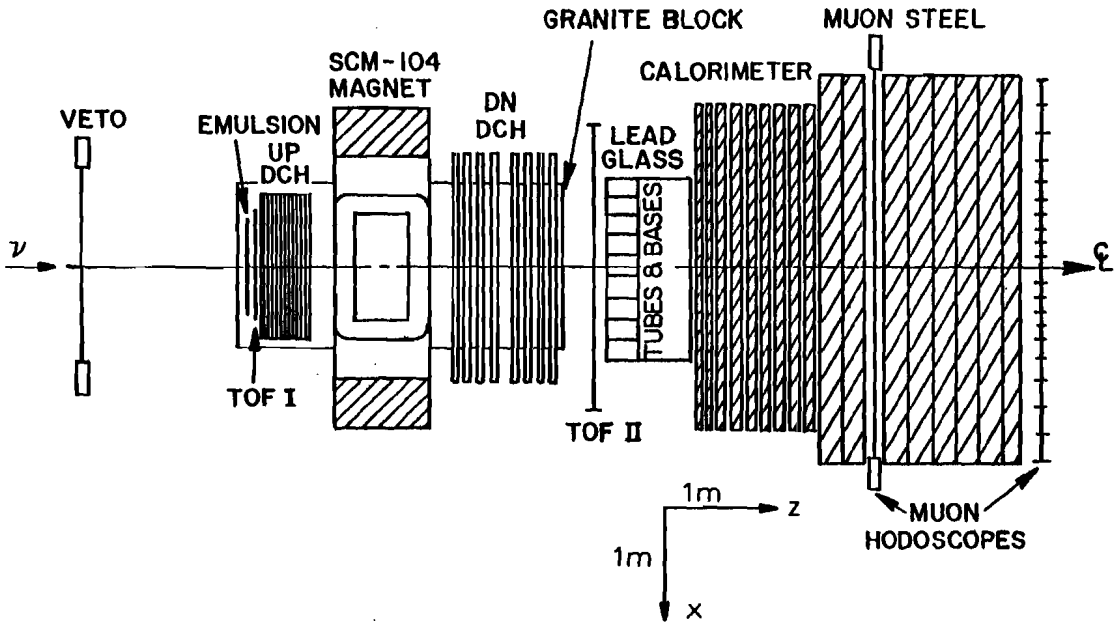

Figure 2-4a: Experiment E-531 (plan view).

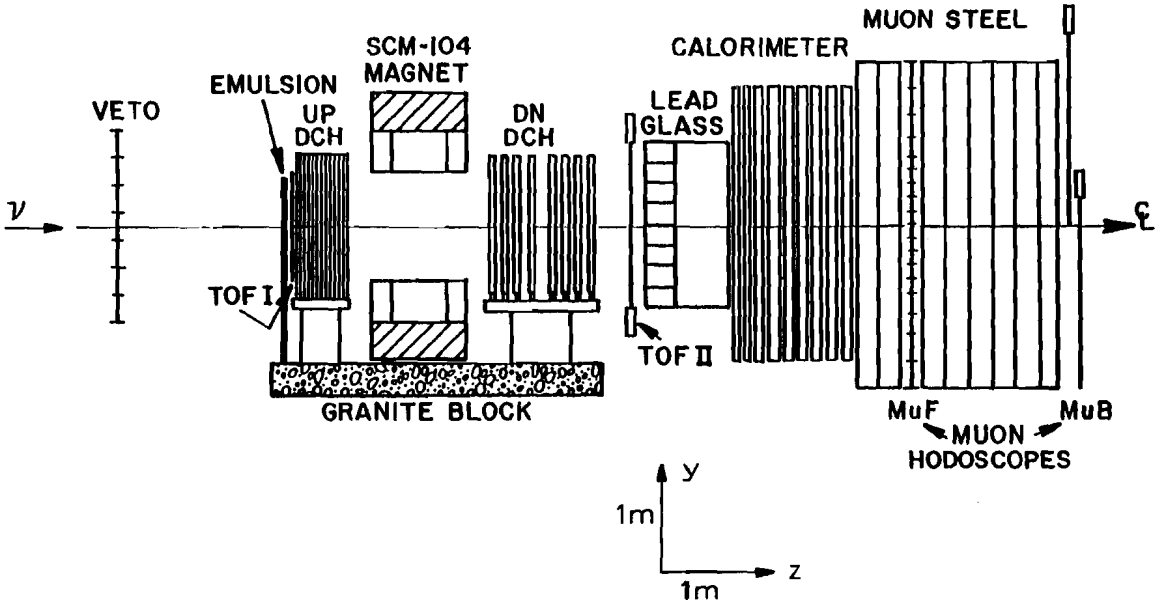

Figure 2-4b: Experiment E-531 (side view).

efficient at detecting charged particles passing through it. The overkill, the fraction of real neutrino triggers vetoed accidentally because the veto detected a charged particle, was 13±2%.

2.3 The Emulsion Target

The emulsion target consisted of 23 litres (88 kg) of Fuji ET-7B nuclear emulsion (Table 2-1) packaged in 39 modules. The modules were mounted (Figure 2-5) on the downstream face of a precision made, rigid, low density aluminium Hexcel plate. This plate, in turn, was supported by a precision stand bolted to the granite block (Figure 2-6). The emulsion target was contained in a volume 86 cm wide by 71 cm high by 5 cm thick. The emulsion was cooled (to 10±2.5°C) to minimize clouding and image fading during the long running period.

Two types of emulsion modules were used in the experiment (Figure 2-7). The upper half of the target consisted of 12 "horizontal" modules each containing 177 pure emulsion pellicles (sheets) 600 μm thick oriented with the emulsion plane parallel to the beam direction. The lower half of the target consisted of 27 "vertical" modules each containing 68 sheets of 70 μm thick polystyrene coated on both sides with 330 μm of emulsion; the sheets being oriented perpendicular to the beam direction.

Immediately downstream of the emulsion modules was a large sheet of 800 μm thick lucite coated on both sides with 75 μm of emulsion. This "changeable" sheet was changed every few days during the data taking period; it was a high-spatial-resolution low-background detector used to help find in the emulsion target individual tracks reconstucted in the spectrometer. The drift chambers predicted the position (x-y) of tracks at the changeable sheet with an accuracy of 300μm, and once found in the changeable sheet, the position of the track at the downstream face of the emulsion could be predicted within 50 μm. The sheet was changed frequently so that there would be only small background track density in each sheet. Within a 300 μm radius circle there would be ~50 tracks in

Table 2-1: Composition of Fuji ET7B Nuclear Emulsion [98]

Nuclear emulsion is basically the same as common photographic emulsion. It is a colloidal suspension of silver bromide (AgBr) in gelatin. The mean atomic number and atomic weight of emulsion is <Z>=36 and <A>=81; the average nucleon is in a nucleus with 36 protons and 45 neutrons.

Element	Atomic Number	% Weight	
Iodine	53	1.3	
Silver	47	46.1	44% protons,
Bromine	35	33.4	56% neutrons
Sulphur	16	0.4	
Oxygen	8	4.3 (7.6) *	48% u valence quarks,
Nitrogen	7	2.7	52% d valence quarks
Carbon	6	7.3	
Hydrogen	1	0.9 (1.3) *	
Water	-	3.7 **	

* Unbracketed value does not include water, bracketed value does.
** @ 68% relative humidity

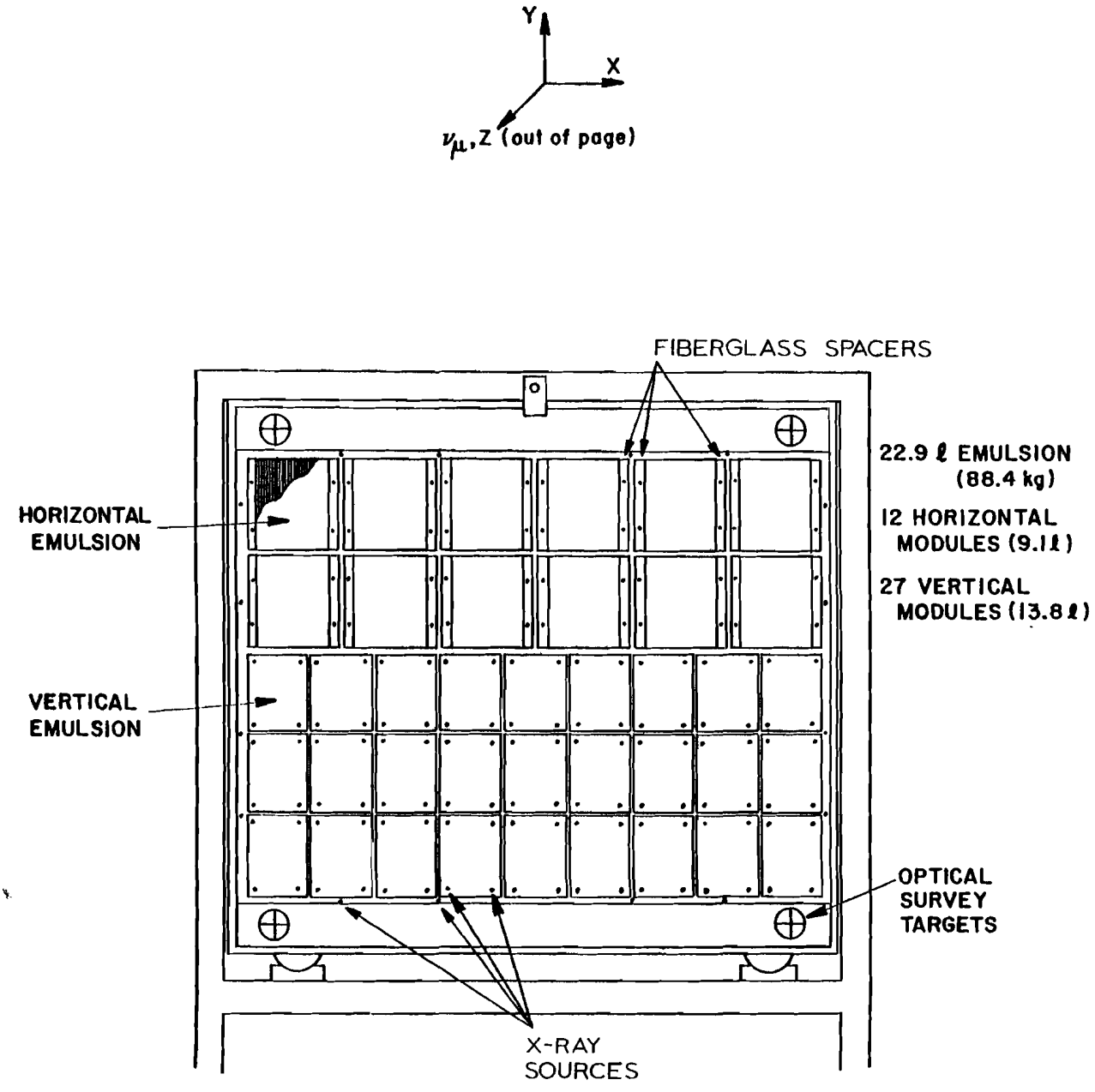

Figure 2-5: Emulsion target.

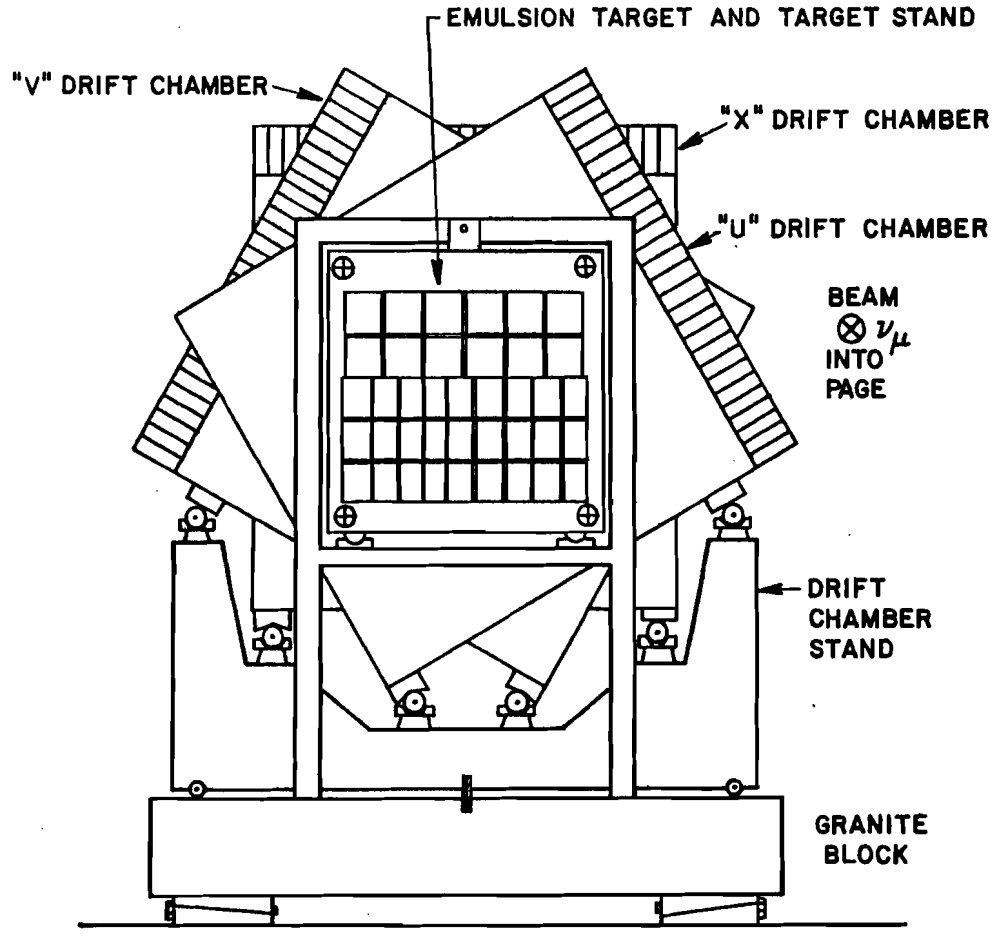

Figure 2-6: Emulsion target and upstream drift chambers.

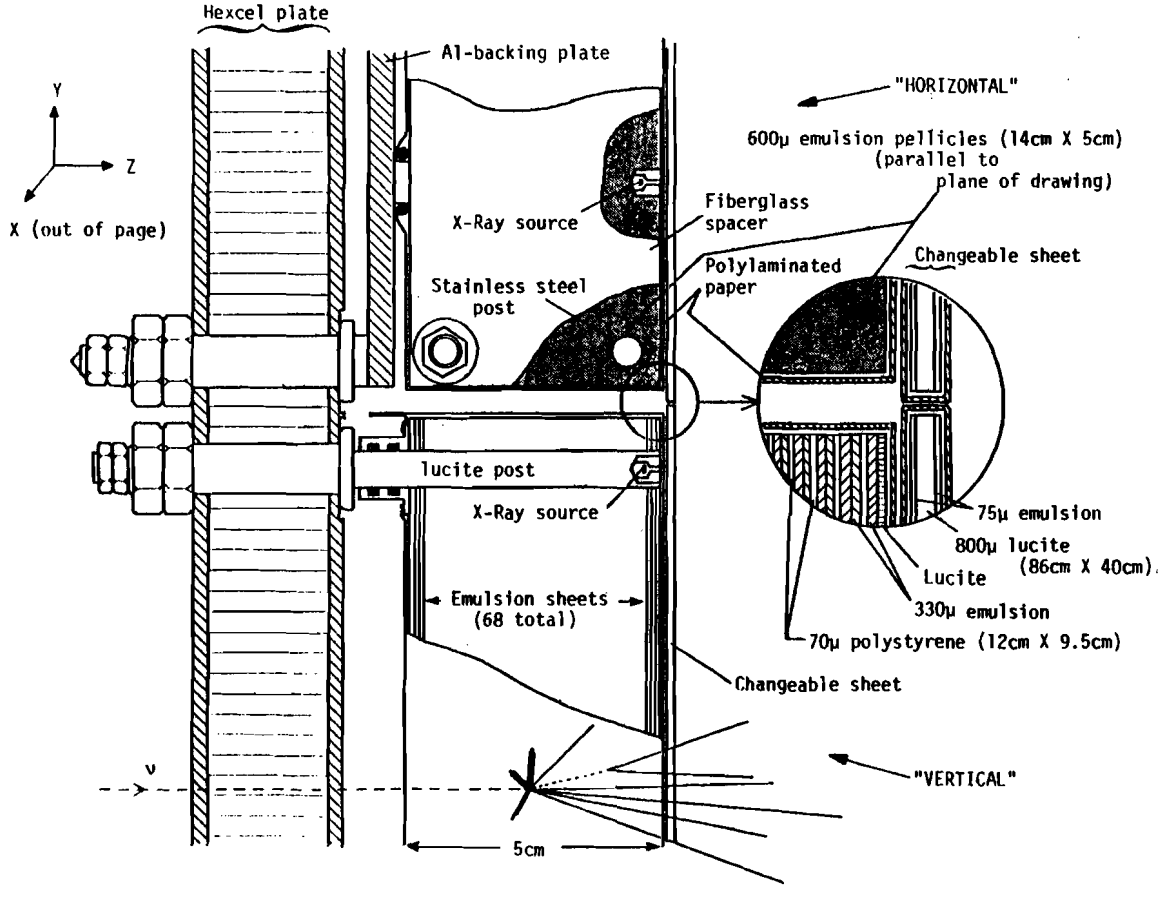

Figure 2-7: Emulsion modules (side view).

the vertical module sheets (in place for the whole data run); in contrast, a changeable sheet might only have 1 track in the same area. A predicted track would usually be found on the changeable sheet in about 10 minutes, and followed into the primary vertex in an hour.

2.4 Position Survey

In a high (spatial) resolution experiment, it is important to know where things are. In this experiment, the high resolution critical devices - the emulsion target and the drift chambers - were all mounted on and bolted to a 30 cm thick granite slab. This $3\frac{1}{2}$ tonne block provided a stable base, and even if it moved, all the critical devices would move with it. The slab floated, in effect, on top of the unstable concrete floor underneath, which rose, fell, and cracked in imitation of the driftings of the continental plates. The spatial orientation and position of the critical devices relative to each other and the granite block were measured by optical survey (~25 μm resolution) at the beginning and at the end of the data run. During the data taking period, the positions were continuously monitored by a linear variable differential transformer (LVDT) gauging system with a resolution of 15 μm. All stands and support structures were built to high mechanical tolerances. For example, the position of the emulsion support plate, which was moved in and out many times in order to change the changeable sheet, was designed to (and did) always return to within 25 μm of its original position. The position of the changeable sheet itself was precisely determined from spots produced on the sheet by collimated X-ray sources in the ends of the target module support rods and on the sides of the target support frame.

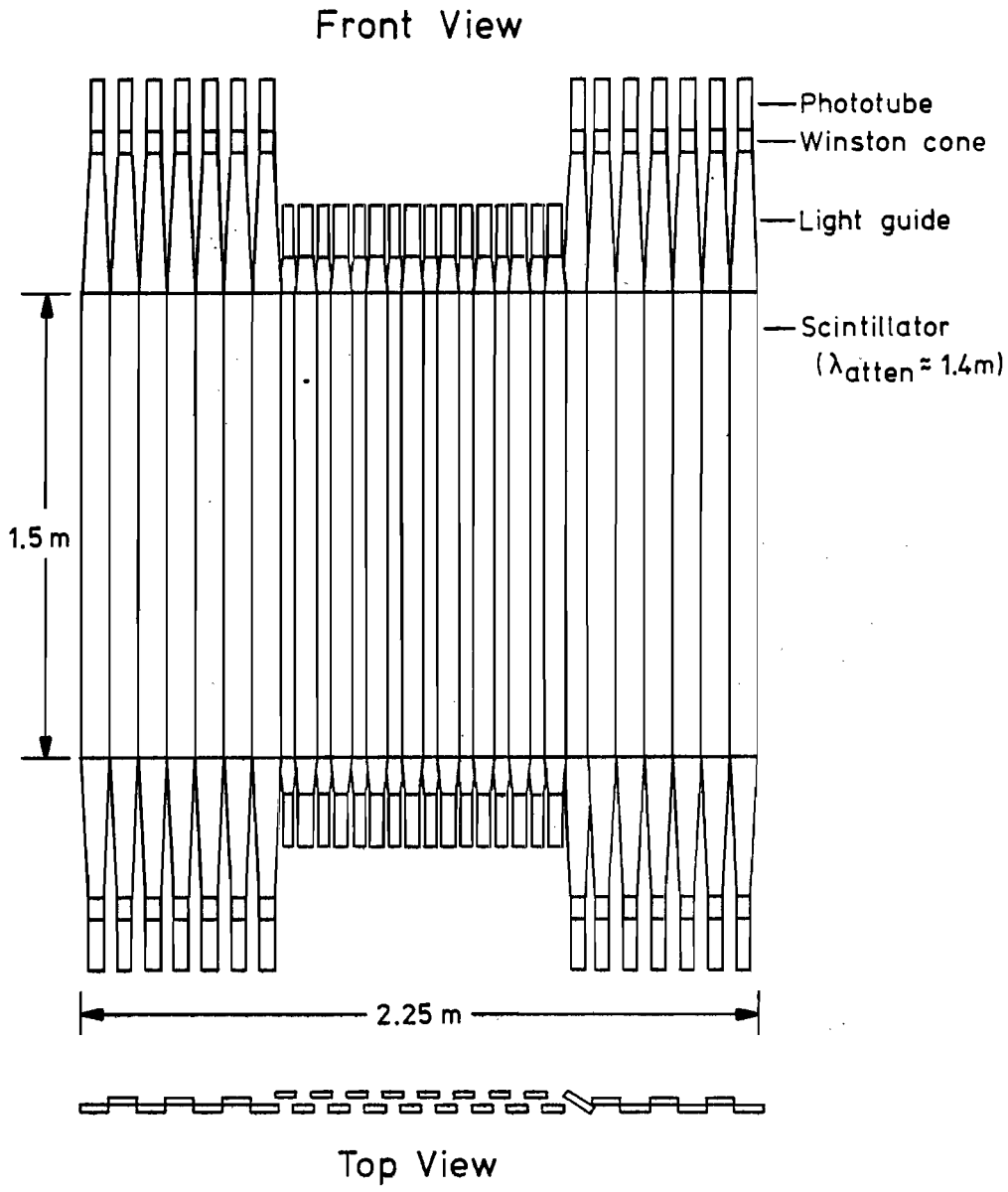

Figure 2-8b: TOFII time-of flight/trigger counters.

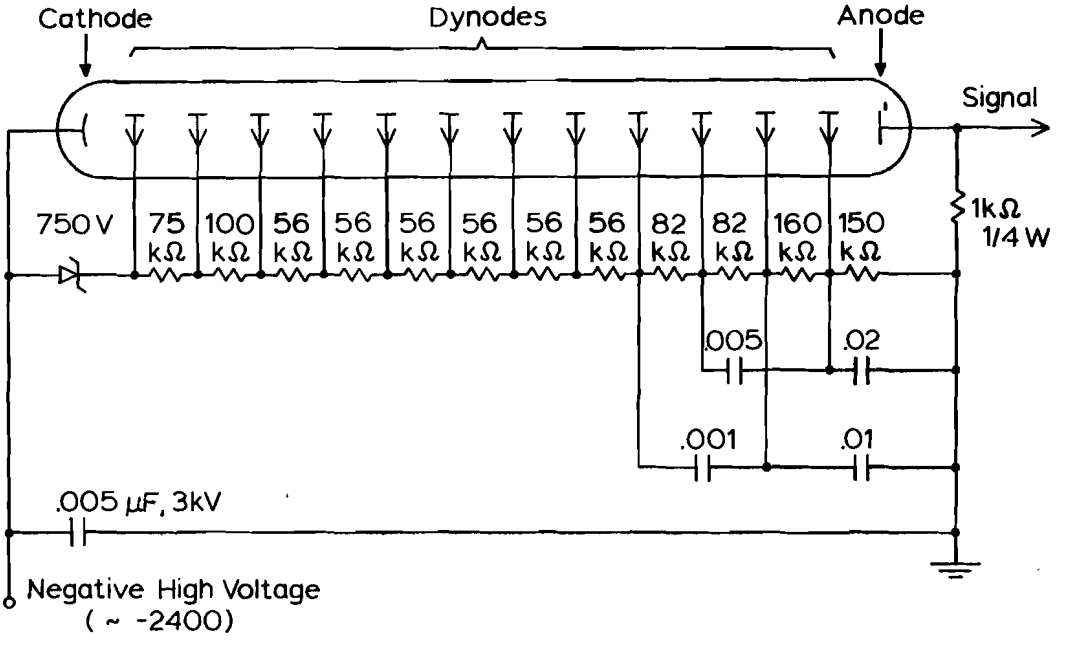

Figure 2-9: TOFII phototube base. The photocathode to first dynode voltage is fixed at 750V by zener diodes, irrespective of the total cathode-anode voltage. (Most of the time jitter in a phototube occurs in the first stage where there are very few electrons. The highest safe voltage (750V) gives maximum electron acceleration and hence minimizes the time fluctuations.)

speed of the scintillator, on the number of photons reaching the phototube, and on the speed of the phototube. Thick scintillator was used to maximize the production of scintillation light photons, and very short light guides and few optical joints minimized photon absorption. Tests of prototype counters showed that Pilot F scintillator gave better time resolution than Pilot U scintillator, even though Pilot U is intrinsically faster; this is because Pilot U has a shorter optical attenuation length than Pilot F, and the faster light production of Pilot U was offset by the fewer photons reaching the phototube. (In such long scintillators, many more of the photons are absorbed by Pilot U than Pilot F.) The 2230H phototubes were chosen because faster (and much more expensive) phototubes did not significantly improve the time resolution of the prototype counters.

The final TOFII prototypes had test resolutions of 100 ps for the 7 cm counters and 140 ps for 10 cm wide counters. The difference in the resolutions of the 7 cm and 10 cm wide counters is expected. The phototube has an active area of ~18 cm^2, well matched to the area of the 7 cm scintillator, but the 10 cm scintillator has an area of ~25 cm^2 and so 30% of the light is lost. Light is also lost in the light guides that the 10 cm counters, but not 7 cm counters, have. Figure 2-10 shows the prototype time resolution as a function of y for the 7 cm counters; the combined two tube (T+B) resolution (σ) is almost constant over the entire length of the scintillator. (The combined resolution is given by $1/\sigma(T+B)^2 = 1/\sigma(T)^2 + 1/\sigma(B)^2$.)

During the data run, the whole TOF system was monitored continuously and care taken not to disturb it. The high voltage supplies were held constant to ±1 Volt and were turned off only under duress. The TDC's were periodically tested over their entire operational range using test pulses through known time delays. The timing and gains of all tubes were monitored using both muons and laser light pulses. A nitrogen pulse laser (337.1 nm, 3 ns risetime) was fired between spills, the light transported by optical fibers to each of the 72 tubes, and the signals (ADC and TDC) read out in the laser/flasher event (Sec. 2.11). After the data run, the positions of the TOF counters were measured with <3 mm accuracy.

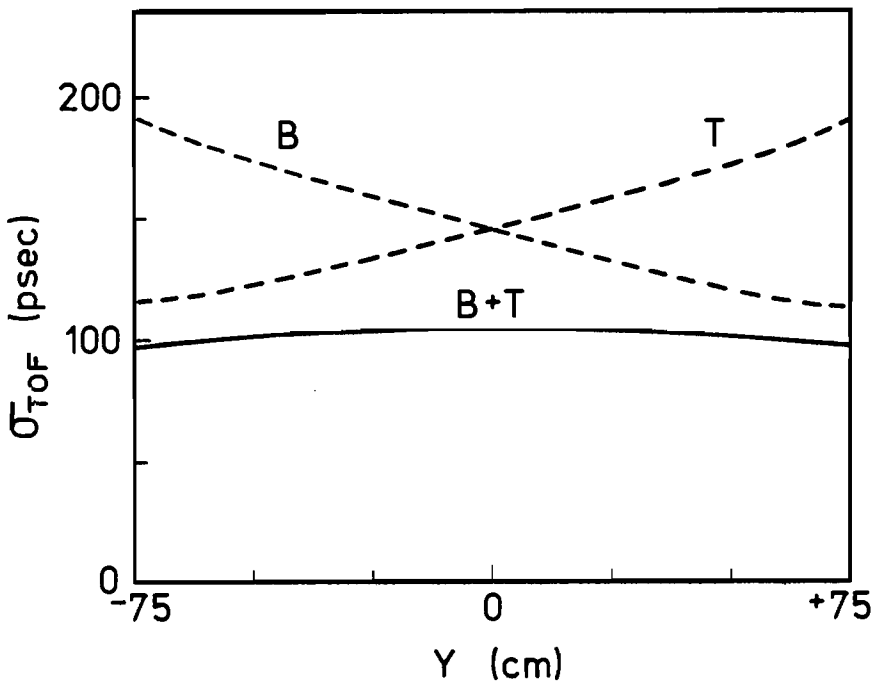

Figure 2-10: Intrinsic (pulse height corrected) RMS time resolution (σ_{TOF}) of minimum-ionizing particles as a function of distance (Y) from the centre of a 7 cm wide TOFII counter. The separate resolutions of the top (T) and bottom (B) phototubes and the combined (T+B) resolution are shown.

2.5.1 Calibration and Chronometry

A time-of-flight scintillator counter is designed to measure the time at which a charged particle passes through the counter.

When a charged particle passes through the plastic scintillator of a TOFII counter (at a position y - see Figure 2-11a), a pulse of light is emitted. Some of this light propagates with an effective velocity, v, to the phototubes at either end of the counter. The phototube detects the light and produces an electrical pulse whose charge is proportional to the amount of light seen, and this signal pulse goes into an Analog-to-Digital-Converter (ADC) and a Time-to-Digital-Converter (TDC); the ADC measures the integrated charge, A(ADC), and the TDC records the time, t(TDC). The actual time, t(TOF), at which the particle passes through the scintillator can be calculated from

$$t(TOF) = t_o + y/v + B\sqrt{\ln(A(ADC)/A(DISC))} + t(TDC) \quad .$$

t_o is a time "zero" correction that takes into account all the time necessary for the signal to propagate through the phototube and base, and through the signal cables and electronics. The absolute value of t_o is unimportant, but what must be known are the differences in t_o between all the phototubes in the system.

Figure 2-11b shows a TOF signal pulse at the input to a TDC. The TDC records the time at which the voltage of the pulse first exceeds a set discriminator voltage level, V(DISC). This level is fixed (100±2mV for TOFII), so the bigger the pulse is, the sooner it will exceed V(DISC), and the earlier will be t(TDC). The effect of the pulse height on t(TDC) is determined by the shape of the leading edge of the pulse, and can be described by $B\sqrt{\ln(A(ADC)/A(DISC))}$. (An ADC measures charge, not voltage, but the integrated pulse charge, A(ADC), corresponds linearly to the pulse height voltage, V(ADC). The pulse shape is essentially constant and independent of the pulse charge.)

The parameters t_o, v, and B were initially unknown and were

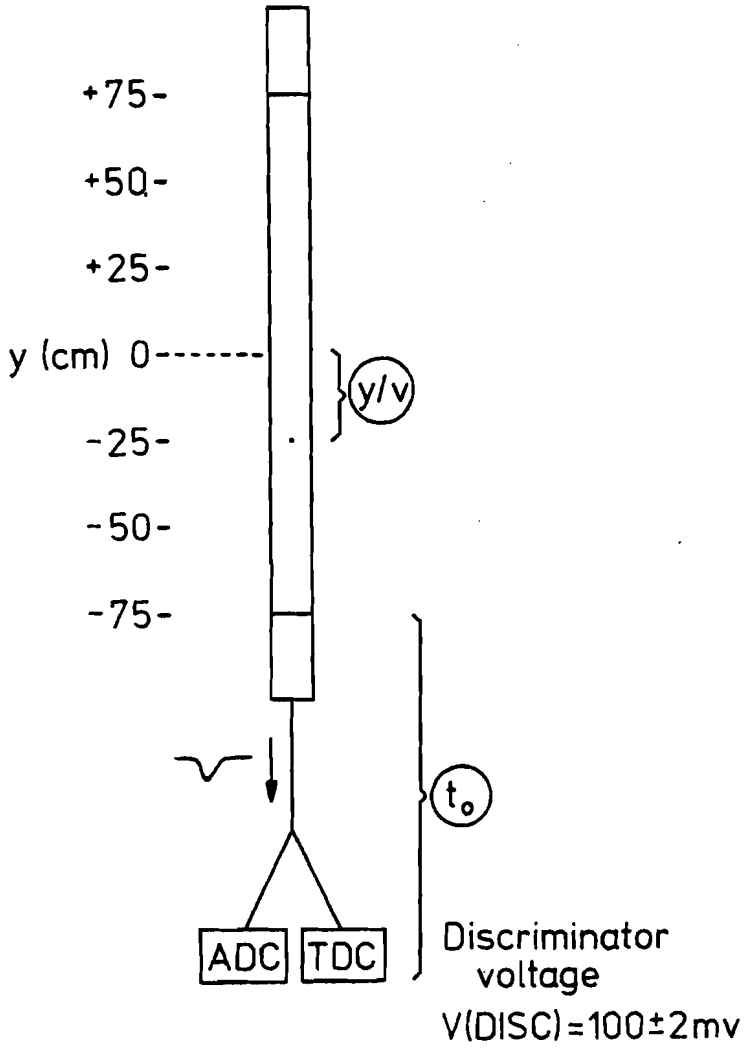

Figure 2-11a: Detecting a particle in a TOFII counter. The particle passes through the counter at a distance y from the centre of the counter (time correction y/v); from the phototube the signal is send to an ADC and TDC.

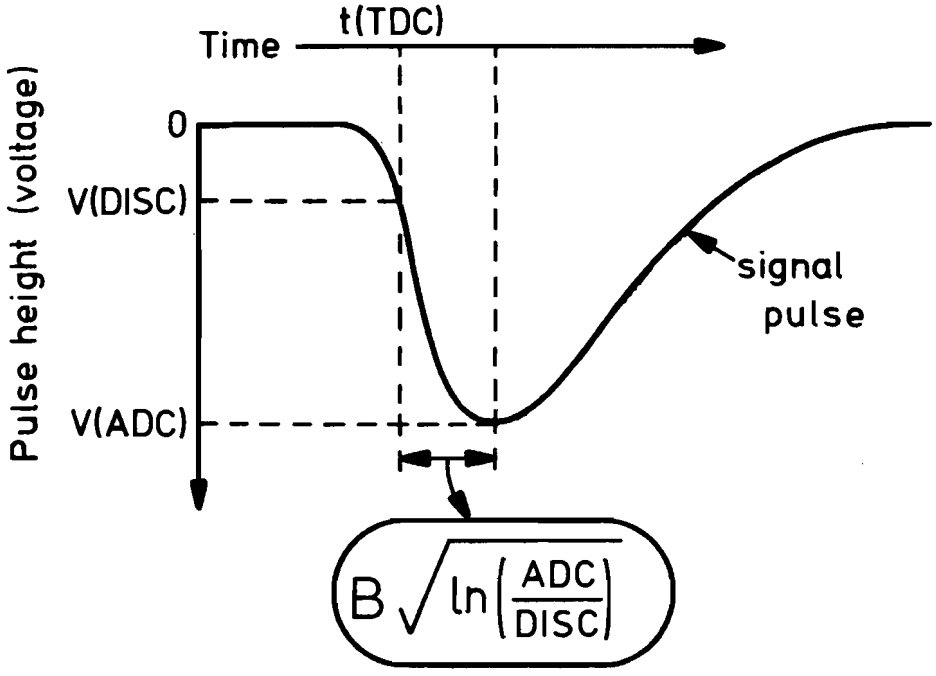

Figure 2-11b: A phototube signal pulse at the input of a TDC discriminator.

determined from muon calibration data. The beam muons provided precisely known time intervals, their travel times from TOFI to TOFII, which could be used to calibrate the system. The muon travel times were calculated from their momenta and flight paths reconstructed from the drift chambers, and the positions of the muons at the TOF counters were also extrapolated from the drift chamber tracks. The TOF system was calibrated by fitting the correlations between time, position, A(ADC), and t(TDC) for the beam muons. B and t_o were determined for each of the 12 TOFI and 60 TOFII phototube channels, and v was measured for the TOFI counter and each of the 30 TOFII counters.

The mean values and RMS variations of the fitted parameters for TOFII are

$\langle t_o \rangle = -10.6$ ns, $\Delta t_o = 1.3$ ns (60 phototube channels)

$\langle B \rangle = 2.52$ ns, $\Delta B = 0.30$ ns (60 phototube channels)

$\langle v \rangle = 16.36$ cm/ns, $\Delta v = 0.21$ cm/ns (30 counters)

These numbers show the uniformity of the TOFII system: The net transit time varied only a nanosecond or so among the 60 channels, and the pulse height correction varied only about 10% (corresponding to slightly different pulse rise times). The fitted value of v agreed within 1% for all 30 TOFII counters - this spread being consistent with the statistical accuracy with which v was determined. The mean pulse height (at y=0) and average attenuation (1/e) lengths of the 30 counters were

$\langle V(ADC):y=0 \rangle = 0.83$ Volts, $\Delta V = 0.14$ Volts

$\langle L_{atten} \rangle = 136$ cm, $\Delta L = 16$ cm

The fully corrected resolutions of the TOFII counters were excellent. The average resolutions, measured over the entire three month data run, were

σ(7 cm TOFII) = 112, $\Delta\sigma$ = 11 picoseconds

σ(10cm TOFII) = 153, $\Delta\sigma$ = 22 picoseconds

The time resolution of TOFI varied from ≈450 ps for single muons to ≈250 ps for neutrino interactions, the resolution depending on the number of tracks, the event topology, and the position of the event in the emulsion target.

2.5.2 Particle Identification

Particle identification by time-of-flight is done by determining the mass (m) of a particle from its momentum (P) and velocity (v), with the velocity being determined by measuring the time of flight (t) of the particle over a known path length (L). The mass of the particle is then given by

$$m = P/(\beta\gamma) \qquad [\beta=v/c,\ \gamma=(1-\beta^2)^{-\frac{1}{2}}]$$
$$= P/\sqrt{(ct/L)^2 - 1}$$

In this experiment, the TOF system measures the time of flight of charged particles from the target to the TOFII array, and the path lengths are calculated from the tracks reconstructed in the drift chambers.

To measure a time-of-flight, the times at both the beginning (start time) and end (stop time) of the flight path must be measured. The stop time for a track is measured by the TOFII counter(s) it passes through, but the start time (the time of the neutrino interaction) is not best determined by the TOFI counter alone. If the identity of a particle is known (e.g. a muon identified by the muon counters), or if it is so fast (e.g. 20 GeV/c) that $\beta\cong1$ irrespective of its identity, then the start time can be accurately calculated by subtracting the path length from the stop time. (This start time was used for the mass spectrum shown in Figure 2-12.) In general, even if the identity is unknown, there are only 5 discrete possible start times determined from the path length and stop time for each track. Hence a "best" start time can be calculated by a least squares fit to the start times from TOFI, from any identified particles, and from the 5 possibilities for unidentified particles. This procedure is illustrated by Figure 2-13. In events with many tracks, the start time resolution can be as small as ~50 ps (limited by factors such as the TDC resolution). So the total TOF resolution varies slightly on a track by track basis, depending on the type of TOFII counter and on the ionization of the particle, and also varies depending on the topology of

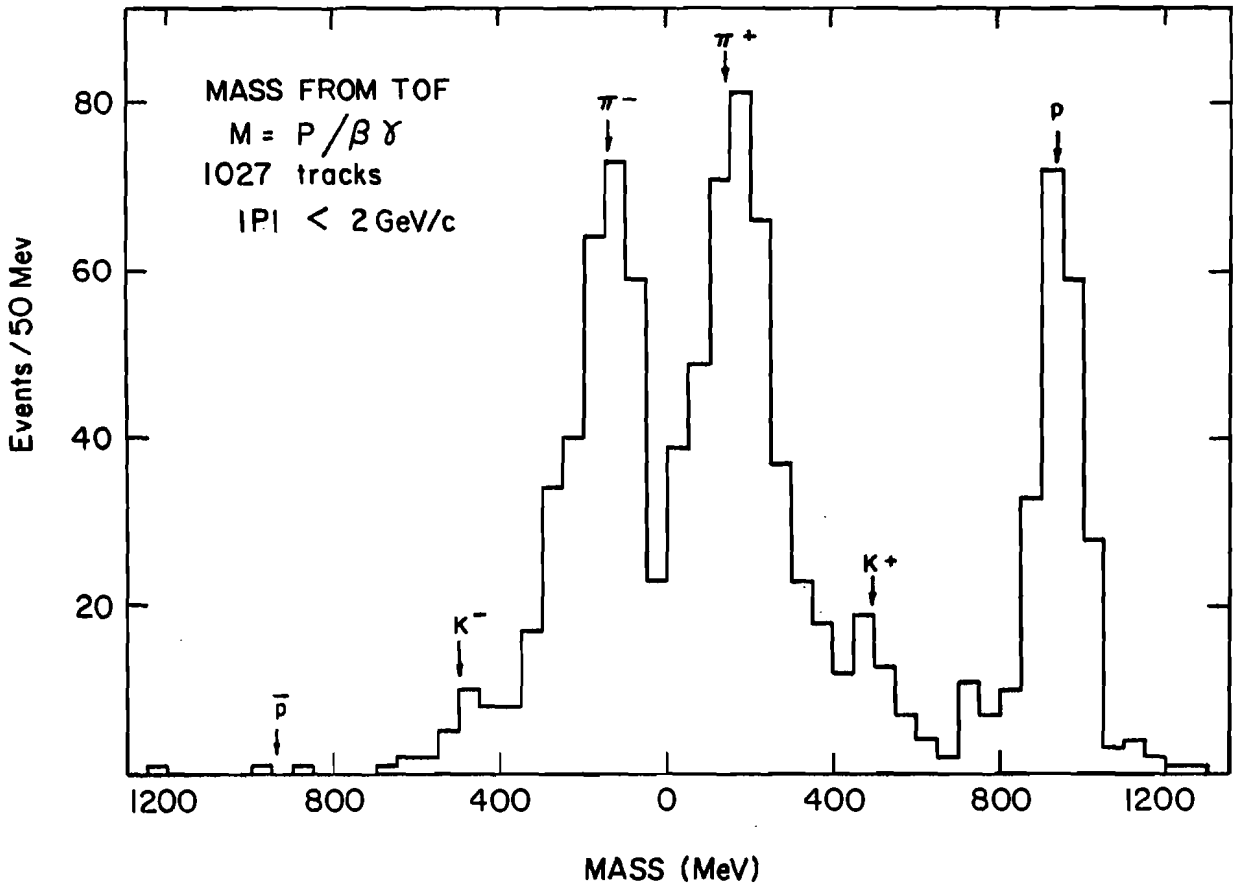

Figure 2-12: An E531 TOF mass spectrum for low momentum particles. The proton mass is measured here to be 939±4 GeV/c^2.

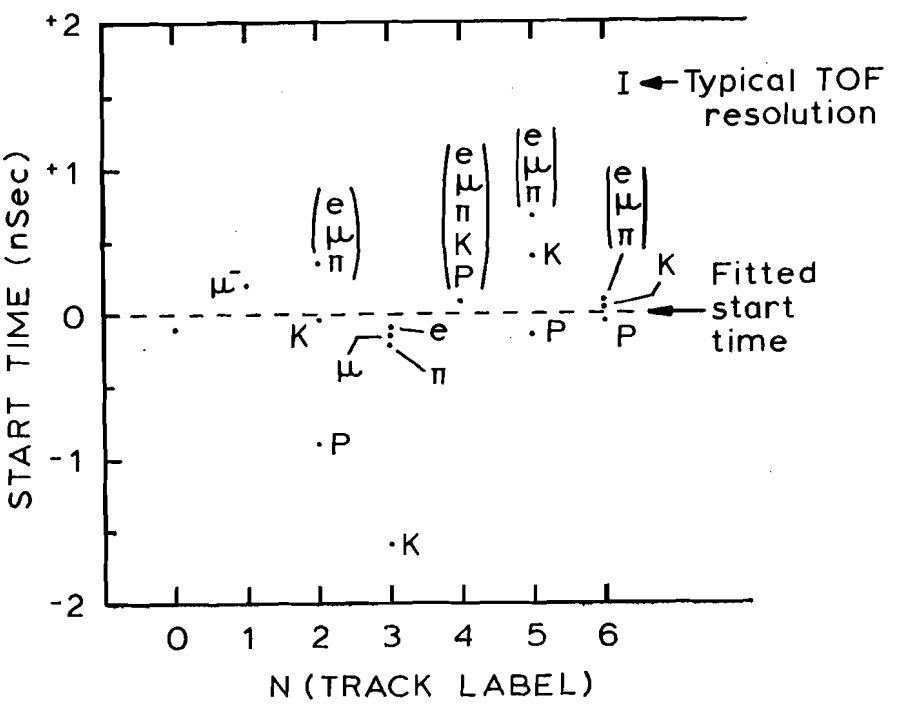
+2
+1
0
-1
-2
START TIME (nSec)
0 1 2 3 4 5 6
N (TRACK LABEL)
I ← Typical TOF resolution
Fitted start time
e μ π
e μ π K P
e μ π
μ⁻
K
μ
e
π
P
K
P
P
K

Figure 2-13: Example of a start time fit. Each point in the figure is a possible measurement of the start time; N=0 is the TOFI measurement, the other points are calculated from particles passing through TOFII. N=0 and 1 each have only one possible value; the other measurements have possible values for each possible identity (e,μ,π,K,P) of the (unidentified) particle. In the case of the very high momentum track 4, all 5 possibilities lie atop each other at a single point.

The fitted start time is the time, t_f, that minimizes

$$\sum_{i=0}^{N} (t_f - t_{i,n})^2/\sigma_i^2$$

where the sum is over TOFI and all TOFII hits, σ_i is the time measurement resolution of each case, and $t_{i,n}$ is (in the cases of multiple possibilities) the start time possibility closest to t_f. (e.g. $t_{5,n} \equiv t_{5,P}$ and $t_{2,n} \equiv t_{2,K}$ in the figure.)

N = 0 : TOFI
1 : μ^- (MUFB identification by muon counters)
2 : 1.7 GeV/c positive track
3 : 0.8 GeV/c negative track
4 : 20 GeV/c positive track
5 : 2.2 GeV/c positive particle
6 : 7 GeV/c negative particle

(The TOF system identifies N=2 as a kaon, N=5 as a proton, and N=3 as not a kaon or proton; N=4 and 6 are completely ambiguous because of their high momentum.)

the event.

In practice, particles are not identified by explicitly calculating their masses, but by comparing their velocity with the possible velocities for a given momentum. There are only a few possible identities for a stable long-lived elementary charged particle: $e^{\pm}$, $\pi^{\pm}$, $\mu^{\pm}$, $K^{\pm}$, or $p^{\pm}$. The velocity vs. momentum dependence for these particles is shown in Figure 2-14. Typical flight paths in this experiment correspond to times-of-flight of $\approx$10 ns (for β=1), and the TOF resolutions were 100-150 ps corresponding to β resolutions of 0.01-0.015. Thus electrons can be identified up to $\lesssim$500 MeV/c, pions and kaons distinguished up to $\lesssim 2\frac{1}{2}$ GeV/c, and protons identified up to $\lesssim$5 GeV/c.

2.6 Drift Chambers [85]

The drift chambers measured the tracks of charged particles. This information was used to reconstruct neutrino interactions in the target, to observe the decays of strange particles (Λ^o and K^o_s), and to determine the momentum of charged particles. These objectives required both high resolution and, because a single neutrino interaction can produce many particles, the ability to resolve and measure multiple simultaneous tracks.

A drift chamber measures the position of a charged particle by measuring how long it takes for the ionization electrons produced by the particle to drift to an anode sense wire (Figure 2-15). Each chamber measures only one coordinate of the position - the coordinate in the plane of the wires, perpendicular to the orientation of the wires. (An "X" drift chamber has vertical wires and measures the (horizontal) "x" position of the track.) When a particle is detected, a "hit" is recorded by the drift chamber electronics.

Two groups (and sizes) of drift chambers were used in this experiment. The 12 upstream drift chambers (see Fig. 2-6) were between TOFI and the magnet. These chambers were arranged in 4 groups, each group

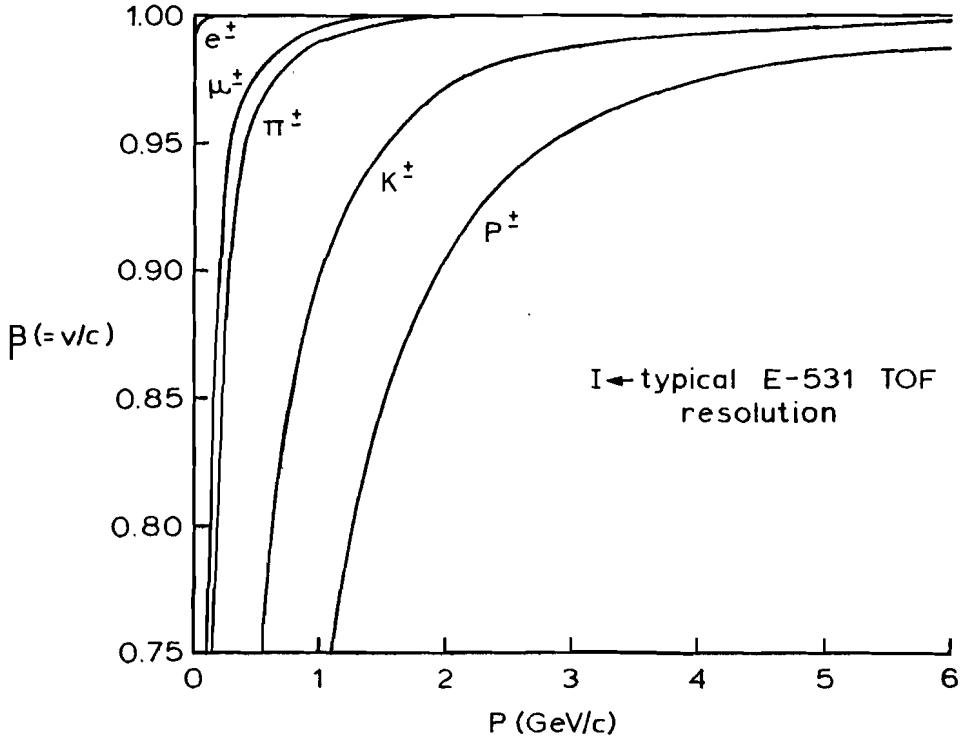

Figure 2-14: Velocity (β) vs momentum (P) for the electron, muon, pion, kaon, and proton.

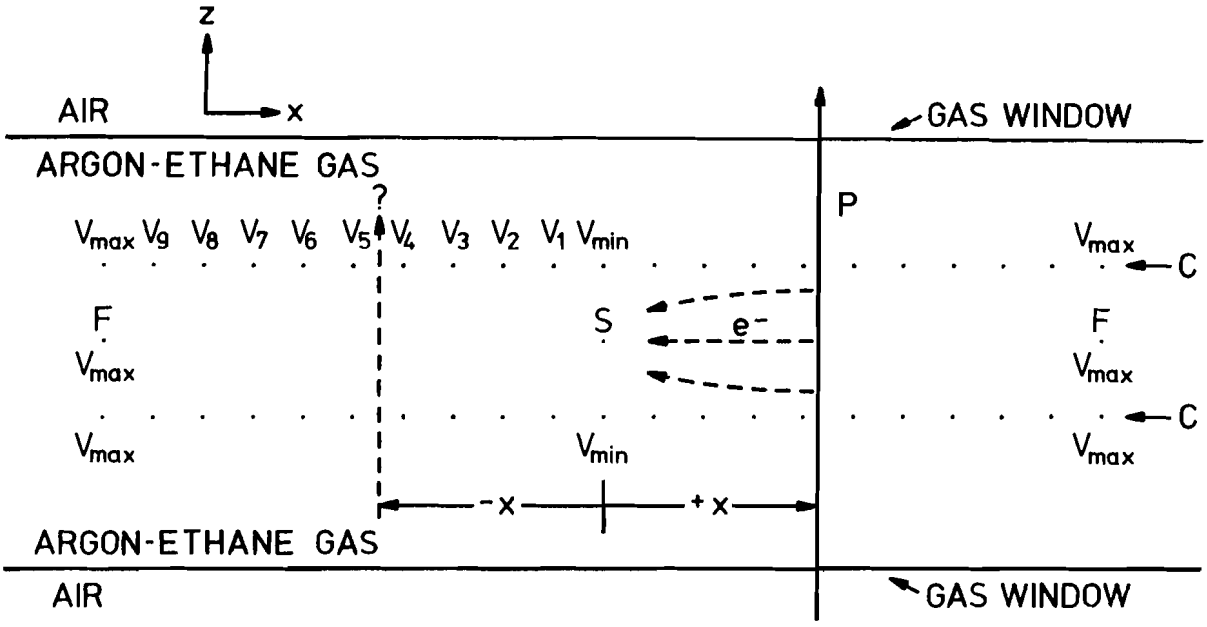

Figure 2-15: A drift chamber cell (Top view): S - sense wire (anode), C - plane of cathode wires, F - field shaping wire (boundary of cell). A charged particle (P) passes through the cell and ionizes the drift chamber gas. The negative high voltages (V_{max},V_9,...,V_1,V_{min}) of the cathode wires cause the ionization electrons to drift to the sense wire. The electrons drift with almost constant velocity, so the distance, $|x|$, of the track from the sense wire is given by the time needed for the electrons to reach the sense wire. The measurement is left-right ambiguous: the drift time corresponds to possible tracks at either +x or -x.

being an U-X-V triplet, and alternate groups were displaced a half cell width transverse to the beam. U and V are coordinate axes in the X-Y plane rotated -30° and +60° from the vertical (Y); the 3 different (XUV) axes and transverse displacementss are necessary to resolve ambiguities and fully reconstruct the particle tracks. All 12 chambers were physically identical except for mounting hardware, and each consisted of thirty-two 4 cm wide cells with a total active area of 128cm x 128cm. The chambers were 1 inch (2.54 cm) thick, had gas windows of 25 μm aluminium on 50 μm of mylar, and were positioned at 4.7 cm intervals (in z). The chambers used a gas mixture of 50% argon & 50% ethane and operated at drift fields of 700 V/cm.

The eight downstream chambers were arranged in 2 groups of 4 chambers. The arrangement was X-V-U-X' X-V'-U'-X', where the "'" indicates a half cell position shift, and the U & V axes were rotated ±11° from the X axis. (These angles are small because gravity makes long wires sag (curve) if they are not almost vertical. The upstream chambers are smaller and have shorter wires, so the upstream U and V axes are at larger angles.) The downstream chambers had active areas (x-y) of 2.0 m by 1.2 m, were 3.2 cm thick with 25 μm(Al)-75 μm(mylar) gas windows, and had 2 inch (5.08 cm) wide cells. These chambers operated at drift fields of 750 V/cm and also used 50%-50% argon-ethane gas.

Each drift chamber wire had a 100X amplifier-discriminator that fed standard NIM [86] signals into a multi-hit time digitization system [87]. The time digitization unit was 1.5 ns (75 μm in space), and the system could record up to 15 hits per wire, being limited by a 36 ns deadtime per hit. (This deadtime corresponds to a 1.8 mm minimum separation between hits. The system could record data from multiple events (neutrino and muon triggers) during a single spill. At the end of the spill, all the drift chamber data was read via CAMAC into the computer (Sec. 2.11).

The drift chambers were calibrated and their resolutions measured using beam muons. A tuning program optimized various track fitting parameters (e.g. the electron drift velocity ≈50 μm/ns) in order to best reconstruct these calibration tracks. The spatial RMS resolution of the chambers (per chamber) was 125 μm for upstream and 175 μm for downstream

chambers; the angular resolutions for reconstructed tracks upstream and downstream of the magnet were 0.6 mr and 0.8 mr.

2.7 Analysis Magnet and Momentum Measurement

The wide-gap SCM-104 magnet provided the magnetic field for charged particle momentum measurement. The magnet is a vertical dipole with a 0.8 m long (in z) by 2.0 m wide by 1.0 m high aperture. During the data run, the magnet gap was completely filled with helium (in a bag) to reduce multiple Coulomb scattering and the resulting degradation in momentum resolution. The magnet was operated at a current of 2400(±10) Amperes with a total power consumption of 700 kW. The magnetic field, B, was not uniform over the aperture, but was well known from a map of ~45,000 measurements made at 1 inch intervals. Outside the mapped region a polynomial field parameteriztion was used. The field was 5760 Gauss at the centre of the magnet, and the paths of particles passing through the magnet aperture had an average integrated field length of $\langle \int B \cdot dl \rangle = 6.2$ kG-m.

The momentum of a charged particle whose track is bent by an angle θ by passing through the magnet is approximately given by

$$P \cong 0.03 \int B \cdot dl / \theta$$
$$\approx 0.186/\theta \quad \text{GeV/c}$$

i.e. Charged particles receive an average horizontal (x) momentum "kick" of $P \cdot \theta \approx 186$ MeV/c from the magnetic field. The magnetic field bent the paths of positive charged particles to the right (facing downstream) and negative particles to the left.

The momentum resolution (RMS) for tracks passing through the magnet aperture and all 20 drift chambers was

$$\sigma(P)/P = [(0.009)^2 + (0.005P)^2]^{+\frac{1}{2}}$$

or, in terms of the inverse momentum $Q \equiv 1/P$,

$$\sigma(Q) = [(0.009Q)^2+(0.005)^2]^{-\frac{1}{2}} \quad .$$

The first term (0.009) is the contribution from multiple scattering of the tracks in the air, helium, and drift chambers, and the second term (0.005) is from the intrinsic drift chamber spatial resolution. The momenta of charged particles that did not pass through the downstream drift chambers could sometimes be determined, but poorly, from the small curvatures (due to the fringe field of the magnet) of tracks seen in the upstream drift chambers only. The upstream-only momentum resolution was $\sigma(P)/P \gtrsim 0.35P$.

The absolute momentum calibration was checked using the mass of the proton and the Q distribution of muons from neutrino interactions. The mass of the proton measured by time-of-flight was 939±4 MeV/c^2 (true value: 938.28 MeV/c^2); this good agreement gives

$$\langle Q(\text{measured})/Q(\text{true})\rangle = 0.999\pm0.005$$

Comparing the observed and expected Q distributions of muons near Q=0 (Figure 2-16) gives, however,

$$\langle Q(\text{measured})\rangle - \langle Q(\text{true})\rangle = 0.005\pm0.0015 \quad (\text{GeV/c})^{-1}$$

This indicates a small systematic offset approximately equal in size to the resolution. (The charm data of Chapter 4 has been corrected for this small offset.)

2.8 Lead Glass Array

The lead glass array was an electomagnetic calorimeter: it measured the energy of photons and electrons. This measurement served to detect and identify these 2 particles, and to provide the information necessary to reconstruct $\pi^o \to \gamma\gamma$ decays.

An electron or photon entering a lead glass block will interact and

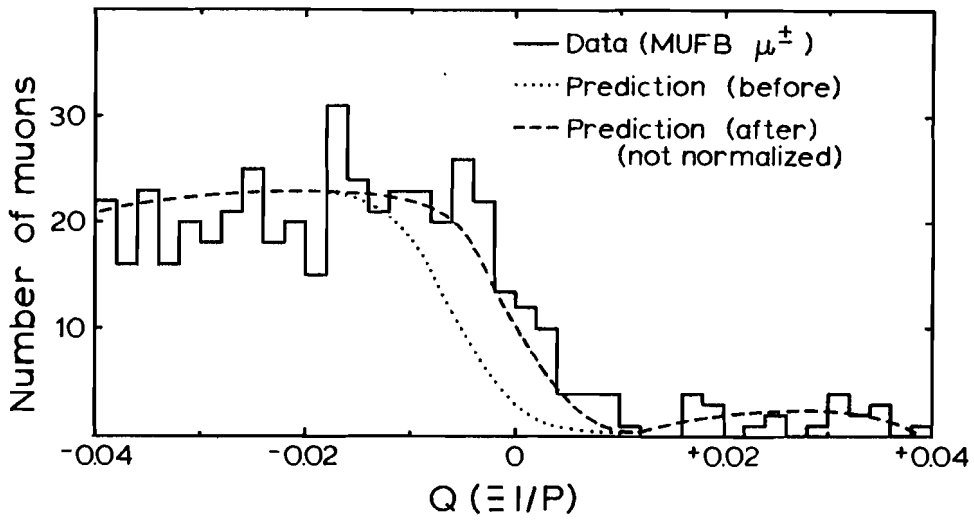

Figure 2-16: Q (inverse momentum) distribution near Q=0. The predicted curves are before and after including a systematic Q offset of Q(measured)=Q(true)+0.005. The shape of the observed distribution at Q≈0 is dominated by the measurement resolution and any systematic errors; it is not very sensitive to the true shape.

produce an electromagnetic shower - a cascade of electrons and photons. A phototube detects the Cerenkov light produced by the electrons, and the total amount of light is proportional to the energy of the initial particle. Muons (and most hadrons) will pass through a lead glass block without interacting, producing only a minimum-ionization light pulse. Some hadrons will interact in the lead glass (the blocks are $\sim\frac{2}{3}$ of an absorption length thick) and produce signals larger than muons, but usually less than electrons.

The lead glass array consisted of 68 lead glass blocks (Figure 2-17a). The blocks were 19 cm by 19 cm square and were either 30.5 cm ($9\frac{1}{2}$ radiation lengths, made of F2 lead glass) or 35.0 cm ($12\frac{1}{2}$ r.l., SF2 lead glass [88]) long. Each block was viewed by a 5 inch phototube glued directly to its downstream face (Figure 2-17b). Signals from the tubes were amplified, split in a 1:20 ratio, and fed into two 0.25 pC/count ADC's; this arrangement provided a dynamic range adequate to measure both the small pulses from single muons (for calibration) and the large pulses from electromagnetic showers. The maximum (ADC saturation) signal corresponded to an electromagnetic shower energy of ~30 GeV per block.

The pulse height to energy calibration of the blocks was determined using data from tests in an electron/pion beam. The response to electrons of both long and short blocks is shown in Figure 2-18. The pulse height for minimum-ionizing particles was (in equivalent electromagnetic energy)

E_{min} = 400±30 MeV/(minimum ionizing track) (long block)

E_{min} = 330±20 MeV/(minimum ionizing track) (short block)

The energy resolution as a function of energy was $\sigma(E) \cong 0.15\sqrt{E}$ (RMS).

During the data run, all blocks in the array were monitored and calibrated using beam muons. Relative gains and inter-ADC calibrations were also monitored using light pulses from a neon flash tube ("flasher") that was fired between spills, the light being fed into the front of each block via a fibre optic cable.

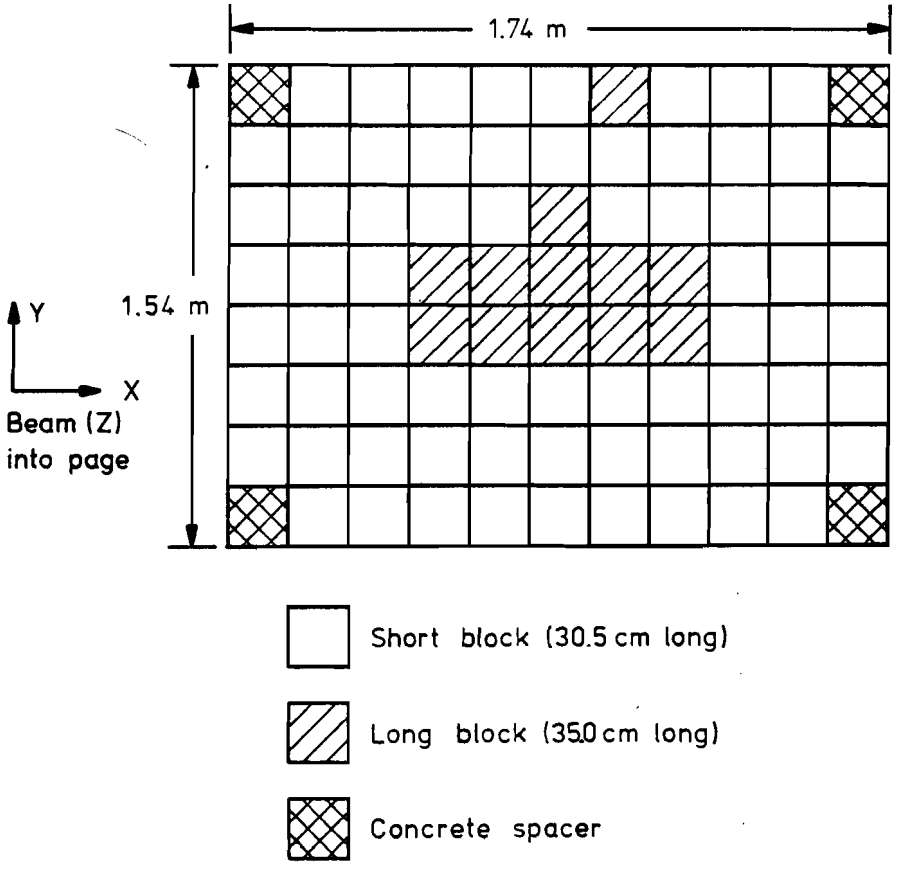

Figure 2-17a: The Lead Glass Array.

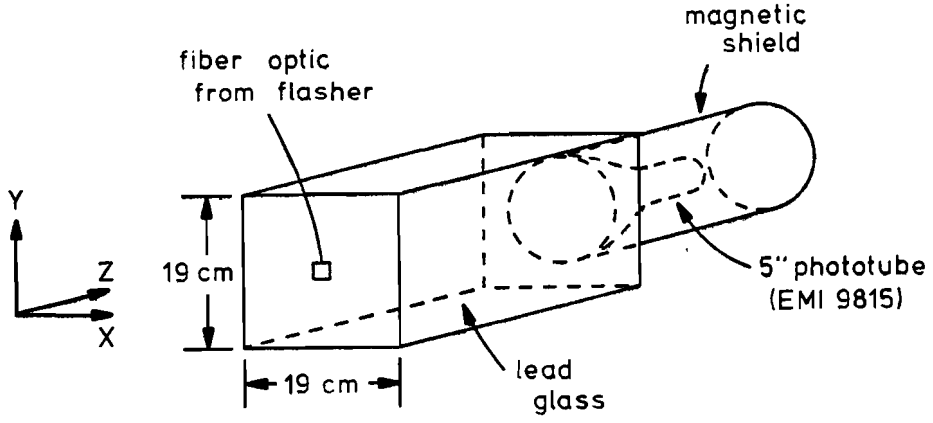

Figure 2-17b: A Lead Glass Block.

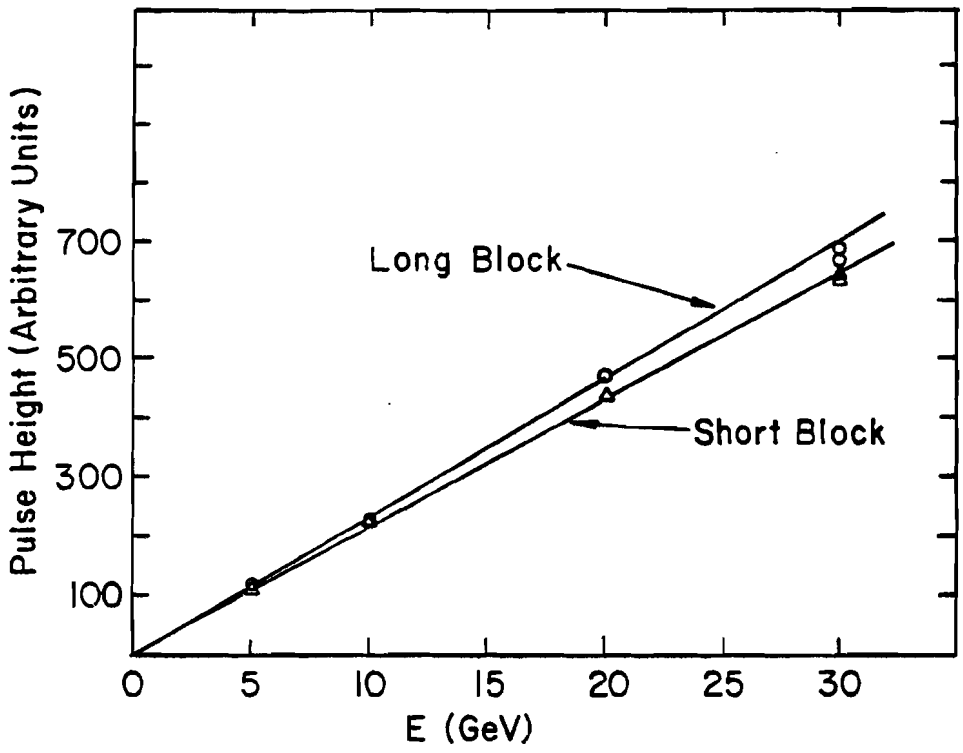

Figure 2-18: Average lead glass pulse height for electrons (of energy E).

2.9 Hadron Calorimeter

The hadron calorimeter measured the hadronic energy of the neutrino interaction and provided some ability to detect neutrons and neutral kaons. The calorimeter consisted of 5 planes of four 1.3 cm thick scintillator counters sandwiched between 10 cm thick steel plates (Figure 2-19). The counters were each viewed by a single 5 inch phototube coupled to the scintillator by an adiabatic light guide. The signals from each tube were split in a 1:7 ratio and fed into two 1024 channel ADC's. This arrangement could accurately measure both the small pulses from single minimum-ionizing muons and the large signals from hadronic showers.

The energy response and resolution of the calorimeter were [89]

$$E(CAL) = \frac{N}{2a}(1+\sqrt{1+4ab/N})$$

and

$$\sigma(E) = 1.1\sqrt{E}$$

where

N = pulse height in terms of equivalent number of minimum-ionizing pulses

a = 5.428/GeV, b=0.721 GeV

The pulse height distribution for minimum-ionizing muons is shown in Figure 2-20. The minimum-ionizing peak corresponds to a hadronic energy of 1.75 GeV. The calorimeter response was linear up to ~20 GeV per column, but saturated at $\lesssim$50 GeV per column (Figure 2-21) because each counter (of 5 per column) could record a maximum ADC signal corresponding to ~10 GeV. The calorimeter acceptance was larger than the lead glass array, so the total calorimeter energy will include contributions from electrons and photons that miss the lead glass but hit the calorimeter.

2.10 Muon Counters

The muon counters (Figure 2-22) identified muons by their range in steel. (All particles except muons cannot penetrate the steel.) There were 2 crossed arrays of scintillator counters embedded in steel at

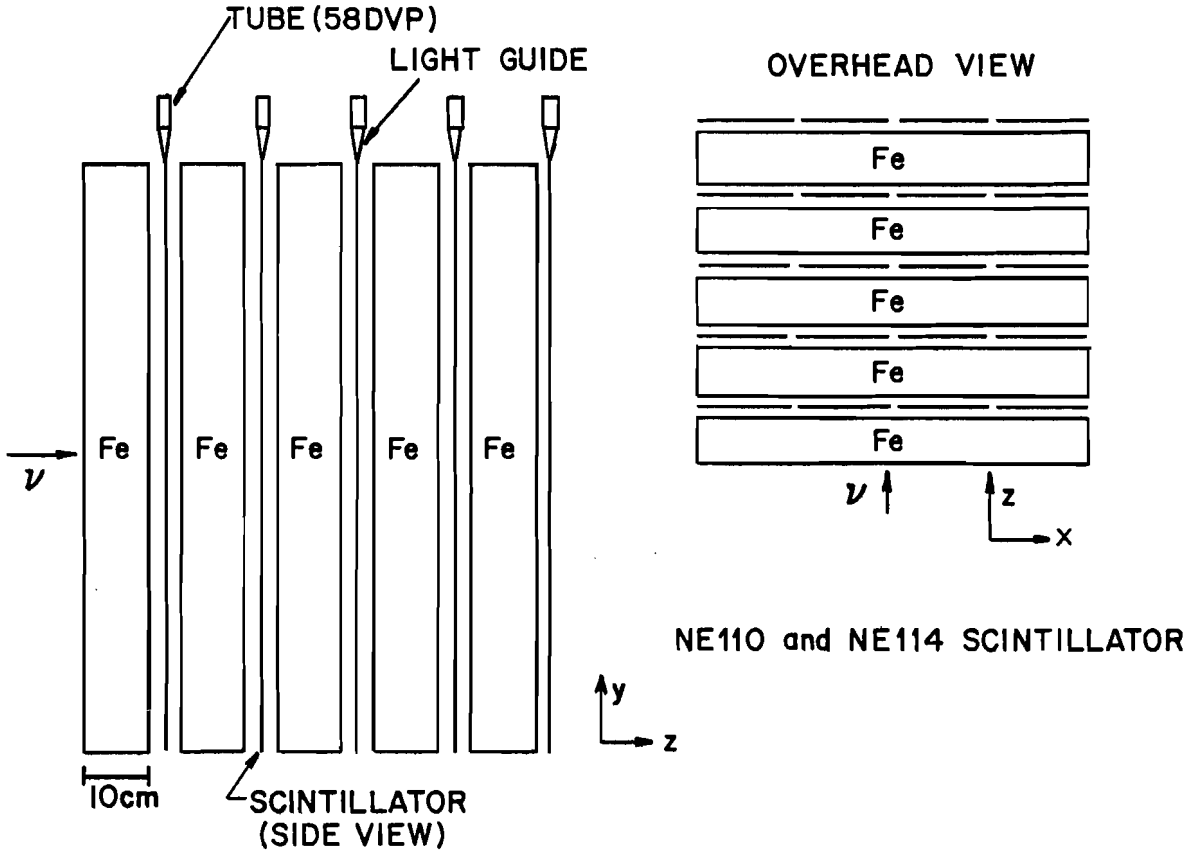

Figure 2-19: The Hadron Calorimeter. The scintillators are 8' (2.44 m) long and 2'6" (76 cm) wide, and have an optical attenuation length of ~5 m. The counters are aligned in 4 columns and 5 rows.

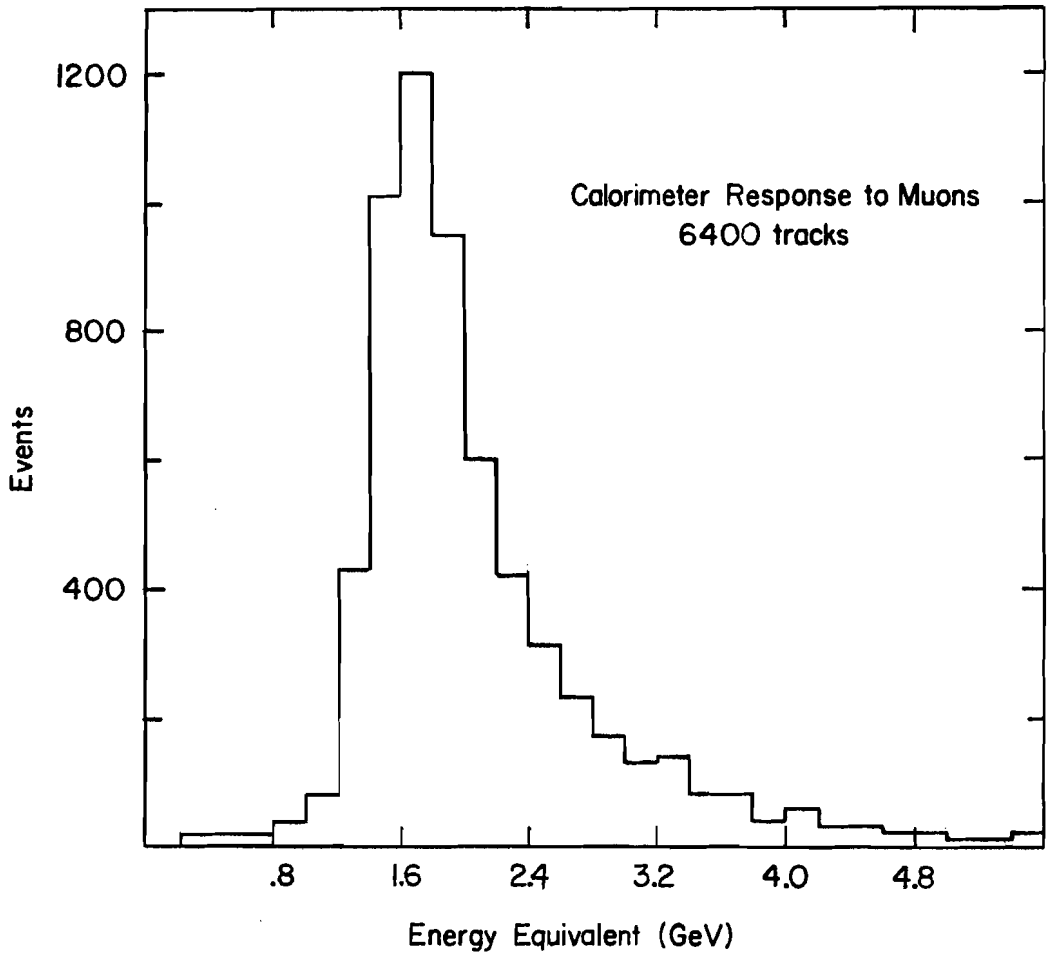

Figure 2-20: Pulse height distribution (in equivalent energy) of muons passing through the hadron calorimeter.

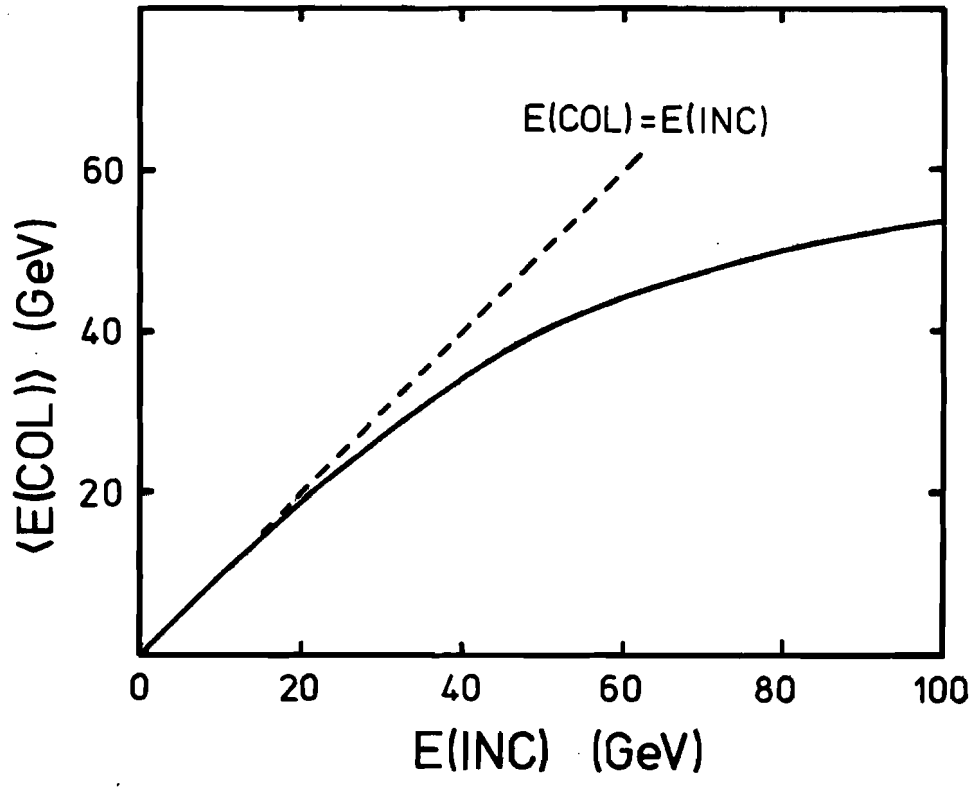

Figure 2-21: Expected deviation of <E(COL)> from E(INC) due to ADC saturation. <E(COL)> is the average energy measured by a single calorimeter column, and E(INC) is the actual hadronic energy incident on the column.

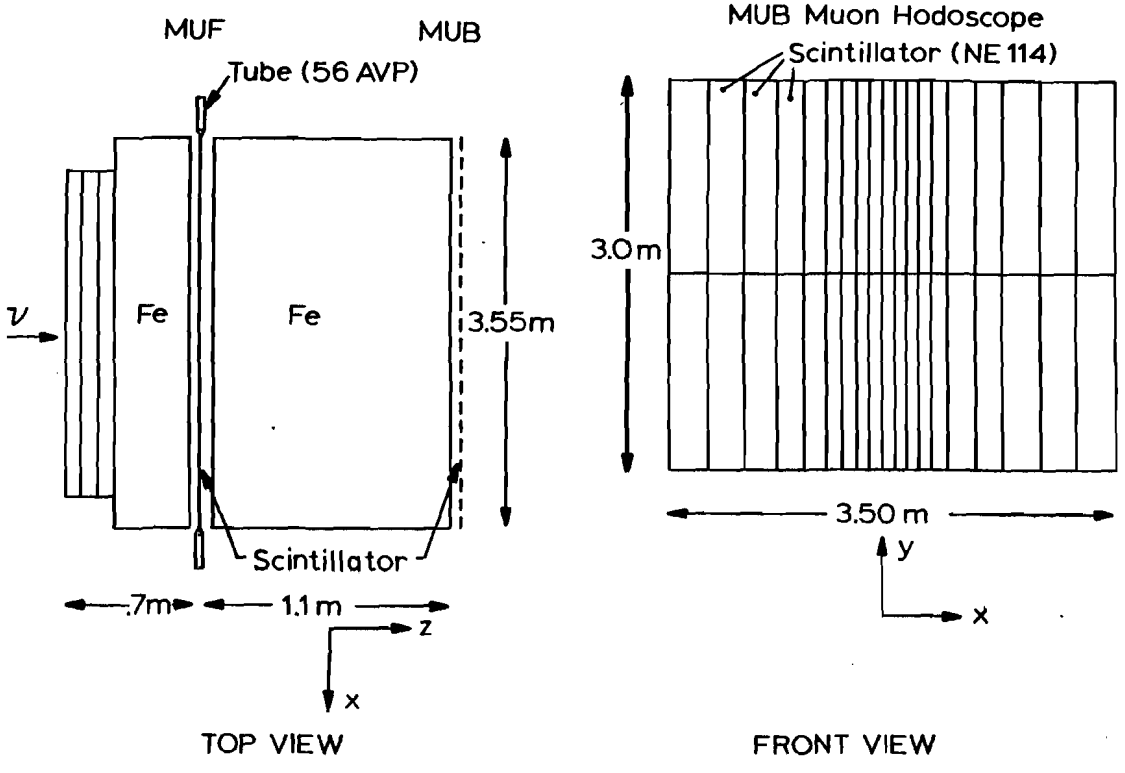

Figure 2-22: The Muon Hodoscopes. The front view shown is the back (MUB) hodoscope (sans tubes and light guides); the front hodoscope (MUF) is similar, but the counters are horizontal, not vertical. The lead glass and calorimeter, not shown, have a total equivalent thickness of 0.5 m of steel.

depths (in z) of 1.2 and 2.3 m (including the calorimeter steel and the steel equivalent thickness of the lead glass). These thicknesses correspond to the ranges of 1.9 and 3.4 GeV muons, and to 7 and 14 hadronic absorption lengths.

The muon counters were calibrated in a manner similar to that used for the TOF counters. The average muon counter time resolution was $\sigma(t)=0.8$ ns - this corresponds to a position resolution along the counter of 13 cm. The transverse position resolution was simply the counter's width.

A charged particle observed in the drift chambers was considered as "tagged" by the muon counters if the front or back planes had a hit within 2.5 S.D. of the extrapolated position of the drift chamber track. (The resolution here includes multiple scattering in the steel.) The track was tagged as a "muon front" (MUF), a "muon back" (MUB), or "muon front-back" (MUFB) depending on which muon hodoscopes detected it. Particles were not tagged unless their measured momentum was sufficient for a muon to penetrate the steel - this cut was normally $P>2$ GeV/c for a MUF tag and $P>4$ GeV/c for MUFB and MUB tags. The measured efficiencies for tagging real muons passing through the muon detector were 95±1% for MUF, 94±1% for MUB, and 89±2% for MUFB. The 5% inefficiency per plane is due to timing and pulse height cuts and gaps in the arrays. The probability that a true muon is not tagged by either array is 0.3%.

The rate of false muon tags was very small. Only 5 events (out of 2022) had two tracks tagged as MUFB muons using independent muon counters, and 2 of these extra muons came from semileptonic decays of charmed particles. The remaining 3 events, compared to the 1051 events with a single MUFB μ^- or μ^+, give a MUFB misidentification rate of ~0.3% per event. This rate is consistent with that expected from muons produced by the decays of pions and kaons from the neutrino interactions. The MUF and MUB misidentification rates are similarly estimated to be ~4% and ~3% per event. (Some of the MUF misidentifications may be due to hadronic punch-through [90], but most of the MUF and MUB false tags are due to random coincidences, noise, and background beam muons.)

2.11 Data Acquisition

Electronic data from this experiment were transmitted via a standard CAMAC [91] dataway into an ECLIPSE S/200 computer [92] which recorded the data on magnetic tape. The electronic systems were read 3 times during each accelerator cycle, each time being called an "event": a sensor event, a laser/flasher event, or a spill event.

A sensor event occurred at the beginning of each accelerator cycle. The many sensors (e.g. position, temperature, voltage, magnet) monitoring the whole experiment were read at this time. As well, all ADC's were gated and read, so pedestals (background signal levels) could be measured.

A laser/flasher event occurred several seconds after the sensor event. The TOF laser and the lead glass light flasher were fired and the calibration pulses recorded.

A spill event occurred after the end of the neutrino beam spill. It was impossible to read out the entire experimental system and reset it for new data within the time of the spill, so all data (from neutrino interactions or beam muons) were read out after the end of the spill.

2.11.1 Triggers

During a beam spill, the electronic detectors recorded data if either a muon or neutrino trigger had occurred. The muon trigger was designed to detect single beam muons passing through the experiment, and the neutrino trigger was designed to detect neutrino interactions in the emulsion target.

The triggers' (symbolic) logical definitions were

$$T_\mu \text{ (muon trigger)} = G_\mu \cdot \text{TOFI}>1 \cdot \text{TOFII}=1$$

and

$$T_\nu \text{ (neutrino trigger)} = G_\nu \cdot V \cdot \text{TOFI}>2\tfrac{1}{2} \cdot \text{TOFII}>2$$

where the "•" indicates time coincidence.

"TOF>n" indicates that the TOFI counter has a total pulse height

(summed over all 12 tubes) greater than nPH_{min}, where PH_{min} is the pulse height for a single minimum-ionizing particle. Figure 2-23 shows the TOFI integral pulse height (ADC) spectra for muons and reconstructed (real) neutrino interactions. "TOFII=(or>)n" indicates that n (or more) TOFII counters simultaneously detect particles. The muon trigger TOF reguirements define a single charged particle passing through TOFI and TOFII, the neutrino trigger TOF requirements roughly define 2 or more charged partcles.

"V" indicates that the veto counter array detects no charged particles entering the experiment from upstream. This requirement rejected most beam muons and background hadrons. (The E-531 veto detector was $\frac{1}{2}$m downstream of a $1\frac{1}{2}$m thick steel wall, so almost all beam hadrons, charged and neutral, were part of large showers detected by the E-531 veto. Only ~10 high energy (E>10 GeV) interactions of photons, neutral kaons, and neutrons were expected in the emulsion target, and less than ~1 of these was expected to be not vetoed and found in the emulsion. i.e. There should be less than one background event in our found neutrino interaction sample, and, because of our good muon identification, there should be $\lesssim 10^{-3}$ background events in our charged current data.)

G_μ and G_ν are the muon and neutrino gates. These gates are the time periods in which muon and neutrino triggers would be accepted. The neutrino gate was long enough (~10 ms) to safely cover the whole 1 ms spill when beam neutrinos were passing through the detector; the start of the G_ν was a signal from the accelerator. The muon gate was quite short and typically covered the last 5% of the spill. The start of G_μ was accurately set by using the muon counters to detect the beam muons. It was important that G_μ be restricted to the end of the spill; this is because the ADC's and TDC's could only record data from the first muon or neutrino trigger in a spill. (Only the drift chambers could record data from multiple triggers.) Thus if a muon (calibration data) trigger occurred before a neutrino (real data) trigger there would be counter information only for the muon and not the neutrino interaction. G_μ and G_ν were set up so that usually (~$97\frac{1}{2}$% of the time) a neutrino trigger would not have a muon trigger precede it.

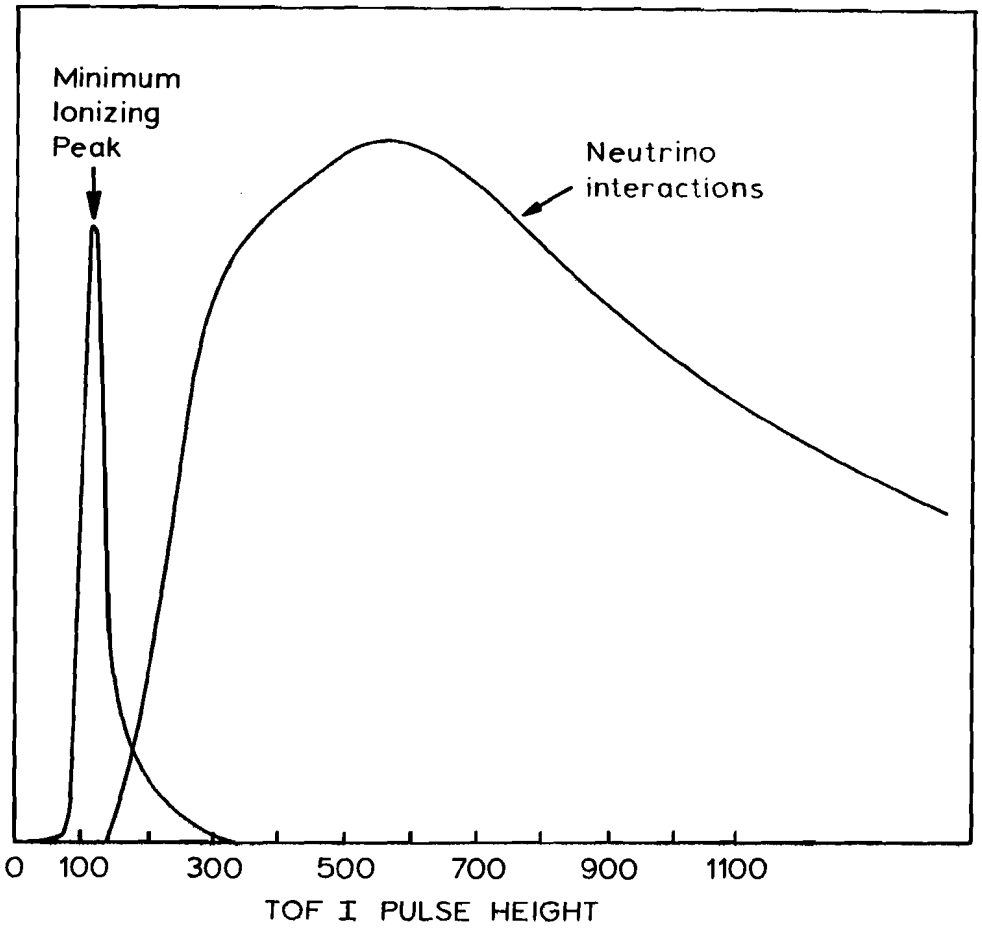

Figure 2-23: Summed TOFI pulse height (all 12 phototubes) distributions for reconstructed beam muons and neutrino interactions. (The two curves have an arbitrary relative normalization - there are actually 1000 times as many muons as neutrino interactions.) The minimum ionizing muon peak is at a pulse height of 115; the average pulse height for neutrino interactions is ~1300.

The neutrino trigger was designed to reject beam muons while rejecting as few real neutrino interactions as possible. Less than 0.1% of the beam muons caused neutrino triggers, but there were so many beam muons that these false neutrino triggers occurred in about 1 out of 7 spills. A real neutrino interaction could not be fully recorded after a false neutrino trigger, so the false neutrino triggers caused a loss of $\frac{1}{2} \cdot \frac{1}{7} = 7\%$ of the real neutrino interactions. (The factor of $\frac{1}{2}$ is because the false neutrino triggers came, on average, halfway through a spill.) The total deadtime fraction, measured directly online during data taking, was 0.21. i.e. 21% of real neutrino interactions were missed because of veto overkill (Sec. 2.2), muon triggers, or false neutrino triggers.

2.11.2 Data Run

The emulsion modules were installed and E-531 data acquisition began on November 18, 1978. The run ended on February 7, 1979 after over 1250 hours of beam and a total of 7.2×10^{18} protons incident on the neutrino target. Less than ~5% of the beam was wasted (changing the changeable emulsion sheet and magnetic tapes), or lost due to E-531 equipment failures.

A total of $\sim 10^{15}$ neutrinos and $\sim 10^{8}$ muons passed through the emulsion target. Over 900,000 muon triggers and 68,000 neutrino triggers were recorded on tape. One hundred and forty of the neutrino triggers were taken during antineutrino running (horn focussing negatives), and $\sim 2\frac{1}{2}\%$ of the data was taken with the magnet off. Roughly, there was a neutrino trigger every minute, a real neutrino interaction every half hour, and a charmed particle produced once a day.

2.12 Event Reconstruction

Neutrino interactions were reconstructed by several computer programs. The tracks of charged particles were reconstructed from the drift chamber data, and this information was used to predict the positions of neutrino interaction vertices. The data from all neutrino triggers were processed to find neutrino interactions, and after being found in the emulsion, events with charm decays were reprocessed and reanalysed in great detail.

A program at the University of Toronto written by Prof. Taek Soon Yoon (TSY) was used during and immediately after the data run in order to find neutrino interactions in the emulsion as soon as possible. This early program was later superceded by a program written by Prof. Noel R. Stanton (NRS).

Drift chamber tracks were reconstructed back to front - the tracks were found first in the downstream drift chambers, and then extrapolated upstream to connect with track segments in the upstream drift chambers. The tracks were more easily distinguished (were more widely separated) in the downstream than upstream drift chambers. This was because the upstream drift chambers were much closer to the origin of the tracks at the interaction vertex, and also because the magnet tended to sweep away the low momentum tracks that often cluttered the upstream drift chambers. Figure 2-24 is a display of the spectrometer data for a real (if somewhat idyllic) neutrino interaction.

Track segments in the downstream drift chambers were reconstructed by finding 3 or 4 collinear hits in the X chambers, and then looking for consistent U and V hits. Upstream track segments were reconstucted by extrapolating the downstream track segments to the centre of the magnet, and then creating "roads" from these points to the estimated interaction vertex in the emulsion. Upstream track segments were required to be within these roads (the roads were typically 0.7 cm wide at the magnet mid-plane, and 2.5 cm wide at the estimated vertex position. The preliminary estimates of the vertex position were made by either finding the average intercepts (at z=0, approximately the upstream face of the

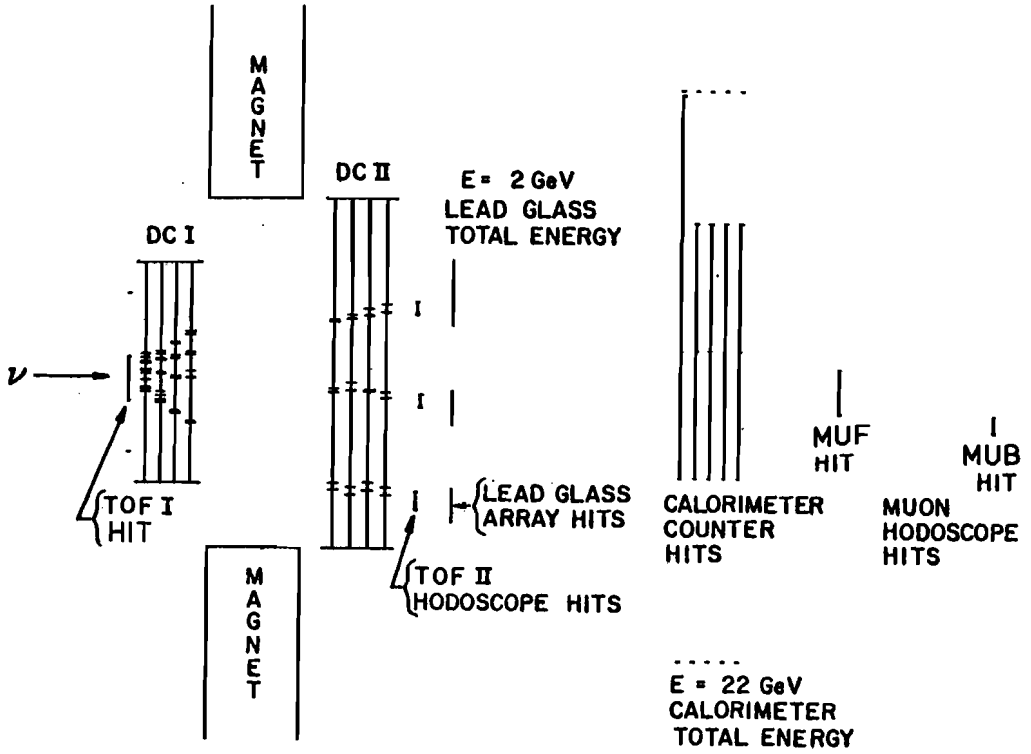

Figure 2-24: An on-line display of a neutrino interaction (plan view in x-z plane). Three clean UPDN charged particle tracks are seen (in both upstream and downstream drift chambers); one of these particles is a MUFB muon (with hits in both front, MUF, and back, MUB, muon counter hodoscopes). There is also at least one UP-only track (seen only in the upstream drift chambers). Only X drift chambers are shown; the 2 hits in each drift chamber for each track indicate the left-right position ambiguity about the sense wires.

emulsion) of all upstream X, U, V line segments (TSY program), or by projecting a high momentum track (preferably a MUFB or MUF muon, or a very fast hadron) to the emulsion (NRS program).

Tracks were fitted by the quintic spline method which parameterized the tracks in terms of their inverse momentum (Q) and their slopes (dx/dz, dy/dz) and positions (x,y) at z=0. The χ^2 of each track was calculated from the differences between the fitted track and the actual drift chamber hits. The NRS program fitted only tracks with hits in both upstream and downstream drift chambers (UPDN - pronounced "up-down" - tracks); the TSY program and charm event reanalysis programs (Sec. 3.7) also fitted UP-only tracks that missed the downstream drift chambers and that were seen only in the upstream chambers.

The position of the neutrino interaction vertex is calculated by finding the point of closest approach of the reconstructed tracks. The tracks are weighted by their χ^2, their number of hits, their momentum, and whether they are identified muons. Tracks are excluded from the primary vertex position estimate if they are inconsistent with coming from the primary vertex. (Such tracks may be electrons from γ conversions, hadrons from secondary interactions or particle decays; secondary vertices are estimated if possible.) A neutrino interaction vertex can be reconstructed with as few as two UPDN tracks, so the reconstruction programs impose no new cuts beyond the two-track requirement of the neutrino trigger (Sec. 2.11.2).

2.13 Emulsion Processing and Characteristics

The emulsion was developed over a period of 2 months at the University of Ottawa [9,10,93]. The developed emulsion sheets are half their original thickness and have warped and distorted edges. The shrinkage is easily corrected for and all emulsion geometrical measurements are quoted in terms of the original undeveloped emulsion dimensions. Because of the distortion, about a 3 mm margin is rendered

unusable at the edges of the emulsion sheets and around post-holes.

The tracks of charged particles are delineated in developed emulsion by silver grains (see Figure 2-25) - the number of grains per unit track length being proportional to the ionization of the particle. Our emulsion quality was excellent and the grain density for electrons from stopped muons was

I_o = 28.4±0.7 grains per 100 μm (horizontal emulsion sheets)
I_o = 31.3±1.2 grains per 100 μm (vertical emulsion sheets)

(Note: A truly minimum-ionizing particle, at the minimum of the ionization curve (see Fig. 2-27), has a ionization $I_{min}=0.86I_o$.) The variation in I_o amongst different emulsion sheets was less than 3%, and the fog density (randomly developed grains) was $1.3\times10^6/mm^2$. There were 30±5 cosmic ray tracks per mm^2 and the beam muon density was 130±20 muons/mm^2 for $\theta<5.5°$ (and 225±23 muons/mm^2 for $\theta<20.5°$). The angular distribution of all minimum-ionizing background tracks is shown in Figure 2-26.

The local spatial resolution of the emulsion corresponds roughly to the ~1μm size of the silver grains. For measurements over long distances the uncertainties due to warpage and shrinkage become dominant. The emulsion angular resolution for tracks seen in the drift chambers was measured to be

$\sigma(\theta) = (0.0015+0.01\theta)$ radians (vertical)
$\sigma(\frac{dy}{dz}) = 0.5\sigma(\frac{dx}{dz}) = (0.0033+0.02\theta)$ radians (horizontal)

2.13.1 Momentum Measurement in Emulsion

The multiple Coulomb scattering of a charged particle is inversely proportional to its momentum times velocity (Pβ). For a particle of unit charge travelling a distance L in a material with radiation length r.l., the mean angular displacement (in space) due to multiple scattering is [94]

$$\theta_o = \frac{20\ \text{MeV/c}}{|P\beta|}\sqrt{\frac{L}{r.l.}}\left[1+\frac{1}{9}\log_{10}\left(\frac{L}{r.l.}\right)\right] \quad \text{radians}$$

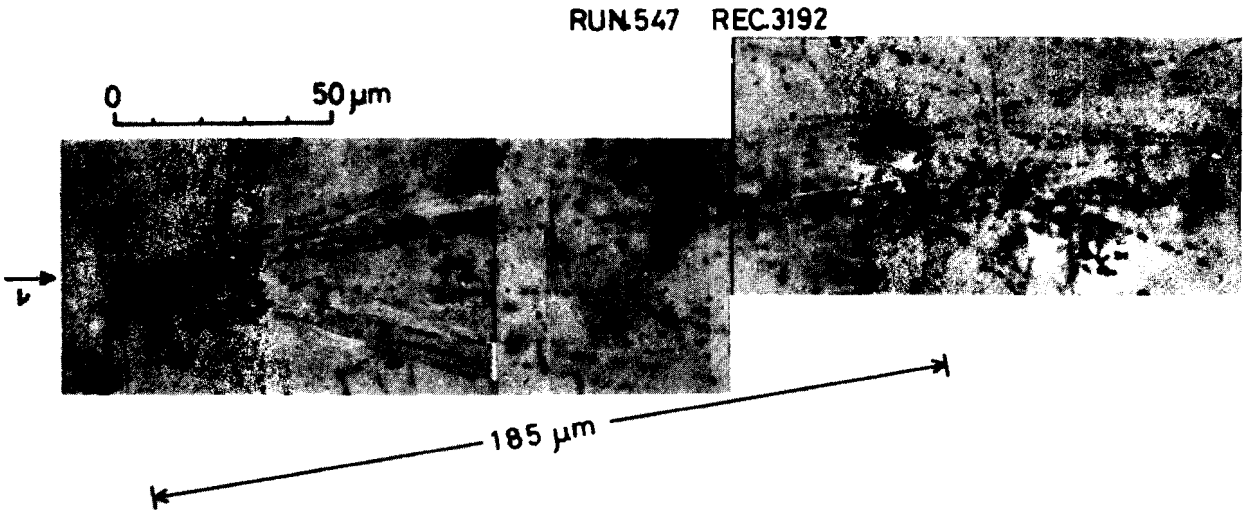

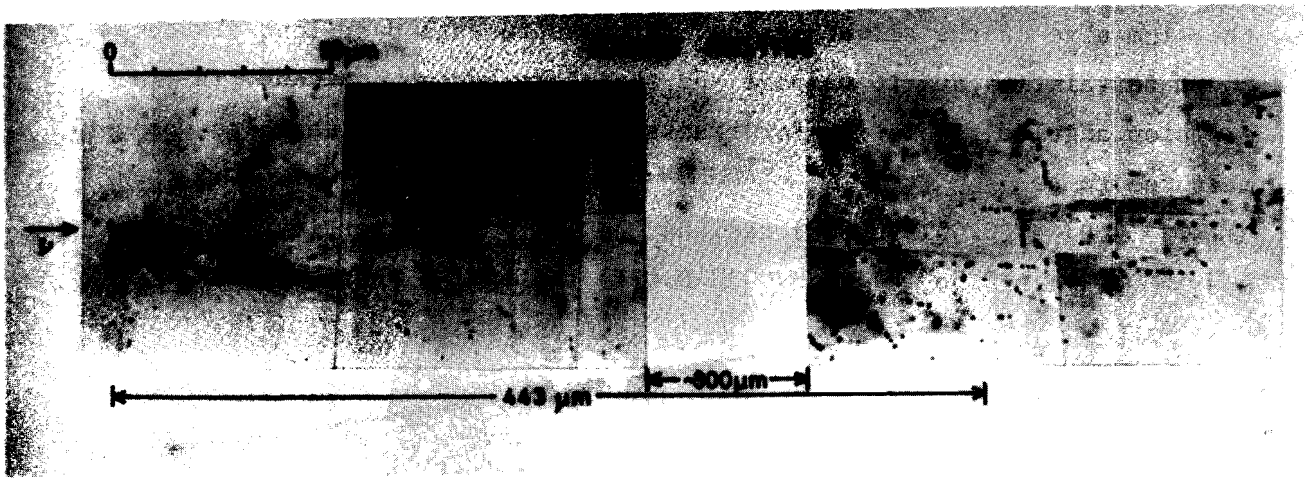

Figure 2-25: Photomicrographs of neutrino interactions with charmed particle production and decay.

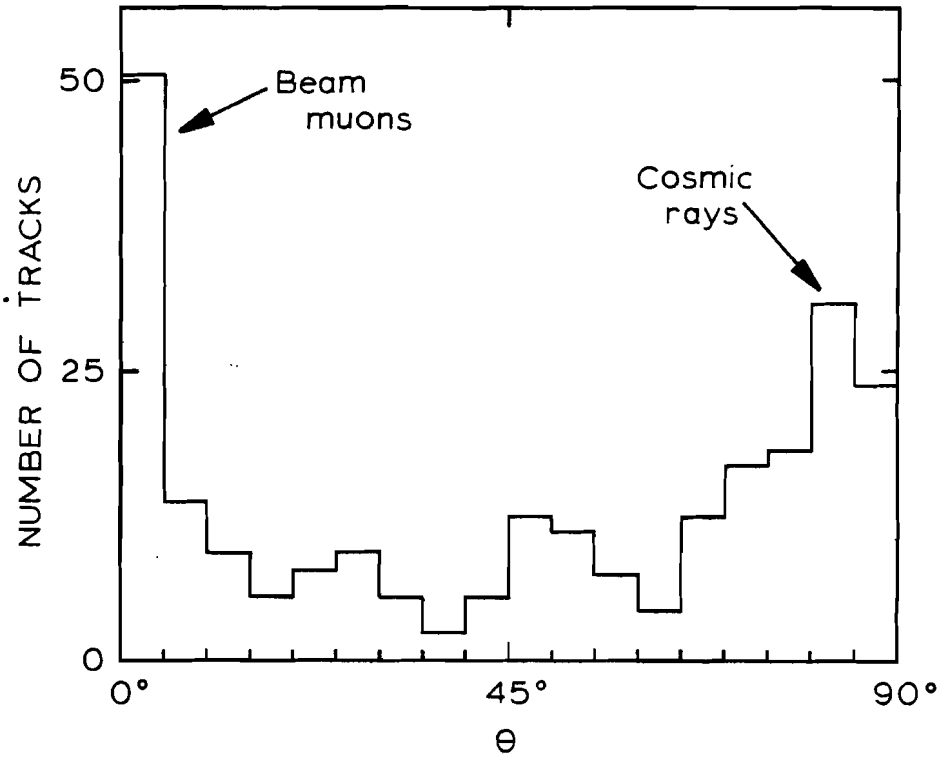

Figure 2-26: Angular distribution of minimum ionizing background tracks in the emulsion (248 tracks in this sample). θ is the azimuthal angle of the track with respect to the neutrino beam direction (z).

The Pβ of tracks that were not seen or were poorly measured in the downstream spectrometer could often be determinined from multiple scattering in the emulsion [10,95,96]. The angular deviations of the tracks were measured by comparison with some fast track (e.g. the primary muon) in order to remove emulsion distortion and microscope jitter. The Pβ measurement was usually more accurate than the up-only drift chamber momentum for tracks below 700 MeV/c. Pβ could sometimes be determined from track segments as short as 1-2 mm.

2.13.2 Particle Identification in Emulsion

Figure 2-27 shows the calculated ionization I/I_o versus Pβ curves for different particles in emulsion [10,95,96]. Particles can be identified if their ionization is much greater than I_o and their Pβ is known. Protons can be distinguished from kaons up to 1.5 GeV/c, and kaons distinguished from pions up to 800 MeV/c. Electrons (not shown in the figure, but always $I=I_o$ for $P\beta \gtrsim 10$ MeV/c) can be identified for $P\beta \lesssim 100$ MeV/c.

Pions can be identified by their decays if they are slow enough to stop in the emulsion; the kinetic energy of such stopping particles can be determined by their range. Figure 2-28 shows an E-531 neutrino interaction in which a π^+ from a Λ_c^+ decay is identified and its energy measured from its $\pi \rightarrow \mu \rightarrow e$ decay chain.

2.14 Event Finding

Two methods were used to locate neutrino interactions in the emulsion target: "volume scanning" and "track followback" [10,9,97].

A volume scan for a reconstructed interaction was a search of a region 4mm(x) by 4mm(y) by 20mm(z) centred on the predicted vertex location. The search was usually carried out under low magnification

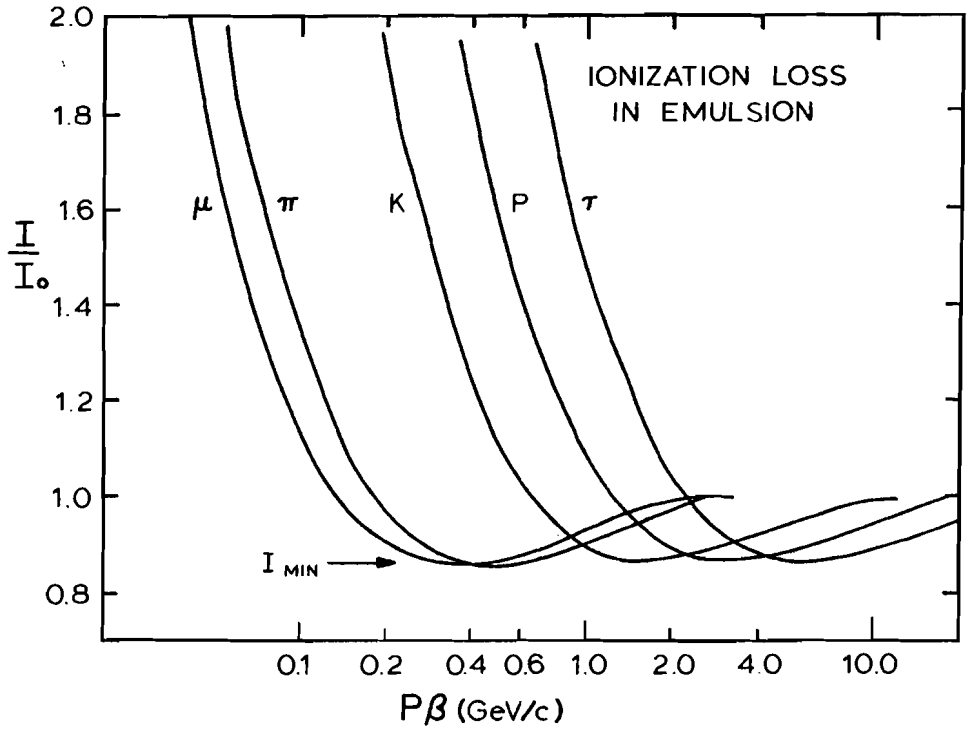

Figure 2-27: Ionization vs Pβ for different particles in emulsion.

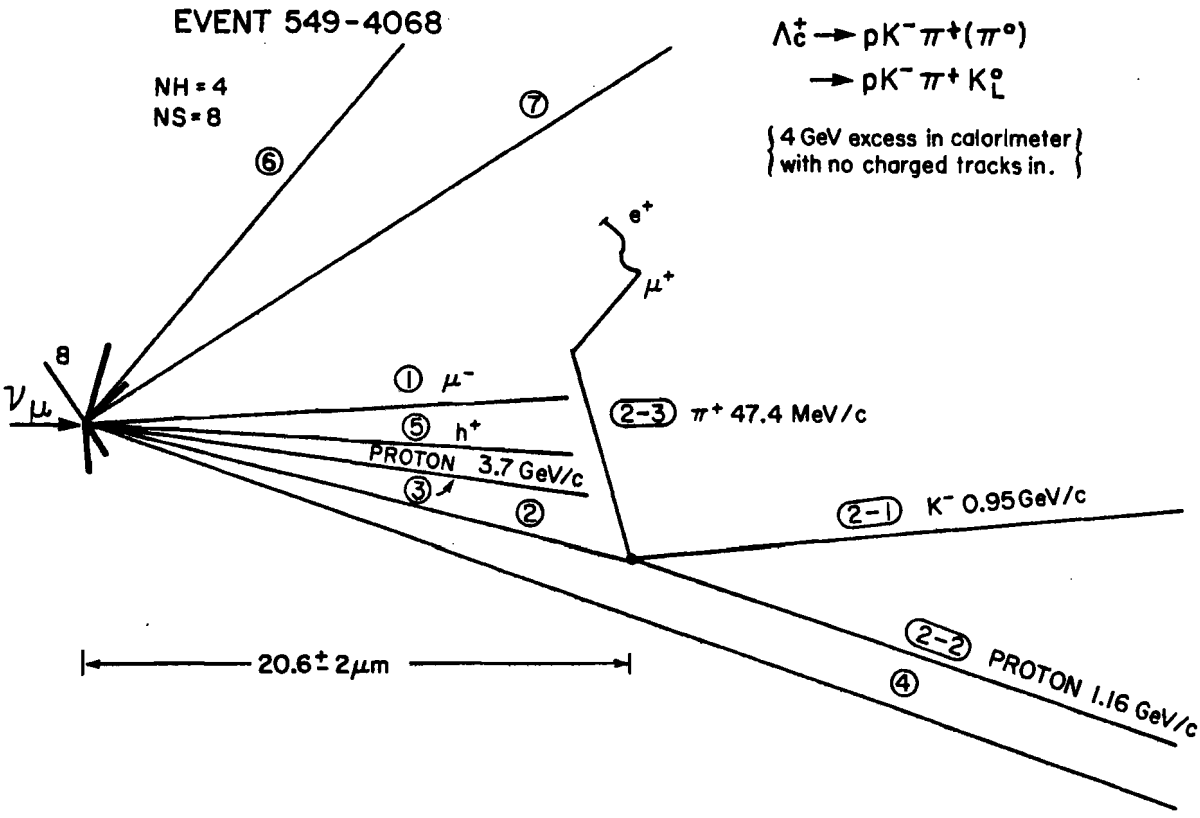

Figure 2-28: Sketch of a charged current neutrino interaction in which a Λ_c^+ is observed to decay.

(x100 or x200), so neutrino interactions with no highly visible "heavy" tracks were difficult to find. These events can be found using higher magnification, but scanning speed drops as 1/magnification$^{2\sim3}$. (It typically took several hours to find one event.) Heavy tracks are tracks with ionization (I) in the emulsion such that $I/I_0>1.4$. When a interaction occurs in a heavy nucleus a number of "black" ($I/I_0>4$) nuclear fragment tracks usually are produced. (The event in Fig. 2-28 has 4 black tracks from the neutrino interaction vertex.) Volume scanning was used primarily for scanning horizontal emulsion. The horizontal orientation meant that the emulsion sheets were edge on to the downstream faces of the modules, so the distortion in the edges made it very difficult to use the track followback technique. The net efficiency for finding neutrino interactions by volume scanning was 51±3%.

For track followback, candidates for tracks from neutrino interactions were located on the changeable sheet and then followed into the emulsion modules. Events were usually found in less than an hour. This method was used primarily for vertical emulsion. The efficiency for finding a good track on the changeable sheet was 96±2%, (A "good" track here means a reconstructed UPDN track with $\theta<200$ mr and momentum $P>2$ GeV/c.) The net efficiency for finding at least one track from an interaction and then following it back to find the primary neutrino vertex was 88±3%.

The event finding efficiencies as a function of Z position are shown in Figure 2-29. These are calculated from the ratio of found to predicted events. The vertical scanning efficiency is quite flat since track followback is little affected by the location of the primary vertex. The horizontal scanning efficiency drops slightly at small Z (deep in the emulsion). This is because the accuracy of the primary vertex location prediction is degraded by the multiple scattering and interactions of the tracks in the emulsion. The accuracy of the vertex predictions is shown in Figure 2-30. The mean resolutions and displacements are

$$\sigma_x \equiv \langle(\Delta X)^2\rangle = 370\ \mu m, \quad \langle\Delta X\rangle = 235\ \mu m$$
$$\sigma_y \equiv \langle(\Delta Y)^2\rangle = 290\ \mu m, \quad \langle\Delta Y\rangle = 645\ \mu m$$
$$\sigma_z \equiv \langle(\Delta Z)^2\rangle = 1.4\ mm, \quad \langle\Delta Z\rangle = -75\ \mu m$$

The only significant difference between neutrino interactions found

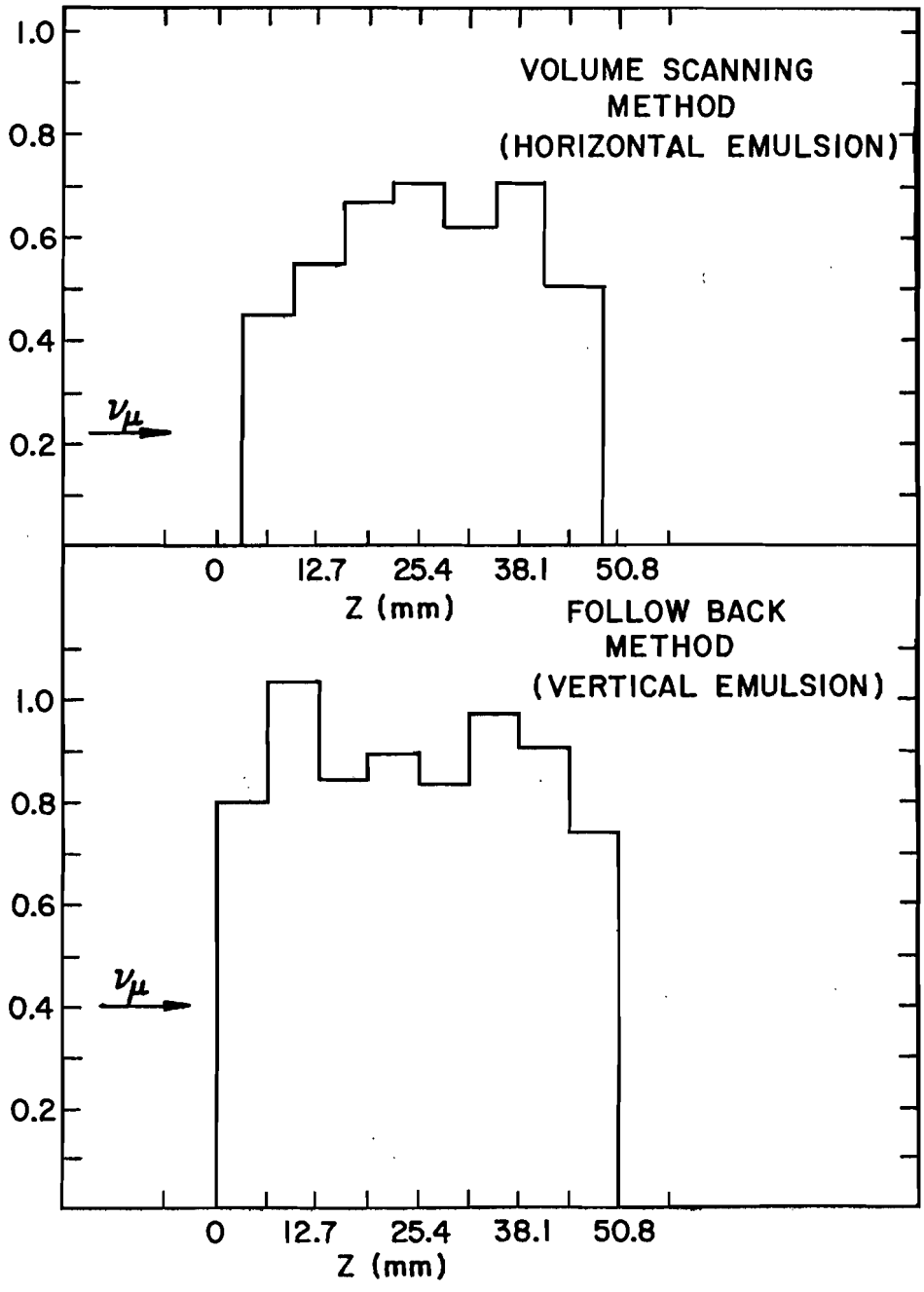

Figure 2-29: Efficiency, E, for finding reconstructed neutrino interactions as a function of depth in the emulsion. (Z=0 is the upstream face of the emulsion target.)

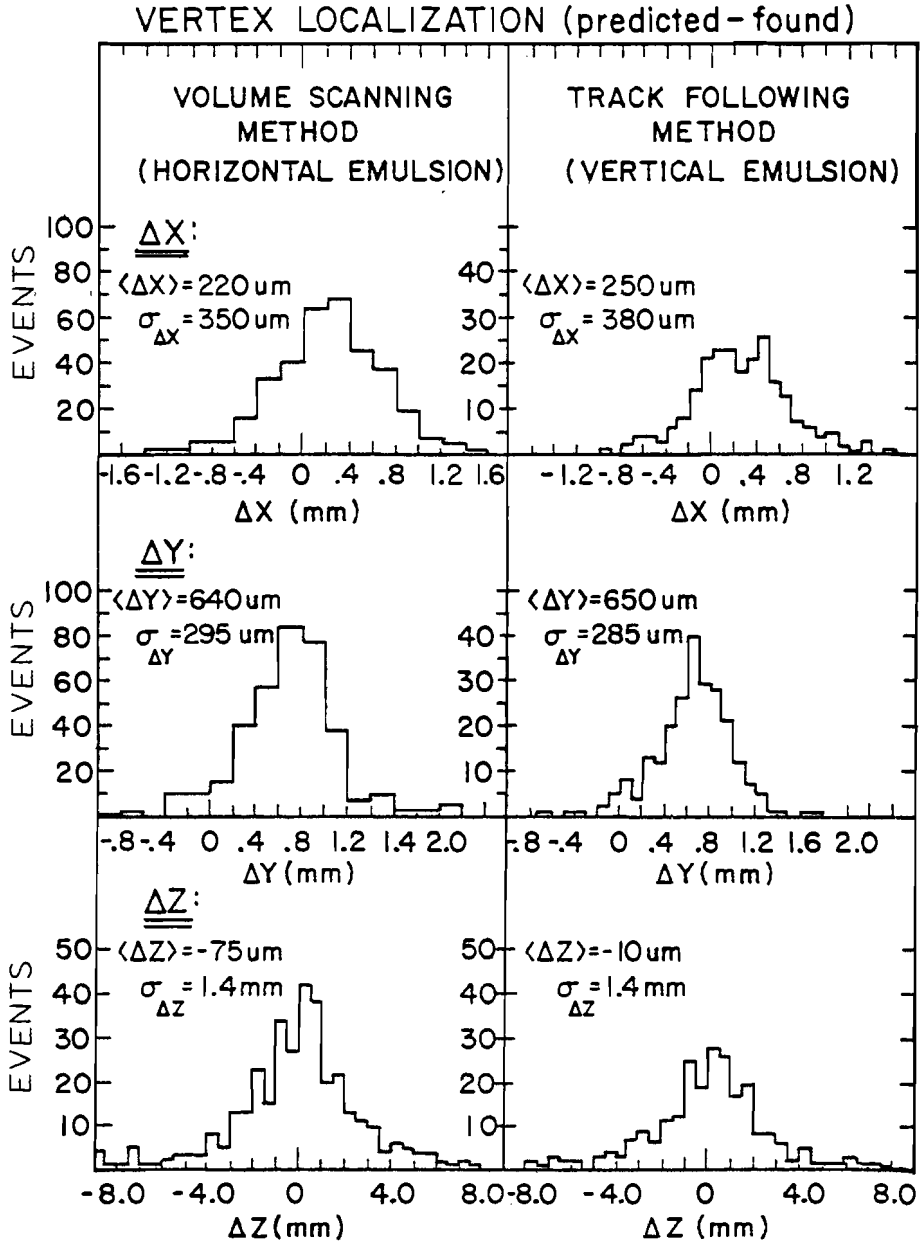

Figure 2-30: Difference between found (emulsion) interaction vertex predictions and predicted (spectrometer) positions. ($\Delta x = x_{predicted} - x_{found}$, ...).

by volume scan and those found by track follow back is their number of heavy tracks (NH). Figure 2-31a shows NH distributions of the found events. The difficulty in finding events with few heavy tracks by volume scanning is clearly seen by comparison with the events found by the virtually bias free and very efficient scanback technique. The interesting tracks (for this experiment) are, however, not heavy tracks, but high momentum "shower tracks". A shower track is a track with $I/I_o < 1.4$. The number of shower tracks (NS) is only weakly correlated with NH (Figure 2-32), so the NS distributions of volume scan and followback events are similar (Figure 2-31b).

2.15 Decay Search

A decay candidate is any track configuration in the emulsion that could be the decay of a short-lived particle. Figure 2-33a shows possible decay topologies. The only pseudo-decays that are a priori not considered to be possible decays are nuclear interactions tagged by their nuclear signatures, and $\gamma \rightarrow e^+e^-$ and $e^{\pm} \rightarrow e^{\pm}e^+e^-$ conversions that are identified by their very small opening angle (see Figure 2-33b).

Decays are looked for by three methods: follow-out, scanback, and volume scan.

2.15.1 Charged Track Follow-out

All charged tracks from the primary vertex were followed out from the vertex for some distance. Multiprong decays were found with $\cong$100% efficiency while following a track because a scanner could not pass over a multiprong decay without seeing it. Kink decays could be missed, however, and this is discussed below (Sec. 2.15.4). The multiprong decay finding efficiency for this method is determined simply by how far tracks were followed. Figure 2-34 shows, for the horizontal emulsion, what fractions of tracks were followed how far. In the vertical emulsion,

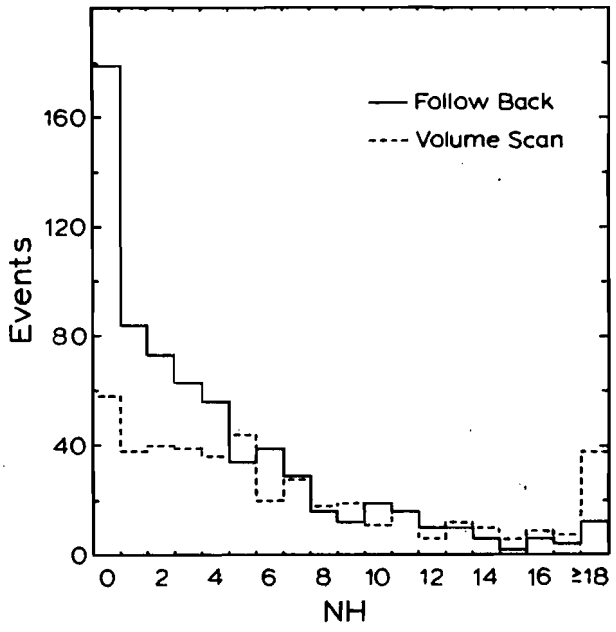

Figure 2-31a: Distribution of NH, the number of heavy tracks (ionization I/I_o >1.4) produced from the primary neutrino interaction vertex, for 668 events found by track follow back (<NH>=3.8), and 455 events found by volume scanning (<NH>=6.4).

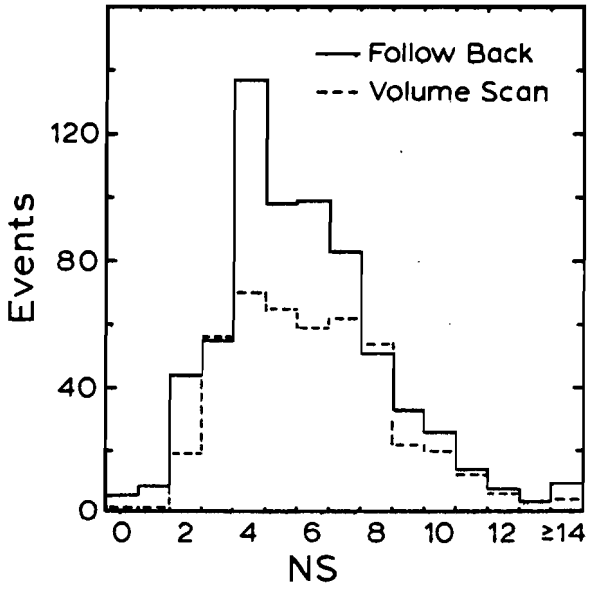

Figure 2-31b: Distribution of NS, the number of shower tracks (ionization I/I_o <1.4) produced from the primary neutrino interaction vertex, for 668 events found by track followback (<NH>=5.8), and 455 events found by volume scanning (<NS>=6.1).

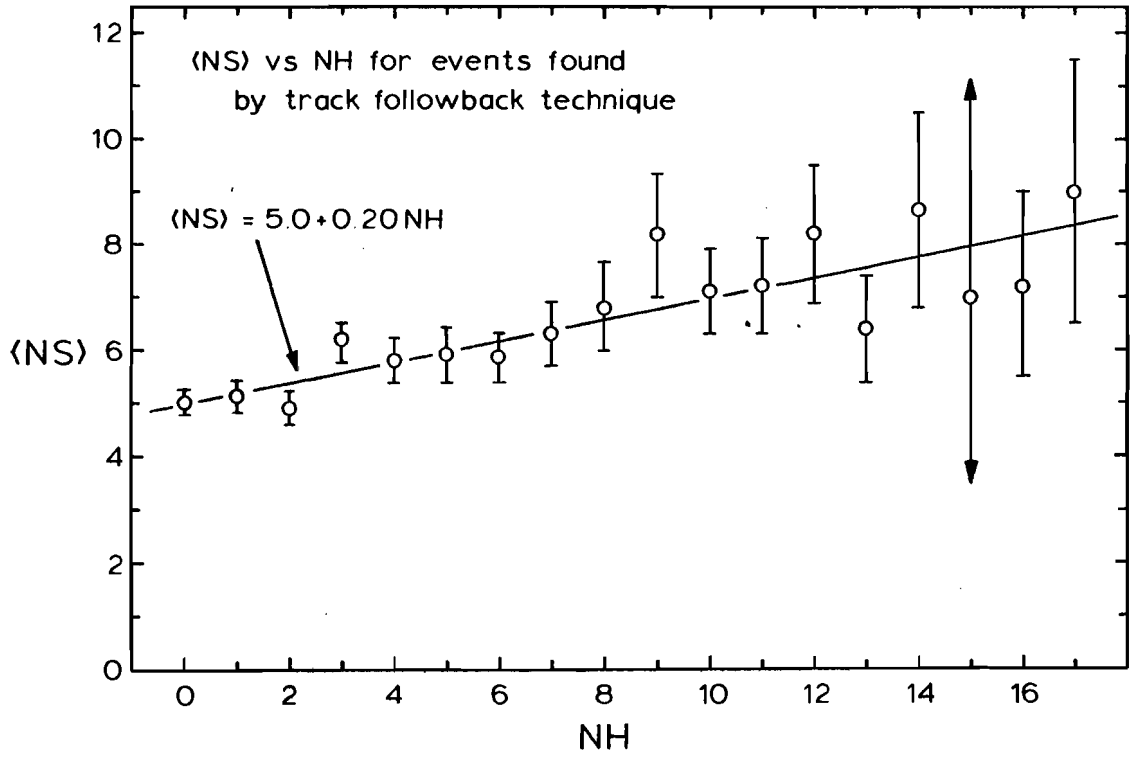

Figure 2-32: Mean number of shower tracks, <NS>, as a function of the number of heavy tracks, NH, for neutrino-emulsion interactions. Only statistical uncertainties are shown; the straight line is a Least Squares fit to the data.

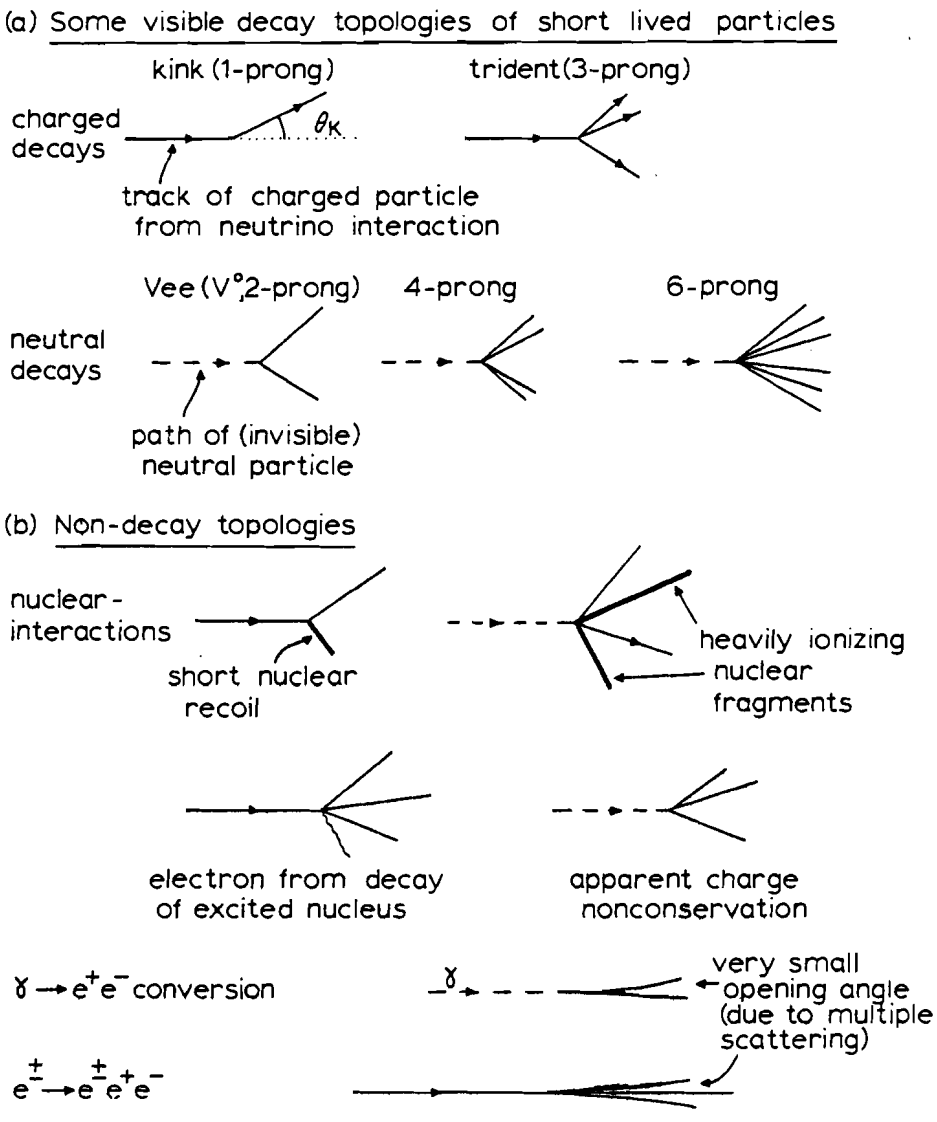

Figure 2-33: Decays and non-decays.

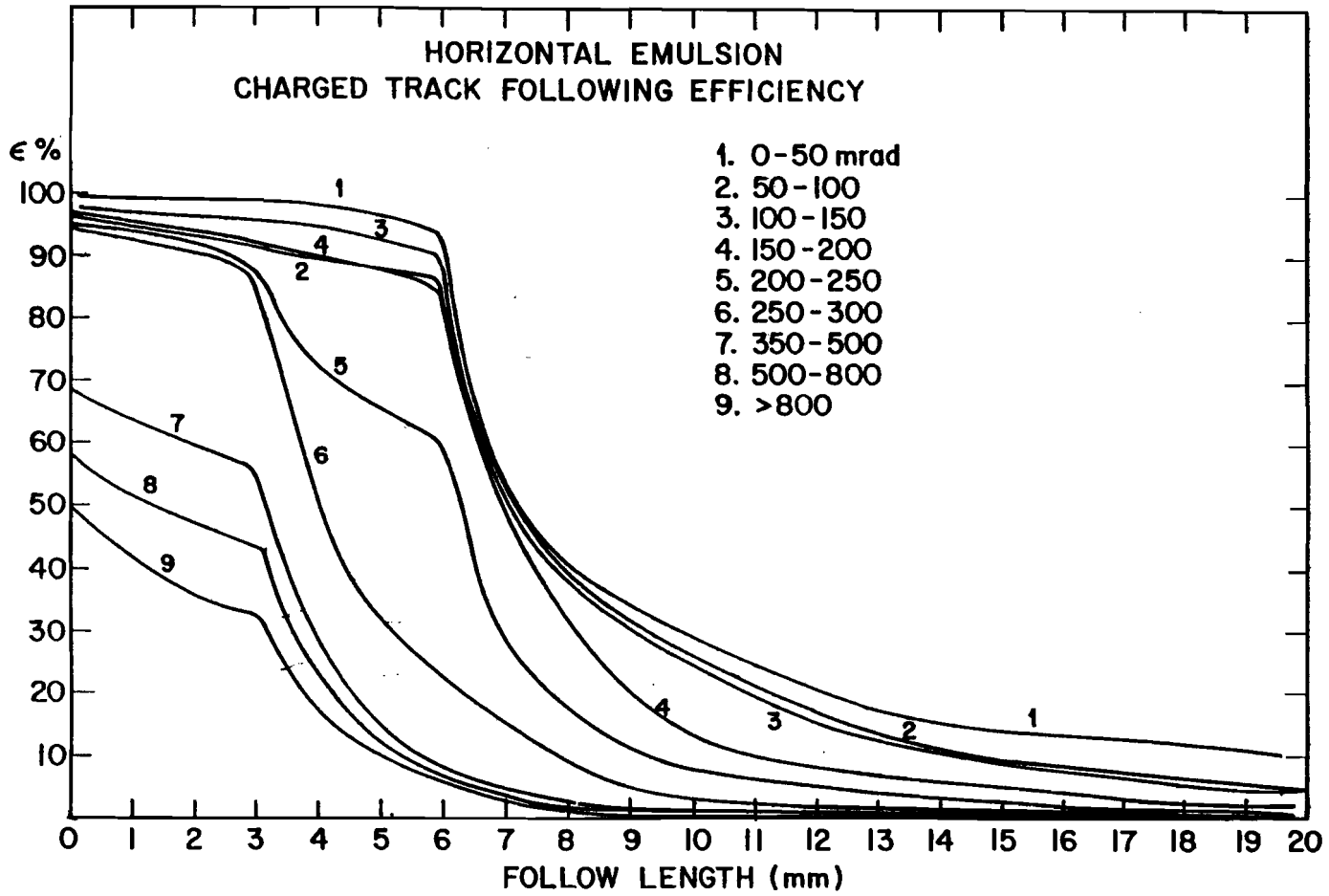

Figure 2-34: Distances that charged tracks were followed from the primary vertices in horizontal emulsion. The different curves are for tracks in various azimuthal angle (θ) bins.

tracks with $\theta<0.2$ were followed out 6.6 mm (10 emulsion sheets) or until the track left the emulsion, tracks with $0.2<\theta<0.4$ were followed out 3.3 mm, and tracks with $\theta>0.4$ were followed out at least 0.66 mm.

It should be noted that it is possible for a found neutrino interaction to be a decay candidate itself. A charmed particle decay or secondary interaction would sometimes be found while looking for the primary neutrino interaction, so charged tracks going upstream from found (presumed) neutrino interactions were followed to be sure that the true primary vertex had been found. Scanback (see 2.15.3) was also used to make sure the primary vertex was found.

2.15.2 Neutral Decay Volume Scan

Neutral decays were searched for downstream of every primary neutrino interaction. The regions scanned were 1000 μm long (in Z), and were a box with area 600μm x 600μm (X x Y) for horizontal emulsion, and a cylinder of radius 200 μm for vertical emulsion. This search was carried out under high magnification, but was still relatively inefficient because particle decays produce no heavy tracks and so are hard to see. Volume scanning had an efficiency of $\lesssim$60%, determined from the ratio of found to expected $\gamma \to e^+e^-$ conversions, and the efficiency was less for longer decay lengths. For example, the efficiency for volume scanning in horizontal emulsion was

$$\varepsilon(L) \cong 0.7 - 0.0006L \qquad 10\ \mu m < L < 1000\ \mu m$$

where L (in μm) is the decay length (the distance from the primary vertex to the decay point); the average efficiency, for 0-1000 μm, was $0.4\pm^{0.2}_{0.1}$.

2.15.3 Scanback

Just as neutrino events were found by track followback, decays were found by track scanback. The scanback technique was used to search for secondary charged particles that were observed in the spectrometer but

which were not found in the emulsion at the primary neutrino interaction vertex. A spectrometer track was a candidate for scanback if it had a momentum P>700 MeV/c, it extrapolated to within 2 mm of the primary vertex, and there was no emulsion track whose angles matched the spectrometer track within 15 mr. Scanback candidates in the vertical emulsion events were looked for on the changeable sheet and scanned (followed) back to their origin in the emulsion. Scanback, like followback, was not used for events in the horizontal emulsion because of the difficulty in following tracks through the distorted edges of the emulsion sheets. Scanback and followback are essentially the same procedure, and sometimes followback would find a decay vertex instead of the primary vertex.

Using the scanback method, decays of any length can be found, limited only by the finite thickness of the target; decays as long as several centimeters can be found as easily as decays only a few hundred microns long. Figure 2-35 shows the "decay length" distribution for $\gamma \rightarrow e^+e^-$ conversions found by scanback; also shown is the distribution expected from the known $\gamma \rightarrow e^+e^-$ conversion length (4.1 cm) and the positions (z) in the emulsion of the found neutrino interactions.

2.15.4 Kink Decays

Finding kink decays is more difficult than finding charged multiprong decays. It is almost impossible to miss one track changing into multiple tracks, but a small bend in a single track can be missed.

In the horizontal emulsion the slopes of single tracks were measured every 500 μm. If the projected slope changed by more than 1°, the 500 μm segment was precisely rescanned and projected kink angles as small as 0.5° found. (The projected angle, θ_{kp}, is the angle as seen through the microscope; the kink angle, θ_k, is the space angle of the kink.) For decay lengths greater than 20 μm the kink scanning efficiency is independent of length and is shown in Figure 2-36a. For decay lengths less than 20 μm, decays (both multiprong and kinks) are searched for by

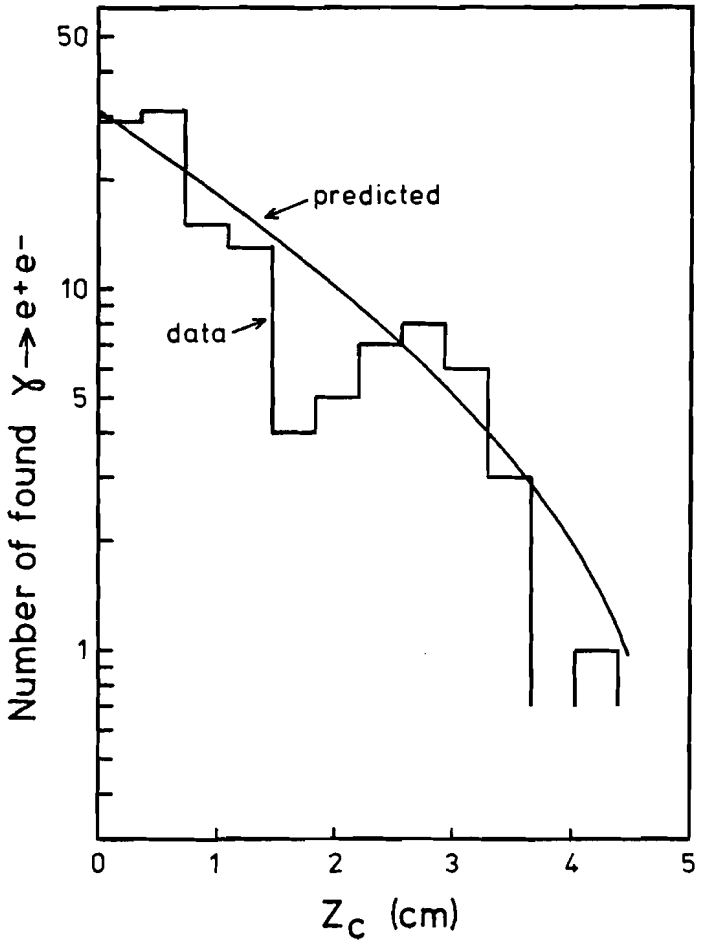

Figure 2-35: Distribution of gamma conversions found by scanback decay search. Z_c is the distance from the primary interaction vertex to the $\gamma \to e^+e^-$ conversion point. The data are consistent (at 25%C.L.) with the distribution predicted from the emulsion target's thickness (5 cm) and the conversion length of emulsion (4.1 cm). The found distribution of $\gamma \to e^+e^-$ gives a conversion length of $2.7 \pm^{1.2}_{0.6}$cm.

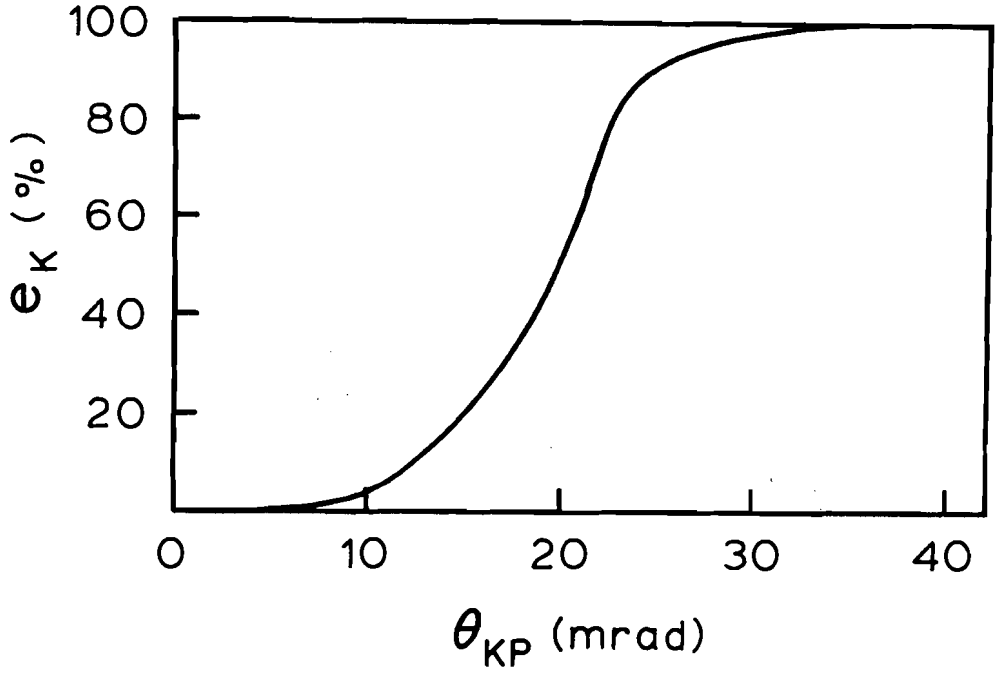

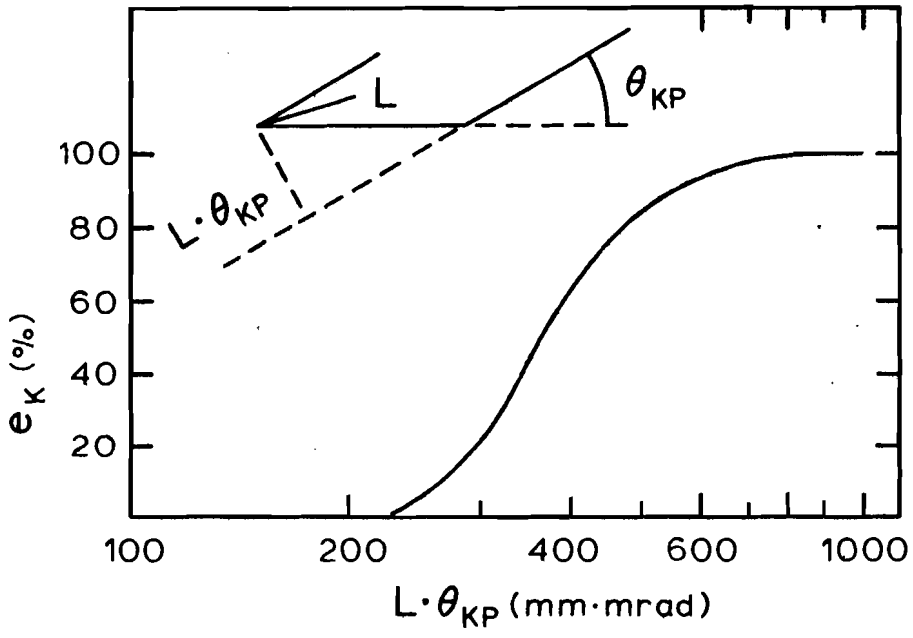

Figure 2-36: Kink decay finding efficiencies in horizontal emulsion for (a) decays longer than 20 μm, and (b) decays shorter than 20μm.

projecting the track back to the vertex and measuring the distance of closest approach. The efficiency for this is a function of the projected decay length, $L \cdot \theta_{kp}$, and is shown in Figure 2-36b.

In vertical emulsion plates, finding kinks is more difficult because the tracks are viewed almost end on through the microscope. Kinks cannot be seen if the kink angle (true, not projected) is less than a critical angle. This critical angle, θ_c, is determined by the resolution and geometry of the scanning procedure. For decays longer than 330 μm,

$$\theta_c = \sqrt{\Delta\theta^2_{\parallel c} + \Delta\theta^2_{\perp c}}$$

where

$$\Delta\theta_{\parallel c} = 0.2\tan\theta + 0.003$$
$$\Delta\theta_{\perp c} = 0.02\tan\theta + 0.024$$

and θ is the azimuthal angle of the decay track. For shorter decay tracks the critical angle is a complex function of $L, \theta, \Delta\theta_k$, and the position of the decay relative to the plastic backing of the emulsion sheet.

2.15.5 Scanning Efficiencies

The efficiency for finding particle decays was a function of both distance and topology.

Decays very near the primary vertex are difficult to see because the many tracks close together confuse and obscure each other. The short distance scanning efficiency was determined from the "diameter" of the primary vertex. If a track is not clearly seen - distinguished from other tracks - its decay cannot be seen. The diameter of the primary vertex is the diameter within which no decays can be seen; this was empirically determined to be typically

$$D = 0.25(NH+NS/2) + 1.80 \qquad D > 3\ \mu m$$

The efficiency of the scanback technique was calculated from the emulsion track scanback efficiency and from the number of found charmed particle decays that had secondary decay tracks that could have been found by track scanback. The scanback efficiency is independent of decay length (as long as the decay is actually in the emulsion), but it does

depend on momentum. (Scanback requires reconstructed secondary tracks, and low momentum tracks are less likely to be reconstructed.) For multiprong charged charm decays with momenta $P_c > 10$ GeV/c, almost 90% of all secondary tracks from the decays are reconstructed by the NRS reconstruction program (Sec. 2.12), and the calculated efficiency for reconstructing at least one secondary track and scanning it back to find the decay is $99\pm^{0.5}_{4}$%. For multiprong charged charm decays with momenta $P_c < 10$ GeV/c, only ~1/3 of the secondary decay tracks are initially reconstructed, and the multiprong scanback efficiency is $69\pm^{15}_{10}$%. The scanback efficiencies for decays of neutral charmed particles are comparable, but almost all these particles are high momentum D^o mesons, so separate high and low momentum efficiencies are not calculated. The total scanback efficiency for finding neutral D meson decays was $96\pm^{3}_{4}$%; the scanback efficiency for finding the decays of low momentum neutral charmed particles (e.g. neutral charmed baryons) should be comparable to the scanback efficiency for finding low momentum charged decays.

Total scanning efficiencies were determined by combining the efficiencies of the different methods, weighted according to the number of neutrino events the methods had been applied to. Figure 2-37 shows the net scanning efficiencies for charged and neutral multiprong decays. The long distance scanning efficiencies drop to $\lesssim$60%, because only ~60% of the events were in vertical modules which could be scanned back.

Figure 5-3 shows the total finding efficiency for kink decays as a function of kink angle; this is integrated over the predicted decay length distribution of τ^- leptons.

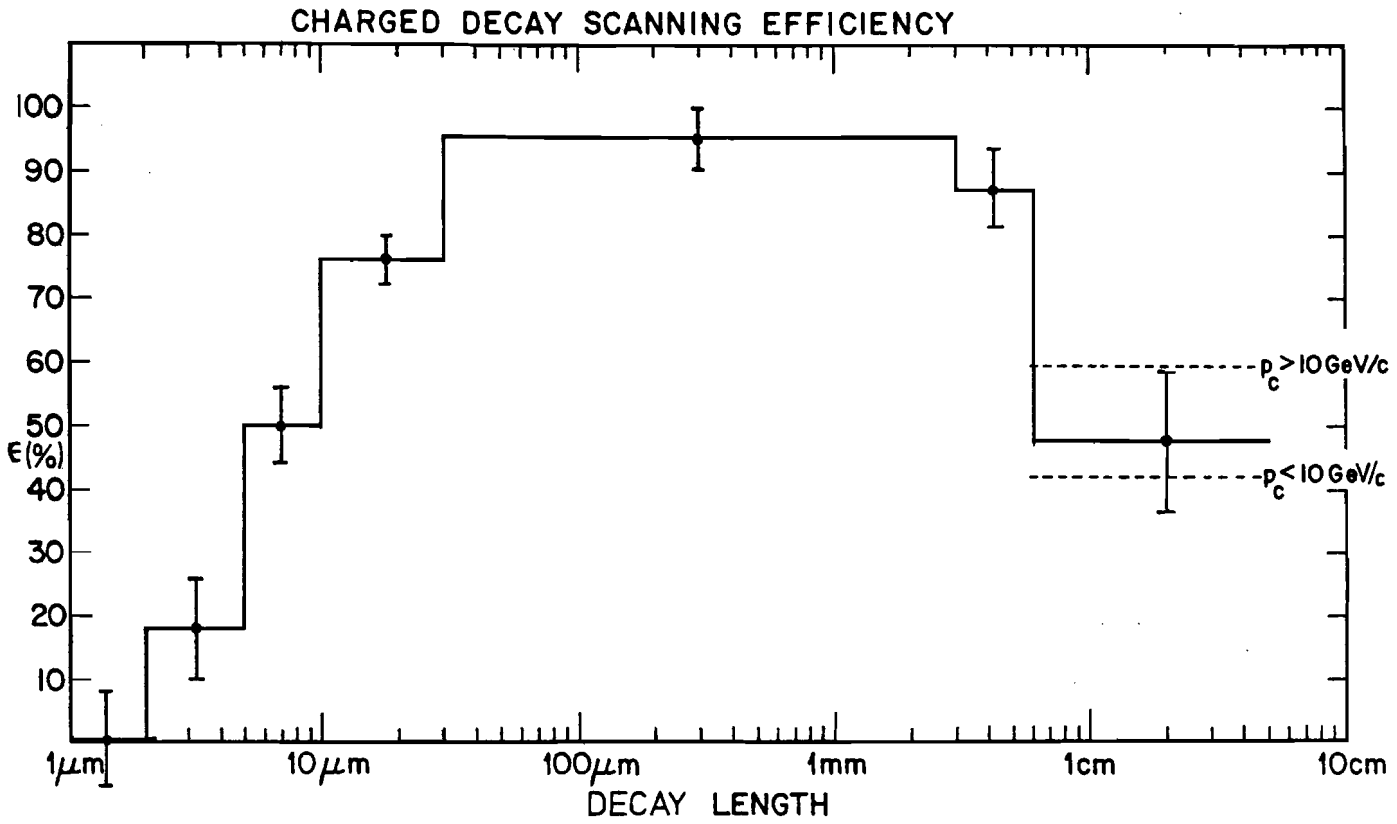

Figure 2-37a: Total multiprong decay finding efficiencies as a function of decay length for decays of charged particles.

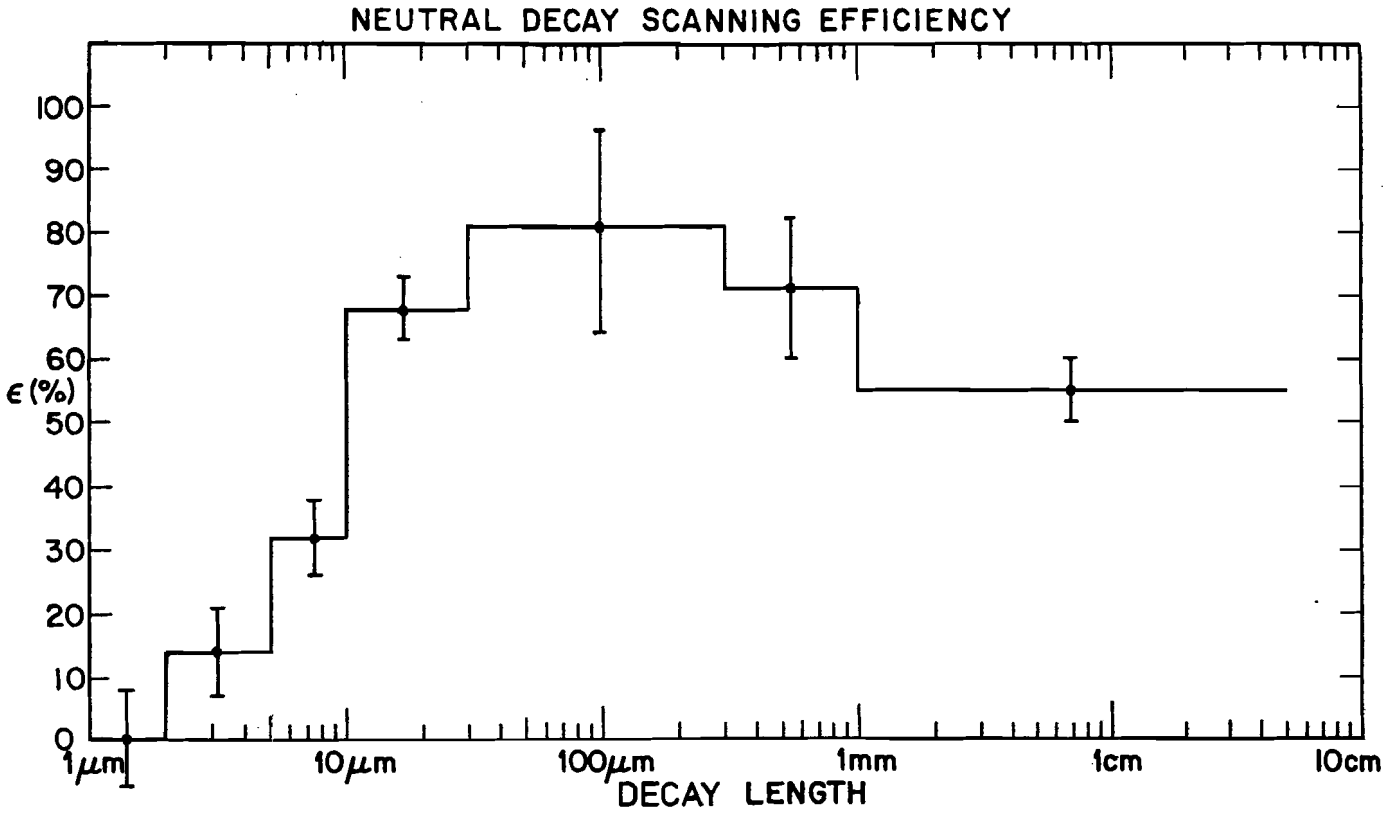

Figure 2-37b: Total multiprong decay finding efficiencies as a function of decay length for decays of neutral particles.

CHAPTER 3: Analysis

3.1 Neutrino Event Data Sample

More than 2500 neutrino interactions were reconstructed in the spectrometer, and ~2100 of these events were predicted to have interaction vertices lying within the target volume. After detailed fiducial cuts, 1821 events remained to be searched for in the emulsion. These cuts excluded events that were predicted to have vertices within ~3 mm of any of the edges of the emulsion sheets. (Events could not be found in these edge regions because of emulsion distortion.)

A total of 1254 neutrino interactions were found in the emulsion - an event finding efficiency of 69% (=1254/1821). Six of these events were interactions found by scanback in the changeable sheet, so the final found fiducial sample was 1248 events.

3.2 The Neutrino Interaction Energy Spectrum

A fundamental difficulty with neutrinos is that they are invisible (even in emulsion). In order to measure an absolute cross section, one must know how many beam particles enter the detector as well as how many interact. Experiments that measure the absolute neutrino cross section cannot directly monitor the neutrino beam, so the beam parameters are predicted by a Monte Carlo simulation of the beam's production and propagation. Most neutrino cross section experiments use beams that are designed to be easily understood, but uncertainties in the beams still dominate the measurements. The wide-band beam used by this experiment is designed to maximize the neutrino flux, not to easily predict it. Because the absolute flux of the wide-band beam is almost impossible to calculate accurately, this experiment measures only relative cross sections.

3.2.1 Neutrino Beam Monte Carlo

The production of the wide-band neutrino beam is simulated in 3 steps: (1) Pions and kaons produced by primary protons interacting in the target are generated by the Stefanski-White parameterization [99]. (2) The pions and kaons are then passed through the horn focussing system (Fig. 2-2b) and positive (negative) particles focussed (defocused) or absorbed (See Sec. 2.1, [100]). (3) The pions and kaons then are allowed to decay in the decay pipe (Fig. 2-2a) until they are absorbed in the sides or end of the pipe. The only decays considered here are

$\pi^+ \to \mu^+ \nu_\mu$	B.R. = 100%	P_{decay} = 30 MeV/c	[65]
$\pi^- \to \mu^- \bar{\nu}_\mu$			
$K^+ \to \mu^+ \nu_\mu$	B.R. = 63.5%	P_{decay} = 236 MeV/c	
$K^- \to \mu^- \bar{\nu}_\mu$			

The contributions to the beam from other decay modes (e.g. $K^+ \to e^+ \nu_e \pi^o$) have been calculated by S.Mori [101].

The pion and kaon spectra needed in step (1) are not well known, and the Stefanski-White parameterization used was chosen over other spectra [102] which gave worse reproductions of our observed neutrino spectrum. The problem with all parameterizations is that the spectra of low momentum mesons, being mostly tertiary particles from secondary interactions in the target, have not been well measured. The Stefanski-White spectrum is known to seriously underestimate the number of low energy hadrons produced at the target. In addition, the produced hadron spectra depend on the details of the targetting of the primary proton beam.

Figure 2-3 shows the expected total and component flux at our emulsion target. Also shown in this figure is the neutrino flux at the E-531 detector inferred from the energy spectrum observed by experiment E-545 [103] using the Fermilab 15' bubble chamber. (E-545 took data in the N-0 beam during the first half of the E-531 data run.)

3.3 Experiment Monte Carlo Simulation

The predicted neutrino beam is an input to a Monte Carlo simulation of our detector. This computer simulation predicted the characteristics of observed interactions in our target. Some of the features of the Monte Carlo procedure were:

(1) The input neutrino flux is assumed to interact with charged-current cross-sections

$$\sigma_{\nu}(E_{\nu}) = A_{\nu} \cdot E_{\nu}$$
$$\sigma_{\bar{\nu}}(E_{\nu}) = A_{\bar{\nu}} \cdot E_{\nu}$$

where A_{ν} and $A_{\bar{\nu}}$ are constants. Charged-current interactions were assumed to be 76% [104] of the total cross-section.

(2) The $d\sigma/dxdy$ distributions were generated using Eqns. 1.4a,b,c (Sec. 1.4). The structure functions used are a parameterization of Gluck, Hoffmann, and Reya [105].

(3) Events are generated uniformly over the target volume, and values of the kinematic variables (x, y, W, and Q^2) are assigned according to the $d\sigma/dxdy$ distributions. The momentum and direction of the outgoing lepton are calculated from E_{ν}, x, and y.

(4) The number of charged particles in the hadronic system is generated using

$$\langle NS_h \rangle = 0.36 + 2.66 \ell nW$$

and assuming a Koba-Nielsen-Olesen (KNO) form [106] for the hadronic shower track (NS_h) multiplicity distribution. The above $\langle NS_h \rangle$ dependence is based on $\nu_{\mu} p \rightarrow \mu^- X$ data (the ABCMO data of Fig. 3-2), modified for the complex and almost isoscalar nuclei of our emulsion target. The KNO distribution used was [107]

$$\langle NS_h \rangle P(NS_h) = (3s+26s^3+4.6s^5+0.18s^7)e^{-4s}$$

where $P(NS_h)$ is the probability of an interaction producing NS_h hadronic shower tracks, $\langle NS_h \rangle$ is the average number of hadronic shower tracks per interaction, and $s \equiv NS_h/\langle NS_h \rangle$. The generated NS_h distribution was constrained by charge and baryon conservation. (The electric charge, $Q_{hadronic}$, of the total hadronic system is +2,+1,0 for ν_{μ} charged

current, neutral current, $\bar{\nu}_\mu$ charged current interactions with protons, and is correspondingly +1,0,-1 for interactions with neutrons; NS_h cannot be less than $|Q_{hadronic}|$.)

The E-531 NS distribution is compared with the Monte Carlo prediction in Figure 3-1; these distributions (both data and Monte Carlo) are for all shower tracks and thus include the primary muon in charged current interactions as well as the hadronic shower tracks. (The total number of shower tracks is $NS=NS_h+1$ in charged current interactions, and $NS=NS_h$ in neutral current interactions.)

The <NS> vs W dependence for E-531 ν_μ charged current interactions is shown in Figure 3-2; both raw and corrected data are shown. The <NS> dependence of neutrino emulsion interactions is similar to that observed in $\nu_\mu p \to \mu^- X$ interactions. Systematic uncertainties are not shown in Fig. 3-2, but they are probably comparable to the statistical uncertainties.

(5) Hadrons are generated as protons, neutrons, and pions in the ratios $p:n:\pi^+:\pi^o:\pi^- = 5:5:30:30:30$. (These ratios are constrained by charge and baryon conservation, so π^+ are actually produced more often than π^-, and there is at least one baryon per event. The experimental efficiencies and resolutions calculated by the Monte Carlo are not sensitive to adding strange particle production, so for convenience, only nucleons and pions are generated.) The hadrons are generated with random phase space limited longitudinal momenta.

(6) The produced particles are then propagated through the emulsion and spectrometer. In the emulsion, charged particles multiple scatter (see Sec. 2.13.1) and $\gamma \to e^+e^-$ conversions occur (see Fig. 2-35). The magnet is assumed to give all charged particles a transverse momentum kick of 186 MeV/c.

(7) The probability of triggering on the generated event is determined from the probability of TOFI having a pulse height $>2\frac{1}{2}$, and whether at least 2 particles pass through TOFII counters. The pulse height in TOFI is proportional to N_{up}, the total number of charged particles emerging from the emulsion. (On average, almost half of the charged tracks are expected to be electrons from γ conversions, so $N_{up} \approx 2NS$. Data from E-531 neutrino interactions give $\langle PH_{TOFI}(NS) \rangle = (2 \pm 0.3)NS$.)

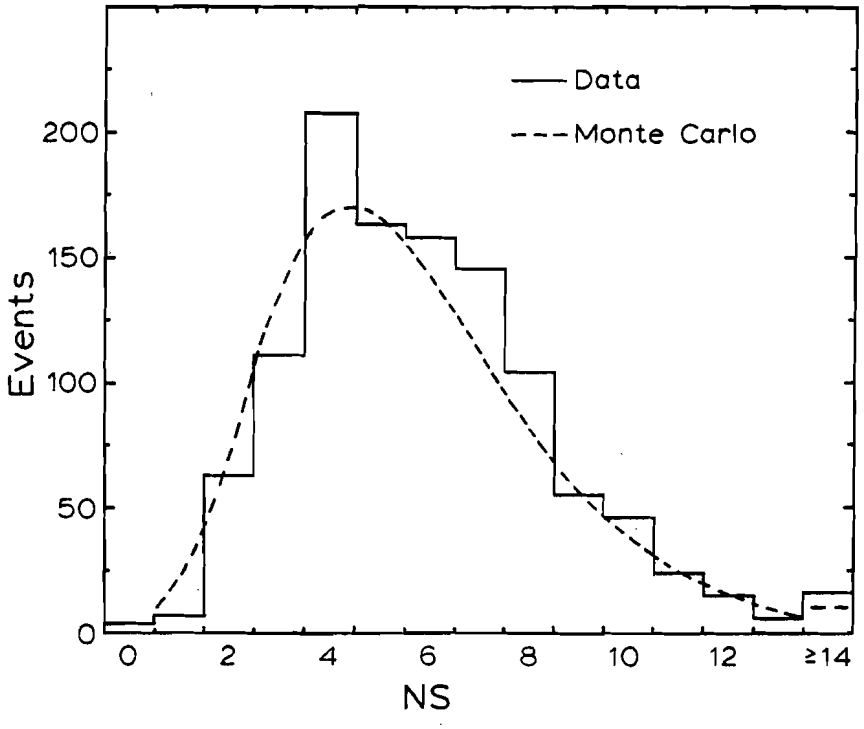

Figure 3-1: Comparison of the NS distribution from data (1123 events found in the emulsion) to the normalized Monte Carlo prediction.

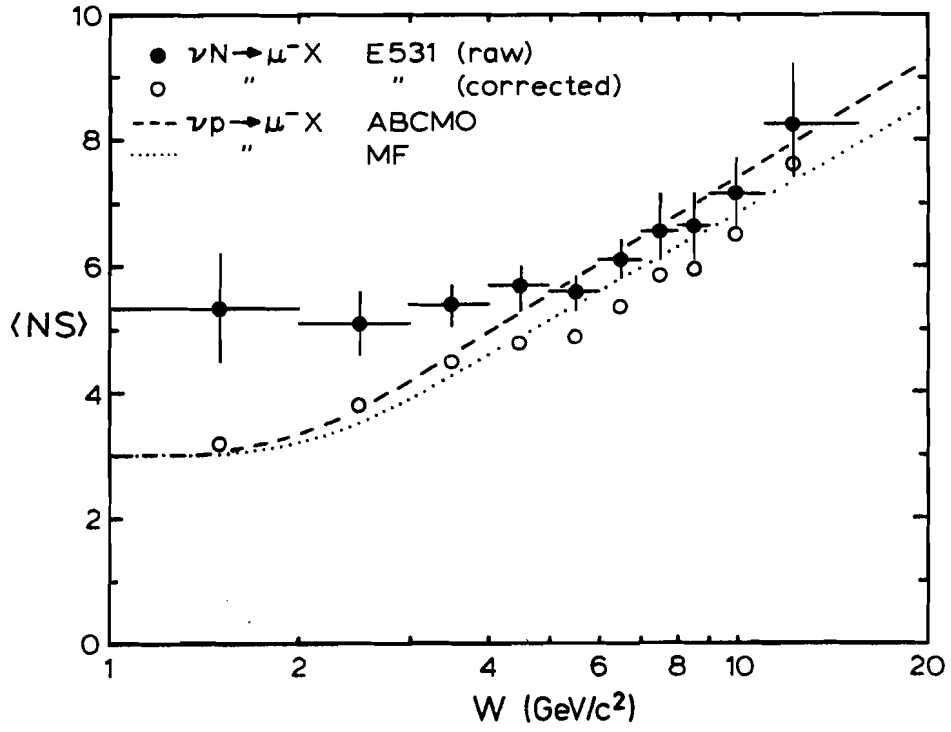

Figure 3-2: Mean shower track multiplicity (<NS>) as a function of the hadronic system mass (W) for charged current interactions. The solid circles are raw E-531 data (the error bar in W is the bin width, the error in <NS> is statistical); the open circles are the data after correction for resolution and acceptance (these have the same statistical errors as the raw data, plus possible systematic errors). Also shown for comparison are the W dependence of the average charged particle multiplicity measured in $\nu_\mu p$ interactions by two experiments (ABCMO [116], MF [117]).

(8) The probability of reconstructing the event is the probability of reconstructing 2 UPDN tracks. It is assumed that a hadron or electron cannot be reconstructed if it hits the magnet poles, and any particle will not be reconstructed unless it passes through at least 6 downstream drift chambers. The track reconstruction efficiency for particles that do pass these cuts is $(0.9-0.004N_{up})$. It is difficult to reconstruct tracks in events with many drift chamber hits, so the individual track reconstruction efficiency is less in events with many particle tracks. The efficiency for reconstructing muon tracks is somewhat higher than for hadron tracks, because muons are usually high momentum and are often separate from the hadron jet, and also because the standard NRS reconstruction program preferentially reconstructs muons. The efficiency for reconstructing UPDN MUFB muons was 94% for muons with azimuthal angles $\theta<0.2r$ and 83% for $\theta>0.2r$.

3.3.1 Comparison of Monte Carlo and Data

For comparison of Monte Carlo and data, a standard data sample of real neutrino interactions was defined. This sample of 2022 neutrino interactions with vertices in the target volume was reconstructed by a single run of the NRS program.

The number of tracks reconstructed per event is shown in Figure 3-3 for all reconstructed neutrino interactions and for events with identified MUFB μ^-. The data and Monte Carlo are in good agreement. The slight excess of high multiplicity events in the data is because the NRS program sometimes reconstructs several versions (each slightly different) of a single track and so the track is counted several times. This happens in confusing events with many drift chamber hits. (There are neutrino events that have more than 2000 hits in the 20 chambers.) The Monte Carlo program did not include the effect of multiple track counting because it had no effect on the total event reconstruction efficiency - this efficiency depends only on whether or not a track is reconstructed, not how many times it is reconstructed.

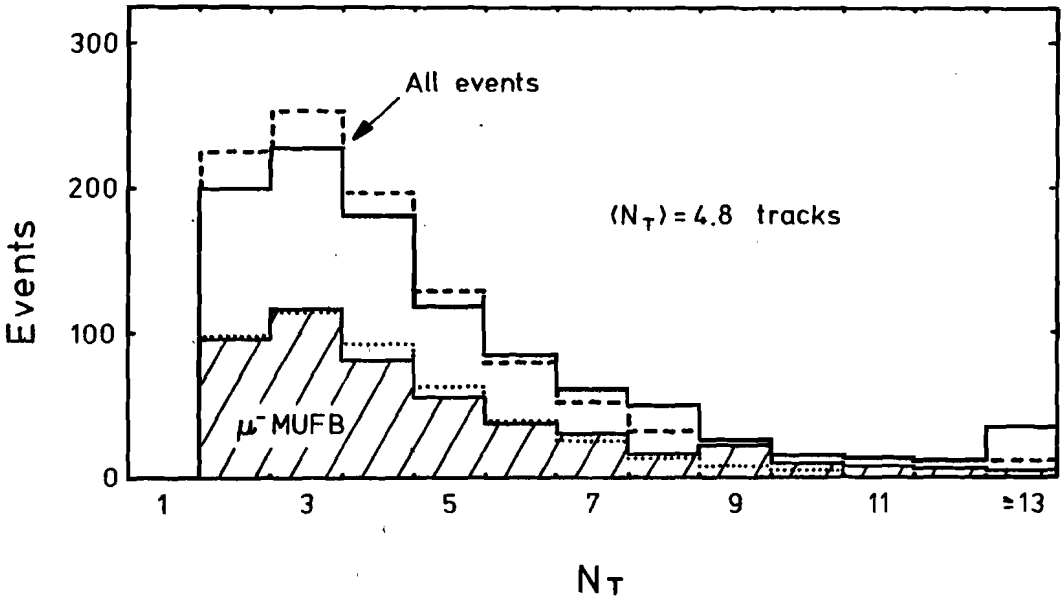

Figure 3-3: Number of tracks, N_T, reconstructed per event by primary NRS reconstruction program. The broken curves are (normalized) Monte Carlo predictions.

The "observed" characteristics of the event are generated according to the known acceptances and resolutions of the experiment. For example, the observed muon momentum is randomly generated from a Gaussian distribution in $Q(\equiv 1/p)$ centred on the true value with a RMS width given by the momentum measurement resolution (see Sec. 2.7). The probability of identifying the muon is determined from the track reconstruction efficiency, and muon counter efficiencies and acceptance. The expected and observed momentum spectra for identified MUFB muons are shown in Figure 3-4 (See also Fig. 2-16).

3.3.2 Total Event Rates

The Monte Carlo programs predict a total of 1800 reconstructed neutrino ($\nu_\mu+\bar{\nu}_\mu$) interactions in the E-531 target volume, calculated for total charged-current neutrino interaction cross sections of $A_\nu=0.70\times10^{-38}cm^2/GeV/nucleon$ and $A_{\bar{\nu}}=0.33\times10^{-38}cm^2/GeV/nucleon$ (Sec. 3.3(1)). This prediction is in quite reasonable agreement with the 2100 interactions actually reconstructed - the 20% difference between data and Monte Carlo is completely consistent with the large uncertainties in the predictions for the absolute neutrino flux. The E-531 event rates are also consistent with those observed in the 15' bubble chamber by experiment E-545 [103]; extrapolating from the E-545 data, we would expect a total of 2600 ± 500 reconstructed neutrino interactions in the E-531 target volume.

3.4 Measurement of E_ν

The energy of neutrino interactions could be calculated in several ways from the energy measurements of the E-531 calorimeters and spectrometer. The simplest measure of the total energy, E_{vis}, was normally used for the energy of all neutrino interactions and for Monte

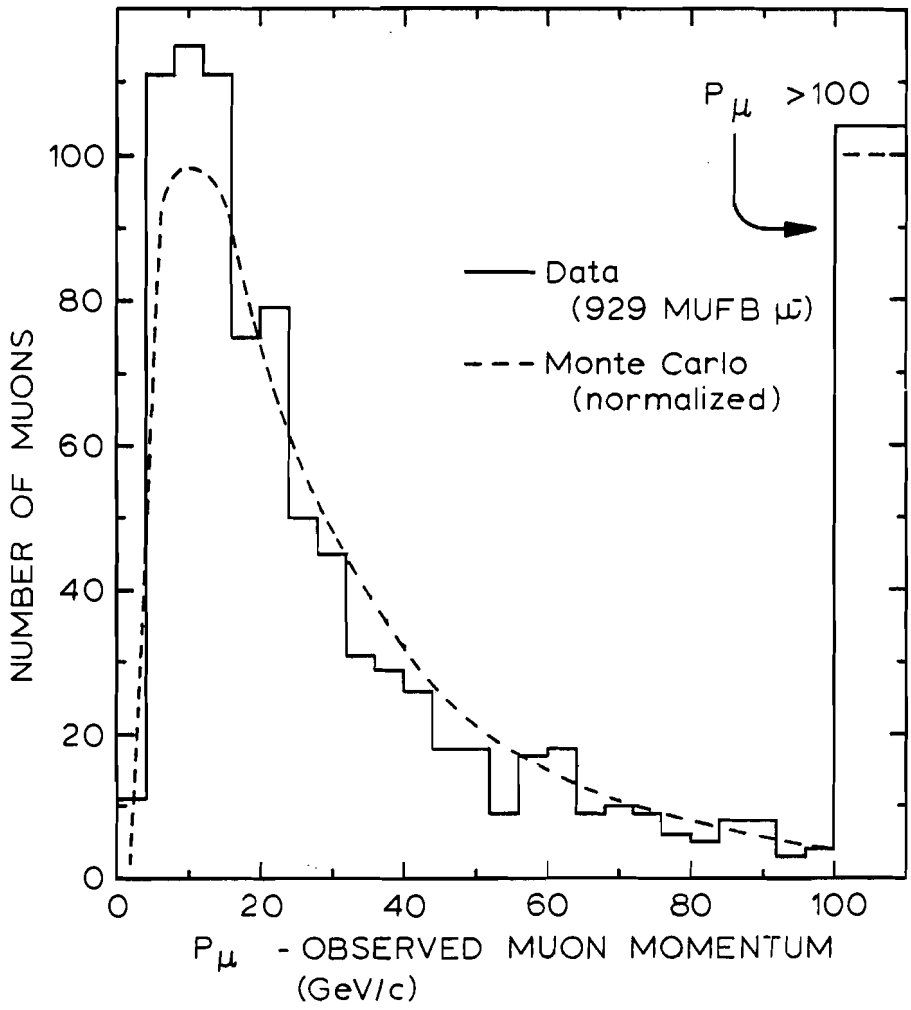

Figure 3-4: Comparison of observed and predicted momentum spectra for identified (MUFB) muons.

Carlo energy calculations, but a more complex and more accurate variable, E_{cor}, was used for the total energy of charm events.

3.4.1 E_{vis}

E_{vis} is the total energy of an event visible in the calorimeters plus the energy of any muon. E_{vis} is the sum of the observed muon energy, $E_{\mu o}$, and the observed calorimeter energy E_{Co}:

$$E_{vis} \equiv E_{\mu o}+E_{Co} \qquad \{3.4a\}.$$

$E_{\mu o}$ is calculated from the measured momentum of the primary muon ($E_{\mu o}=0$ if no muon is identified). E_{Co} is the total calorimetric energy, with any muon contribution subtracted:

$$E_{Co} \equiv (E_{EPG}-E_{PBG\mu}) + (E_{CAL}-E_{CAL\mu}) \qquad \{3.4b\}.$$

E_{PBG} and E_{CAL} are the energies measured in the lead glass and hadron calorimeter, and $E_{PBG\mu}$ and $E_{CAL\mu}$ are the (minimum ionizing) contributions to E_{PBG} and E_{CAL} from any identified muon.

E_{vis} is used as the observed neutrino energy for non-charm neutrino interactions. E_{vis} is simple enough to be easily generated by the experiment Monte Carlo simulation, using the known acceptances, resolutions, and efficiencies of the spectrometer/calorimeter. E_{vis} is, on average, a reasonable measure of the interaction energy (See Figure 3-5). The true event energy (E_ν) spectrum is determined by comparing the Monte Carlo E_{vis} spectrum with the data, and using the Monte Carlo to unfold the effects of resolution and energy acceptance from the observed E_{vis} spectrum to give the actual E_ν spectrum.

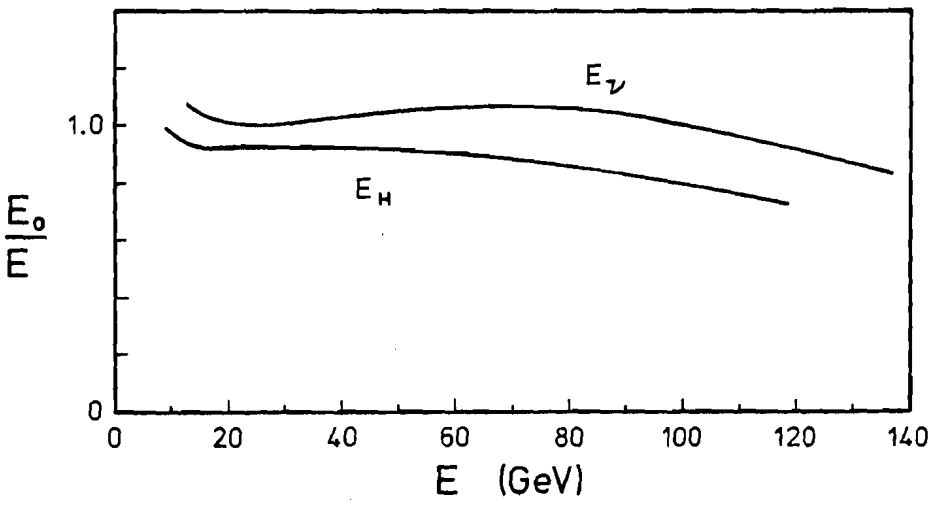

Figure 3-5: Calculated (Monte Carlo) ratios of observed to real energy (E_o/E) as a function of energy (E). The upper curve is E_{vis}/E_ν vs E_ν for charged current interactions; the lower curve is E_{H_o}/E_H vs E_H.

3.4.2 E_{cor}

E_{cor} is the total corrected energy of an event, calculated in detail from both calorimeter energy and charged particle momentum measurements, and corrected event-by-event for measurement biases and estimated acceptance losses. E_{cor} is used as the total energy for neutrino interactions in which a charm decay is found. E_{cor} is a more detailed calculation than E_{vis} and takes advantage of the very extensive analysis of each charm event.

E_{cor} is the sum of the corrected muon and hadronic energies:

$$E_{cor} \equiv E_{\mu c}+E_{Hc} \qquad \{3.4c\}.$$

$E_{\mu c}$ is the measured primary muon energy corrected for the systematic momentum shift of $\Delta Q=+0.005$. E_{Hc} is the total corrected hadronic energy, and for charm events is generally of the form

$$E_{Hc} = E_{c\nu} + (1+a)E_{Tout} + E_{Cout} + (1-b)MAX(E_{Tin},E_{Cin}) \qquad \{3.4d\}.$$

Each of the four terms in this relation is discussed below.

When a charmed particle decays semileptonically, it produces an unobservable secondary decay neutrino. $E_{c\nu}$ is the energy of this neutrino. (The energy is taken to be the average of the high and low solutions to the 0-C momentum calculation, see Fig. 3-9.) If the decay is semi-muonic, then the secondary decay muon's energy will not be detected by the lead glass array or hadron calorimeter, so the secondary muon's energy is included in $E_{c\nu}$. If the charm decay is non-leptonic, then $E_{c\nu}=0$.

E_{Tout} is the total energy of all reconstructed charged particles that miss the lead glass array and hadron calorimeter. (A large fraction of these particles have tracks that can only be seen in upstream drift chambers, so they are only reconstructed by the charm reanalysis programs. This is one of the reasons why E_{cor} is used only for charm events and not for all neutrino interactions.) In order to correct for unobserved neutral particles that miss the lead glass and calorimeter, E_{Tout} is scaled by a factor (1+a), with a=1/3. (If pions were the only

hadrons produced (in ratios $\pi^+:\pi^o:\pi^- = 1:1:1$) and the emulsion target was infinitely thin, then the value of "a" would be 1/2. The value of "a" is not 1/2 because not all hadrons are pions, and because some of the photons from neutral pions convert in the emulsion target and produce electrons that are reconstructed and their energy is included in E_{Tout}.) E_{Tout} is typically only ~10% of the total hadronic energy, so E_{Hc} is not very sensitive to the value of "a".

E_{Cout} is the total calorimetric energy measured by all lead glass blocks and hadron calorimeter columns that are not struck by any of the reconstructed charged particles:

$$E_{Cout} \equiv \sum_i E_{EPGi} + \sum_j E_{CALj} \qquad \{3.4e\}.$$

where E_{PBGi} and E_{CALj} are the energies measured in the i^{th} lead glass block and the j^{th} hadron calorimeter row, and the sums are over all blocks and columns that do not have incident charged particles. If the only charged track passing through a lead glass block or calorimeter column is an identified muon, then the energy of that block or column is included in E_{Cout}. (Note: The minimium-ionizing pulse height of any identified muon incident on a lead glass block or calorimeter column is always subtracted before the energy of that block or column is calculated.

E_{Tin} is the total energy of all charged particles (except identified muons) with reconstructed tracks incident on the lead glass array or hadron calorimeter. (Note that if a muon is reconstructed but not identified, its energy will be included in either E_{Tout} or E_{Tin}.)

E_{Cin} is the total calorimetric energy measured by all lead glass blocks and hadron calorimeter columns that are struck by any of the reconstructed charged particles (except for identified muons).

$$E_{Cin} \equiv \sum_i E_{EPGi} + \sum_j E_{CALj} \qquad \{3.4f\}$$

where the sums are over all blocks and columns that have incident charged particles. E_{Cin} and E_{Cout} together add up to the total calorimetric energy, i.e. $E_{Cin}+E_{Cout}=E_{Co}$.

$MAX(E_{Tin},E_{Cin})$ is equal to whichever of E_{Tin} and E_{Cin} has the larger

value. The momenta of charged particles are much better measured than calorimetric energies, so E_{Tin} is an accurate lower bound to E_{Cin}. Using the maximum of E_{Tin} and E_{Cin} reduces the measurement error in the hadronic energy by reducing the possible range of fluctuations to low energy values. Because it is a maximization procedure, however, $MAX(E_{Tin},E_{Cin})$ will be larger on average than the true value. In order to correct for this systematic effect, $MAX(E_{Tin},E_{Cin})$ is scaled by a factor of (1-b) in Eqn. {3.4d} above. The value of b can be calculated from the hadronic energy resolution and the average ratio of E_{Tin}/E_{Cin} ($\approx 3/4$), typical values range from $b \approx 0.1$ for $E_{Cin} \approx 10$GeV, to $b < 0.01$ for $E_{Cin} > 50$GeV.

3.5 Corrected Neutrino Interaction Energy Spectrum

Figure 3-6 shows the observed neutrino energy spectrum for actual E-531 events and the Monte Carlo predictions. The spectra for all events (charged and neutral current, neutrino and antineutrino interactions) and only charged current ν_μ events with a well identified (MUFB) μ^- are shown. The data and Monte Carlo are in good agreement except at low energies ($E_\nu < 20$ GeV) where the neutrino beam Monte Carlo spectrum is known to be unreliable. The experiment Monte Carlo can, however, be used to unfold the effects of resolution and acceptance from the E-531 observed energy spectrum to give the corrected (true) energy spectrum for found neutrino interactions. This unfolded spectrum is shown in Figure 3-7. The corrections from the unfolding procedure are not large except at low energies. The observed raw spectra (from the previous figure) are shown for comparison.

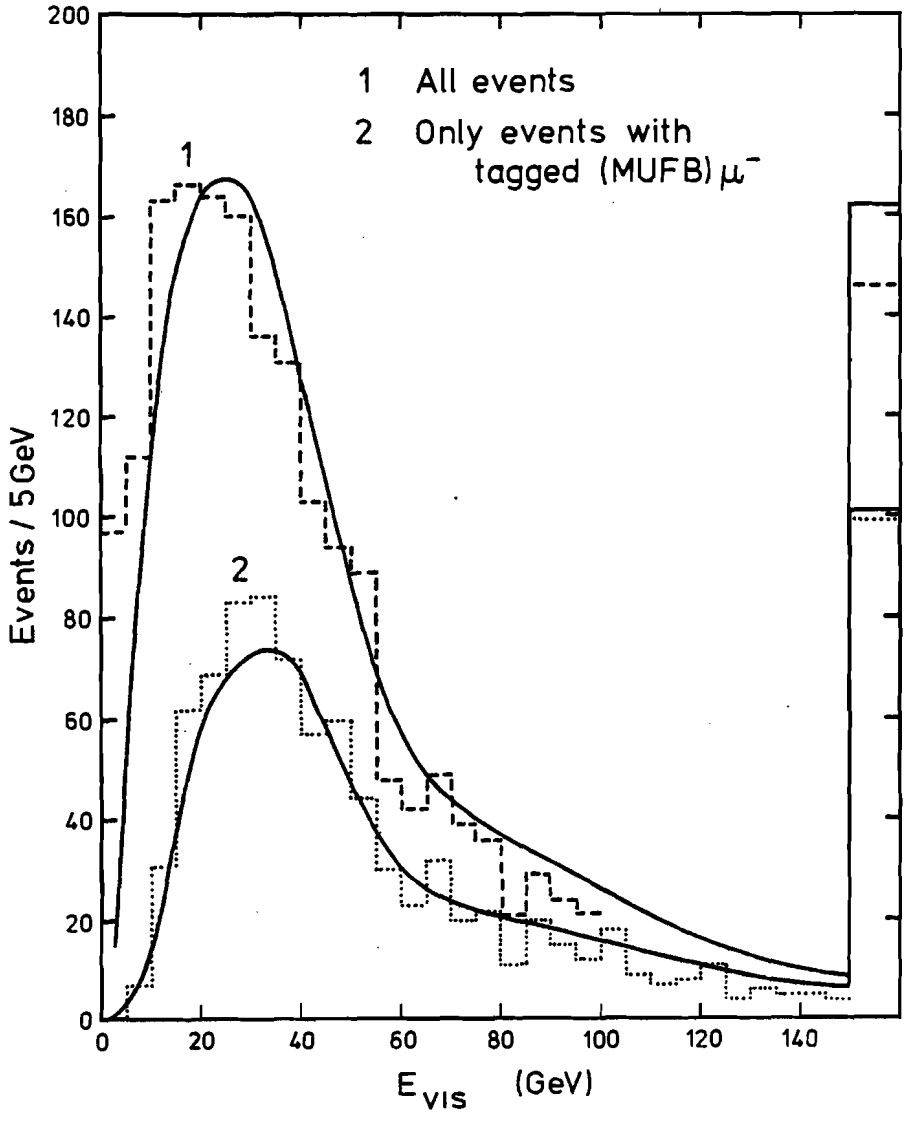

Figure 3-6: Uncorrected observed event energy (E_{vis}) for reconstructed neutrino interactions in the E-531 target fiducial volume. The smooth curves are (normalized) Monte Carlo predictions, the broken curves are data. (For clarity, only the MUFB event data are shown in the range 100-150 GeV.)

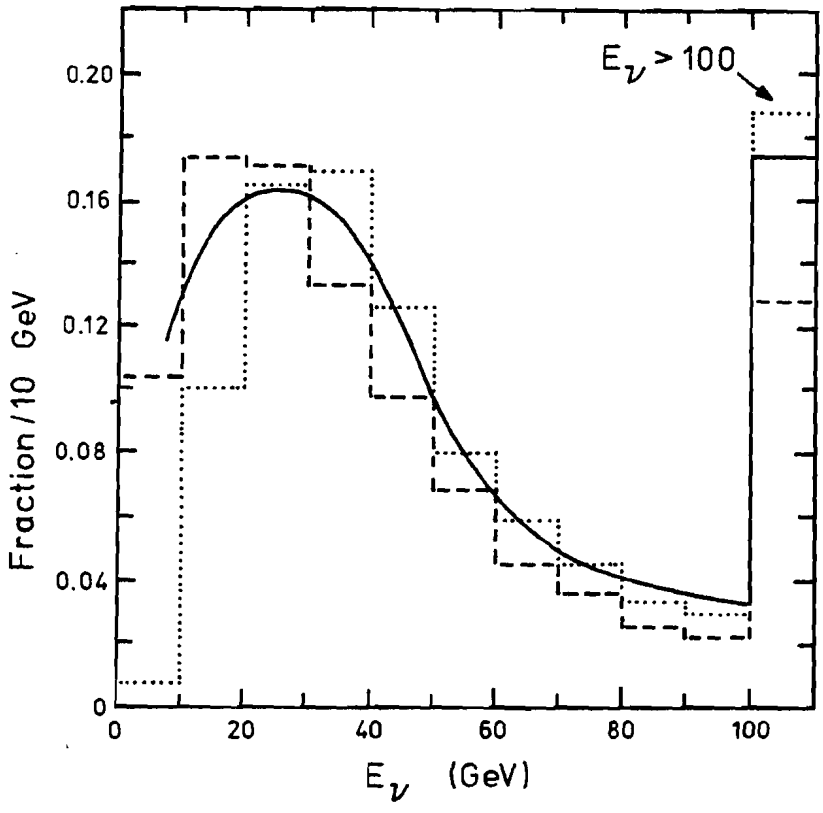

Figure 3-7: Event energy spectra (normalized to unity). The solid smooth curve is the unfolded (acceptance and resolution corrected) E_ν spectrum for found ν_μ charged current interactions. The broken histograms are the E_{vis} distibutions for all reconstucted events (dashes) and only events with identified MUFB μ^-. The average energies are, respectively, 54±4GeV, 50 GeV, and 65 GeV.

3.6 Identifying Muons

Particles are identified as muons if they are tagged by the muon counters (Sec. 2.10). There are two levels of muon identification: (1) MUFB and (2) MUF or MUB.

In all neutrino events, a particle is considered to be an identified muon if it has a MUFB tag. In an event in which there is no real primary muon passing through the muon counters, the probability of mistakenly identifying some particle as a muon is 0.3%. (For example, 3 out of 1000 neutral current interactions will have some particle falsely tagged as a MUFB muon.) In an event in which there is a real primary muon passing through the muon counters, there is also a small probability that the wrong particle will be identified as the muon, and this probability is higher if the track of the real muon is not reconstructed. For the standard NRS program, which reconstructed UPDN tracks with only ~85% efficiency, the probability of identifying the wrong particle as the MUFB muon is 2±1%; for the charm event reanalysis, with ~100% UPDN track reconstruction efficiency, the probability of identifying the wrong particle as the MUFB muon is $\lesssim\frac{1}{2}\%$.

The primary muon will have a MUFB tag in about two thirds (67±3%) of all charged current ν_μ interactions reconstructed by the NRS program. The MUFB tagging efficiency is 89% (Sec. 2.10), and the MUFB acceptance and track reconstruction efficiency for UPDN muons are calculated (by the Monte Carlo program) to be 83% and 92%. The acceptance and efficiency for μ^+ from $\bar{\nu}_\mu$ interactions are higher, 91% and 93%, than for μ^- from ν_μ interactions, but the μ^+ sample also contains a significant background from misidentified charged current ν_μ interactions. It is estimated that 25% of all observed MUFB μ^+ are actually either MUFB μ^- events in which the wrong particle (a positive hadron) has been identified as the MUFB muon, or are MUFB μ^- events in which the μ^- momentum is so large that the charge of the muon is mistakenly identified as positive. (Because of the probable positive Q shift of 0.005 (See Sec. 2.7), and because $\sigma(Q\equiv 1/P)\cong 0.005$, any negative particle with a momentum greater than 200 GeV/c will probably be misidentified as a positive particle by the

NRS program. Because the Q shift is positive, and because there are ~15 times more ν_μ events than $\bar{\nu}_\mu$ events, there is only a tiny (<<1%) contamination by misidentified μ^+ events in the observed MUFB μ^- event sample.) The observed number of μ^+ events is estimated to be 100±25% of the total number of true charged current $\bar{\nu}_\mu$ interactions.

The Monte Carlo simulation predicts that 76±3% ($5\pm\frac{1}{2}$%) of the found events will be charged current ν_μ ($\bar{\nu}_\mu$) interactions. Of the 1248 found neutrino interactions, 51% (5.2%) have a MUFB μ^- (μ^+). After correcting for the calculated ratio of the observed number of MUFB muons to the true number of charged current interactions (67±3% for $\nu_\mu \to \mu^-$, 100±25% for $\bar{\nu}_\mu \to \mu^+$), the corrected fraction of found events that are charged current ν_μ ($\bar{\nu}_\mu$) interactions is 76±4% ($5\pm1\frac{1}{2}$%). Thus the Monte Carlo predictions and the data are in exact agreement. (Such exact ageement is only fortuitous.)

The combined probability of either a false MUF or MUB tag in an event without a real muon is 6%. In an event with a MUF or MUB muon, the probability of identifying the wrong particle as the muon is ≈13% for the standard NRS program, but only ≲3% for reanalysed charm events. The total probability that a particle with a MUF or MUB tag is actually a muon is 82% for normal events and 91% for charm events. We only consider 90% probability to be sufficient for identification, so only MUFB tags are adequate muon identification for normal events reconstructed by the NRS program, while MUFB, MUF, and MUB tags are acceptable for charm events.

Of the 43 events that have a single charm decay candidate, 36 events had a MUFB muon ($31\mu^-$, $5\mu^+$), 4 events had a MUF μ^-, 1 event had a MUB μ^-, and 2 events had no identified muon. If all these single charm events are charged current interactions, then the observed charm event muon identification efficiency is $41/43 = 95\pm\frac{3}{6}$%. This is in agreement with the estimated efficiency of 90%. The net efficiency (including acceptance) for identifying muons in reanalysed events is shown in Figure 3-8; the efficiency is ≳90% for all values of W. (This high efficiency for all W implies that the muon identification efficiency should be fairly independent of kinematic thresholds, e.g. the muon identification efficiency in beauty production events should also be ≳90%.)

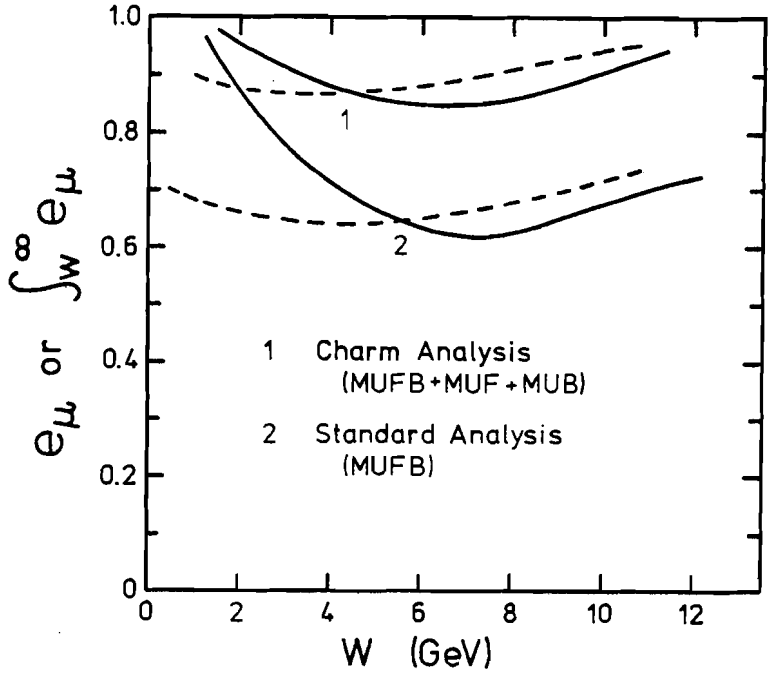

Figure 3-8: Primary muon identification efficiency as a function of the hadronic system mass. Curves 1 are for the sum of MUFB, MUF, or MUB identification by the charm event analysis programs; curves 2 are for MUFB identification by the standard analysis programs used to process all neutrino events. The solid curves are the identification efficiencies as a function of W; the broken curves are average efficiencies integrated over all events with hadronic system masses greater than W.

3.7 Charm Event Reconstruction and Reanalysis

Neutrino events with charmed particle decay candidates were intensively analysed in order to reconstruct and identify the charmed particle decays. A typical charm event reanalysis would use several CPU hours of CYBER 175 computer time (or equivalent) and require one physicist-month of work [108].

The charm event track reconstruction programs were expanded versions of the general TSY and NRS event reconstruction programs (Sec. 2.12). These programs could reconstruct both UPDN and UP-only tracks, could use emulsion track information as input, and had extensive interactive track fitting capabilities. If a track could be seen (in an event display, e.g. Fig. 2-24), it could be reconstructed. The net track reconstruction efficiency for these programs was $\cong$100% for UPDN tracks.

3.7.1 Kinematic Fitting

Energy and (vector) momentum are always conserved, so there are 4 kinematic constraint equations (E, P_x, P_y, & P_z conservation) applicable to any charmed particle decay. These equations can be used to constrain the observed (measured, with known uncertainties) kinematic parameters, to calculate the unknown parameters, and to determine a confidence level describing how well a decay hypothesis satisfies energy and momentum conservation [108].

When all secondary decay particles are observed and measured, the parent charmed particle's direction known, and the masses of all particles either known or assumed, then there is only 1 unknown kinematic parameter - the momentum of the charmed particle. This is best determined by a 3-C (4 constraints - 1 unknown) fit. The charmed particle masses used in 3-C fits were [109]

$m_{D^+} = 1868.3\ GeV/c^2$

$m_{D^0} = 1863.1\ GeV/c^2$

$m_{F^+} = 2030\ GeV/c^2$

$m_{\Lambda_c^+} = 2285\ GeV/c^2$

If the charmed particle mass is not assumed to be one of the above values, then both the charmed particle mass and momentum can be determined by a 2-C fit.

In some decays, not all secondaries are observed or the parent direction is not known, so 2-C and 3-C fits are not possible. One E-531 neutral decay is so short (6μm) that the slopes of the charmed particle before its decay cannot be measured. These slopes and momentum are determined by a 1-C fit assuming the mass to be m_{D^0}.

If the secondary particles from a charm decay include an unobserved neutral particle (such as a neutrino from a semileptonic decay), then there is insufficient information to calculate both the mass and the momentum of the parent particle. In such a case, the mass of the parent particle is related to the momentum of the missing neutral particle as shown (for example) in Figure 3-9. (The curve in the figure is called a "-1C" curve because there is one more unknown variable than the number of constraint equations; once the parent mass is chosen, the number of unknowns equals the number of equations, so the calculation of the momentum is called a zero-constraint ("0-C") calculation.) If the mass of the parent particle is chosen, then there are only two possible 0-C values for the momentum (and direction) of the unobserved neutral particle and two corresponding values for the momentum of the parent charmed particle. The momentum value is then taken to be the average of the two possibilities, with an uncertainty encompassing both the high and low values. It is always conservatively assumed that the unobserved particle has the lightest possible mass, because (as can be seen in Fig. 3-9) assuming a larger mass for the unobserved particle (or assuming that there is more than one unobserved particle) brings the high and low momentum solutions closer together and does not change the average value by very much.

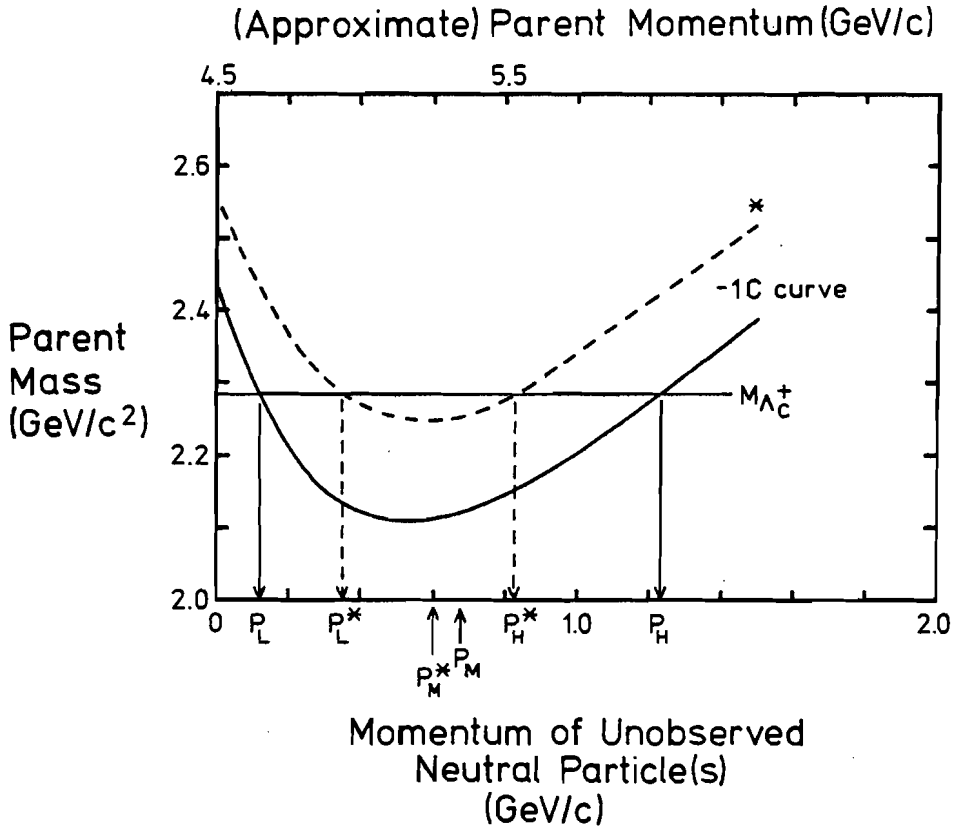

Figure 3-9: Example of a 0-C momentum calculation for a charmed particle decay. The solid -1C curve is for a massless unobserved neutral secondary particle (a neutrino or photon); the dashed curve (labeled by a *) is the corresponding -1C curve calculated for an unobserved neutral pion. The parent momentum scale is only approximate because the parent momentum does not have an exactly linear correspondence to the momentum of the unobserved particle(s).

The Λ_c^+ is the only known weakly decaying charmed particle with a mass greater than the minimum mass ($\approx 2.1 GeV/c^2$) of the -1C curve, so we assume that this charmed particle must be a Λ_c^+ and fix the parent mass to be $2.285 GeV/c^2$. This fixes the momentum of a massless unobserved secondary particle to be either P_L or P_H. P_M is the average of the high and low momentum solutions, i.e. $P_M=(P_L+P_H)/2$ and $P_M^*=(P_L^*+P_H^*)/2$.)

If the unobserved particle is a hadron, then the two momentum solutions are often close together (near the minimum) because the unobserved hadron is quite slow. (If a neutral hadron is fast, then it is likely to be detected by the lead glass array or hadron calorimeter.) The parent charmed particle momentum is fairly well determined in such cases in spite of the fact that there is an unobserved secondary particle.

If a D^o decay has an unobserved neutral secondary particle, it is possible to determine the D^o momentum accurately if the D^o comes from a $D^{*+} \rightarrow D^o \pi^+$ decay (see Fig. 4-13). The D^o momentum can be calculated by a 1-C fit using the known D^{*+} and D^o masses [109], and the measured D^o and π^+ directions and π^+ momentum.

3.8 Identification of Charmed Particles

An E-531 charmed particle decay candidate is said to be identified if it has acceptable decay hypotheses for only one type of known weakly decaying charmed particle. An acceptable decay hypothesis is one that is kinematically viable and that is consistent with the measured characteristics and secondary particle identifications of the decay.

The identification procedure requires making kinematic fits to all possible decay hypotheses. Secondary charged particles from the decay are considered to be identified if they are identified at the 90% confidence level by Time-of-Flight, by ionization in the emulsion, by the lead glass (electrons only), or by the muon counters (muons). Decays of neutral strange particles (K^o_S or Λ^o) observed in the drift chambers were identified by their reconstructed mass. If a secondary particle is not identified, for example it was ambiguous among $\pi^+/K^+/p$, then hypotheses with all three identities are tried. All possible parent charmed particle identities are considered: D^+, F^+, Λ_c^+ for charged decays, and D^o for neutral decays. A decay hypothesis with no unobserved secondary particles was considered acceptable only if its constrained kinematic fit had a confidence level of at least 1%. Any hypothesis with a neutral secondary

hadron was required to be consistent with the spectrometer and calorimeter (e.g. a 0-C hypothesis with an unobserved secondary π^o must have a π^o momentum and direction such that the π^o would not have been detected by the lead glass array.)

The analyses of the charmed particle decays are described in references [7-13], and in particular detail in [12], [8], and [7].

In a general way, Λ_c^+ baryons are identified as Λ_c^+'s because they have identified baryons (p or Λ^o) among their decay products, D^o's are identified as D^o's because they are neutral, and $F^\pm$'s are identified because there are no acceptable fits to $D^\pm$ or $\Lambda_c^\pm$ hypotheses. $D^\pm$ decays are not usually unambiguously identified on an event by event basis because they often have acceptable $F^\pm$ or $\Lambda_c^\pm$ hypotheses. In one event, (described in more detail elsewhere [8]), a neutral decay was observed that had an identified proton among its secondary decay particles. This decay candidate cannot be a D^o and is an excellent candidate for a charmed neutral baryon.

Charged D meson decays usually produced secondary particles that were too fast to be identified by time-of-flight or in the emulsion, so most $D^\pm$ decays could not be unambiguously identified on an event by event basis. The number of $D^\pm$ mesons in the decay candidate sample could, however, be statistically determined using the difference in lifetimes between the D^+ and the other charged charmed particles. Figure 3-10 shows the weighted integral proper decay time distribution for all charged charmed particles with P>4GeV/c, excluding identified Λ_c^+ and $F^\pm$ decays. These proper decay times are calculated for $D^\pm$ decay hypotheses; the decay times would be even longer if $F^\pm$ or $\Lambda_c^\pm$ decay hypotheses were used. Also shown in the figure are the measured mean lifetimes of the F^+ and Λ_c^+, as well as the 1 standard deviation high value for the F^+ lifetime (the 1σ high Λ_c^+ lifetime is less than this value). This sample of 11 non-F/Λ_c^+ decays includes 1 well identified D^- and several decays in which the D^+ decay hypotheses are favoured. It is clear from the figure that, on the basis of decay time, most of the particles are not F^+ or Λ_c^+. We assume that most of these particles are D^+ mesons. A (one dimensional) maximum likelihood analysis of the 11 decays gives a mean lifetime of

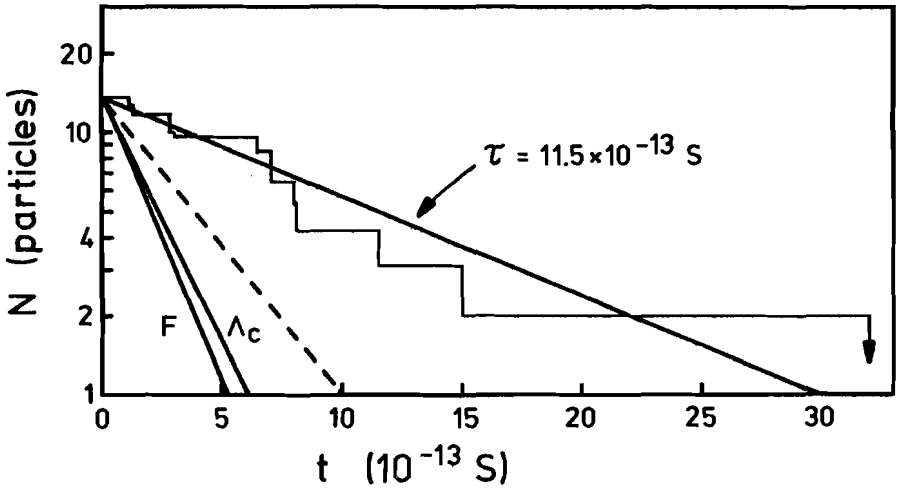

Figure 3-10: Integral decay time distribution of the 11 charged charged charmed particle decays with $P_c > 4$GeV/c and which are not identified as $F^{\pm}$ or Λ_c^+ decays. N is the weighted number of decays which have not decayed after a time t. (Each decay is weighted in proportion to the finding efficiency for the decay.)

12.0×10^{-13}s.

Both the mean lifetime of the $D^{\pm}$ and the number of $D^{\pm}$ decays in the sample can be determined by a two dimensional maximum likelihood calculation [12,110], where the two independent variables are the lifetime of the $D^{\pm}$ and the fraction of the sample that were $D^{\pm}$. This analysis used the average of the the measured F^+ and Λ_c^+ lifetimes (2.2×10^{-13}s) as the mean lifetime of any non-$D^{\pm}$ decays in the sample of 10 ambiguous D^+ decays, and included the uncertainty ($\pm 1.8 \times 10^{-13}$s) in this value in calculating the likelihood function. Figure 3-11 shows the calculated contours of equal probability for the $D^{\pm}$ lifetime and $D^{\pm}$ fraction. The most probable lifetime is $11.5 \pm^{7.5}_{3.5} \times 10^{-13}$s, and the most probable fraction of D^+ in the 10 high momentum ($P_c > 4$GeV/c) ambiguous charged decays is $1.0 \pm^{0}_{0.3}$. It is most likely that all the ambiguous particles are D^+ mesons, but 3 non-D^+ charm decays in the sample is a 1 standard deviation possibility. In all subsequent discussions and figures, these 10 decays are labeled as D^+'s, but it should be remembered that they are only statistically identified. The fraction, $1.0 \pm^{0}_{0.3}$ (plus appropriate statistical errors) is used in all calculations involving the number of D^+'s in the sample.

3.9 Decay Candidates

A total of 95 candidates for the decays of short-lived particles were found in the emulsion: 25 neutral, 23 charged multiprongs, and 47 kinks. Five of the decays are reconstructed as strange particle decays ($2K^o_S$, $2\Lambda^o$, and $1\Omega^-$ kink), and 1 neutral and 2 charged multiprongs are not in the final fiducial data set: two occurred when the magnet was off (and hence are intractable), and one occurred in the plastic of a changeable sheet. The remaining 20 neutral decays are fitted as 15 D^o and 4 $\bar{D}^o$ decays [11,7,5], and 1 charmed neutral baryon candidate (NB) [8]. The remaining 21 charged multiprong candidates are fitted as 6 Λ_c^+, 2 F^+, 1 F^-, 1 D^-, 8 (probable) D^+ decays, and 3 low momentum ($P < 4$GeV/c) ambiguous

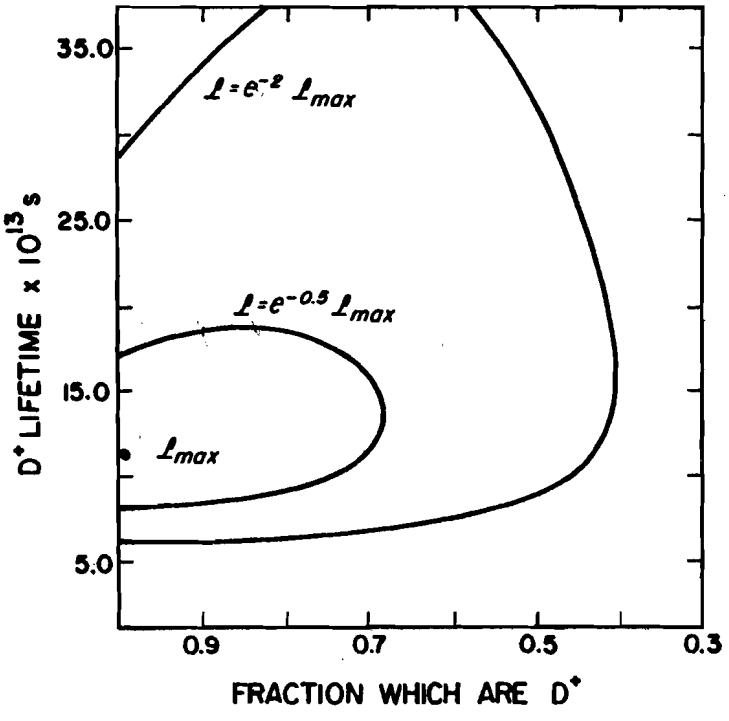

Figure 3-11: Equal probability contours for the two dimensional maximum likelyhood analysis of the ambiguous decay sample plotted in Fig. 3-10. The most probable values of the D^+ lifetime and fraction of the 11 decays which are D^+ are 11.5×10^{-13}s and 1.0; this is the maximum of the likelyhood function and is indicated by $\mathcal{L}_{max}$. The one and two standard deviation contours are where the likelyhood function has values of $e^{-0.5}\mathcal{L}_{max}$ and $e^{-2}\mathcal{L}_{max}$ respectively.

decay candidates (C^+). Only 4 kinks have been well identified as charmed particles: 2 Λ_c^+ and 2 (probable) D^+. All the decay candidates are summarized in Appendix II.

3.10 Backgrounds to Multiprong Charm Decays

Two possible types of uninteresting background events could contaminate our multiprong charm decay candidate sample: strange particle decays and nuclear interactions. Other "interesting" backgrounds from exotic new particles or processes are conceivable but not predictable.

3.10.1 Strange Particles

Of the 48 multiprong decay candidates, 4 are identified as strange particles ($2K_S^o$ and $2\Lambda^o$). Except for these fitted strange particle decays, none of the multiprong decay candidates is consistent with strange particle production and decay.

3.10.2 Nuclear Interactions

The interaction of a hadron will imitate a particle decay if (1) there are no nuclear fragments from the interaction (NH=0), and (2) charge appears to be conserved (NS = even (odd) for neutral (charged) decay candidates). In addition to the 47 kink decay candidates (most of which are nuclear interactions, see Sec. 3.11.1), a total of 89 nuclear interactions of secondary hadrons have been found (5 neutral and 84 charged, 80 of which have been measured in detail). Using these found interactions, and thus automatically including finding efficiencies, we can calculate the hadronic interaction background to multiprong charm decays.

Only 5 of 80 interactions (6.3%) have NH=1: 1 neutral interaction with NS=1 (a neutral→charged "kink") and 4 charged interactions with NS=2,2,4 and 6. These NH=0 interactions are identified as interactions because they violate charge conservation if interpreted as particle decays. To calculate the multiprong background from these events, we must subtract interactions with hydrogen and correct for the NS distribution of the interactions.

Interactions of hadrons with hydrogen nuclei (protons) are almost always NH=0 (there can be no nuclear breakup because the nucleus only contains a single nucleon), and always appear to be charge violating (because the target proton is initially not seen). Hydrogen nuclei account for 2.9±0.4% of the inelastic cross section of the emulsion. We thus expect 2.3±1.8 of the 5 NH=0 charge violating interactions to be hydrogen interactions.

From the NS distribution of the interactions, the estimate of the ratio of charge-conserving to not-charge-conserving multiprong interactions is $0.4\pm^{0.3}_{0.1}$ for charged interactions, and $0.6\pm^{0.3}_{0.1}$ for neutral interactions.

The average number of decay-like nuclear interactions expected is

$$(6.3\%-2.9\%)\times 0.4\times 84 = 1.1\pm^{1.8}_{0.6} \text{ charged interactions}$$

and

$$(6.3\%-2.9\%)\times 0.6\times 5 = 0.1\pm^{0.2}_{0.08} \text{ neutral interactions}$$

i.e. The expected hadronic interaction background to the decays of charged charmed particles is 1.1 events, the background to decays of neutral charmed particles is only 0.1 events, and the total background is $1.2\pm^{2}_{0.6}$ events.

The background is further constrained by the difference in the momentum distributions of charmed and non-charmed hadrons. Figure 3-12 shows the momentum distribution of the reconstructed charged particles. After correcting for acceptance and for electron and muon contamination, the momentum distribution of the non-charmed hadrons is found to be described by $dN/dP \propto e^{-0.4P}$. About 4/5 of interacting hadrons will have

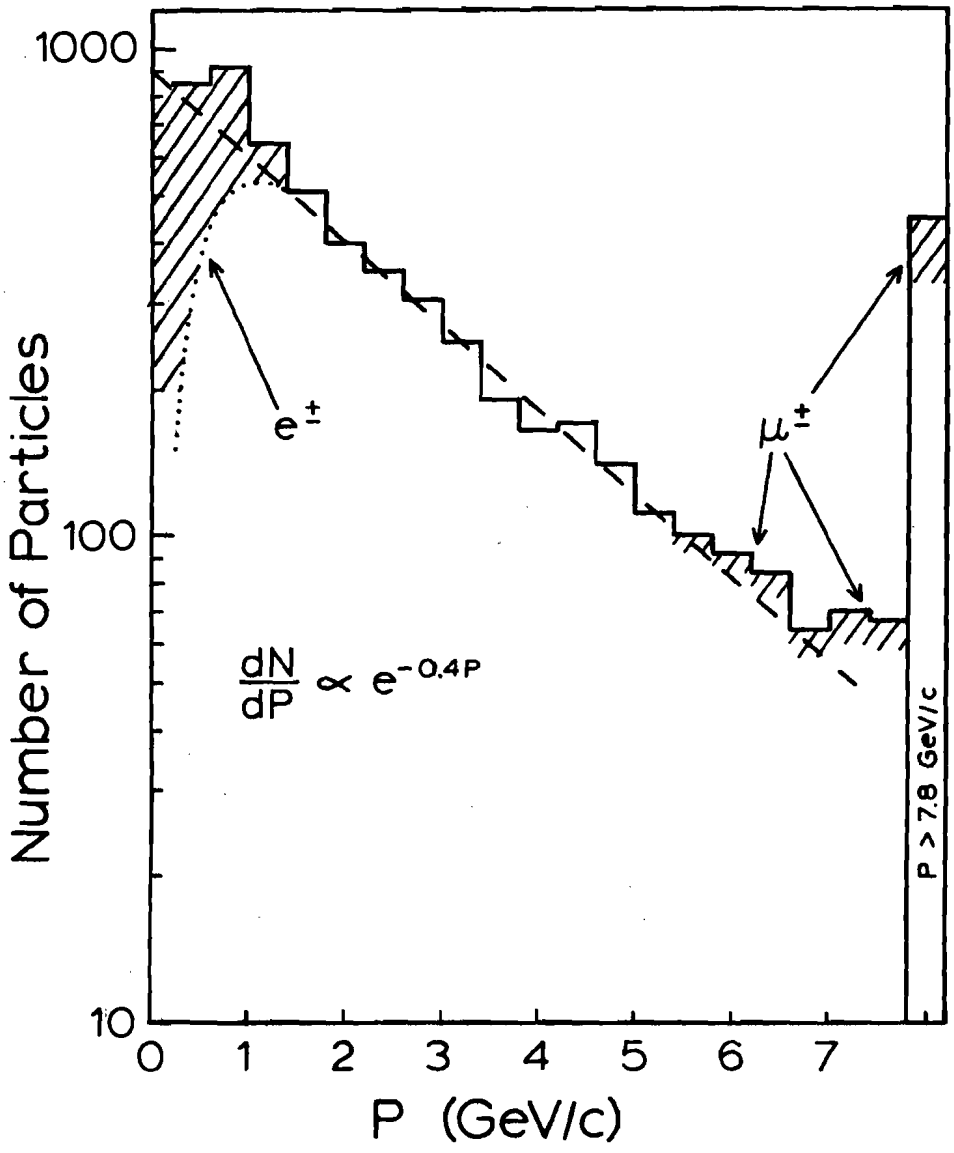

Figure 3-12: Momentum distribution of charged particles with reconstructed NRS UPDN tracks (excluding MUFB identified muons). The dotted line indicates the distribution of hadrons known to come from the primary neutrino interaction vertex. The shaded areas indicate the number of unidentified electrons and muons in the sample.

momenta less than 4 GeV/c, but only 4 out of 45 charm decay candidates (Fig. 4-14) have $P_c<4$GeV/c. Thus only about 0.2 background events are expected among the ~40 high momentum charm decay candidates, while about 1 background event is expected among the 4 low momentum ($P_c<4$GeV/c) decay candidates. Since hadronic interactions will have different kinematic characteristics than charmed particle decays (see, for example, Fig. 3-17), the interactions will not "look" like charm decays, and so the interaction background will also be concentrated among ambiguous decay candidates which cannot be well fit or identified.

3.11 Charm Kinks

Charmed kinks are not, in general, easy to identify. Most kink decay candidates are not charmed particle decays, and although some charmed kink decays can be kinematically reconstructed and identified as charm, the total number of charmed kinks can only be counted indirectly. Charmed kinks and background (non-charm) kinks differ, on average, in their kinematic properties, and these differences are used to determine the fractions of charmed and background kinks in the total kink sample.

Kink decay candidates are primarily analysed in terms of their decay length (L), their secondary momentum (P_s), and their transverse kink momentum (P_T). P_s is the momentum of the secondary charged particle coming from the kink, and P_T is the momentum of this particle relative to the direction of the primary charged particle before the kink (Figure 3-13). Sometimes additional measurements are available (e.g. the $P\beta$ or ionization of the primary particle, or the identity of the secondary particle), but L, P_s, and P_T are the basic parameters for all kinks.

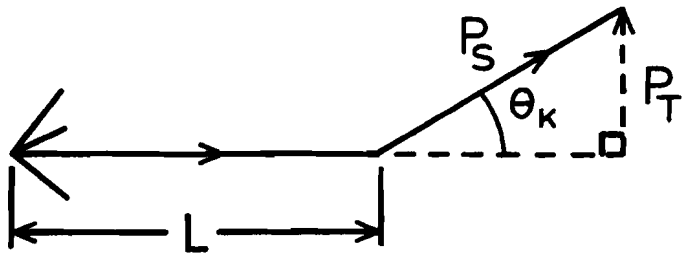

Figure 3-13: Basic kink parameters: L, P_s, P_T.

3.11.1 Kink Characteristics: P_T, P_s, L, and X_s

The P_T distribution of the found kink decay candidates is shown in Figure 3-14. This distribution is quite different from that of the secondary charged particles from reconstructed charged charmed particle decays (Figure 3-15). The charm distribution is broad and almost flat, while the kink distribution (excluding the four reconstructed charmed kink decays) is a steeply falling spectrum,

$$dN/dP_T \sim e^{-9P_T} \qquad \{3.11a\}.$$

The kink distibution is, in fact, very similar to that expected simply from hadronic scatters. Also shown in Fig. 3-14 is the scattering spectrum for aluminium, which has a nuclear cross section close to the average cross section (0.6 barns) of emulsion nuclei. This comparison shows that most kinks are not charm decays, and that only charmed kinks with very large transverse momentum, $P_T > 0.5$ GeV/c, can be well identified. (The identified charmed kinks have even greater P_T than the secondaries from trident decays. This is partly because low P_T charmed kinks cannot be identified, but is also because kink decays have an average total (charged + neutral secondaries) multiplicity less than multiprong decays, so the average P_T per secondary is larger for kinks than multiprongs.) The 4 reconstructed charmed kinks have a background, estimated from their P_T and X_s values, of only about 0.2 events, a background comparable to that of the multiprong decays.

The P_s distributions of the kinks and charm decays fall exponentially, $dN/dP_s \sim e^{-P_s/\langle P_s\rangle}$, as does the general hadronic momentum spectrum (see Fig. 3-12). From our data, the average secondary momenta are $\langle P_s\rangle \sim 1\frac{1}{2}$ GeV/c for background kinks and Λ_c^+ and F^+ decays, and $\langle P_s\rangle \sim 7$ GeV/c for $D^\pm$ decays. Λ_c^+ and F^+ kinks have secondary momenta comparable to background kinks; $D^\pm$ secondaries are usually much faster. The signs of 25 of the kinks are known (17 positive, 8 negative).

The average decay length of the 43 kinks not identified as charm is $\langle L\rangle \approx 4$mm, longer than the average decay length ($\langle L\rangle \approx 2$mm) of the reconstructed charged charm decays. Because the hadronic scattering

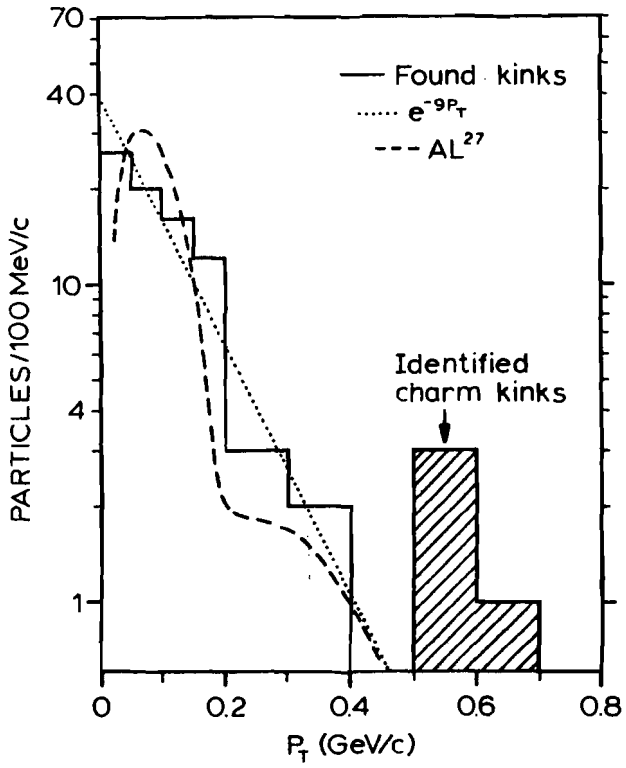

Figure 3-14: P_T distribution for kink decay candidates. The dashed curve is the P_T distribution for hadronic scatters from aluminium.

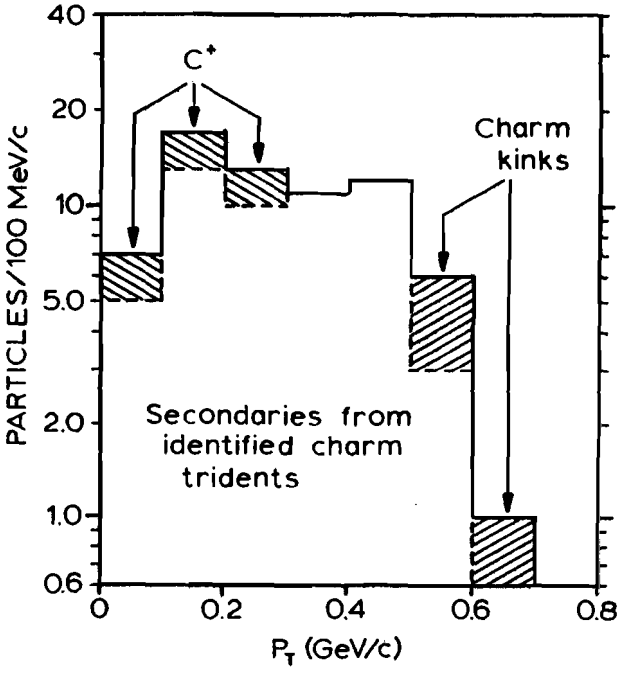

Figure 3-15: P_T distribution for charged decay secondaries from charged charmed decay candidates.

length (≈23 cm) is much longer than the thickness of the emulsion target, the distribution in L of the background kinks is determined by the decay finding efficiency (almost flat from 0 to 6 mm). The decay lengths of the charmed particles depend on their lifetimes and momenta. The Λ_c^+ and F^+ have very short decay lengths because of their short lifetimes and low momenta ($\langle L\rangle$=0.21 mm, for the 11 identified Λ_c^+ and F^+ decays); the $D^\pm$ decays are much longer ($\langle L\rangle$=4.0mm for the 11 $D^\pm$ candidates) because of their long lifetime and large momenta. The decay lengths of F^+ and Λ_c^+ kinks are usually much shorter than the lengths of the background kinks; the average $D^\pm$ decay length is actually longer than the average background kink length. ($D^\pm$ secondaries usually have higher momenta than background secondaries, and hence are more easily found and scanned back.)

L and P_s are complementary in their usefulness in distinguishing charm kinks from background kinks: Λ_c^+ and F^+ have a shorter $\langle L\rangle$ than background, and $D^\pm$ have a greater $\langle P_s\rangle$ than background. Because we have only a small number of kinks (i.e. little statistical power), it is convenient to combine L and P_s together into a new variable:

$$X_s \equiv L/P_s$$

Figure 3-16 shows the X_s distribution of the kink sample and the secondaries from the trident charm candidates. The charm and kink (mostly background) data are similar in shape, but different in width. Background kinks are expected to have a broad distribution

$$dN/dX_s \propto 1/\sqrt{X_s} \qquad \{3.11b\}$$

and this is in good agreement with the kink data. This $1/\sqrt{X_s}$ dependence follows from dN/dL = constant and $dN/dP_s \propto e^{-P_s/\langle P_s\rangle}$. The charm data are consistent with

$$\frac{dN}{dX_s} \propto \left(\frac{1}{f_{F\Lambda}\cdot X_{F\Lambda}} e^{-(X_s/X_{F\Lambda})} + \frac{1}{f_D\cdot X_D} e^{-(X_s/X_D)}\right) \qquad \{3.11c\}$$

where $X_{F\Lambda}$=0.25 mm/GeV/c (≈$\langle X_s\rangle$ for $F^\pm$ and Λ_c^+ decays), X_D=1.2 mm/GeV/c (≈$\langle X_s\rangle$ for $D^\pm$ decays), and $f_{F\Lambda}$ and f_D are the relative fractions of found

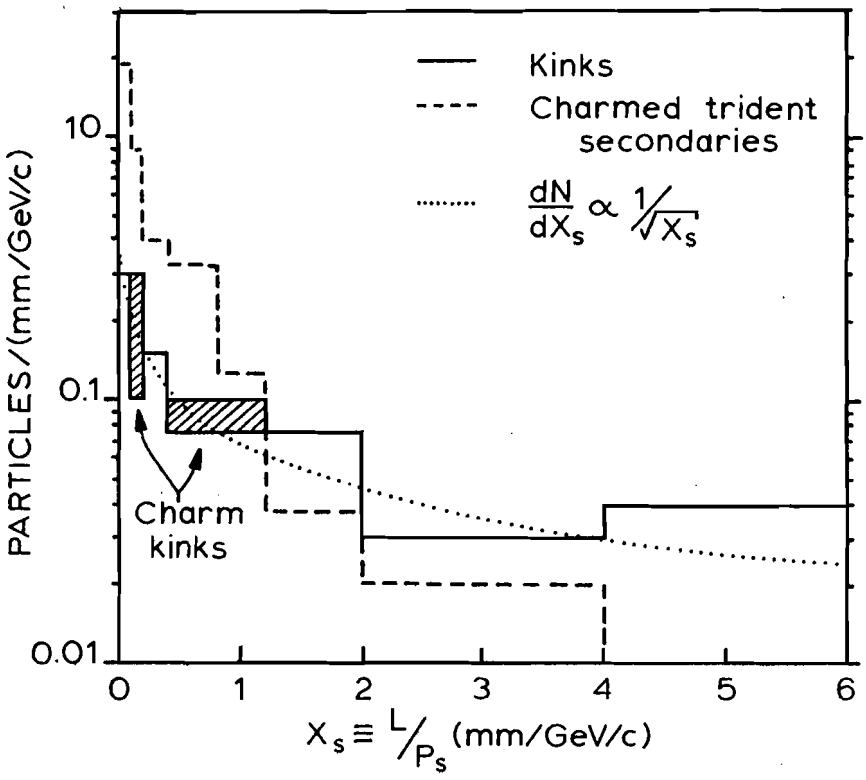

Figure 3-16: X_s distribution for found kinks and charged secondaries from trident (3-prong) charmed particle decays.

F^+/Λ_c^+ and D^+ kinks. The reconstructed charmed kinks are 2 Λ_c^+ decays and 2 D^+ candidates, and the identified charged multiprong sample is half $D^\pm$ and half $F^\pm + \Lambda_c^+$, so $f_{F\Lambda} \approx f_D \approx \frac{1}{2}$.

3.11.2 Number of Found Charmed kinks

Using the combined P_T and X_s data, it is possible to calculate the total number of found charmed kink decays in the found kink sample. Figure 3-17 shows the distribution in the X_s-P_T plane of the kink and trident decay candidates. (There are 3 entries per trident decay, one for each secondary track.) Two of the 47 kink decay candidates are not plotted because their angles and positions were such that P_s and P_T could not be adequately measured either by the spectrometer or in the emulsion. The final calculated number of found charmed kinks is corrected for this 4% (2 out of 47) inefficiency. The dashed line is a (somewhat arbitrary but illustrative) boundary between the "charm" (lower right) and "non-charm" (upper left) regions. Only 7 of the kinks are in the charm region, and only 6 out of 54 entries from the 18 low background charm tridents are in the non-charm region. (5 of the 9 C^+ entries are in the non-charm region, which is consistent with 1 or 2 of the C^+ decay candidates being background.)

The number of found charmed kinks (N_{ck}) is determined by fitting the two dimensional X_s-P_T distribution of the kinks to

$$\frac{dN}{dX_s dP_T} = N_{ck} \left.\frac{dN}{dX_s dP_T}\right|_{ck} + N_{bk} \left.\frac{dN}{dX_s dP_T}\right|_{bk}$$

where N_{bk} is the number of background kinks. (The total number of found kinks is $N_{ck}+N_{bk}=47$.) The $dN/dX_s dP_T$ distributions for charm and background are from equations {3.11a,b,c} and Fig. 3-15.

The number of found charmed kinks is calculated to be

$$N_{ck} = 7 \pm^{3.1}_{2.5} \text{ charmed kinks}$$

No anti-charmed kinks are observed.

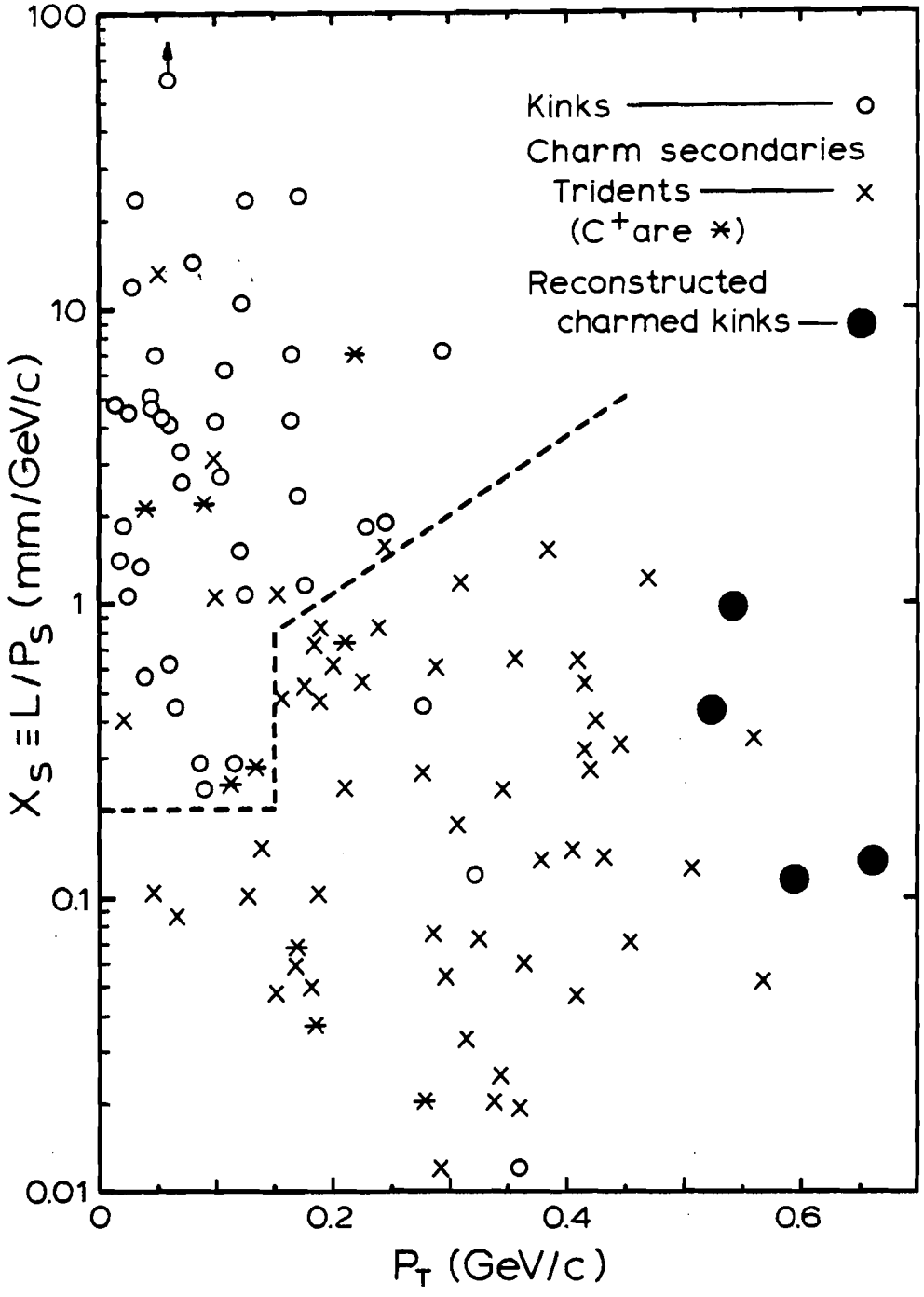

Figure 3-17: P_T vs X_s distribution for found kinks and charged secondaries from trident charm decay candidates.

The uncertainties quoted are dominated by the statistical fitting uncertainty, but also include possible systematic errors (~±1) from the X_s and P_T parameterizations and from the accuracy of the P_s and P_T measurements. Because the charm and background populations are fairly distinct (Fig. 3-17), the fitted values of N_{ck} and N_{bk} are not very sensitive to the parameterizations or measurement uncertainties. Similarly, the value of N_{ck} turns out to depend almost entirely on the four identified charm kinks (all positive) and one probable F^+ kink (see following section), and so is not sensitive to the fact that almost half the kinks have unknown sign.

3.11.3 Charmed Kink Corrected Rates

Four kinks are well identified as charmed particle decays: 2 Λ_c^+ and 2 (probable) D^+. (The 2 D^+ kinks are among the 10 D^+ decays statistically identified on the basis of their lifetimes, see Sec. 3.8.) In addition to these 4 charm kinks (all with $P_T>0.5$GeV/c), there is one probable charm kink which has $P_T=0.35$GeV/c and whose secondary track is identified as a charged kaon by ionization and multiple scattering measurements in the emulsion. This kink decay candidate is reconstructed as a low momentum ($P_c \lesssim 3$GeV/c) $F^+ \to K^+ K_S^o$ decay [12], but it is not included in the standard charm decay candidate sample because it has an estimated background of 0.2 events. This F^+ candidate is included, however, with a background subtracted weight of 0.8 in calculating the fractional charmed particle production rates (Sec. 4.9.2).

The total efficiency for finding charm kink decays can be calculated from the characteristics of the found charged charmed particle decays, using the known E-531 kink decay scanning efficiencies (Sec. 2.15.4). By treating each trident (3-prong) charm decay as three kinks, it is possible to calculate the total scanning efficiencies for charmed kinks. The finding efficiencies for kink decays relative to trident decays are calculated to be 62±17%, 96^{+3}_{-12}%, and 94^{+4}_{-10}% for $D^\pm$, $F^\pm$, and Λ_c^+ decays respectively. The relative efficiency for finding $D^\pm$ decays is low

because charged D mesons tend to be produced with large lab momenta (see Fig. 4-14) and so D^+ kink decays will have small kink angles and will be hard to find. By contrast, the observed F^+ mesons and Λ_c^+ baryons are produced with smaller lab momentum and so their kink decays will have large kink angles and will be almost as easy to find as trident decays. In addition, because there are fewer charged particle tracks produced by trident decays, the event reconstruction efficiency is lower for charm events with kink decays than for charm events with trident decays (see Sec. 3.15.1). The event reconstruction efficiency for charm events with kink decays relative to events with multiprong decays is estimated to be $96\pm^{3}_{10}$% for D^+ decays and 80±10% for F^+ and Λ_c^+ decays. (These efficiencies are estimated from the trident decays by determining if the event would have been reconstructed had the charm decay been a kink decay.)

The total number of found charmed kinks is calculated to be $7\pm^{3.1}_{2.5}$. After correcting for the absolute kink decay scanning efficiency and the relative kink/multiprong event reconstruction efficiency, the total number of charmed kinks is $13.1\pm^{8.8}_{6.6}\pm^{9.3}_{3.9}$, where the first error is the systematic uncertainty in the efficiencies and acceptances and the second error is the total statistical uncertainty.

Although the calculated number of found charm kinks is 7, only 4 or 5 of these have been individually identified, so the probability of identifying a found charm kink is only about 70%. This identification efficiency has little effect on the calculation of the total charm event rates, but is important in calculating the relative rates of production of the different charmed particles. Including this identification probability, the total combined efficiency (event reconstruction × decay finding × identification) for kink decays relative to trident decays is estimated to be $41\pm^{30}_{15}$% for D^+ decays and $52\pm^{30}_{17}$% for F^+ and Λ_c^+ decays. The total relative efficiency for all kink decays (averaged over the sample of 2 D^+, 2 Λ_c^+, and "0.8" F^+ kinks) relative to multiprong decays is $46\pm^{27}_{16}$%. The total multiprong charged charm decay sample is $8D^+ + 2F^+ + 6\Lambda_c^+ + 3C^+$ with an expected background of 1 event, so the corrected

ratio of kink to charged multiprong decays in the E-531 data sample is $(4.8/0.46)/(21-1) = 58\%$. i.e. Kink decays are 37±19% of all charged charmed particle decays. This observed kink rate is consistent with theoretical expectations [111]; the only measured charmed particle kink branching ratio is for the charged D meson: B.R.($D^+ \rightarrow$1-prong)=45±5% [112].

3.12 Charm Decay Efficiencies and Charm Event Weights

Each charm decay is assigned a weight that is inversely proportional to the probability for finding the decay. These weights are used to calculate the charm production rates, and in hybrid Monte Carlo calculations of resolutions and acceptances for the charm kinematic distributions (Sec. 3.14). The charm weights are calculated from the experiment's decay finding efficiencies, from the lifetimes and branching ratios of the charmed particles, and from the characteristics of each decay.

3.12.1 Multiprong Charm Decay Finding Efficiencies

The finding efficiency for a multiprong decay is parameterized for this experiment in terms of the decay length (L) and the particle's momentum (P_c) and direction (slopes: $x'_c \equiv \frac{dx}{dz}$ and $y'_c \equiv \frac{dy}{dz}$). Other factors can affect the decay finding efficiency, but these factors are small and can be ignored for the small data sample of this experiment. (An example of such minor factors is the possible effect of D^{*+} decays on the D^o finding efficiency mentioned in Sec. 4.9.1.)

The decay finding efficiency $\varepsilon(L,P_c,x'_c,y'_c)$ can be calculated from the scanning efficiencies discussed in Section 2.15. These raw efficiencies are, however, not normally used directly - the effects of decay time and decay multiplicity are removed if possible. The intrinsic characteristcs of a charmed particle decay are independent of all

external factors. Thus the proper decay time and charged particle multiplicity of the decay are not determined in any way by the external production characteristics (P_c, x'_c, y'_c, E_ν, Z, Q^2, ...) in which we are interested.

If the lifetime (τ) and topological branching ratios of a charmed particle are known, then the fluctuation in the scanning efficiency due to the decay lifetime and multiplicity can be eliminated by integrating over all decay times (t) and summing over all topological branching ratios (B_m). The finding efficiency for a given decay is

$$e_d(B,\tau) = \sum_m \int_0^\infty B_m \varepsilon(\ell, P_c, x'_c, y'_c) \frac{e^{-t/\tau}}{\tau} dt, \qquad \ell = \gamma\beta ct = (P_c/M_c)ct$$

where M_c is the mass of the charmed particle and B_m is the branching ratio into m charged particles (m=1,3,5,... for decays of charged particles, m=0,2,4,... for decays of neutral particles). In practice, if the charmed particle is not identified (e.g. the C^+ decay candidates) then the efficiency is averaged over all possible particle identities. If the momentum is not well determined (e.g. some 0-C decays), then the efficiency is averaged over all possible momentum values.

If the branching ratios of the decay are not known, then the best efficiency is

$$e_d(\tau) = \int_0^\infty B_m \varepsilon(\ell, P_c, x'_c, y'_c) \frac{e^{-t/\tau}}{\tau} dt \quad ,$$

and if the mean lifetime τ is also not known, then the best value for the efficiency is simply the raw efficiency

$$e_d = \varepsilon(\ell, P_c, x'_c, y'_c) \quad .$$

In the limit of an infinitely large data sample, it would not matter which of the above three efficiencies was actually used, but it does matter when the data sample is small. For an extreme example, consider a data sample of two decays, a Λ_c^+ and an F^+, with equal momenta and angles, and assume that they have equal mean lifetimes and topological branching ratios. These decays would have equal finding efficiencies $\varepsilon_d(B_m,\tau)$, so the efficiency corrected $\Lambda_c^+ : F^+$ ratio would simply be 1:1. If, however,

the Λ_c^+ and F^+ had proper decay times such that the Λ_c^+ had a decay length of 5μm and the F^+ had a decay length of 100μm, then the raw efficiencies would be ~20% for the Λ_c^+ and ~100% for the F^+. So the corrected $\Lambda_c^+:F^+$ ratio using the raw efficiencies would be 5:1. So we see that using the raw efficiencies can introduce large fluctuations in the calculated ratio due to different proper decay times, even though the true ratio is totally independent of the decay times. The scanning efficiencies for this experiment are relatively flat and so the extreme range of raw efficiencies for the found decays is only a factor of two, but it is still important to eliminate the decay time and branching ratio factors when possible.

For this experiment, the efficiency for finding each multiprong charm decay candidate is calculated as follows. (The E-531 values for the charmed particle mean lifetimes, see Table 1-3, are used in all cases.)

For D^o and $\bar{D}^o$ decays,

$$e(D^o) = (1-B_o)\int_0^\infty \varepsilon_N(\ell,x_c',y_c')\frac{e^{-t/\tau}}{\tau}dt \quad , \quad \tau=\tau_{D^o}, \ \ell=\gamma\beta ct$$

where B_o=9.1±1.9% [113] is the branching ratio for the D^o to decay entirely into neutral hadrons. (Such all-neutral 0-prong decays are totally invisible in emulsion and cannot be found.) ε_N is the neutral multiprong decay finding efficiency (see Sec. 2.15.5); ε_N has no explicit P_c dependence.

Neither the identity, mean lifetime, nor branching ratio of the charmed neutral baryon candidate (NB) are known, so the raw decay finding efficiency must be used, and it is assumed (as a best guess) that the all-neutral branching ratio for NB decays is the same as for D^o decays:

$$e(NB) = (1-B_o)\varepsilon_N(L,x_c',y_c') \quad .$$

For multiprong $D^\pm$ decays,

$$e(D^\pm) = \int_0^\infty \varepsilon_C(\ell,P_c,x_c',y_c')\frac{e^{-t/\tau}}{\tau}dt \quad , \quad \tau=\tau_{D^+}$$

ε_C is the charged multiprong decay finding efficiency (See Sec. 2.15.5). The kink branching ratio (B_k) is known for D^+ decays but not for the

other charged charmed particles. Because $B_k(F^+)$ and $B_k(\Lambda_c^+)$ are not known, and because $D^\pm$ decays are not always well identified, all kinks are treated separately (Sec. 3.11). In some cases, in particular for the D^+/D^o production ratio (Sec. 4.9.1), it is possible to ignore the kinks and use the known value of $B_k(D^+ \rightarrow 1\text{-prong}) = 0.45 \pm 0.05$ [112] to calculate a kink corrected efficiency for the D^+ multiprongs:

$$e'(D^\pm) = (1-B_k) \int_0^\infty \varepsilon_N(\ell, P_c, x_c', y_c') \frac{e^{-t/\tau}}{\tau} dt$$

It does not actually matter whether $e(D^\pm)$ is used and kinks included, or $e'(D^\pm)$ is used and kinks excluded, because the observed $D^\pm$ kink rate is in agreement with the known value of $B_k(D^+)$.

For Λ_c^+ and F^+ decays,

$$e(F^+) = \int_0^\infty \varepsilon_C(\ell, P_c, x_c', y_c') \frac{e^{-t/\tau}}{\tau} dt \ , \quad \tau = \tau_{F^+}$$

and

$$e(\Lambda_c^+) = \int_0^\infty \varepsilon_C(\ell, P_c, x_c', y_c') \frac{e^{-t/\tau}}{\tau} dt \ , \quad \tau = \tau_{\Lambda_c^+}$$

The values of $e(F^+)$ and $e(\Lambda_c^+)$ are usually similar because the observed Λ_c^+ and F^+ decays have similar lifetimes and momenta.

For the C^+ decay candidates,

$$e(C^+) = \frac{1}{N} \sum_{i=1}^{N} \int_0^\infty \varepsilon_C(\ell, P_{ci}, x_c', y_c') \frac{e^{-t/\tau_i}}{\tau_i} dt$$

where the summation indicates that the efficiency is calculated as the average over all acceptable C^+ decay hypotheses and momenta. The C^+ efficiencies are fairly well determined because the calculated efficiency does not usually change much for different decay hypotheses.

3.12.2 Charm Event Weights

The weight for each charm decay candidate is the inverse of the background corrected finding efficiency for the decay. By assigning such a weight to each decay, corrected production rates and distributions can

be conveniently calculated.

For a multiprong decay candidate (labeled α), the event weight is given by

$$W_\alpha = \frac{(1-C_\alpha)}{e_\alpha}$$

where e_α is the finding efficiency for the decay, and C_α is the background for the decay. Except for the NB and C^+ events the background per decay is negligible and is ignored, i.e. $W_\alpha = 1/e_\alpha$ for all fitted D^o, $\bar{D}^o$, $D^\pm$, $F^\pm$, and Λ_c^+ decays. The total background to neutral charm decay candidates is subtracted from the NB charmed neutral baryon candidate: $C_{NB}=0.1\pm^{0.2}_{0.08}$ (Sec. 3.10.2). Similarly, the total background to charged multiprong decays is subtracted proportionally from the 3 low momentum ambiguous C^+ decay candidates: $C_{C^+} = (1\pm^{2}_{0.6})/3$.

For kink decays, the weight is the inverse of the total kink efficiency; this includes the kink identification efficiency and the relative kink/trident event reconstruction efficiency. The F^+ kink is not part of the standard charm decay sample, but it is included in all rate calculations with a weight that is corrected for a background of 0.2 events (i.e. $C_\alpha=0.2$).

The weight for each decay candidate is given in Appendix II.

3.12.3 Finding Efficiency for Charm Pair ($c\bar{c}$) Decays

Once a charm decay is found, the event is scanned and analysed exhaustively. All charged tracks are followed from their origin until they leave the emulsion, and drift chamber tracks are followed back into the emulsion. Because of this intensive scanning, the efficiency for finding any additional short decays in a charm event is very high.

The total efficiency for finding a single charmed particle is 64%. (This is simply the ratio of found single charmed particles, 42 (38 charm + 5 anti-charm - 1 background), over the total corrected number of charmed particles, 59 charm + 7 anti-charm (see Sec. 3.13), in the E-531 data sample.) Thus if a $c\bar{c}$ charm pair is produced in an event, the probability

of finding at least one of the charmed particles is 87%. Once one decay is found, the event is intensively analysed and the probability of finding the second decay is estimated to be >90% for a multiprong and >70% for a kink decay. The total probability for finding both the charm decay and the anti-charm decay is estimated to be 67%. The relative efficiency for finding both decays in a $c\bar{c}$ event compared to the efficiency for finding the single decay in a c event is $\varepsilon_{c\bar{c}/c} = 1.04 \pm 0.15$.

3.13 Corrected Number of Charmed Particles Produced

The total corrected number of charmed particles produced in the neutrino event data sample is simply the sum of all the charmed particle weights (W_i). The total number of single charmed particles produced in charged current neutrino interactions is

$$N_{tot}(\nu_\mu N \to \mu^- cX) = \sum_i W_i = 59^{+17}_{-14}$$

where the sum is over the 38 events with single charmed particle decay candidates (i.e. all charm events except the 5 anti-charm events and the $D^o\bar{D}^o$ charmed pair event). The uncertainties in N_{tot} include both statistical error and systematic uncertainties in the charm weights due to the uncertainties in the charm decay finding efficiencies and in the background subtraction. The largest part of the systematic uncertainty is due to the charm kink correction factors. The corrected number of single anti-charmed particles is

$$N_{tot}(\bar{\nu}_\mu N \to \mu^+ cX) = \sum_i W_i = 6.8^{+5.7}_{-2.5}$$

based on the 5 observed anti-charm events.

3.14 Hybrid Monte Carlo

The effects of experimental resolutions and acceptances on the measured charm production distributions are calculated using a hybrid Monte Carlo method: the parameter of interest is varied while all other characteristics are obtained from the observed charm events, with each charm event being weighted by its charm event weight (Sec. 3.12.2). The hybrid method differs from a standard Monte Carlo Simulation in that the experimental effects are determined only with respect to the parameter of interest. Such hybrid techniques [114] are similar to the likelihood analyses used to measure particle lifetimes [115]. (In a lifetime likelihood analysis, only the lifetime is varied, and each decay is weighted inversely proportional to the probability of its being found.) The hybrid Monte Carlo method will be illustrated by a discussion of its application to the fragmentation variable Z. (See Sec. 4.11.)

The fragmentation variable Z is E_c/ν, where $\nu=E_H-M_N$. If D(Z) is the true charm fragmentation function (normalized to one event), then the observed distribution is calculated by the hybrid Monte Carlo method in the form

$$D_o(Z_o) = \sum_i W_i \int_{Z_{min}}^{1} D(Z) R(Z,Z_o) E_i(Z) dZ$$

where the sum is over all single charm events, W_i is the charm event weight for each event, and the integral over Z has a lower kinematic bound of $Z_{min}=M_c/\nu$. (This simple kinematic bound could easily be replaced by a more complex threshold function if desired.) The integration over Z is done by Monte Carlo simulation because neither $R(Z,Z_o)$ nor $E_i(Z)$ is an analytic function.

$R(Z,Z_o)$ is the resolution function that gives the probability for measuring a value Z_o when the true value is Z, e.g. $R(Z,Z_o)=\delta(Z-Z_o)$ in the limit of an infinitely accurate experiment. For each event, the value of $\nu=E_H+M_N$ is taken from the event. $R(Z,Z_o)$ is calculated for each value of Z by generating Monte Carlo "observed" values of $Z_o=E_{c_o}/\nu_o$ from the true values of ν and $E_c=Z\nu$, each smeared by the known experimental energy resolution and acceptance for ν and E_c. (The experimental resolutions are

actually calculated in terms of E_H and P_c; the average RMS resolutions for the charm events are $\langle\sigma(E_H)/E_H\rangle=0.2$ and $\langle\sigma(P_c)/P_c\rangle=0.07$.)

$E_i(Z)$ is the efficiency for the i^{th} event calculated for a given value of Z:

$$E_i(Z) = e(P_c, X_i)$$

where $P_c=\sqrt{(Z\nu)^2-M_c^2}$, and X_i represents all other factors that determine the efficiency for the event. The values of ν, M_c, and X_i are all taken from the event, so $E_i(Z)$ is the finding efficiency for an event that is exactly the same as the real event except for the value of Z (and P_c).

Using this hybrid procedure, an "observed" charm fragmentation distribution $D_o(Z_o)$ can be calculated for any true charm fragmentation function D(Z). By comparing $D_o(Z_o)$ with the actual Z distribution of the charm data (See Sec. 4.11), the experimental resolutions, efficiencies, and thresholds can be unfolded from the data to give D(Z).

3.15 Relative Event Efficiencies

3.15.1 Relative Event Reconstruction Efficiency

The event reconstruction efficiency is not exactly the same for charm and non-charm events. On average, the primary NRS program reconstructs more UPDN tracks in charm events, and so the probability for reconstructing at least two tracks (the basic requirement for event reconstruction) is higher for charm events than non-charm events. The relative event reconstruction efficiency for charm events is calculated by comparing the number of NRS UPDN tracks (N_T) reconstructed in charm and non-charm events.

The N_T distribution of the charm events is shown in Figure 3-18. The average number of tracks reconstructed is $\langle N_T\rangle=5.8$ tracks, one more track than the average N_T for all events (Fig. 3-3). This difference is expected because of the higher energy of charm events, and because the

probability of reconstructing a charm event is weakly correlated with the probability of finding the charm decay. Three effects contribute to the difference:

(1) $\langle N_T \rangle$ increases with larger E_ν, and charm events have, on average, more energy than non-charm events.

(2) The scanback charm decay finding efficiency depends on reconstruction of secondary decay tracks, so the scanback efficiency (ε_{sbk}) depends on the NRS UPDN track reconstruction efficiency (ε_{NRS}). Since N_T also depends on ε_{NRS}, ε_{sbk} and N_T are indirectly correlated.

(3) The efficiency for finding a decay depends on the number of charged decay tracks (ND), and N_T is proportional to the total number of charged particles (~NS+ND) produced in the event, so ε_D and N_T are indirectly correlated. Events with all-neutral or kink charm decays will have fewer NRS UPDN tracks than equivalent events with multiprong decays, so events with multiprong decays are more likely to be reconstructed than events with 0- or 1-prong decays. (This correlation is distinct but related to the scanback correlation (2) above.)

Figure 3-18 shows both the expected and observed N_T distributions for the charm events. The effect of the higher charm event energies is calculated from the energy distribution of the charm events, using the N_T vs E distribution of all events. (This estimate is not sensitive to whether N_T vs E_ν or N_T vs E_H distributions are used.) The effects of the correlations between decay finding and event reconstruction efficiencies are calculated from the characteristics of the observed charm decays. (The effect of decay multiplicity on the event reconstruction efficiency is estimated by pretending the multiprong decays are kinks or all neutral decays, and then determining N_T. If $N_T<2$, the event would not have been reconstructed (see Sec. 3.3)). The average value expected for the found events is $\langle N_T \rangle = 6.0 \pm 0.6$, in agreement with the observed value of $\langle N_T \rangle$. The difference in $\langle N_T \rangle$ between charm events and all events is ~1/3 due to the differences in E_ν, ~1/6 due to scanback, and ~1/2 due to the correlation between ND and N_T.

The reconstruction efficiency for all charged current events relative to the efficiency for reconstructing charm events is estimated

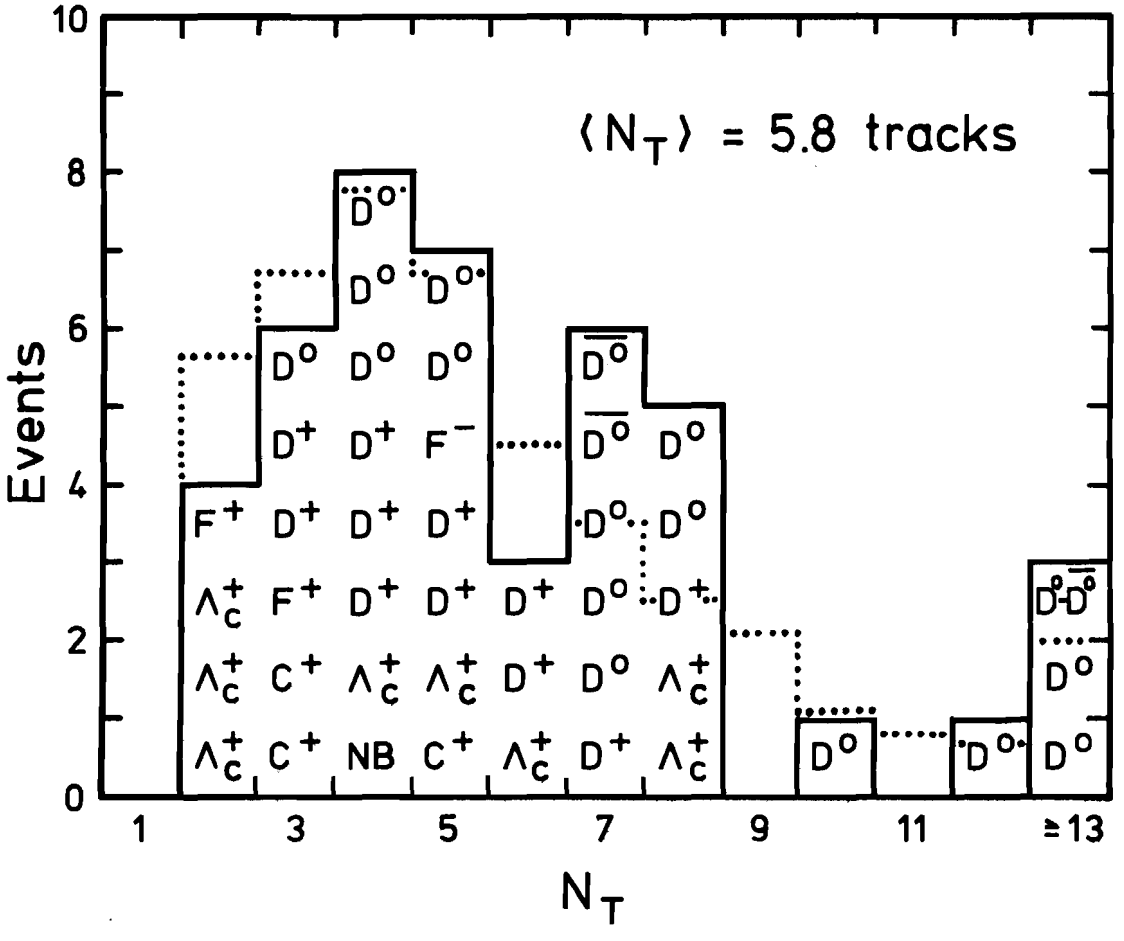

Figure 3-18: Number of tracks, N_T, reconstructed per charm event by primary NRS reconstruction program. The broken line is the (normalized) distribution calculated from the charm event energy distribution and the correlation between event reconstruction and charm decay finding efficiencies.

to be

$$e_r\left(\frac{\nu_\mu \to \mu^- X}{\nu_\mu N \to \mu^- cX}\right) = 0.93^{+0.07}_{-0.1}$$

for neutrino interactions, and

$$e_r\left(\frac{\bar{\nu}_\mu N \to \mu^+ X}{\bar{\nu}_\mu N \to \mu^+ cX}\right) = 0.87^{+0.11}_{-0.13}$$

for antineutrino interactions. Because the anti-charm sample is so small, e_r for antineutrino interactions is calculated from the neutrino charm data by assuming that the charm and anti-charm N_T distributions are the same except that anti-charmed antibaryons are not produced in antineutrino interactions. This assumption is not true, but the few anti-charmed antibaryons produced cannot be target fragments and so will be kinematically similar to mesons. In any event, the E-531 anti-charm sample is so small that a very rough estimate to e_r is sufficient.

These relative efficiencies are primarily dependent on E_ν because most of the effects ((2) and (3) above) of the decay finding efficiencies are already included in the decay finding weights, and so are not included again in e_r. For example, the correction for unobserved $D^o \to$all-neutral decays is already included in the event weight for each D^o decay. It would be incorrect to also include a $D^o \to$all-neutral correction to the event reconstruction efficiency, because this would "double count" the correction.

3.15.2 Relative Event Finding Efficiency

The efficiency for finding charm events relative to the efficiency for finding non-charm events is determined by the relative event reconstruction efficiency, e_r, and by the relative scanning efficiency for finding charm and non-charm interactions in the emulsion.

For the track followback technique, the scanning efficiency is essentially independent of the emulsion characteristics of each event, so the relative event finding efficiency can be assumed to be determined by

the event reconstruction efficiency.

For the volume scan technique, the scanning efficiency depends on the number of heavy tracks produced at the neutrino interaction vertex (see Sec. 2.14), so the total event finding efficiency is determined by both e_r and NH. Figure 3-19 shows the NH distribution of the charm events. The track followback finding efficiency is independent of NH, so the charm events found by track followback provide a bias-free measurement of the true charm NH distribution. The charm distribution is consistent with the distribution for all events. The charm events are slightly more concentrated at smaller values of NH, but this is not a statistically significant effect, and even if it is a real difference, the effect on the total charm event finding efficiency is only ~3%.

We thus assume that the total relative charm event finding efficiency is determined entirely by the relative event reconstruction efficiency. For neutrino interactions,

$$e_f\left(\frac{\nu_\mu N\to\mu^- X}{\nu_\mu N\to\mu^- cX}\right) = e_r = 0.93^{+0.07}_{-0.1} \quad ,$$

and, for antineutrino interactions,

$$e_f\left(\frac{\bar{\nu}_\mu N\to\mu^+ X}{\bar{\nu}_\mu N\to\mu^+ cX}\right) = e_r = 0.87^{+0.11}_{-0.13} \quad .$$

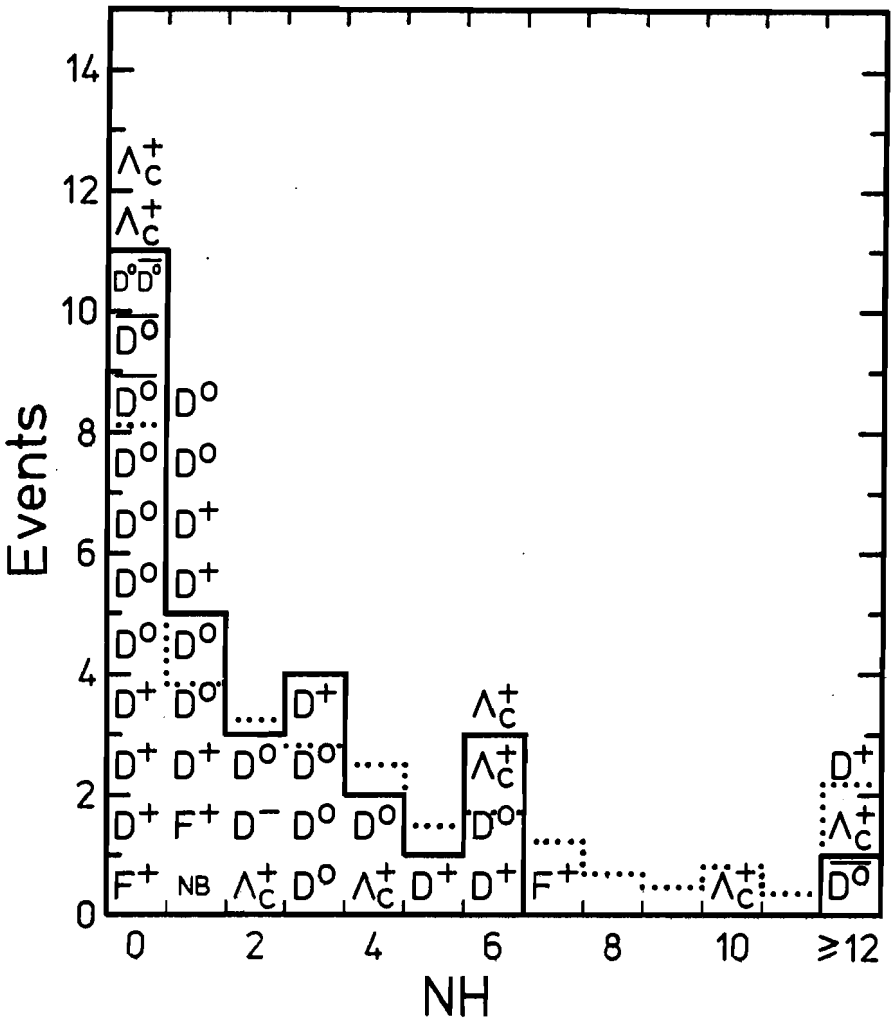

Figure 3-19: Heavy track multiplicity (NH) distribution for events with well identified charmed particles (C^+ excluded). The 30 events enclosed in the solid histogram are those vertical events found by track followback; the dotted histogram is the NH distribution for all followback events (from Fig. 2-31a) renormalized to 30 events.

CHAPTER 4: Neutrino Charm Production

This chapter presents the characteristics of charm production by neutrinos. These are the first inclusive measurements of neutrino charm production made by direct observation of charmed particles. The rates of charm particle production, the properties of the charm events, and the types and kinematic characteristics of the charmed particles have been measured.

4.1 Charm Production Total Rates

A single charmed or anti-charmed particle is observed in all charmed events but one, and all these single charm events are consistent with direct charged current charm production. Limits to more exotic production processes will be discussed later, but for the moment we shall consider only this simplest production mechanism.

To calculate the rate for charm production, relative to the total charged current cross section, it is necessary to know both the number of charm production events and the total number of found charged current neutrino interactions.

There are a total of 43 events in which a single charmed particle has been found, and 41 of these events have identified primary muons. This fraction, 41/43 = 95%, is consistent with the primary muon identification efficiency of 91% expected for charm events (Sec. 3.6). The fully corrected total numbers of single charmed particles are $59\pm^{17}_{14}$ charmed and $6.8\pm^{5.7}_{2.5}$ anti-charmed particles (Sec. 3.13).

Charged current $\nu_\mu(\bar{\nu}_\mu)$ interactions constitute 76±4% (5±1%) of the 1248 found neutrino interactions, and 94±4% ($98\pm^{1}_{5}$%) of these have E_ν>10 GeV. Events with E_ν<10 GeV are excluded (in all E-531 rate calculations)

because fluxes, efficiencies, and resolutions are not well known at very low energy. As well, 2.5% of the events are not in our final fiducial data set. (These are mostly events with the analysis magnet off; such events have already been excluded from the charm sample (Sec. 3.9).) The final charged current interaction samples are 860±54 ν_μ and 60±15 $\bar{\nu}_\mu$ interactions.

The relative charm production cross sections are calculated from

$$\frac{\sigma(\nu N \to c\mu^- X)}{\sigma(\nu N \to \mu^- X)} = \frac{N_{cor}(\nu N \to c\mu^- X)}{N_{tot}(\nu N \to \mu^- X)} \cdot e_f$$

where $N_{cor}(\nu N \to c\mu^- X)$ is the corrected number of single charm production events, $N_{tot}(\nu N \to \mu^- X)$ is the total number of charged current interactions, and e_f is the efficiency for finding all charged current events relative to the efficiency for finding charm events (Sec. 3.15.2).

The corrected total cross section ratios for charged current production ($E_\nu > 10$ GeV) of single charmed particles are

$$\frac{\sigma(\nu N \to c\mu^- X)}{\sigma(\nu N \to \mu^- X)} = 6.5 \pm^{1.9}_{1.8}\%$$

and

$$\frac{\sigma(\bar{\nu} N \to \bar{c}\mu^+ X)}{\sigma(\bar{\nu} N \to \mu^+ X)} = 10 \pm^{9}_{4}\%$$

The ratio for D^o production is

$$\frac{\sigma(\nu N \to D^o \mu^- X)}{\sigma(\nu N \to \mu^- X)} = 2.5 \pm^{0.9}_{0.6}\%$$

(The fractional rates of production for all the different charmed particles are discussed in Sec. 4.9.)

These measured charm production rates can be compared with rates calculated for the E-531 E_ν spectrum, using predicted $d\sigma(\nu N \to c\mu^- X)/dE_\nu$ cross sections based on, or constrained by, dilepton data. There are several such calculations [50,48,49], all giving similar results (since they all use the same dilepton data). Using the cross section of Campbell

et al. [48] (this is the smooth curve in Fig. 4-2), I calculate expected total charm production rates for E-531 found charged current interactions of 5.7% for $\nu_\mu N \to c\mu^- X$, and 4% for $\bar{\nu}_\mu N \to \bar{c}\mu^- X$ [118]. (This is for an integrated strange quark ocean of $2S/(Q+\bar{Q})=0.04$ and $U_{cd}^2/|U_{cs}^2|=0.053$; a strange ocean of 0.06 gives charm and anti-charm production rates of 6.7% and 6%.)

4.1.1 Energy Dependence of the Charm Production Cross Section

The neutrino energy spectrum of the single charm events is shown in Figure 4-1, and the mean charm event energies are presented in Table 4-1. D meson production dominates the total charm production cross section for $E_\nu>30$ GeV. The finding efficiency for D decays is less than the efficiency for finding $F^\pm$ or Λ_c^+ decays, so the many high energy D events make the corrected (weighted) mean charm event energy slightly larger than the simple average.

The energy dependence of the charm and D^o production cross sections are shown in Figure 4-2. The data are consistent with the expected energy dependence for charm production.

The only previous measurements of the energy dependence of neutrino charm production have been made indirectly by studying opposite sign dilepton production. To compare dilepton data to the E-531 charm data, an average charm semileptonic branching ratio is needed. This can be calculated from the fractional production rates and semileptonic branching ratios of the different charmed particles. The semi-electronic branching ratios of the D^+ and Λ_c^+ are $19\pm^4_3$% [65] and 4.5±1.7% [119]; the ratio for the D^o is measured to be small, <6% (90%C.L.) [65], and I use a value of $5\pm^1_3$% [120]. There is no measurement for the semileptonic branching ratio of the F^+, but on the basis of the F^+ lifetime, a semi-electronic branching ratio of $4\pm^{10}_3$% can be estimated [121]. From these branching ratios and the fractional D^o, D^+, F^+, and Λ_c^+ production rates presented in Sec. 4.9.2 (the neutral baryon rate is ignored here), the average semileptonic branching ratio for the charmed particles

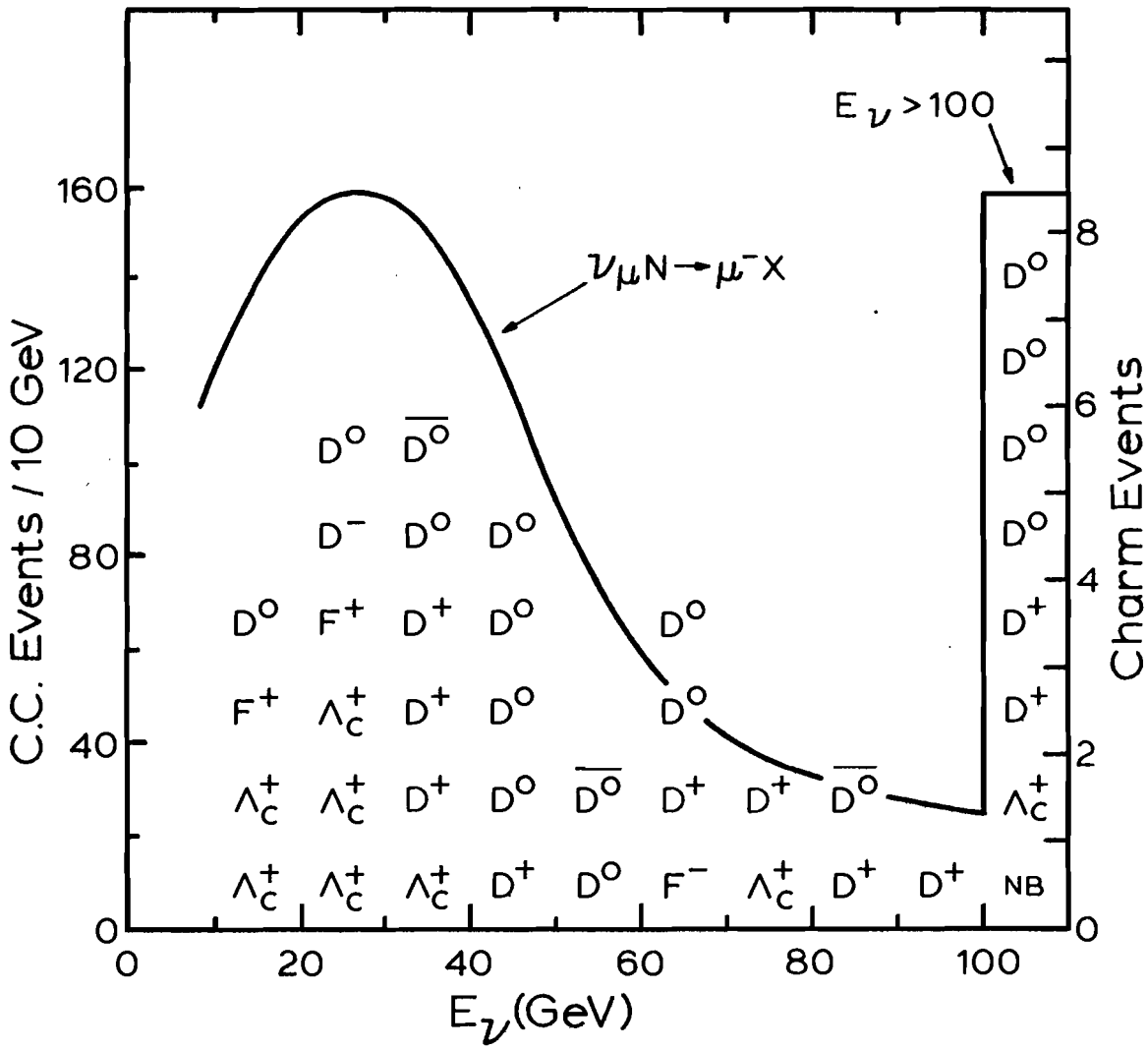

Figure 4-1: Energy spectrum of well identified single charm events. The smooth curve is the energy spectrum of found charged current ν_μ interactions, corrected for energy resolution and muon acceptance (from Fig. 3.7).

Table 4-1: Mean neutrino energies of charm events. The weighted $\langle E_\nu \rangle$ is calculated with each charm event weighted by its event weight (see Sec. 3.12.2 and Appendix II). The average systematic uncertainty in the charm event energies is ~5 GeV, but the accuracy of the mean energy measurement is dominated by the statistical uncertainty (the RMS widths of the energy distributions are ~60 GeV).

Type of events	Number of events	Unweighted $\langle E_\nu \rangle$	Weighted $\langle E_\nu \rangle$	Accuracy
Charm	38	66 GeV	73 GeV	±10 GeV
C^+ excluded	35	68	75	11
$D^+ + D^o$	24	79	85	13
Anti-charm	5	55	56	30

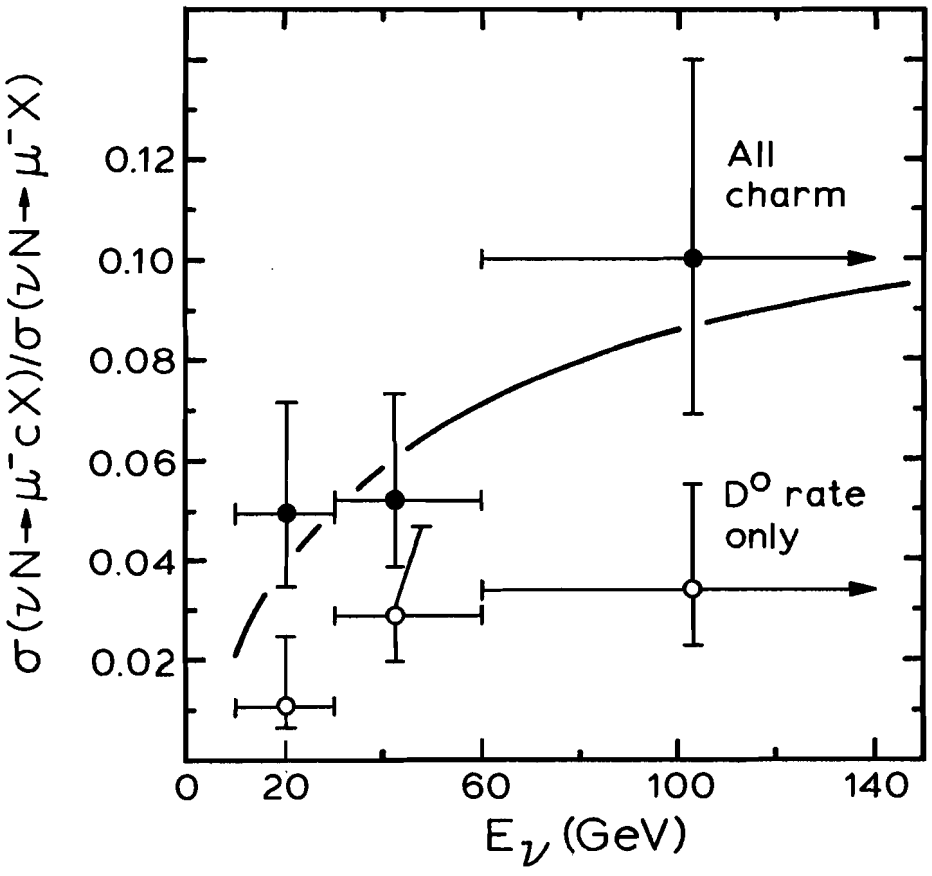

Figure 4-2: Energy dependence of the ν_μ charged current single charm production cross section. The smooth curve is a prediction by Campbell et al. [145].

produced is

$$\langle B.R.(c\rightarrow \ell X)\rangle = 9\pm 3\%.$$

This average is for all energies. Because the fraction of Λ_c^+ (and possibly F^+) decreases with increasing E_ν, the average semileptonic branching ratio increases with energy. (From the E-531 data, $\langle B.R.(c\rightarrow \ell X)\rangle$ ~5% for $10<E_\nu<30$ GeV, ~9% for $30<E_\nu<60$ GeV, and ~12% for $E_\nu>60$ GeV.)

Figure 4-3 shows the E-531 charm production data and μ^-e^+ and corrected $\mu^-\mu^+$ data. (Other dilepton experiments [74] with very low statistics or uncorrected rates are not shown.) All the data are clearly consistent, except possibly at low energies (<30GeV) where the charm production rate and average semileptonic branching ratio may be changing too much for easy comparison of the data. The uncertainties for all the measurements are primarily statistical (from $\lesssim$100 events), except for the very beautiful results from the CDHSB experiment which has ~11000 $\mu^-\mu^+$ (and ~3500 $\mu^+\mu^-$) events. The errors on the CDHSB data are dominated by uncertainties in the charm fragmentation function; there is further uncertainty (not included in the error bars in the figure), because they assume all charmed particles produced are D mesons. This assumption is based on the E-531 observation that D meson production is dominant for $E_\nu>30$ GeV. (The E-531 D^+/D^o ratio (Sec. 4.9.1) is also used to calculate $\langle B.R.(c\rightarrow \mu X)\rangle$, for their calculations of $U_{cd}^2/|U_{cs}|^2$ and $2S/(\bar{U}+\bar{D})$.)

4.1.2 Limit to Charm-Changing Neutral Currents

All the observed single charm events are consistent with charged current charm production, but the primary muon is not identified in two events. These two events set an upper limit to charm-changing neutral current production of

$$\frac{\sigma(\nu N\rightarrow \nu c X)}{\sigma(\nu N\rightarrow \nu X)} < 3\tfrac{1}{2}\% \quad (90\%\ \text{C.L.})$$

This value for the limit is conservative. The primary muon is expected to

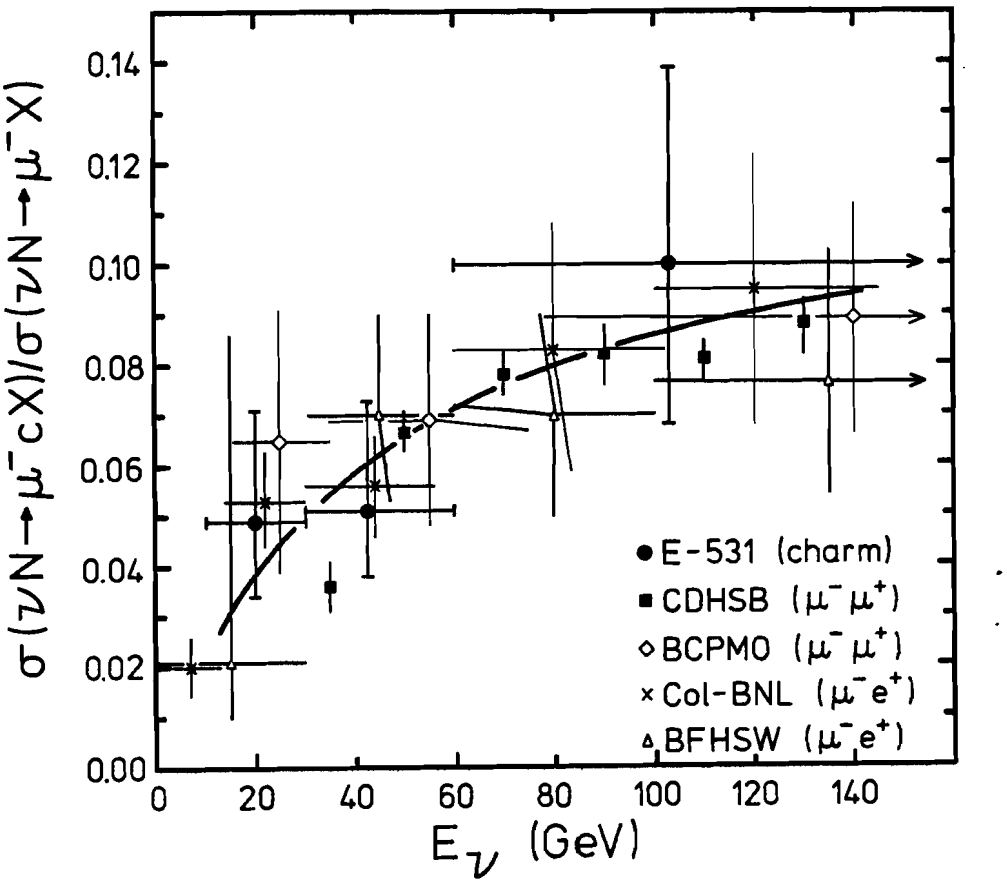

Figure 4-3: Comparison of opposite sign dilepton data and E-531 charm data. The dilepton production rates have been uniformly scaled by a factor of 10, (i.e. $\langle B.R.(c \to \ell X) \rangle = 10\%$, ℓ = e or μ). The CDHSB (massive iron detector) data are for $P_\mu > 5$ GeV/c and $E_\nu > 30$ GeV [20], the BCMPO (Gargamelle+EMI) data are for $P_\mu > 2$ GeV/c [122]; both sets of $\mu^-\mu^+$ data are corrected for muon acceptance, missing energy, background, and slow rescaling. The Col-BNL (Fermilab 15' Ne-H_2) [123] and BFHSW (Fermilab 15' H_2, EMI, $P_\mu > 4$ GeV) [124] data are for $P_e > 0.3$ GeV/c and are corrected for backgrounds and efficiencies.

be not identified in 10% of charged current charm production events, i.e. 4 events in the E-531 data sample. If these 4 expected charged current events without identified muons are subtracted from the 2 observed events without muons, then the above limit becomes 2%. (Such low statistics background subtractions are somewhat risky, so I prefer to quote the larger limit.)

This limit to charm changing neutral current neutrino interactions is comparable to previous upper limits from experiments that search for muons from charm decays in neutral current interactions (<2.6% for $\nu_\mu N \to \nu_\mu c$ [125] and <4% for $\bar{\nu}_\mu N \to \bar{\nu}_\mu \bar{c}$ [126]). Antineutrino data are, however, intrinsically 9 times more sensitive to the strength of any right-handed charm changing neutral current [127], so the $\bar{\nu}_\mu$ experiment [126] gives a much more stingent limit to the coupling strength than this experiment.

4.2 Charm Pair Production

4.2.1 An Observation of Charm Pair Production by Neutrinos

We have found one event in which a $D^o\bar{D}^o$ pair is produced. This event is the first direct observation of a pair of charmed particles produced in a neutrino interaction.

The D^o and $\bar{D}^o$ have momenta of 13 and 48 GeV/c, and the $D^o\bar{D}^o$ system has an invariant mass of 4.7±0.1 GeV. The charm pair are almost exclusively produced, carrying most ($90\pm^{5}_{10}$%) of the event's total visible energy of 68±8 GeV. No primary muon is identified, and this one event corresponds to a neutral current charm pair production rate of

$$\frac{\sigma(\nu N \to c\bar{c}X)}{\sigma(\nu N \to \nu X)} = 0.6\pm^{1.5}_{0.3}\%$$

(Note: The small antneutrino sample is combined with the neutrino data for all the the results of Secs. 4.2-4.4, e.g. "$\nu \to c$" includes $\bar{\nu} \to \bar{c}$.)

We should identify the primary muon in ~90% of any C.C. charm pair

events (this estimate is insensitive to the mass threshold behavior of the production process, see Fig. 3-8), but if this event is a charged current interaction then the production rate is

$$\frac{\sigma(\nu N \to \mu c\bar{c}X)}{\sigma(\nu N \to \mu X)} = 0.16^{+0.4}_{-0.07}\% \quad .$$

If this event is a charged current interaction, one of the charged particles from the interaction vertex must be the primary muon. All these charged particles have low momenta ($P \lesssim 3$ GeV/c), so if this is a charged current event it must have very high y ($E_H/E_\nu \gtrsim 0.97$).

The rate of charm pair production relative to single charmed particle production is given by

$$\frac{\sigma(\nu N \to c\bar{c}X)}{\sigma(\nu N \to cX)} = \varepsilon_{c\bar{c}/c} \frac{(N_{c\bar{c}} - B_{c\bar{c}})}{(N_c - B_c)} = 2.4^{+5.6}_{-0.8}\%$$

where $N_{c\bar{c}}=1$ and $N_c=43$ are the number of charm pair and single charm events, and $\varepsilon_{c\bar{c}/c}=1.04$ is the relative efficiency for finding both charmed decays in a $c\bar{c}$ event compared to the efficiency for finding the single decay in a single charm (c) event (Sec. 3.12.3). $B_{c\bar{c}}=0.04$ and $B_c=1$ are the backgrounds to charm pair and single charm decays (see Sec. 3.10); $B_{c\bar{c}}$ is given by $B_c \cdot N_c/1248$ (1248 is the total number of found neutrino interactions). The relative production rate is a useful number because the efficiencies and backgrounds (and possibly some kinematic threshold effects) tend to cancel out in the ratio.

4.2.2 Limit to Charged Current Charm Pair Production

A limit to the ratio of charged current pair to single charm production is also interesting, especially with respect to observed same-sign dilepton data (Sec. 4.5). A total of 41 events with a single charmed and an identified primary muon have been found, but no identified charged current pair production events are seen. This sets a limit

$$\frac{\sigma(\nu N \to c\bar{c}X\mu)}{\sigma(\nu N \to Xc\mu)} < 6\% \qquad (90\%\ \text{C.L.})$$

or

$$\frac{\sigma(\nu N \to c\bar{c}X\mu)}{\sigma(\nu N \to X\mu)} < 0.004 \qquad (90\% \text{ C.L.})$$

Other interesting possible processes that we do not see are direct (not part of a $c\bar{c}$ pair) "wrong sign" charm production or beauty production.

4.3 Limit to Wrong-Sign Charm Production

A "wrong-sign" charm event is a charged current charm event in which both the primary muon and the charmed quark have the same sign (e.g. $\nu_\mu N \to D^- \mu^- X$, the D^- is the same sign as the μ^-). This is opposed to "right-sign" charm production (Sec. 4.1) where the primary muon and the charmed quark have opposite signs. Wrong-sign events might be incompletely reconstucted charm pair events or beauty events,

$$\nu_\mu N \to \mu^- (c)\bar{c}X \qquad (c \text{ not seen})$$

$$\nu_\mu N \to \mu^- (\bar{b})X \qquad (\bar{b} \text{ decay not seen}) \ ,$$
$$\quad \downarrow \to \bar{c}$$

or they might have a new and unforseen origin.

No wrong-sign charm events were observed in this experiment. It is not always possible to distinguish charm from anti-charm on a decay by decay basis, and the probability of mistakenly identifying a wrong-sign event as a right-sign event is ~20%. This is estimated by trying to fit our right-sign decays as wrong-sign decays. Charged charm and anti-charm decays have opposite electric charges, and in all but two of our charged decays, the charge is measured either directly, or for a few Λ_c^+, by identifying decay secondaries as protons or Λ^o's. Six D^o decays have possible, albeit not favoured, wrong-sign hypotheses: $D^o \to K^o X$ decays (3 events) can always be fit as $\bar{D}^o \to \bar{K}^o X$ decays, and $\bar{D}^o \to K^+ X$ modes cannot be

excluded for 3 fitted $D^0 \to K^- X$ decays.

The limit to wrong-sign charm production is

$$\frac{\sigma(\nu N \to \bar{c}\mu^- X)}{\sigma(\nu N \to \mu^- X)} < 0.005 \qquad (90\% \text{ C.L.})$$

The wrong-sign charm decay finding efficiency is assumed to be the same as the observed right-sign charm finding efficiency; this assumption may not be true, but the limit is not too sensitive to differences between wrong-sign and right-sign charm. (If wrong-sign events produce only D mesons, then the limit would be 0.006 instead of 0.005.) The limit to the ratio of wrong/right sign charm production is

$$\frac{\sigma(\nu N \to \bar{c}\mu^- X)}{\sigma(\nu N \to c\mu^- X)} < 8\% \qquad (90\% \text{ C.L.})$$

4.4 Limits to Beauty Production

4.4.1 Direct Search

A beauty decay candidate would be one that is too heavy to be a D, F, or Λ_c^+ charmed particle. This means that all decay hypotheses for a beauty candidate must have masses >2.1 GeV/c^2 (90% C.L.) for a meson and >2.3 GeV/c^2 for a baryon. This criterion will exclude most charmed particles, while accepting $\gtrsim$90% of real beauty decays. This acceptance is calculated by scaling up from from our charm decays. The lowest beauty meson mass is thought to be 5.2 GeV/c^2 [128], so a 2.1-2.3 GeV/c^2 cut on beauty decays corresponds proportionally to a 850-1000 MeV/c^2 cut on charm decays. Even if all charged particles from the charm decay candidates are assumed to be pions, and all observed neutral secondaries are ignored, assuming a missing massless neutrino, then only 5 of the 45 charm candidates have a minimum mass less than 1000 MeV/c^2, and only one has a minimum mass less than 850 MeV/c^2.

The finding efficiency for beauty decays is calculated as a function of the beauty lifetime, τ_b, using a beauty momentum spectrum calculated

from the charm event energy spectrum and a gaussian fragmentation function [129]. The unknown $B^{\pm}$ kink rate is assumed to be 10%, and the charged multiprong decay rate for neutral beauty particles is assumed to be 100%. (These are reasonable assumptions based on the very large beauty mass, and corroborated by the very large value, 5.8±0.3 particles [130], measured for the mean charged multiplicity of B-meson decays.) Sequential b→c→u decays would be more easily found than direct b→u decays, because there are two decays to be found, so the beauty finding efficiency also depends on the branching ratio for b→c. (The efficiency for very short beauty decays is much enhanced because charm events are so carefully measured.) From the limits to U_{ub} (Table 1-4), and from experimental measurements [71], it is expected that B.R.(b→c)~100%.

The limit to beauty production is shown in Figure 4-4 as a function of the beauty lifetime and branching ratio to charm. For a typically expected beauty lifetime of $\tau_b \sim 10^{-13}$s [131], and B.R.(b→c)=100%,

$$\frac{\sigma(\nu N \to b\mu X)}{\sigma(\nu N \to c\mu X)} < 5\tfrac{1}{2}\% \qquad (90\%\ \text{C.L.})$$

The limit increases to 7% if $\tau_b = 10^{-14}$s or B.R.(b→c) = 0%. The limit curves are not very sensitive to the energy spectrum or fragmentation function for beauty; a harder (softer) beauty momentum spectrum will only shift proportionately the curves in Fig. 4-4 to the left (right).

4.4.2 Wrong-Sign Limit to Beauty Production

Neutrinos are expected (Fig. 1-14) to produce anti-beauty, which will decay into anti-charm, so beauty production is a process that can produce wrong-sign charm. Thus the limit to wrong-sign charm production (Sec. 4.3) is also a limit to ($\nu_\mu N \to \mu^- \bar{b} X$) production, the limits being exactly equivalent if B.R.(b→c) = 100%. This limit is independent of the beauty lifetime, so

$$\frac{\sigma(\nu N \to \bar{b}\mu X)}{\sigma(\nu N \to c\mu X)} < 8\% \qquad (90\%\ \text{C.L.})$$

for any value of τ_b.

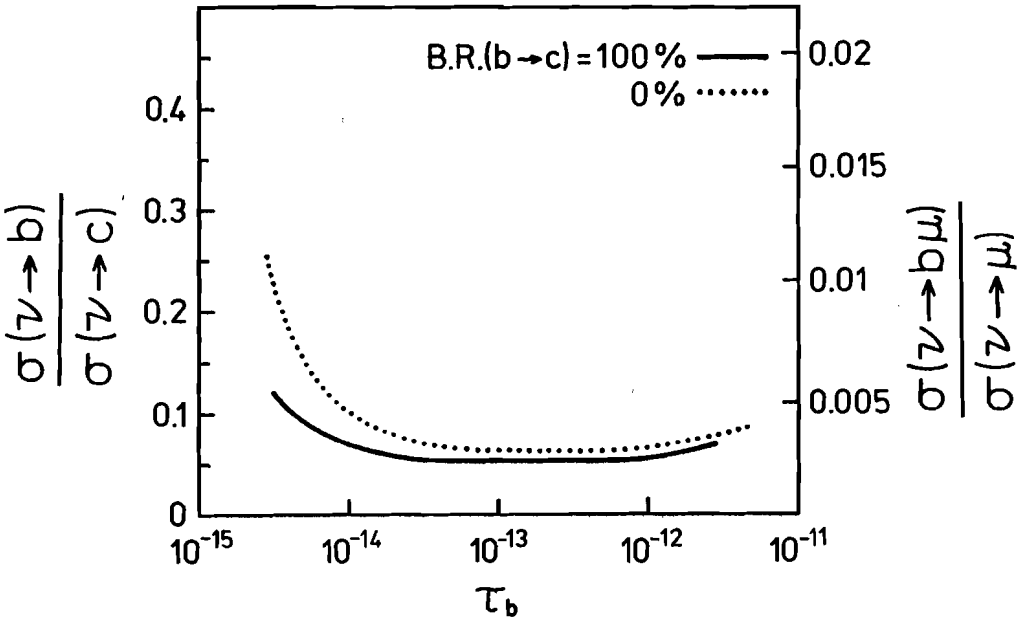

Figure 4-4: Limits to beauty production as a function of the beauty lifetime (τ_b). The experimental upper limit to the beauty lifetime is $\tau_s << 1.4 \times 10^{-12}$s (95% C.L.) [73]; the expected value is $\sim 10^{-14} - 10^{-13}$s [146].

4.5 Charm and Same-sign Dileptons

Charged current production of $c\bar{c}$ pairs, wrong-sign charm, or beauty are all possible sources of same-sign dilepton events.

$$\nu_\mu N \rightarrow X c \bar{c} \mu^-, \quad \bar{c} \downarrow\rightarrow e^- \text{ or } \mu^-$$

$$\nu_\mu N \rightarrow X \bar{c} \mu^-, \quad \bar{c} \downarrow\rightarrow e^- \text{ or } \mu^-$$

$$\nu_\mu N \rightarrow X \bar{b} \mu^-, \quad \bar{b} \downarrow\rightarrow e^- \text{ or } \mu^-$$

The existence of same-sign dilepton production by neutrinos is now well established [132], but their production mechanism is not yet known. This experiment (E-531) has the potential to observe the parent production process, or by excluding the above three production processes, to indicate that the dilepton data have an unexpected origin.

The observed rates, $\sigma(\mu^\mp \ell^\mp)/\sigma(\mu^\mp)$, of same-sign dilepton production vary from 10^{-5} to 10^{-3}, depending on E_ν, on the lepton momentum cuts, and on the experiment. The ratio of same-sign to opposite-sign production is, however, less sensitive to the experimental conditions, and $\sigma(\nu \rightarrow \mu^\mp \ell^\mp)/\sigma(\nu \rightarrow \mu^\mp \ell^\pm)$ is $\sim 10 \pm 6\%$.

Comparison of the E-531 data with the same-sign dilepton data is even more difficult than the comparison with opposite-sign data (Fig. 4-3). There is very little same-sign μe data, and most same-sign $\mu\mu$ data have quite strict muon momentum cuts. Table 4-2 shows measured same-sign dilepton rates from experiments with relatively weak lepton momenta cuts and in wide-band beams similar to that used by this experiment. The measured ratios of same-sign to opposite sign dileptons are typically $\sim 15\%$ - about twice as large as the limits set by this experiment to various same-sign dilepton production processes. The uncertainties in the dilepton ratios are, however, quite large, and the effects of lepton momentum cuts may also be large, so the dilepton rates and the E-531 limits are probably consistent.

Instead of directly comparing the E-531 limits to the same-sign dilepton rates, an alternative method of comparison is to use a phenomenological production model that describes dilepton production from

Table 4-2: Wide-band beam same-sign dilepton rates with minimal lepton momentum cuts.

$\nu_\mu N \to X\mu^-e^-$	$P_\mu>10$, $2<P_e<10$ GeV/c	$\frac{\mu^-e^-}{\mu^-e^+} = 16\pm8\%$	[147]
$\bar{\nu}_\mu N \to X\mu^+e^+$	$P_\mu>4$, $P_e>0.4$ GeV/c	$\frac{\mu^+e^+}{\mu^+e^-} = 13\pm^{15}_{9}\%$	[148]
$\bar{\nu}_\mu N \to X\mu^+e^+$	$\langle E_\nu\rangle = 52\pm20$ GeV *		
$\bar{\nu}_\mu N \to X\mu^+$	$\langle E_\nu\rangle = 32$ GeV		
$\bar{\nu}_\mu N \to X\mu^+\mu^+$	$P_\mu>4$ GeV/c	$\frac{\mu^\pm\mu^\pm}{\mu^\mp\mu^\pm} = 16\pm3(\pm3)\%$ *	[149]
$\bar{\nu}_\mu N \to X\mu^-\mu^-$	$\langle E_{vis}\rangle = 95\pm7.0$ GeV		
$\bar{\nu}_\mu N \to X\mu^-\mu^+$	$= 98\pm3.5$ GeV	$\frac{\mu^-\mu^-}{\mu^-\mu^+} = 14\pm4(\pm3)\%$	
$\bar{\nu}_\mu N \to X\mu^-$	$= 60\pm2.2$ GeV		
$\bar{\nu}_\mu N \to X\mu^+\mu^+$	$\langle E_{vis}\rangle = 73\pm17$ GeV		
$\bar{\nu}_\mu N \to X\mu^+\mu^-$	$= 78\pm4$ GeV	$\frac{\mu^+\mu^+}{\mu^+\mu^-} = 18\pm6(\pm3)\%$	
$\bar{\nu}_\mu N \to X\mu^+$	$= 46\pm1$ GeV		

* I have calculated this number from information provided in the reference - the value is not explicitly given in the reference.

charm. For example, Godpole and Roy [133] assume that 1% of all neutrino interactions produce $c\bar{c}$ pairs. A Suzuki-like [134] fragmentation function and a charm semileptonic branching ratio of 10% are then used to calculate the rate of same-sign dilepton production as a function of E_ν. After appropriate momentum cuts, this phenomenological calculation is in agreement with most same-sign dimuon data. Integrated over the E-531 energy spectrum, the Godpole-Roy model predicts that 0.6% of all charged current neutrino interactions should produce a $c\bar{c}$ pair. This calculated rate is only slightly larger than the E-531 upper limit of 0.4%.

A two- or three-fold increase in the E-531 sensitivity is necessary to be sure of either detecting the charm production process responsible for same-sign dileptons, or to rule out charm production as the source.

4.6 Bjorken X Distribution

Figure 4-5 shows the observed and predicted Bjorken x distribution for E-531 charged current events with well identified (MUFB) muons. Because antineutrinos often interact with ocean antiquarks, which carry only a small fraction of the nucleon momentum, the μ^+ data is concentrated at smaller x than the μ^- data.

Figure 4-6 shows the observed Bjorken x distribution for the charm and anti-charm events; also shown are x distributions for charm production calculated for two values of the fraction of strange quarks in the nucleon, using the parameterization of Campbell et al. [48]. Because s quarks are ocean quarks (small x values), and d quarks are usually valence quarks (slightly larger x values), the shape of the observed x distribution depends on the ratio of s to d quarks in the nucleon. If we assume (following Campbell [135]) that the strange quark x distribution is of the form $s(x) \propto \frac{1}{x}(1-x)^\beta$, with $\beta=7$, then the observed x distribution of the charm and anti-charm events gives

$$2S/(Q+\bar{Q}) = 0.077^{+0.125}_{-0.047}$$

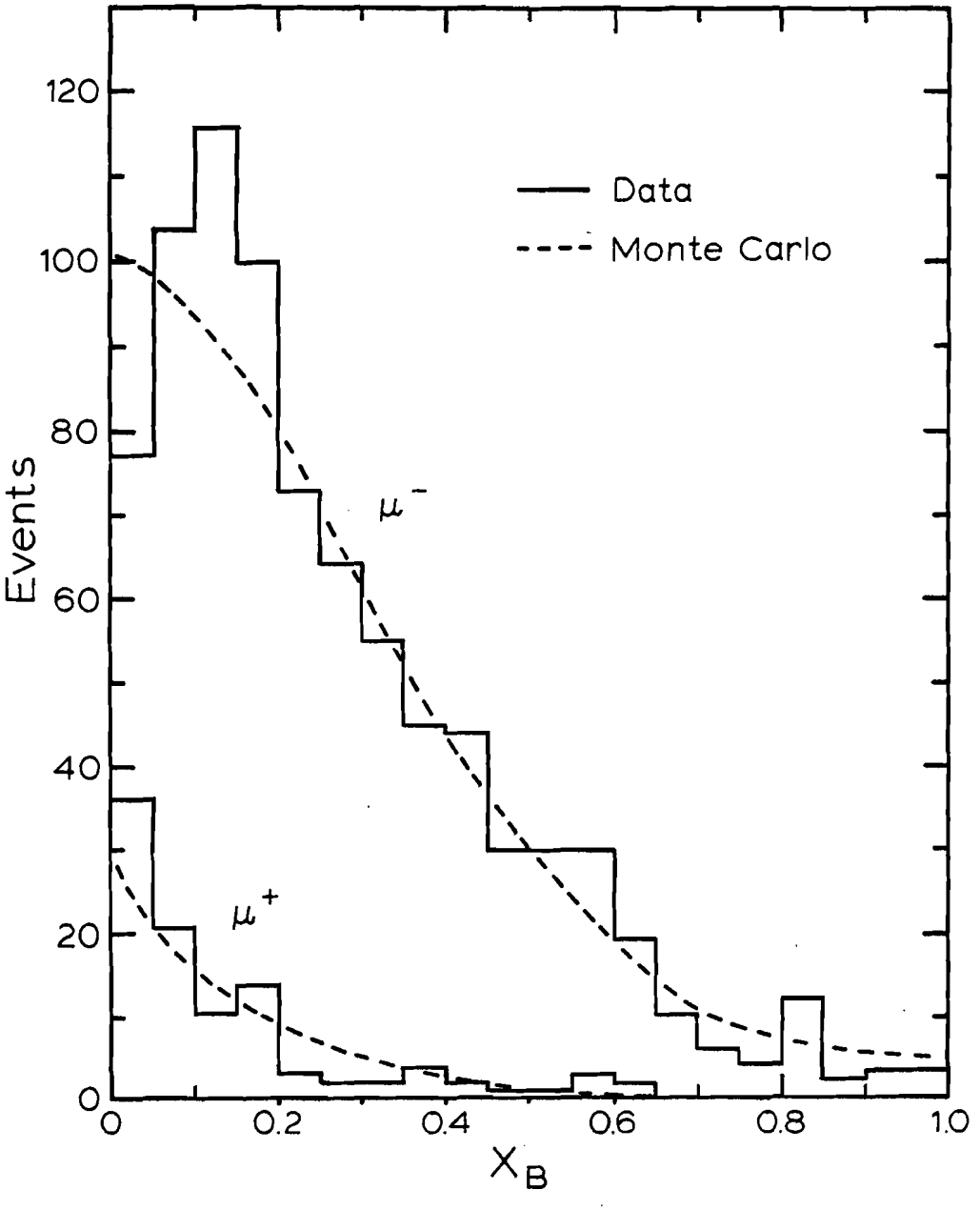

Figure 4-5: Bjorken X distributions of neutrino interactions with identified (MUFB) muons. The solid histograms are data (929 μ^- and 122 μ^+ events); the broken curves are Monte Carlo predictions (resolution and acceptance folded in).

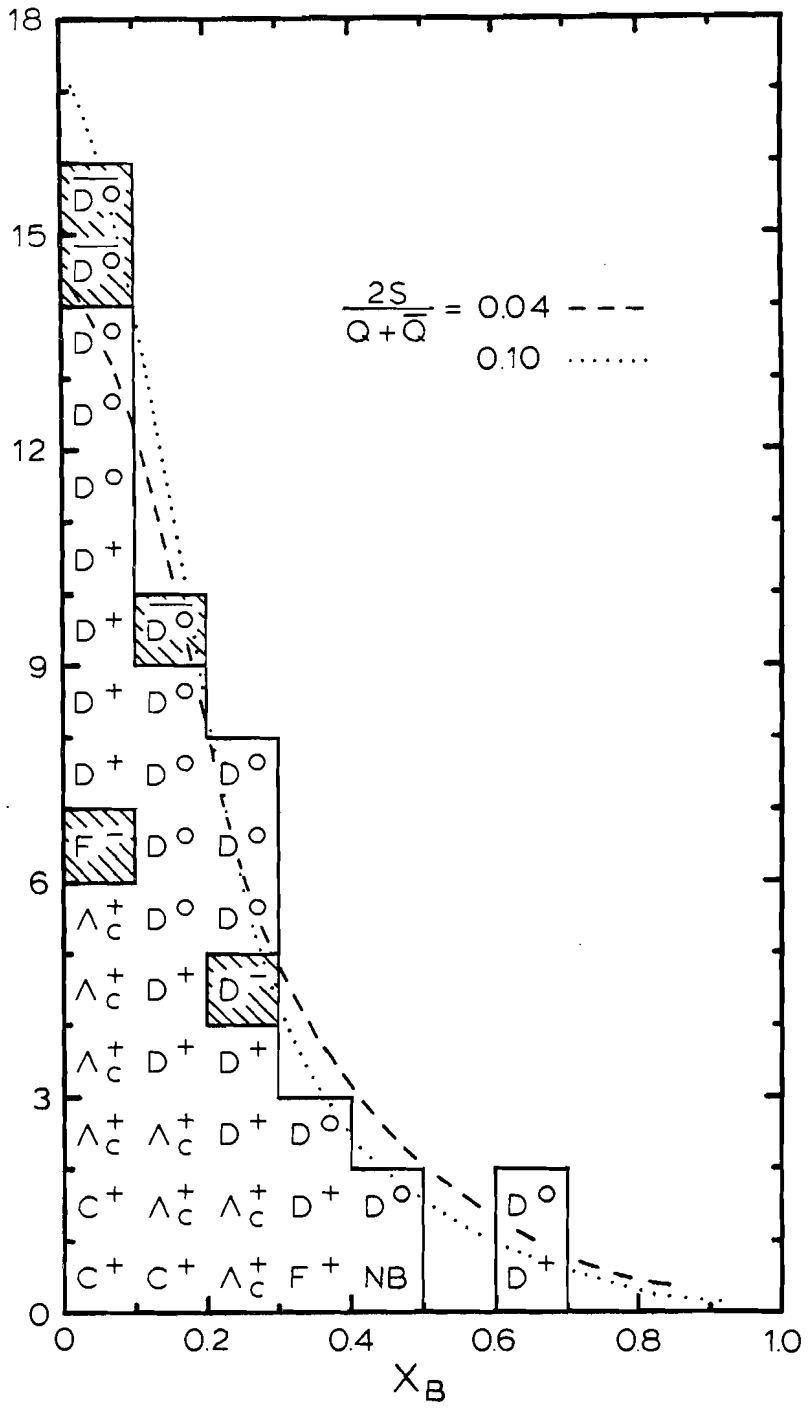

Figure 4-6: Bjorken X distributions of the charm events with identified primary muons. The dashed curve is the expected distribution (acceptance and resolution folded in) for charged current charm production from nucleons with a strange quark fraction of 0.04. The expected distribution is similar for a wide range of strange quark fractions; the dotted curve is the expected distribution for a strange quark fraction of 0.1. The average experimental resolution in X is $\langle\sigma(x)/x\rangle$=0.3. The dotted curve shows that the observed distribution changes little even if the strange ocean is as large as 0.1.

for the fraction of strange quarks in the nucleon (see Sec. 1.4).

Since the x distribution for anti-charm production essentially depends only on s(x), not d(x), it can in principle be determined using the anti-charm data. With only 5 anti-charm events, however, β is poorly determined:

$$\beta = 9^{\infty}_{\pm 4}$$

If β=7 is not assumed, then the strange quark fraction is very poorly determined:

$$2S/(Q+\bar{Q}) = 0.14^{0.6}_{\pm 0.12}$$

This experiment clearly has too few charm events to extract the strange ocean from the x distribution. The observed distribution does, however, provide an important check for strange ocean results from statistically more powerful dilepton experiments: the E-531 distribution indicates that there are no large changes in the types of charmed particles produced as a function of x. (For example, D mesons are 14 out of 23 events below x=0.2, and 14 of 20 above 0.2.) If the relative charm particle production ratios do not change as a function of x, then the average charm semileptonic branching ratio will not change, and the true x distribution of charm can be extracted from opposite sign dilepton data.

4.7 Y Distribution

The y distributions for neutrino charm production and antineutrino anti-charm production should be flat for left-handed weak currents and of the form $(1-y)^2$ for right-handed currents. All known charged weak currents are left-handed, and opposite-sign dimuon data [20] set an upper limit of 7% to the strength (relative to the left-handed current) of any right-handed weak coupling of the charmed quark, so charged current charm production events are expected to have a flat y

distribution.

This experiment could not always identify low momentum muons, and neutrino interactions with little hadronic energy would not always trigger the detector or be reconstructed. The y distribution of E-531 events with a well identified (MUFB) μ^- is shown in Figure 4-7. Losses due to trigger/reconstruction inefficiency (at small y) and losses from muon acceptance (at large y) are obvious, but the shape of the distribution is in good agreement with that expected from the Monte Carlo simulation. (The Monte Carlo simulation also includes the effects of hadron energy and muon momentum resolution that distort (reduce) the distribution near y=0 and y=1.)

Figure 4-8 shows the y distribution of events with charm or anti-charm and an identified primary muon. Also shown is the distribution expected for Standard Model left-handed (flat y) charm production [48], integrated over the E-531 E_ν spectrum, and with resolutions and acceptances folded in. The observed spectrum is in good agreement with the Standard Model prediction.

4.8 Q^2 and W

In Figure 4-9, the observed Q^2 distribution for reconstructed events with a well identified (MUFB) μ^- is shown. Also shown are the (normalized) Monte Carlo predictions for the observed Q^2 distribution and the true Q^2 distribution for all charged current ν_μ interactions. This last curve is also shown in Figure 4-10, for comparison with the Q^2 spectrum observed for events with single charmed particle production.

Figures 4-11 and 4-12 show the total hadronic mass (W) spectra for all events and for charm events.

The charmed baryons appear to be predominantly produced at smaller values of W and Q^2 than the charmed mesons.

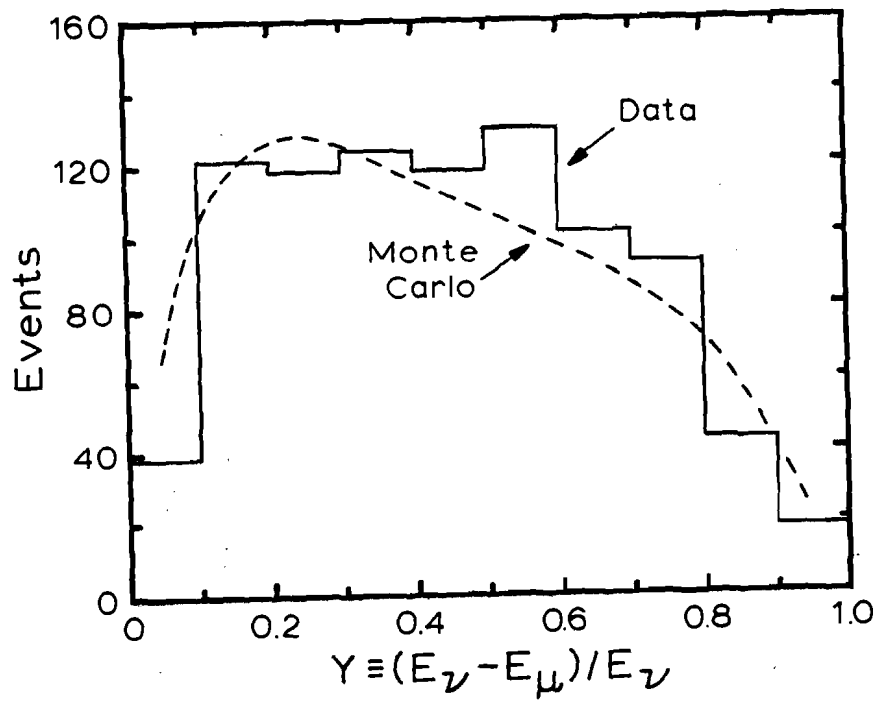

Figure 4-7: Observed and expected Y distributions for charged current ν_μ interactions with identified (MUFB) primary muons.

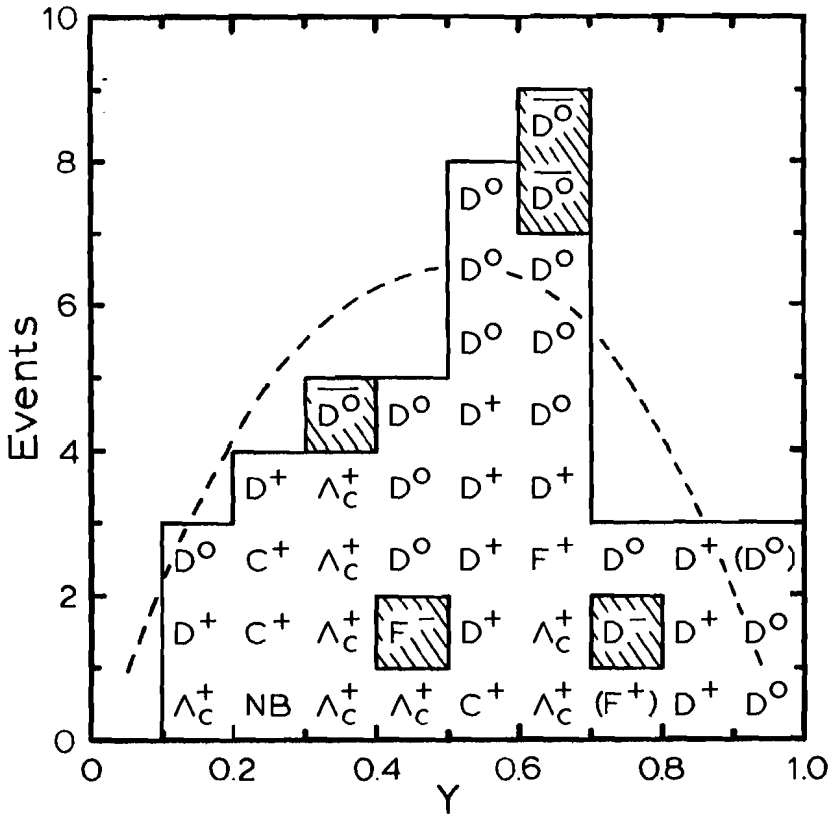

Figure 4-8: Y distribution for charm events with identified primary muons. A kinematic threshold (due to the large mass of the charmed quark) suppresses charm production at small y; the combination of this threshold with muon acceptance and experimental resolution gives the expected distribution (dashed curve) a somewhat rounded appearance, even though the intrinsic charm production y dependence is flat.

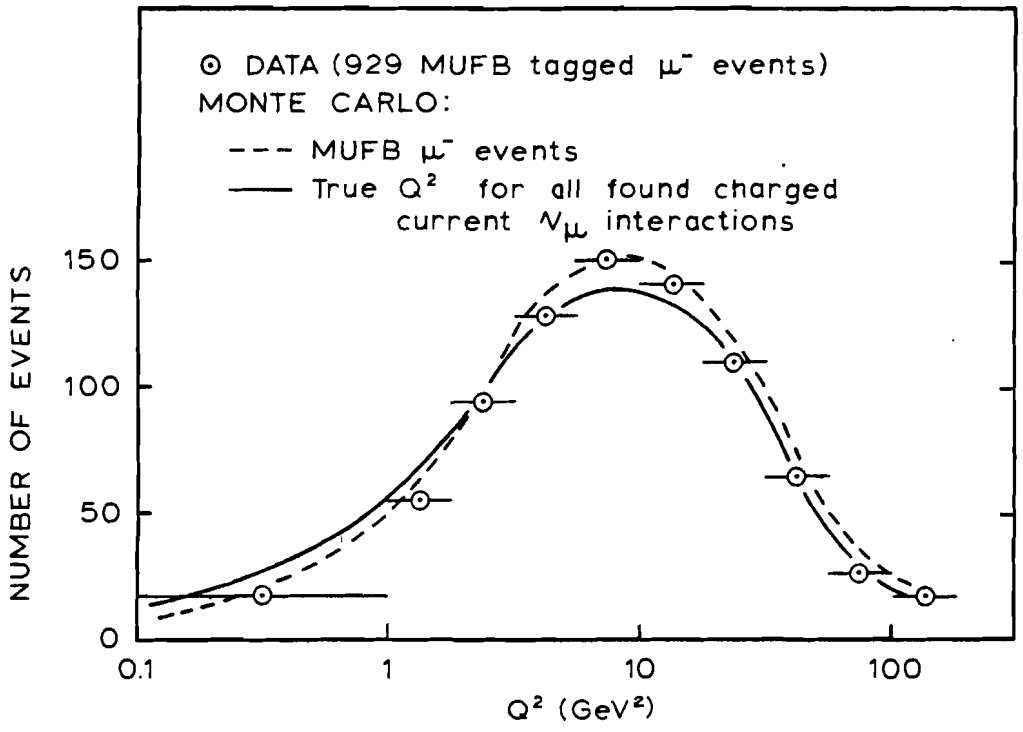

Figure 4-9: Q^2 for charged current ν_μ interactions.

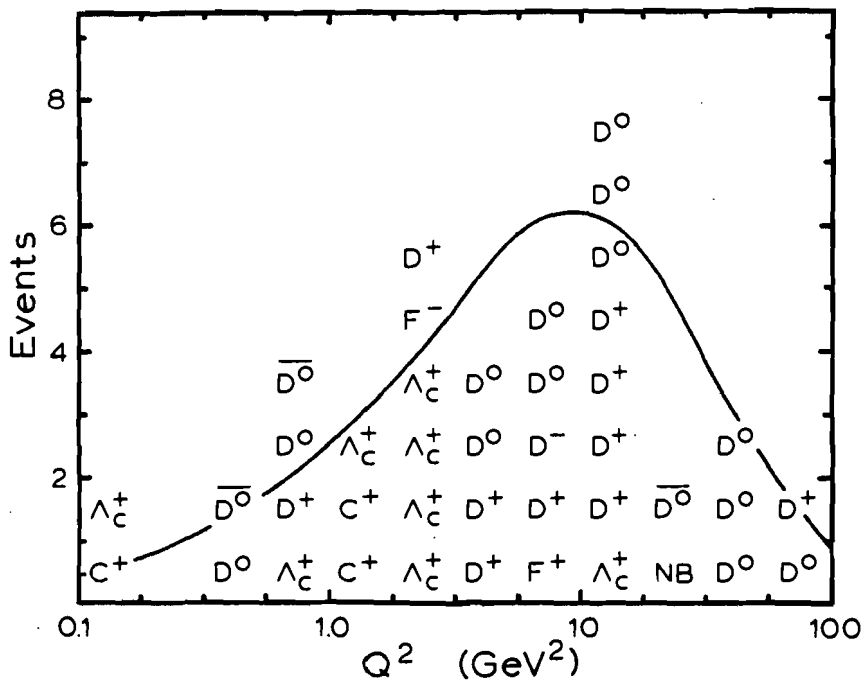

Figure 4-10: Q^2 for charm events with identified primary muons. The smooth curve is the expected true Q^2 distribution for all found charged current ν_μ interactions (from Fig. 4-9).

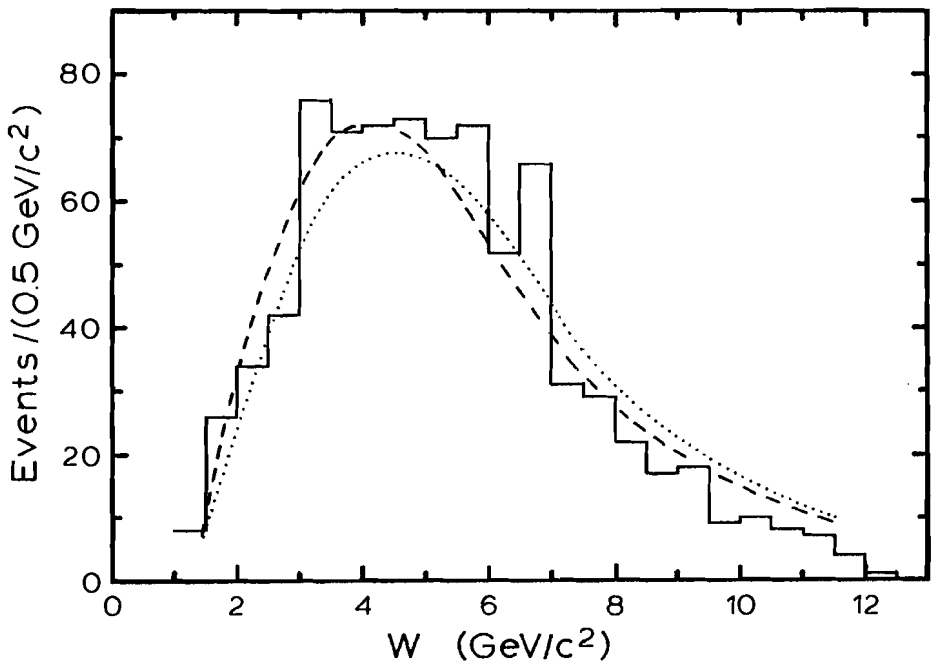

Figure 4-11: Total hadronic mass (W) of charged current ν_μ interactions. The histogram is data (929 events with MUFB muons); the dashed curve is the Monte Carlo prediction for the observed mass in such events. The dotted curve is the Monte Carlo prediction for the true W distribution for all found charged current ν_μ interactions.

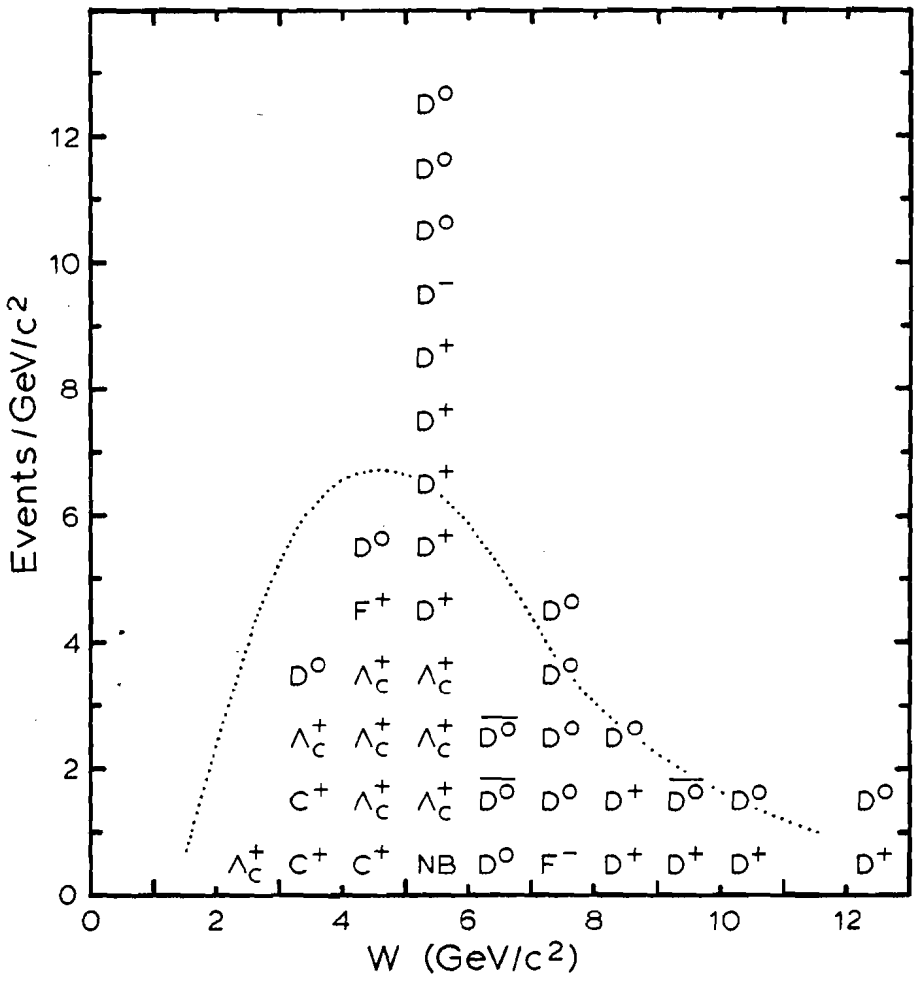

Figure 4-12: Total hadronic mass (W) distribution for charm events with identified primary muons. The dotted curve is the true W distribution for all found charged current ν_μ interactions (from Fig. 4-11).

4.9 Relative Charmed Particle Production Rates

4.9.1 Charge Independence and Spin Statistics

The simplest view of charm production is that there are no dynamical differences in the production of the various charmed hadrons. Thus the relative rates for producing D^{*o}, D^o, D^{*+}, and D^+ mesons, based on charge independence and spin statistics alone, are expected to be 3:1:3:1.

The branching ratios for D^* decays are [136]

$$\begin{aligned} D^{*o} &\to D^o(\gamma,\pi^o) = 100\% \\ D^{*+} &\to D^o\pi^+ \quad\quad = 64\pm11\% \quad (\approx 2/3) \\ &\to D^+(\gamma,\pi^o) = 36\pm11\% \quad (\approx 1/3) \end{aligned}$$

Since D^{*o} mesons decay exclusively to D^o's, and the branching ratio for $D^{*+}\to D^o\pi^+$ is ~2/3 [6], ~1/3 of all final state D^o mesons should come from charged D^* decays, and the final state D^+/D^o ratio should also be ~1/3. If, however, the production rates are independent of the particle spins, i.e. $D^{*o}:D^o:D^{*+}:D^+ = 1:1:1:1$, then ~1/4 of final state D^o mesons should come from charged D^* decays, and the final state D^+/D^o ratio should be ~1/2.

In this experiment 19 D^o and $\bar{D}^o$ mesons have been observed. Once a D^o decay is found and reconstructed, any $D^{*+}\to D^o\pi^+$ decay is reconstructed with ≈100% efficiency and negligible background. Figure 4-13 shows the $D^o\pi^+/\bar{D}^o\pi^-$ mass spectrum for the 19 found D^o's - the $D^{*\pm}$ signal is very distinct because the mass resolution is proportional to the very small D^{*+}-D^o mass difference. Six of the $D^o(\bar{D}^o)$'s come from $D^{*\pm}$ decays, so

$$\frac{\sigma(D^{*\pm}\to D^o(\bar{D}^o)\pi^\pm)}{\sigma(D^o(\bar{D}^o))} = \frac{6}{19} = 0.32\pm^{0.14}_{0.12} \quad ,$$

in agreement with the simple statistical model predictions. (There is a small correction to this fraction because D^o's from $D^{*\pm}$ decays are slightly easier to find than other D^o's - this is because the directions of the D^o and $\pi^\pm$ from a $D^{*\pm}$ decay are very close together (typically ~30 mr apart) and the D^o may be found while following out the $\pi^\pm$ from the primary vertex. This extra efficiency may reduce the above fraction

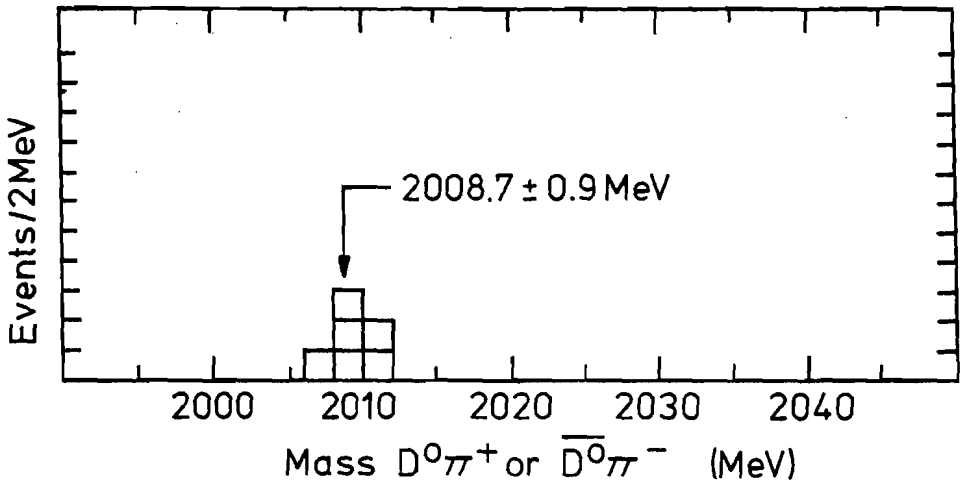

Figure 4-13: Histogram of $D^0\pi^+$ and $\bar{D}^0\pi^-$ masses (calculated for $m_{D^0} = 1863.1$ MeV/c^2). Except for the $D^{*\pm}$ mass peak, all $D^0\pi^+$ and $\bar{D}^0\pi^-$ combinations have masses greater than 2050 MeV/c^2.

by a amount $\lesssim 0.02$.)

Calculating the relative rates of $D^{\pm}$ to $D^{o}(\bar{D}^{o})$ production depends on the event finding and identification efficiencies, which are different for charged and neutral D's. The corrected $D^{\pm}/D^{o}(\bar{D}^{o})$ ratio can be calculated either using only the 9 multiprong $D^{\pm}$ decays and the $D^{\pm}$ kink branching ratio (from [137,113]), or using the 9 multiprong decays plus the 2 D^{+} kink decays corrected by our kink finding and identification efficiency - the two methods give the same answer within 4%. In either case, the multiprong $D^{\pm}$ and $D^{o}(\bar{D}^{o})$ decays are weighted (Sec. 3.12 to correct for detection efficiencies. Since most $D^{\pm}$ mesons cannot be unambiguously identified on an event by event basis (Sec. 3.8), 3 non-$D^{\pm}$ charm decays in the $D^{\pm}$ sample is a 1 standard deviation possibility; this possible error is included in the production rate uncertainties. The fully corrected $D^{\pm}/D^{o}(\bar{D}^{o})$ ratio is

$$\frac{\sigma(D^{\pm})}{\sigma(D^{o}(\bar{D}^{o}))} = 0.7 \pm^{0.45}_{0.35}$$

This ratio is larger than predicted ($\sim 1/3$) for $D^{*o}:D^{o}:D^{*+}:D^{+} = 3:1:3:1$, but the disagreement is not statistically significant. The ratio is consistent with the value of $\sim 1/2$ predicted for $D^{*o}:D^{o}:D^{*+}:D^{+} = 1:1:1:1$.

Both the measured fraction of $D^{*\pm} \rightarrow D^{o}(\bar{D}^{o})\pi^{\pm}$ decays and the measured $D^{\pm}/D^{o}(\bar{D}^{o})$ ratio are consistent with the simple statistical model predictions. The measurements are not, however, precise enough to measure the production ratio of vector and scalar D mesons; $D^{*o}:D^{o}:D^{*+}:D^{+}$ ratios of either 3:1:3:1 or 1:1:1:1 are consistent with the data.

The $D^{*\pm} \rightarrow D^{o}(\bar{D}^{o})\pi^{\pm}$ fraction and $D^{\pm}/D^{o}(\bar{D}^{o})$ ratio were calculated using all observed D mesons, irrespective of their sources, because statistical fragmentation models ignore the origin of the charm quark. This may be a good assumption for D mesons because they are not expected to be often produced by special processes (such as quasi-elastic baryon production or diffractive production) but, in general, relative rates can depend on the production mechanism. For example, global charge conservation may cause a slight increase in the D^{+} production rate relative to the D^{o} rate,

because the hadronic system in charged current ν_μ-emulsion interactions has an average charge of $\sim 1\frac{1}{2}$.

4.9.2 Charmed Particle Fractional Rates in $\nu_\mu N \to Xc\mu^-$ Interactions

Simple arguments do not predict the relative production rates for hadrons with different quark contents, but it is expected that different production processes and beams may produce different proportions of D's, F's, and charmed baryons. In determining relative production rates, we therefore consider only charged current ν_μ interactions producing single charmed particles. (This excludes the 5 single $\bar{\nu}_\mu$ anti-charm events and the $D^o\bar{D}^o$ charm pair.) The ν_μ charged current sample contains 14 D^o, 10 D^+ candidates, 2 well identified F^+ mesons, 8 Λ_c^+, the neutral charmed baryon candidate (NB), and the 3 low momentum ambiguous C^+ charm decay candidates. These raw yields must be corrected for efficiencies, kink and all-neutral decays, and background.

The corrected fractional rates are given in Table 4-3. The quoted uncertainties include possible systematic errors (in scanning and reconstuction efficiencies, particle identification, and background) as well as statistical error. The uncertainties are constrained by the requirement that the separate fractions must together add up to 100%.

The observed rates indicate that about 10% of the charmed mesons produced are strange charmed F mesons. If the neutral charmed baryon candidate is an A^o (csd) strange charmed baryon (see Ref. [8]), then this would be consistent with the expectation (Sec. 1.6.4) that the strange/non-strange ratio for charmed baryons should be comparable to the strange/non-strange ratio for charmed mesons.

Table 4-3: Fractional rates for ν_μ charged current production of single charmed particles. The total D meson fraction is $69\pm^{8}_{10}$%.

Particle	Raw Rate	Corrected Fraction
D^o	14	39 ± 11 %
D^+	10	30 ± 12 %
F^+	2 *	$7\pm^{9}_{5}$ %
Λ_c^+	8	$21\pm^{11}_{8}$ %
NB	1	$3\pm^{7}_{2.5}$ %

* One unconstrained kink has a very probable F^+ hypothesis and has a weight of 0.8 in calculating charm yields (see Sec. 3.11.3).

4.9.3 Quasi-elastic Charm Production

The fractional production rates of the charmed particles are primarily, but not completely, determined by the charmed quark fragmentation process. Some of the charmed particles are, for example, produced by "elastic" reactions in which charm production and fragmentation are inextricably intertwined.

One of the observed charmed baryons (event 610-4088) appears to be produced by the quasi-elastic reaction $\nu_\mu n \to \mu^- \Lambda_c^+$. Integrating the charged current ν_μ cross section over the E-531 E_ν spectrum, and weighting according to the average Λ_c^+ decay finding, reconstruction, and identification efficiency, we can calculate that a single found quasi-elastic event corresponds to a quasi-elastic cross section of $\left(4\pm^{8}_{1}(\text{stat.})\pm 1\tfrac{1}{2}(\text{sys.})\right)\times 10^{-40}\text{cm}^2/\text{nucleon}$ (e.g. if all 8 identified Λ_c^+'s came from quasi-elastic events, this would correspond to a total quasi-elastic cross section of $\sim 30\times 10^{-40}\text{cm}^2$.) The E-531 data are consistent with the range of expected quasi-elastic charmed baryon production cross sections [53] (see Sec. 1.5.2).

4.9.4 Nuclear Effects

The charmed particle production process may be affected by the large size of the emulsion nuclei. The average emulsion nucleus has a diameter of about 2 nuclear interaction lengths, so a charmed quark must traverse, on average, almost an interaction length of nuclear matter while exiting the production nucleus. The fragmentation of light quarks typically takes place on a length scale comparable to or longer than the nuclear diameter, and the fragmentation process may be altered by intranuclear affects [138]. The charm quark is much more massive than the light quarks, and the fragmentation length scale may be correspondingly much shorter (at equal energies) than the fragmentation scale for light quarks. The charmed hadron may form (especially at lower energies) before the charmed quark has left the target nucleus, and this charmed hadron

may interact in the nucleus producing more hadrons. It is possible, therefore, that the charmed particle production process may be altered by nuclear affects both during the fragmentation process and after the initial charmed hadron is formed.

4.10 Charm Momentum Distribution

The different charmed hadrons are not all produced with the same kinematic characteristics. Figure 4-14 shows the momentum distribution of the charm sample. The identified Λ_c^+ charmed baryons are produced with small lab momenta (<8.4 GeV/c), and no identified D mesons are observed below P=6.8 GeV/c. The mean momentum of the reconstructed charmed particles is $\langle P \rangle = 19 \pm 3$ GeV/c. The calculated acceptance shown in the figure is averaged over all the charmed particles; the shaded area indicates the difference in acceptance depending on whether low momentum ambiguous charmed decays (C^+) are included in the identified charm event sample.

4.11 Fragmentation Function

The fragmentation of quarks into hadrons is usually studied in terms of the fragmentation variable $Z \equiv E_c/(E_\nu - E_\mu)$, where E_c is the observed charmed hadron's energy. In the Breit frame, Z is the fraction of the original charm quark momentum carried by the charmed hadron. Figure 4-15 shows the distribution in Z of the single charm events.

The Z values displayed are those of the final state weakly decaying charmed particles. Most of these are expected to come from the decays of parent resonant states. These are not shown because, except for $D^{*+} \rightarrow D^o \pi^+$, strong decays are not well identified by this experiment. Including parent resonant states would shift the distribution to slightly higher Z.

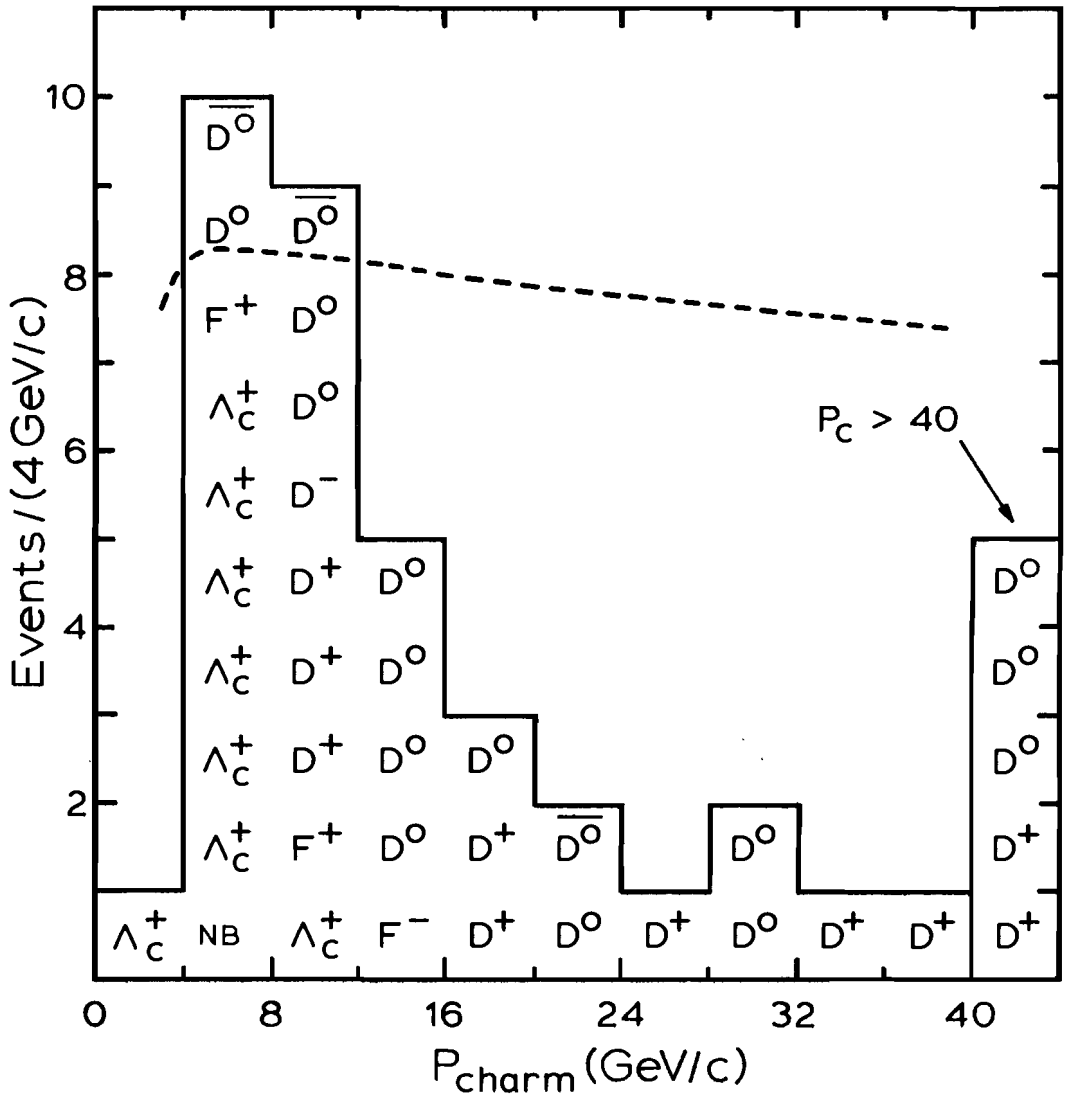

Figure 4-14: Momentum of unambiguous single charmed particles produced in neutrino interactions. (The $D^0\bar{D}^0$ charm pair are not shown.) The dashed line is the momentum dependence of our charmed particle decay finding and reconstruction efficiency.

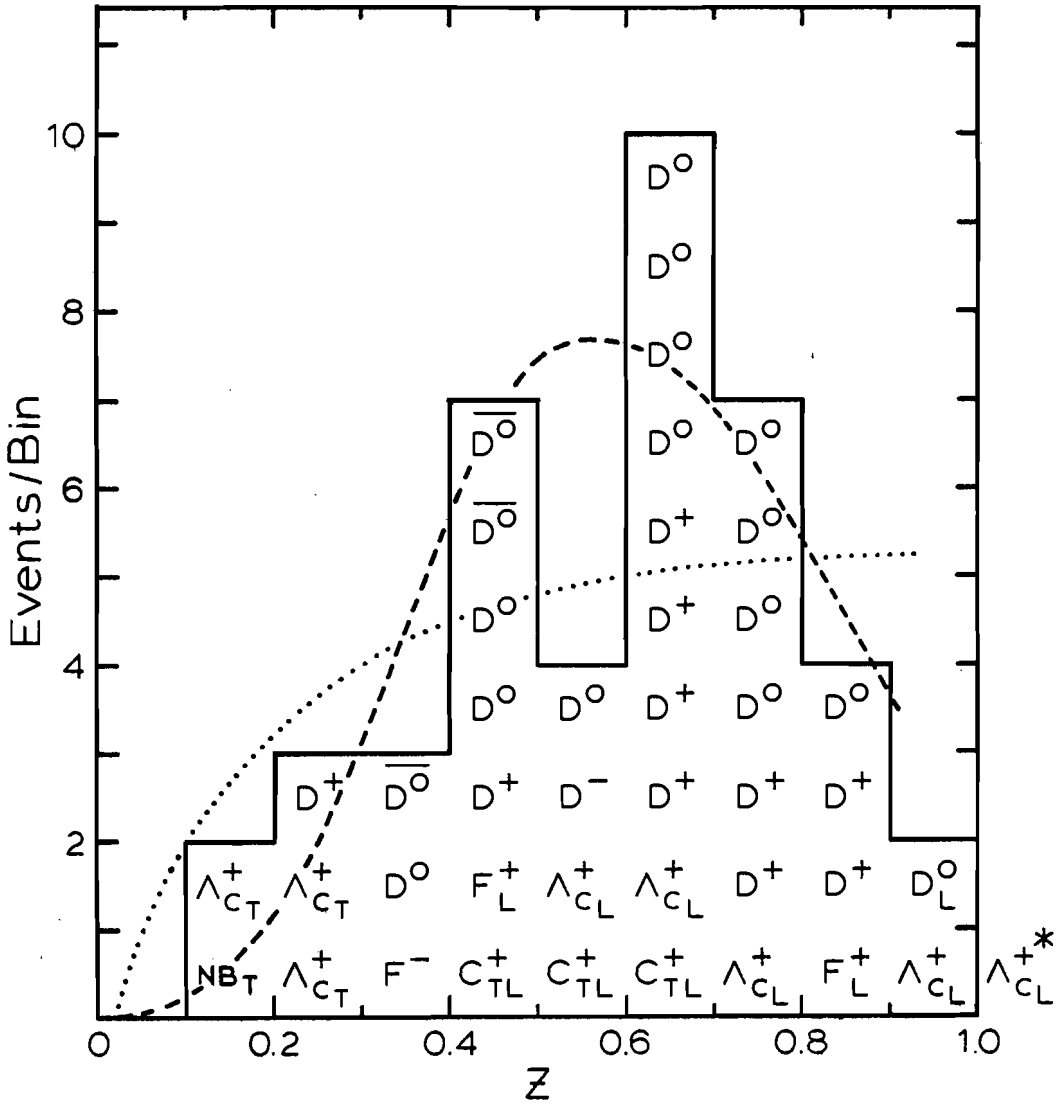

Figure 4-15: Fragmentation distribution of single charmed particles. The event (*) at Z>1 is exclusively produced ($\nu N \to \mu^- \Lambda_c^+$); "T" indicates target fragments (X_F<-0.4 in Fig. 4-20), and "L" are events with total hadronic energy E_H <15 GeV. The dashed curve is a Gaussian distribution (<Z>=0.58, RMS width = 0.2) folded with our acceptance and resolution; the dotted curve is the expected distribution for a flat (dN/dZ=1) distribution.

(For $D^{*+} \rightarrow D^{o}\pi^{+}$ decays, the difference between $Z(D^{*+})$ and $Z(D^{o})$ is $\langle Z(D^{*+})-Z(D^{o})\rangle=0.07$, in proportion to the $D^{*+}-D^{o}$ mass difference.)

Also shown in the figure are Z distributions generated from intrinsic flat (dN/dZ=1) and Gaussian ($dN/dZ \propto e^{-(Z-\langle Z\rangle)^2/2\Delta Z^2}$) distributions. The "flat" prediction falls off at low Z because E_c cannot be less than the rest mass, $M_c \approx 2$ GeV/c^2, of the charmed particle, i.e. $Z \geq M_c/(E_\nu - E_\mu)$. This threshold also affects the calculated "Gaussian" distribution, but the effect is small and not obvious in the figure. $Z \geq M_c/(E_\nu - E_\mu)$ is the minimum possible threshold requirement; the true threshold behaviour is probably more subtle. (The threshold distorts the observed distribution in the opposite direction to the effect of not including parent resonant states, so there will be some cancellation between the two effects.) The relative bin-to-bin systematic uncertainties of these generated distributions are negligible for $Z<0.8$, but are $\sim\pm 10\%$ at $Z \cong 0.9$ and $\sim\pm 50\%$ at $Z \cong 1$. (The distribution near Z=1 is hard to predict because it depends very sensitively on how well the experiment can measure very small differences between E_H and E_c.)

The Gaussian distribution is in good agreement with the data. Such a broad Z distribution with a mean value $\gtrsim 0.5$ is qualitatively what has been expected by Bjorken [139] and others [140,134], based simply on the large mass of the charm quark relative to common u and d quarks. The charm quark is so heavy it gives up little of its momentum to lighter particles in the fragmentation process. The fragmentation functions of lighter quarks ($D_o(Z)$, Sec. 1.6.1) have mean values of 0.4 for u and d quarks and 0.3 for strange quarks, and widths of 0.21 and 0.2; Dias de Deus has predicted $\langle Z\rangle=0.66$ for charm and 0.87 for beauty, and widths of 0.1 and 0.04 [140].

Table 4-4 shows the mean observed Z for various subsets of the charm sample. The large width of the Λ_c^+ distribution is due to the fact that it includes both target and current fragments: the target fragments have little energy and small Z; the current fragments have slightly more energy and large Z. (Particles with $X_F>0.4$ are defined to be current fragments, see Sec. 4.14.) The corrected mean value of Z for charmed current fragments only is $\langle Z\rangle = 0.59\pm 0.03(\text{stat.})\pm 0.03(\text{sys.})$; this value

Table 4-4: Observed means, RMS widths (ΔZ), and mean experimental resolutions ($\langle\sigma(Z)\rangle$) of the fragmentation distributions of the observed charmed particles (Fig.2).

	Number of particles	$\langle Z\rangle$	$\langle\Delta Z\rangle$	$\langle\sigma(Z)\rangle$
All charm	40	0.60	0.23	0.13
Mesons	31	0.61	0.18	0.12
Λ_c^+	8	0.61	0.36	0.14
$-0.4<X_F<1.0$	35	0.63	0.18	0.13
$-0.4<X_F<1.0$ and $E_H>15$ GeV	28	0.60	0.17	0.12

is corrected for acceptance, resolution, and a simple ($E_c > M_c$) threshold. The corrected mean Z for charmed current fragments produced in events with $E_H > 15$ GeV is $\langle Z \rangle = 0.57 \pm 0.03 \pm 0.03$.

Similar charm fragmentation distributions have been observed for D^{*+} mesons produced in e^+e^- annihilation at a centre-of-mass energy of 29 GeV ($\langle Z \rangle = 0.58 \pm 0.06$) [141], and inferred from dimuon data for D production by neutrinos ($\langle Z \rangle = 0.68 \pm 0.05 \pm 0.06$) [20].

4.12 Transverse Momentum

The transverse momentum of hadrons produced in neutrino-nucleus interactions has four sources: (1) the intrinsic momentum of the struck quark within the nucleon, (2) the Fermi momentum of the nucleon within the nucleus, (3) the transverse momentum produced by the fragmentation process, and (4) the transverse momentum resulting from unobserved parent particles decaying into the observed hadrons. Except for Fermi momentum, the contributions of the other three sources are of potential interest.

P_{out} is the momentum of a particle out of the plane defined by the neutrino and the muon. Because it is independent of the muon momentum and neutrino energy, P_{out} is a better measured quantity than $P_\perp$ (the momentum of the hadron transverse to the direction of the total hadronic system). P_{out} can be calculated from $\vec{P}_c$ and the directions, $\hat{P}_\nu$ and $\hat{P}_\mu$, of the neutrino and muon; $\hat{P}_\nu$ is known to $\lesssim \frac{1}{2}$mr from the beam geometry, and $\hat{P}_\mu$ is usually measured with ~2mr accuracy. $P_\perp$ is calculated from $\vec{P}_c$ and the direction, $\hat{P}_H$, of the total hadronic system; $\hat{P}_H$ is not as well determined as $\hat{P}_\nu$ and $\hat{P}_\mu$, because it must be calculated from E_H, P_μ, $\hat{P}_\mu$, and $\hat{P}_\nu$.

The observed P_{out} distribution of charm is shown in Figure 4-16. The mean value and RMS width of the distribution are $\langle P_{out} \rangle = 0.45$ GeV/c and $\Delta P_{out} = 0.55$ GeV/c; the observed ratio of P_{out} to $P_\perp$ is $\langle P_{out}/P_\perp \rangle = 0.58 \pm 0.05$, in agreement with the value of $2/\pi$ (=0.63) expected from azimuthal symmetry (Sec. 1.3). After correcting for the effects of experimental resolution and acceptance, the mean value of P_{out} is

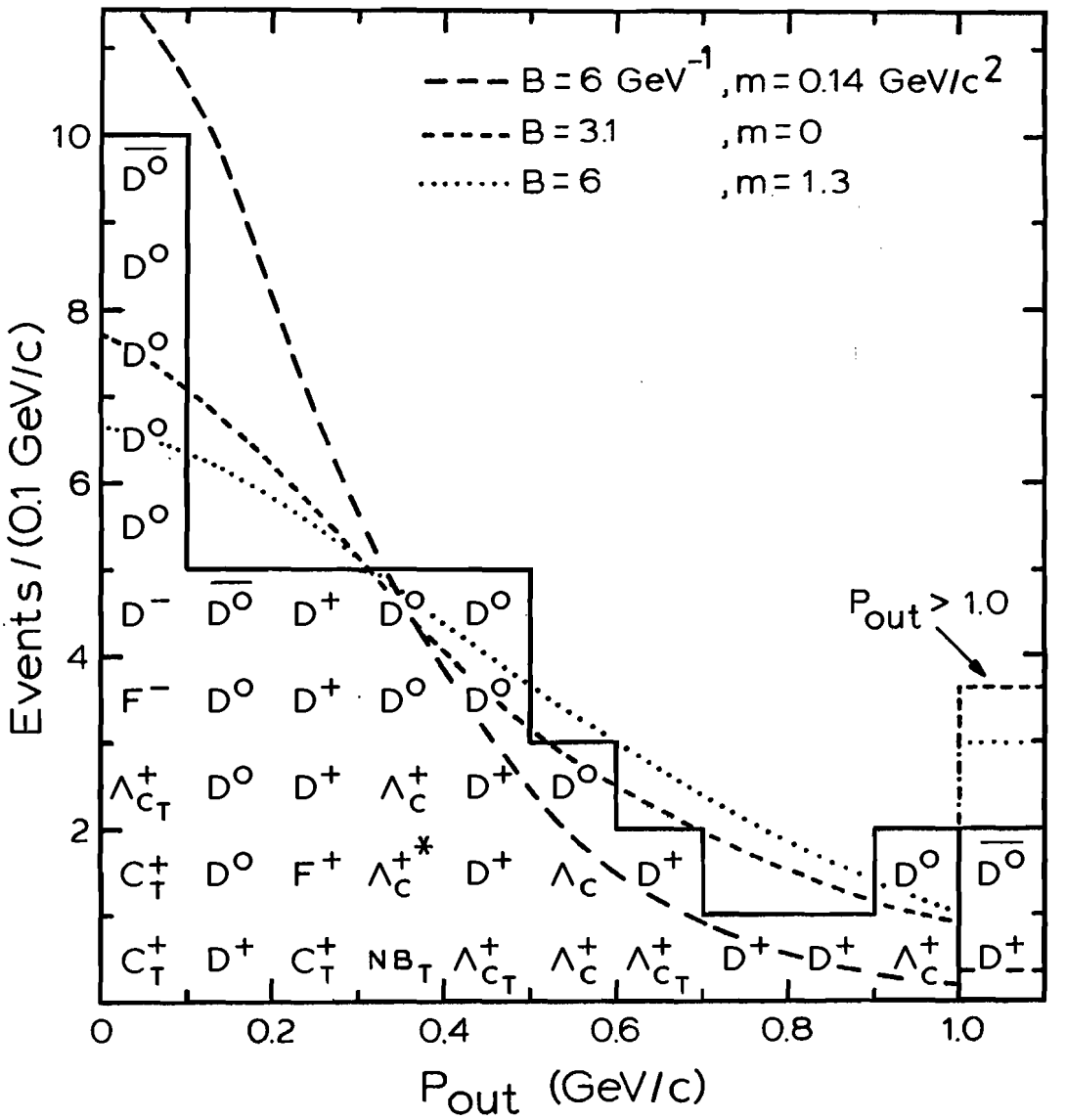

Figure 4-16: Charm P_{out} distribution (events with identified muons). Also shown are P_{out} distributions generated from $dN/dP_\perp^2 \propto \exp(-B\sqrt{m^2+P_\perp^2})$ convoluted with our experimental resolution ($\langle\sigma(P_{out})\rangle \approx 0.1$ GeV/c).

0.41±0.1 GeV/c.

In general, the observed transverse momentum distributions of light hadrons produced in lepton or hadron interactions are well parameterized by

$$\frac{dN}{dP_\perp^2} \propto e^{(-B\sqrt{m^2+P_\perp^2})} \quad ,$$

where B≈6 GeV^{-1} and $m \sim m_\pi$ [142]. Figure 4-17 shows the P_{out} distribution of this experiment for reconstructed (UPDN) charged particles (excluding identified MUFB muons). The data are in good agreement with the expected distribution calculated for B=6 GeV^{-1} and $m=m_\pi$(=0.14 GeV/c^2). (The reconstructed tracks include ~25% electrons, each of which carries, on average, ~1/4 of their original parent π^o transverse momentum. These are included in calculating the solid curve; the dotted curve shows what the distribution would look like if the data consisted only of hadrons.)

The observed charmed hadrons have larger transverse momenta than light hadrons. The charm distribution of Figure 4-16 can be well described by either a simple exponential (B=3.1 GeV^{-1}, m=0 GeV/c^2) or by a massive analog of the light hadron parameterization (B=6 GeV^{-1}, m=1.3 $GeV/c^2 \approx m_c$). (B=3.1 GeV^{-1}, m=0 GeV/c^2 is the best fit to the data if B and m are free parameters; m=1.3 GeV/c^2 is the best fit to the data if B=6 GeV^{-1} is fixed.) The light hadron parameterization (B=6 GeV^{-1}, m=0.14 GeV/c^2) is a poor fit to the charm data and can be rejected at the 95% confidence level.

4.13 Muon-Hadron Angle ϕ_μ

ϕ_μ is the angle between the muon and the hadron in the plane perpendicular to the neutrino direction.

ϕ_μ is useful in determining whether a particle is associated with the lepton vertex or with the hadronic system. In a charged current interaction, the hadronic system is produced back-to-back with the primary muon, so the hadrons have a ϕ_μ distribution that peaks at ϕ_μ=180°. The observed ϕ_μ distribution (Figure 4-18) for the charmed

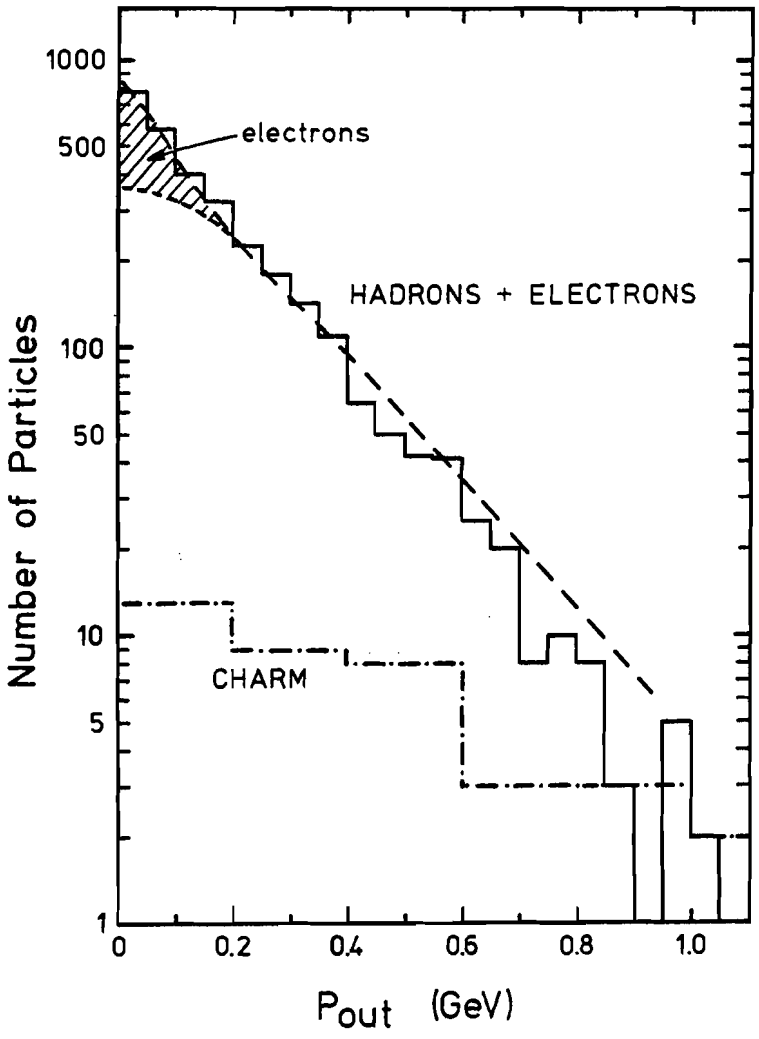

Figure 4-17: P_{out} distribution of light hadrons. The histogram is data (all reconstructed UPDN tracks from events with an identified MUFB muon); the dashed curve is the expected P_{out} distribution for UPDN tracks, assuming a $dN/dP_{\perp}^2$ distribution with $B=6GeV^{-1}$ and $m=m_{\pi}$ (See text), and calculated for an UPDN track mixture of 75% light hadrons and 25% electrons from π^o decays. The shaded area shows the expected contribution from electrons. Also shown is the charm data from Fig. 4-17.

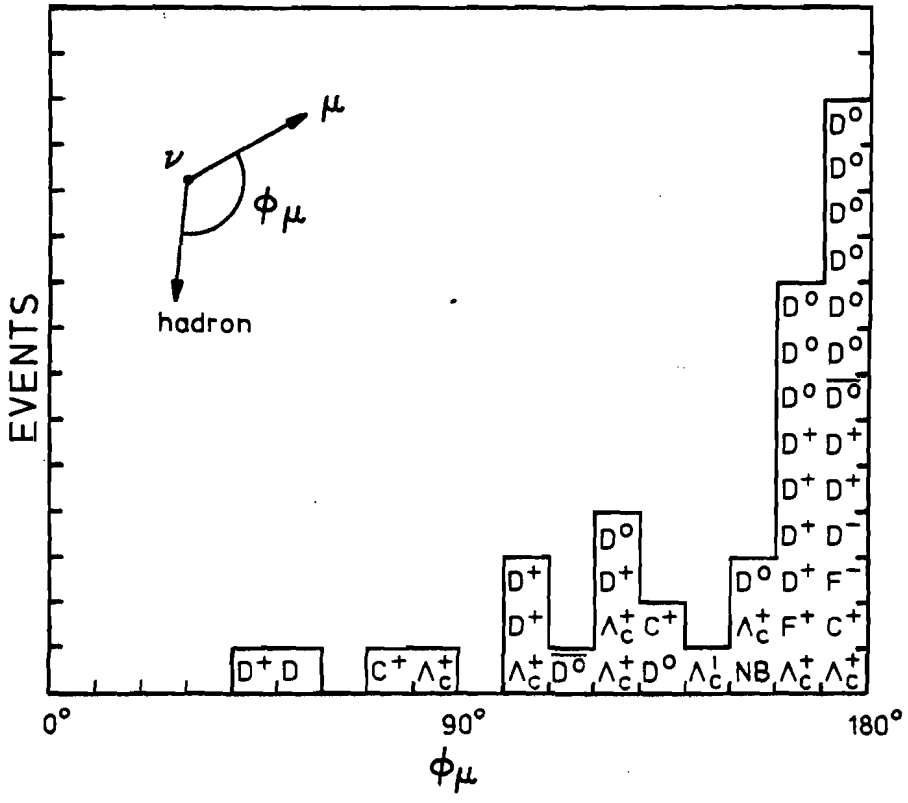

Figure 4–18: ϕ_μ distribution for charmed hadrons.

particles is peaked at 180°, as is expected for normal charged current charm production. There is no sign of exotic processes. (The production of heavy quarks or heavy leptons that decay into a muon plus charm could give $\phi_\mu \sim 0°$.)

4.14 Feynman X

The fragmentation process gives relatively little momentum to the hadrons produced, so most hadrons are produced almost at rest in the hadronic C.O.M. frame, and the Feynman X distribution for all hadrons is peaked at $X_F \approx 0$. Figure 4-19 shows the X_F distribution of reconstructed particles (UPDN tracks) from E-531 neutrino interactions. There is little acceptance for particles produced near $X_F=-1$, because such particles have little momentum, are produced at large angles, and are rarely reconstructed.

The Feynman X distribution of the charmed particles is shown in Figure 4-20 - there are two distinct populations. Most charmed particles are produced in the forward direction ($X_F \gtrsim 0$), but ~10% of the charmed particles are produced near $X_F=-1$, and all of these particles are identified as, or are consistent with, charmed baryons. These are target fragments in which the charmed quark has become part of the recoiling target nucleon. For such charmed target fragments to be produced, the charm quark (initially at $X_F=+1$) must transfer most of its momentum to other hadrons.

The distribution of charmed current fragments is peaked near $X_F=+1$. This distribution differs from the light hadron distribution of Fig. 4-19 because of the large mass of the charm quark, and because the light hadron distribution includes all hadrons, irrespective of whether or not they contain the original struck quark. In normal charged current charm production, the charm quark is always the original struck quark, so "charm" is a tag that allows us to identify the particle containing the original quark. It is not possible to identify the particle containing

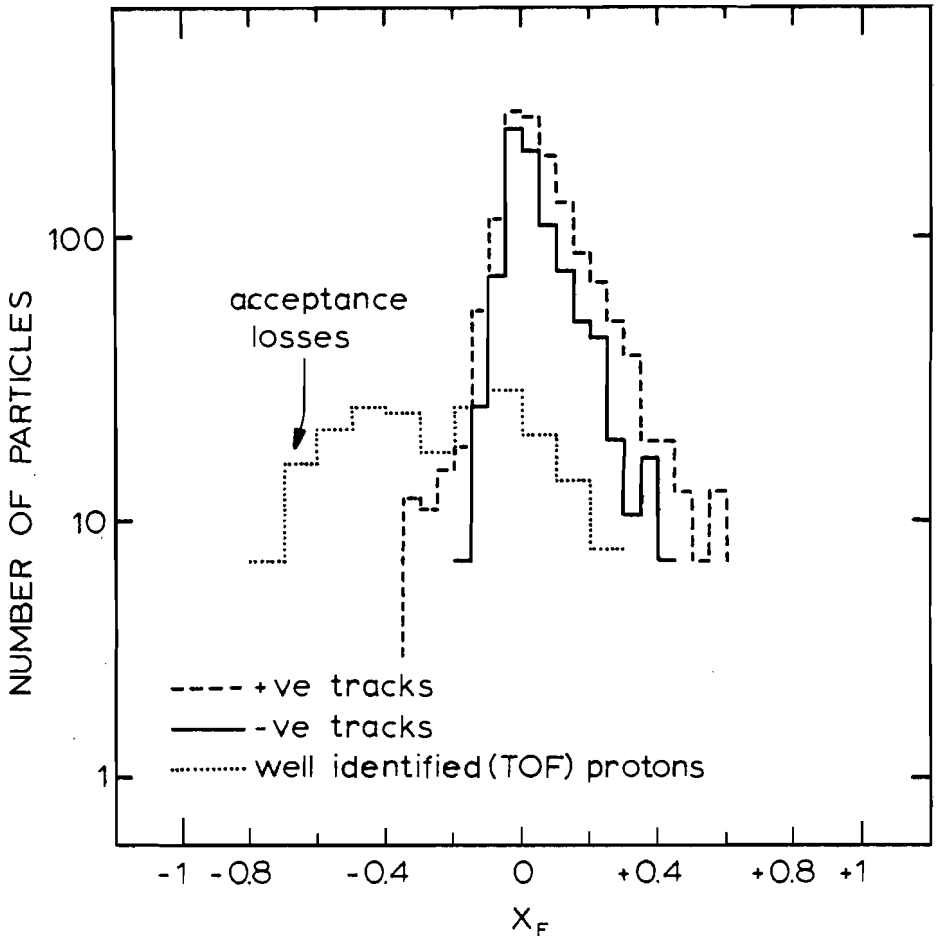

Figure 4-19: Feynman X distribution for particles with reconstructed UPDN tracks in ν_μ charged current interactions.

the original quark in non-charm interactions. The X_F distribution of Fig. 4-20 is the first direct measurement of the X_F distribution of particles containing the original struck quark.

About half of the charmed baryons appear to be produced as target fragments, but baryons are also produced in the current system. If the 4 Λ_c^+'s at $X_F>-0.4$ are due to fragmentation of charmed quarks into baryons, then the fraction of charmed quarks fragmenting into baryons is $10\pm^{10}_{4}$%. This fraction is consistent with the rates ($\sim$10-20%) inferred [143] from baryon production in e^+e^- annihilation [144].

The fraction of recoiling target fragments is not well determined because of both low statistics and difficulty in calculating our acceptance near $X_F=-1$. The acceptance (reconstruction and finding efficiency) shown in the figure is calculated assuming that X_F is uncorrelated with other kinematic parameters, except as constrained by momentum and energy conservation (e.g. $X_F=\pm1$ requires $P_\perp=0$). This assumption may not be accurate for target fragments, which are clearly produced in a different manner than the majority of charmed particles. For negative values of X_F, the calculated acceptance depends on whether found but unidentified low momentum charmed particles are included in the total charm sample. The top of the shaded area is the acceptance if C^+ events are included in the charm sample, the bottom of the shaded area is the acceptance if C^+ events are not included. The possible systematic error due to uncertainty in the kinematic characteristics of charmed particles produced near $X_F=1$, although not shown , is also approximately given by the size of the shaded areas. Also shown in the figure is the experimental X_F distribution (resolution and acceptance folded in) expected for a true flat X_F distribution. Because of the finite experimental resolution ($\langle\sigma(X_F)\rangle\cong0.2$), the populations near X_F ±1 are poorly measured.

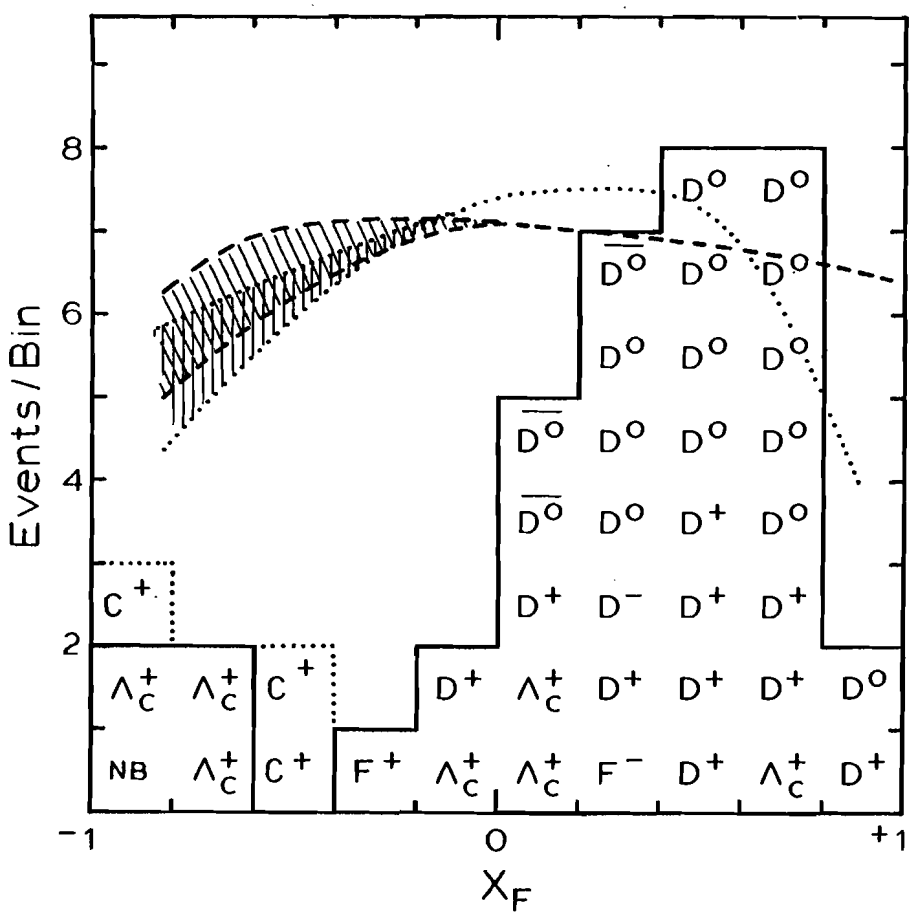

Figure 4-20: Feynman X distribution of charm. Not included are events with no identified primary muon, and the exclusive Λ_c^+. The dashed curve is our acceptance and the dotted curve shows the effect of our experimental resolution .

CHAPTER 5: Upper Limits to ν_μ-ν_τ Oscillation and ν_μ-τ Coupling

5.1 Introduction

Tau lepton production by neutrinos has not yet been observed. The observation of tau production in a muon neutrino beam could indicate exciting new physics, while if taus are not seen, the measured limit to the production rate constrains the possible characteristics of the tau lepton and its interactions.

The lifetime of the tau is similar to the lifetimes of the charmed particles, so this experiment could expect to find most decays of any taus produced in our emulsion. The experiment is thus sensitive to the direct charged current production of a primary tau lepton:

$$\nu_{(\mu)} + \text{nucleus} \rightarrow \tau^- + \text{hadrons} \qquad \{5.1\}$$

where the incident neutrino $\nu_{(\mu)}$ is originally a muon neutrino.

Such reactions would result from $\nu_\mu \rightarrow \nu_\tau$ oscillations or a direct ν_μ-τ coupling. (The neutrino beam may also contain a few primary ν_τ from decays of charmed F mesons hadronically produced in the proton target, but only $\lesssim 10^{-2}$ events are expected [150] from this source in the E-531 data sample.) Neutrino oscillations will occur if the muon neutrino is not a single mass eigenstate (Sec. 1.1.2). A direct ν_μ-τ coupling would indicate that the simple Standard Model structure of the weak flavours is inadequate.

The relative rate of production of τ^- and μ^- by muon neutrinos

$$R \equiv \frac{N(\nu \rightarrow \tau)}{N(\nu \rightarrow \mu)}$$

is a measure of the $\nu_\mu \rightarrow \nu_\tau$ oscillation probability

$$\frac{P(\nu_\mu \rightarrow \nu_\tau)}{P(\nu_\mu \rightarrow \nu_\mu)}$$

and the ν_μ-τ direct coupling strength

$$\frac{G^2_{\nu_\mu\tau}}{G^2_{\nu_\mu\mu}} \quad ,$$

where $P(\nu_\mu \rightarrow \nu_\alpha)$ is the probability that a ν_μ has oscillated into a ν_α (ν_τ or ν_μ), and $G^2_{\nu_\mu\tau}$ and $G^2_{\nu_\mu\mu}$ are the strengths of the ν_μ-τ and ν_μ-μ couplings.

Previous limits to $\nu_\mu \rightarrow \tau$ production and ν_μ-ν_τ oscillations have been set by bubble chamber experiments [33,34,35,37]]. If reaction {5.1} occurs, then the τ^- will decay into $e^-\nu_\tau\bar{\nu}_e$ about 1/5 of the time, and this electron can be detected in a bubble chamber although the τ^- decay cannot be seen because the decay length is too short. Reaction {5.1} will thus mimic a charged current electron neutrino interaction ($\nu_e N \rightarrow eX$). Limits to {5.1} are set by looking for an excess of $\nu N \rightarrow eX$ interactions over the rate expected from the background ν_e flux (typically ~1% of the ν_μ flux) present in all muon neutrino beams.

5.2 Data and Analysis

5.2.1 Candidates and Background

To search for reaction {5.1}, all E-531 events containing charged particle decay candidates have been examined to see if they can be interpreted as charged current ν_τ interactions. A charged current ν_τ interaction would have (1) a negative tau decay candidate and (2) no muon from the primary vertex.

Only ν_τ (τ^-), not $\bar{\nu}_\tau$ (τ^+), candidates are considered because the signal-to-background ratio is much worse for $\bar{\nu}_\tau$ than ν_τ events. This is because the $\nu/\bar{\nu}$ event ratio is ~15 (Sec. 3.6), but the backgrounds to τ decays have a +/- charge ratio of ~4 (Table 5-1). If the sign of a tau candidate is unknown, it is assumed to be negative and accepted as a τ^- candidate.

Table 5-1: Backgrounds to τ^- decays. The middle two columns are the expected number of (positive or negative) charged decay candidates found. The last column is the number of decay candidates that are expected to pass the scanning cuts and ν_τ event criteria.

Type	Expected Decay Candidates +	Expected Decay Candidates −	Background to τ^- decays
Charmed particle decays *	28	$2\frac{1}{2}$	0.4
Strange particle decays	5	$1\frac{1}{2}$	0.2
Hadronic interactions and scatters (NH=0, NS=1,3,...)	24	13	0.4
Total	57	17	$1\pm^{1}_{0.5}$ **

* calculated from E-531 production rates

** plus statistical (Poisson) fluctuations about this expected value

To further reduce the background to tau decays from hadronic interactions, we also require (3) a tau decay candidate not to have $|P\beta|<2.0$ GeV/c (90% C.L.) measured in the emulsion. Most hadrons produced in neutrino interactions are quite slow (see Fig. 3-12) while leptons from the primary vertex are quite fast (Figure 5-1, and also Fig. 3-4). Requirement (3) removes many hadronic interactions while leaving virtually untouched any possible τ^- from ν_τ interactions.

A tau decay candidate is a track that appears to decay into an odd number of tracks with no observed nuclear decay fragments. A kink is not considered a tau decay candidate if the secondary decay track has less than 100 MeV/c momentum (P_T) perpendicular to the parent direction. Within an angular fiducial region of 0.3 radian around the neutrino direction, there are a total of 47 tau decay candidates: 21 multiprong and 26 kinks.

A charged current ν_τ interaction can be imitated by a ν_μ interaction with no identified primary muon and with a charged particle decay or interaction. The backgrounds to tau decays are shown in Table 5-1. Charged charmed particle decays are a large background, but almost all of these are positive decays (c, not $\bar{c}$) in events with identified primary muons. The background from strange particles is expected to be dominated by $\Sigma^\pm$ kink decays; more Σ^+ than Σ^- are expected to be found because Σ^+ are more often produced and are more likely to decay in the emulsion ($c\tau_{\Sigma^+}$ = 2.4 cm, $c\tau_{\Sigma^-}$ = 4.4 cm). Other charged strange baryons (Ξ^- or Ω^-) are not often produced, and charged kaons are almost always too long lived ($c\tau$ = 371 cm) to decay in the emulsion. Charged pion decays, and many kinks due to hadronic scatters (see Fig. 3-14), are eliminated by the minimum 100 MeV/c P_T requirement for τ kink decay candidates.

The three $\nu_\tau \to \tau^-$ event criteria are expected to remove all but $\sim 1 \pm^{1}_{0.5}$ background events.

Table 5-2 shows the effect of the criteria, applied as cuts, on the tau candidate sample. The criteria leave no ν_τ event candidates in our data sample, so the expectation value for the number of ν_τ events must be less than 2.3 events (90% C.L., Poisson statistics). There are 634 events with identified (MUFB) μ^-, so the raw upper limit to the relative

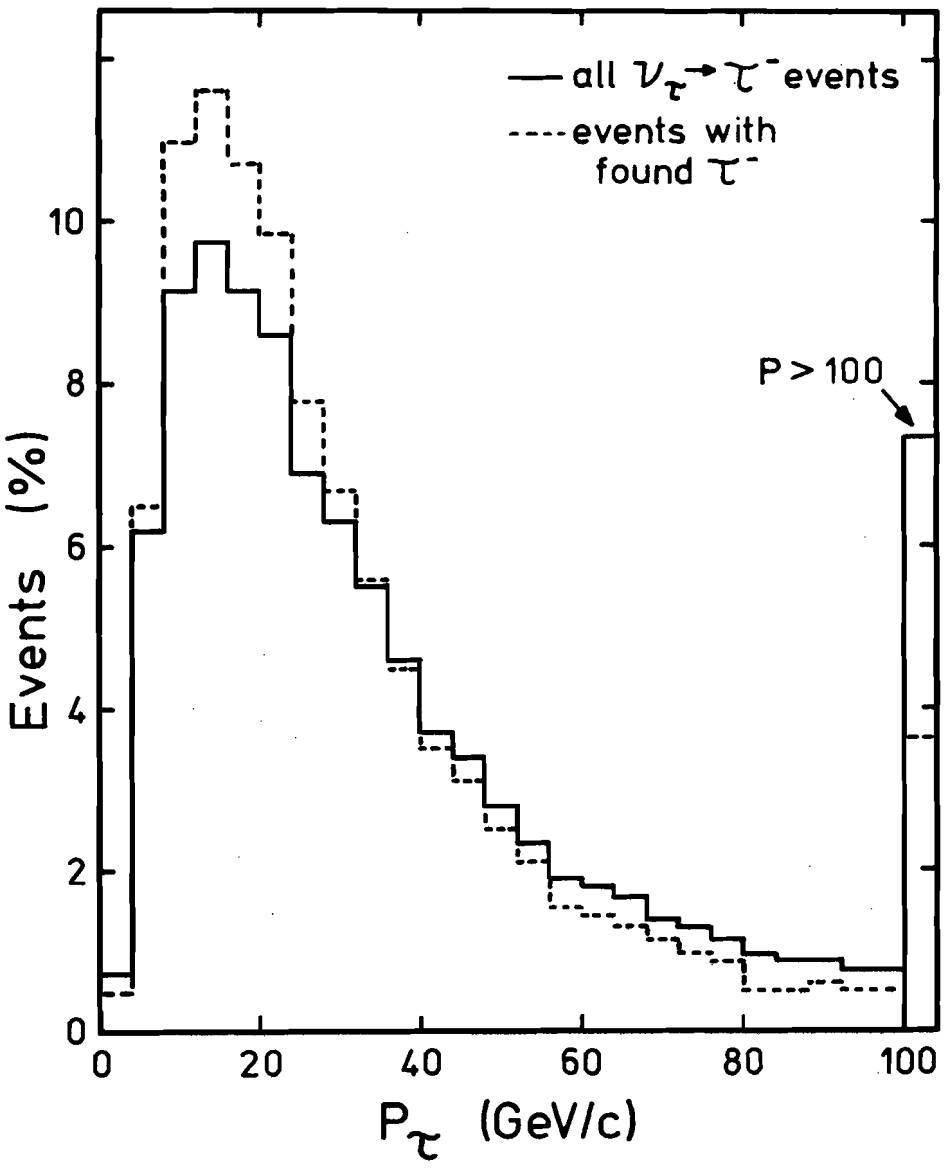

Figure 5-1: Predicted (Monte Carlo) momentum spectra of primary τ^- leptons from charged current ν_τ interactions (calculated for a direct ν_τ-τ coupling and the E-531 neutrino beam). The solid line is the spectrum for all ν_τ C.C. interactions, the dotted line is the expected spectrum for found τ^- decays. Only 0.1% of the found τ^- should have $P\beta < 2.0$ GeV/c (i.e. $P_\tau < 2.5$ GeV/c).

Table 5-2: Effects of event criteria. Column one shows the loss of observed τ candidates as the event criteria are applied; column two, the calculated fraction of τ^- decays lost. Only 1.7% of real decays are lost by initial scanning cuts, and the event criteria should remove only an additional 1.6%.

Criteria	τ Candidates (events)	τ^- (%)
Initial	47	98.3
(1) negative tau candidate	-35	-0.7
(2) no muon from primary vertex	-9	-0.8
(3) $\|P\beta\| > 2.0$ GeV/c	-3	-0.1
Remaining	0	96.7

production rate of τ^-'s is

$$R_{raw} < 2.3/634 = 0.36\% \text{ (90\% C.L.)}$$

5.2.2 Corrections: Cross Sections, Efficiencies, Acceptances

The raw limit is subject to a number of corrections. The total correction factor can be written as

$$C = \left[\int K(E_\nu) \cdot N_\nu(E_\nu) \cdot dE_\nu\right]^{-1}$$

$N_\nu(E_\nu)$ is the energy spectrum (normalized to unity) for found charged current ν_μ interactions, and $K(E_\nu)$ is the energy dependent correction given by

$$K(E_\nu) \equiv \int \left(\frac{\sigma_\tau}{\sigma_\mu}\right) \cdot \left(\frac{e_\tau}{e_\mu}\right) \cdot \left(\frac{A_\tau}{A_\mu}\right) \cdot \left(\sum_i B_i \cdot S_i\right)$$

This integral is over x,y, and decay momentum, and the sum is over all tau decay modes. The integrals are evaluated by Monte Carlo simulation: Using the standard model and the known properties of the tau, the production and decays of τ^- are incorporated in the general experiment Monte Carlo program. τ^- are produced according to $d\sigma/dxdy$ given by Eqn. {1.4a,d,e}, and they are then allowed to decay with a mean lifetime of 2.8×10^{-13}s (Sec. 1.2). The efficiencies and acceptances for event reconstruction and charged decay finding are then applied to determine the probability of detecting the tau.

(σ_τ/σ_μ) is the relative tauonic to muonic charged current neutrino cross section [151]; Figure 5-2 shows this ratio as a function of energy using two different $F_i(x,Q^2)$ parameterizations. The curve of Gluck, Hoffman, and Reya (GHR) is used here, the other curve is for comparison only. The GHR parameterization is recent and gives the lowest τ^- production cross section (i.e. it is the conservative choice). The mean (σ_τ/σ_μ) ratio integrated over the observed E_ν spectrum is 53%.

(e_τ/e_μ) is the relative finding efficiency for τ^- and μ^- interactions - this includes trigger, reconstruction, and event finding efficiencies (most of which cancel out in the ratio: $(e_\tau/e_\mu) \sim 1.04$). τ^- events are slightly easier to find than μ^- events because multiprong tau decays

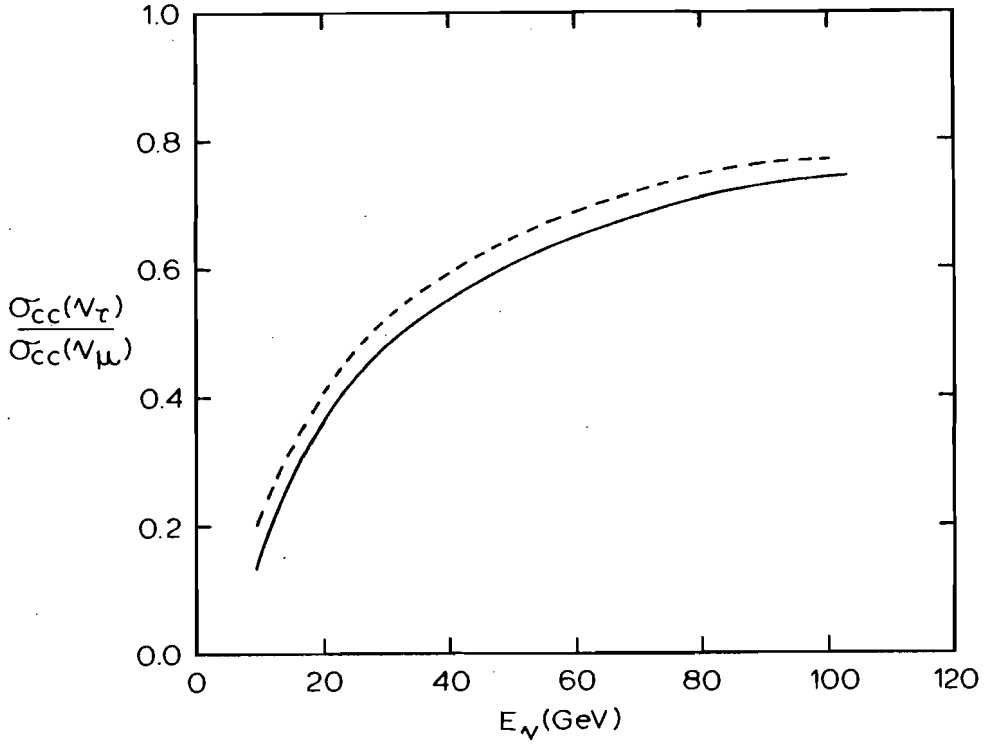

Figure 5-2: Relative cross section for ν_τ charged current interactions. The solid curve is predicted using the GHR $F(x,Q^2)$ parameterization [105]. The dashed curve is from Bongardt [155] using an older parameterization [156]. Other parameterizations [157,158,159] give cross sections between the two curves shown.

provide several easily reconstucted fast tracks.

A_μ and A_τ are the μ^- and τ^- acceptances: A_μ is the muon MUFB identification efficiency (~71%), and A_τ is the probability (~97%) that a τ^- event will pass the scanning cuts and the event criteria. The 0.3 r angular cut and the 100 MeV/c P_T cut would lose 0.6% and 1.1% of found τ^-. (These losses are calculated for τ^- events that would be found. For example, the 100 MeV/c P_T cut loses 2.9% of all τ^- kinks produced but only 1.9% of those we would find - this is because kinks with small P_T have small kink angles and are hard to find. When the kink and multiprong branching ratios are folded in, the cut loses 1.1% of all "found" τ^- events.) The three event criteria should eliminate very few found τ^- decays (Table 5-2).

Finally, B_i are the tau decay branching ratios, and S_i are the decay finding efficiencies. The branching ratios used are: $\tau \to e\nu\bar{\nu}$, 17.5%; $\tau \to \mu\nu\bar{\nu}$, 17%; $\tau \to \pi\nu$, 9.5%; $\tau \to \rho\nu$, 21%; $\tau \to \pi^{\pm} n\pi^0$ ($n \geq 2$), 6%; $\tau \to >3$ charged particles, 29% [40]. Figure 5-3 shows the kink decay finding efficiency as a function of kink angle integrated over the predicted τ^- decay length distribution. The mean τ^- decay finding efficiencies are calculated to be 62% for kinks, and 91% for multiprong decays.

5.2.3 Limit to Tau Production

The total correction factor is 1.73±0.2. This error includes uncertainties in experimental parameters (e.g. E_ν and scanning efficiencies), but not any theoretical uncertainty for $d\sigma_\nu/dxdy$ or the $F_i(x,Q^2)$ parameterization. The final limit is

$$R < 0.63\% \quad (90\% \text{ C.L.})$$

This limit is calculated using a tau decay finding efficiency calculated from the expected tau lifetime (2.8×10^{-13} s). Figure 5-4 shows the limit to R as a function of the tau lifetime; the lifetime would have to differ from the expected value by a factor of 0.1 or 4 to increase the limit from 0.63% to 0.73%. The limit is insensitive to the exact values of the tau decay branching ratios, but it does depend on the kink

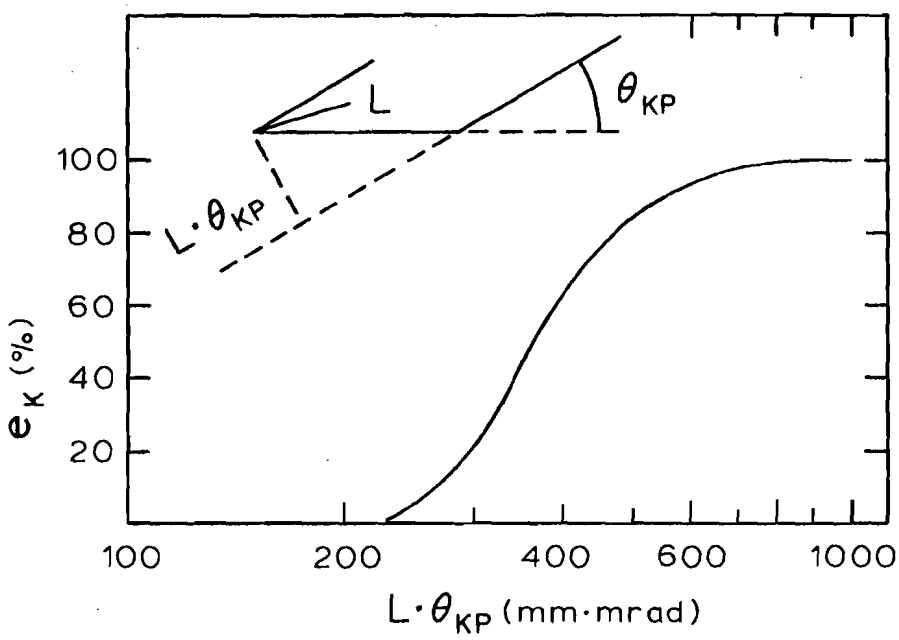

Figure 5-3: Finding efficiency for kink decays as a function of kink angle (integrated over the predicted τ^- decay length distribution).

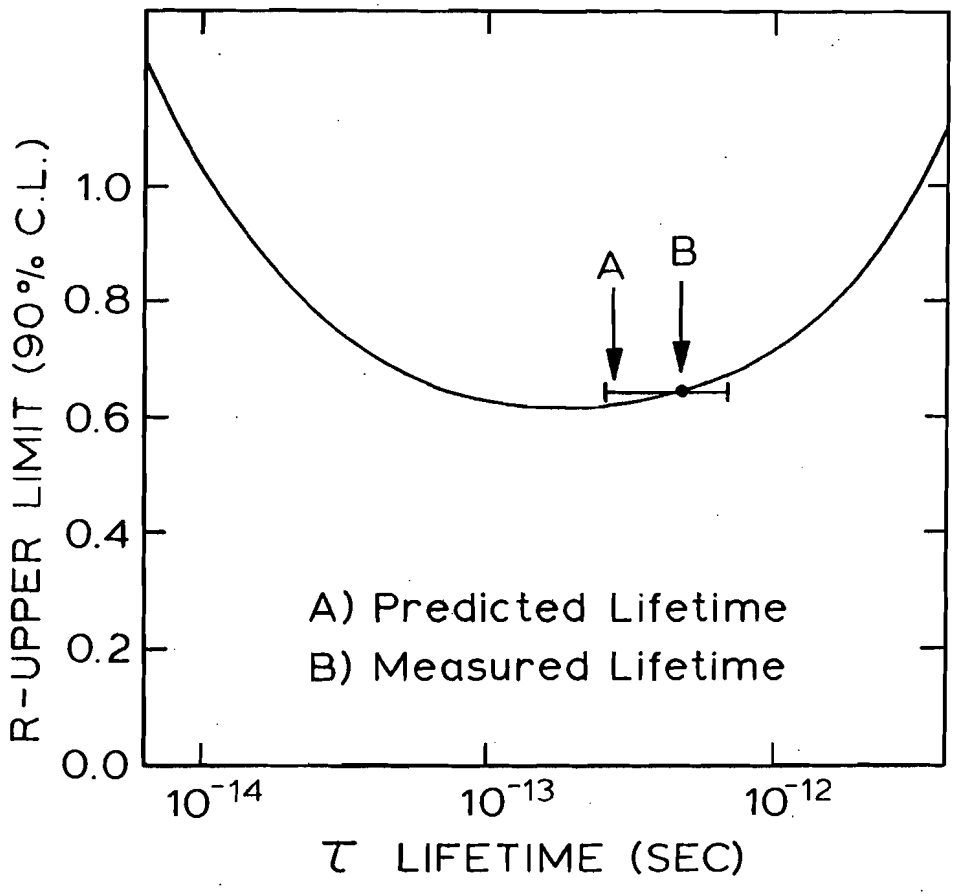

Figure 5-4: Limit to R as a function of the τ lifetime. R is the $\nu_\mu \rightarrow \nu_\tau$ oscillation probability or, alternatively, the ν_μ-τ coupling strength.

topological branching ratio [152]. Figure 5-5 shows the limit to R as a function of the tau kink rate.

This limit is ~4 times better than previous limits [33], and it is the first limit set by a direct search for τ decays.

5.3 Limit to the ν_μ-τ Coupling

In the conventional weak-interaction theory of the Standard Model, the tau couples to a tau neutrino with a strength, $G^2_{\nu_\tau\tau}$, which is equal to the coupling strengths of electrons to electron neutrinos, and of muons to muon neutrinos (i.e. $G_F^2 \equiv G^2_{\nu_\mu\mu} = G^2_{\nu_e e} = G^2_{\nu_\tau\tau}$). The tau is not expected to couple directly to either the electron neutrino or the muon neutrino (i.e. $G^2_{\nu_\mu\tau} = G^2_{\nu_e\tau} = 0$); such a direct coupling would require a more complex weak interaction group structure than the SU(2) of the Standard Model.

Direct tau production by muon neutrinos would indicate that the conventional theory is not completely correct. The relative production rate for ($\nu_\mu N \rightarrow \tau^- +$hadrons) would be proportional to $G^2_{\nu_\mu\tau}$, and the rate would be independent of the distance from the neutrino source (unlike the situation for $\nu_\mu \rightarrow \nu_\tau$ oscillations). The result of this experiment is that

$$\frac{G^2_{\nu_\mu\tau}}{G^2_{\nu_\mu\mu}} < 0.0063 \qquad (90\%\ \text{C.L.})$$

The ν_μ-τ coupling, if it exists, must be very small.

5.3.1 Arguments for the Existence of the Tau Neutrino

The tau neutrino has not yet been observed, but it is possible to make a strong circumstantial argument for its existence.

The lifetime of the tau is expected to be $\tau(\text{theory}) = 2.8 \times 10^{-13}$s, but the actual tau lifetime, τ(measured), will differ from this expected value if the tau has any non-standard couplings:

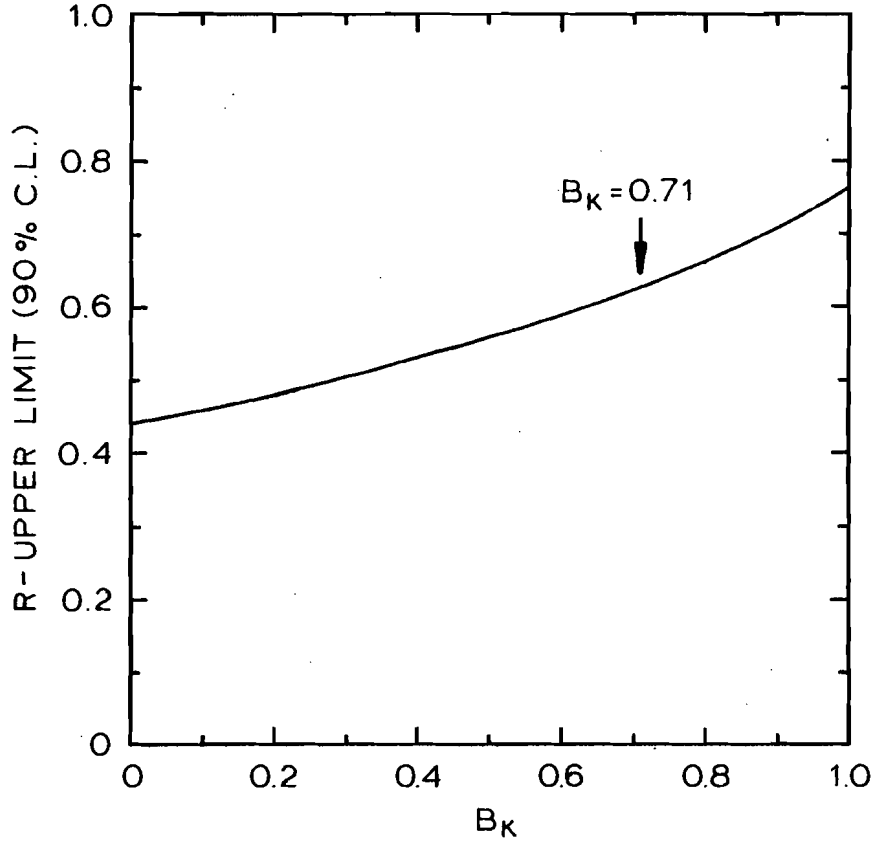

Figure 5-5: Limit to R as a function of the tau single-prong (kink) branching ratio; B_k = B.R.($\tau \rightarrow$ 1 charged particle + neutrals).

$$\frac{\tau(\text{theory})}{\tau(\text{measured})} = \frac{G^2_{\nu_e\tau}}{G_F^2} + \frac{G^2_{\nu_\mu\tau}}{G_F^2} + \frac{G^2_{\nu_\tau\tau}}{G_F^2}$$

The measured value of the lifetime, $\approx(4.7\pm2)\times10^{-13}$s [41], gives

$$\frac{\tau(\text{theory})}{\tau(\text{measured})} = 0.6\pm^{0.4}_{0.2},$$

and the experimental limit (inferred from reactor $\bar{\nu}_e$ data [39]) to the value of $G^2_{\nu_e\tau}$ is

$$\frac{G^2_{\nu_e\tau}}{G_F^2} < 0.1 \quad (90\%\ \text{C.L.}),$$

so

$$\frac{G^2_{\nu_\tau\tau}}{G_F^2} > 0.5\pm^{0.4}_{0.2} \quad (90\%\ \text{C.L.})$$

This indicates that the tau is coupled to some neutrino other than the muon neutrino or electron neutrino: a "tau neutrino" must exist.

(The conclusion is weakened if large CP violation is allowed. The result actually uses $G^2_{\nu_\mu\tau}-$, $G^2_{\nu_e\tau}+$, and charge-averaged tau lifetime measurements; the limits to $G^2_{\bar{\nu}_\mu\tau}+$ and $G^2_{\nu_e\tau}-$ are weaker, and there are no separate measurements of τ^- or τ^+ lifetimes.)

5.4 Limit to $\nu_\mu \to \nu_\tau$ Oscillations

5.4.1 Phenomenology of Neutrino Oscillations [153]

Starting with an initial neutrino ν_α (a weak eigenstate) with energy E, the probability that the neutrino will be a ν_β (a possibly different weak eigenstate) after travelling a distance L is (for $E>>m_\nu$) [154]

$$P(\nu_\alpha\to\nu_\beta) = \delta_{\alpha\beta} + \sum_{i<j} 2\left|U_{\alpha i}U^*_{\beta i}U^*_{\alpha j}U_{\beta j}\right| \cdot \left[\cos(\Delta_{ij}-\Phi_{\alpha\beta ij})-\cos\Phi_{\alpha\beta ij}\right]$$

where the index α refers to neutrino weak eigenstates, the index i refers to the neutrino mass eigenstates (of mass m_i),

$$\Delta_{ij} = \tfrac{1}{2}|m_i^2 - m_j^2|(L/E),$$

and

$$\Phi_{\alpha\beta ij} = \arg\left(U_{\alpha i}U_{\beta i}^{*}U_{\alpha j}^{*}U_{\beta j}\right),$$

(For antineutrinos, interchange U and U^*.)

If CP is conserved, and if only two neutrino mixing is considered, then

$$P(\nu_\alpha \to \nu_\beta) = \delta_{\alpha\beta} - \sin^2 2\Theta_{\alpha\beta}\sin^2(1.27\Delta m_{ij}^2 L/E) \qquad \{5.4\}$$

where $\Theta_{\alpha\beta}$ is the mixing angle between the ν_α and ν_β weak eigenstates, $\Delta m_{ij}^2 = |m_i^2 - m_j^2|$ (in eV^2/c^4), and L/E is in m/MeV.

5.4.2 Limit to Δm^2 vs θ

To interpret this experiment's limit to τ^- production in terms of $\nu_\mu \to \nu_\tau$ oscillations, a two neutrino (ν_μ,ν_τ) mixing is considered. The probability that a ν_μ has oscillated into a ν_τ is, from Eqn. {5.4},

$$P(\nu_\mu \to \nu_\tau) = \sin^2(2\theta)\cdot\sin^2\left(1.27\Delta m^2 \frac{L}{E}\right)$$

where $\theta(\sim\Theta_{\alpha\beta})$ is the mixing angle between ν_μ and ν_τ, and $\Delta m^2 = |m_{\nu_\mu}^2 - m_{\nu_\tau}^2|$ ($=\Delta m_{23}^2$) is the mass-squared difference between the mass states (ν_2 and ν_3) dominated by the ν_μ and ν_τ weak eigenstates.

For real neutrino beams, which are neither monochromatic nor from a point source, this probability becomes

$$P(\nu_\mu \to \nu_\tau) = \sin^2(2\theta)\int d(L/E)\rho_\tau(L/E)\sin^2(1.27\Delta m^2 L/E) \quad .$$

The probability is integrated over the distributions of neutrino energy (E) and neutrino path length (L). (L for an E-531 neutrino is the

distance between the experiment and the point in decay pipe (Sec. 2.1) where the neutrino was produced. Hence L is always between 540 and 950 metres and the distribution is almost flat.) $\rho_\tau(L/E)$ is the L/E spectrum predicted for found charged current ν_τ events (Figure 5-6); this is calculated from the predicted energy spectrum [$N_\tau(E) = C \cdot K(E) \cdot N_\mu(E)$] and the known beam geometry.

The limit to Δm^2 and $\sin^2(2\theta)$, from $P(\nu_\mu \rightarrow \nu_\tau) < 0.63\%$, is shown in Figure 5-7. The minimum value of $\sin^2(2\theta)$ to which we are sensitive is 0.011, the asymptotic (large Δm^2) $\sin^2(2\theta)$ limit is 0.013, and for maximum mixing ($\sin^2(2\theta)=1$) $\Delta m^2 < 3.0$ eV (90%C.L.).

Figure 5-8 shows the oscillation limit of this experiment (Fig. 5-7) together with previous limits (Fig. 1-5). The E-531 result is a significant improvement to the limit to the ν_μ-ν_τ mixing angle, and it complements the previous experiments by being the first limit set by a direct search for tau lepton decays.

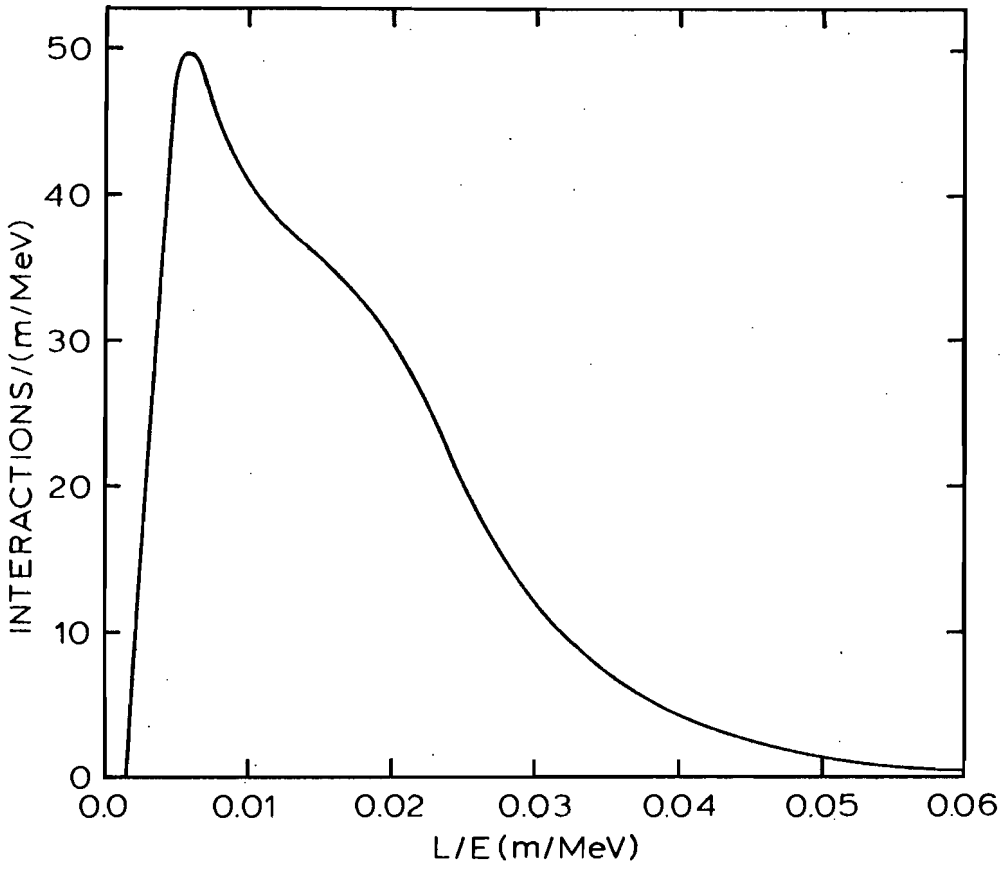

Figure 5-6: Predicted L/E spectrum for found $\nu_\tau \to \tau^-$ interactions (normalized to unity). The mean L/E is 0.018, and 98% of the spectrum is in the range $0.003 < L/E < 0.058$.

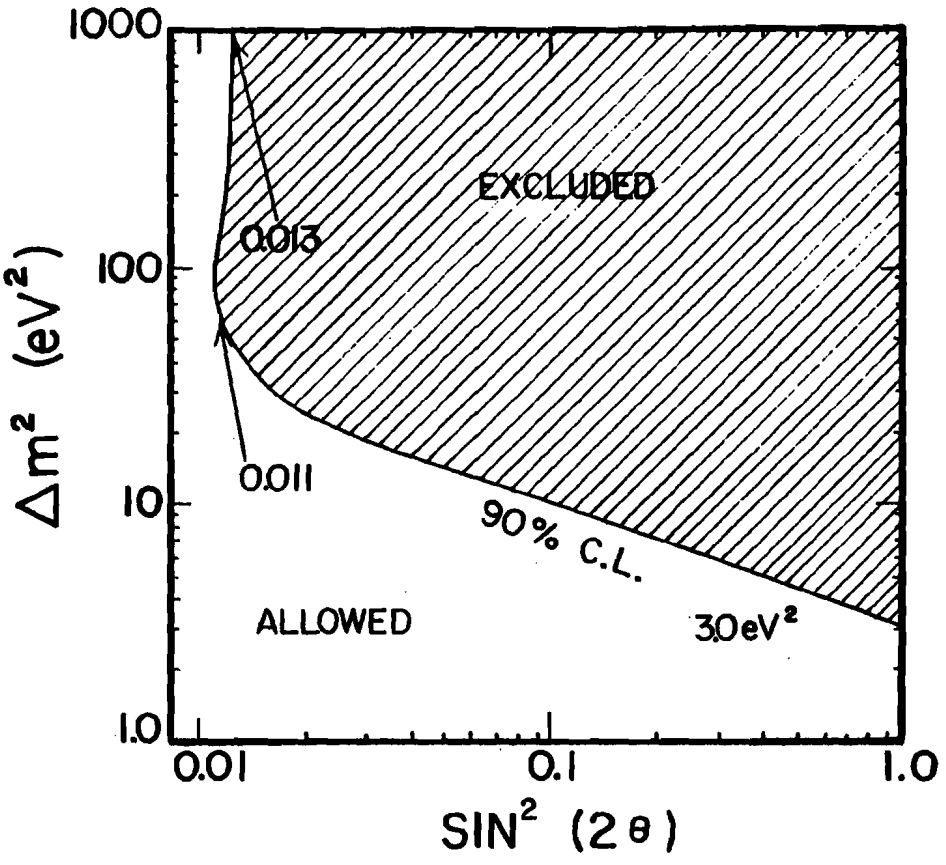

Figure 5-7: Δm^2 vs $\sin^2(2\theta)$ limit curve (90% C.L.) from this experiment for $\nu_\mu \rightarrow \nu_\tau$ oscillations.

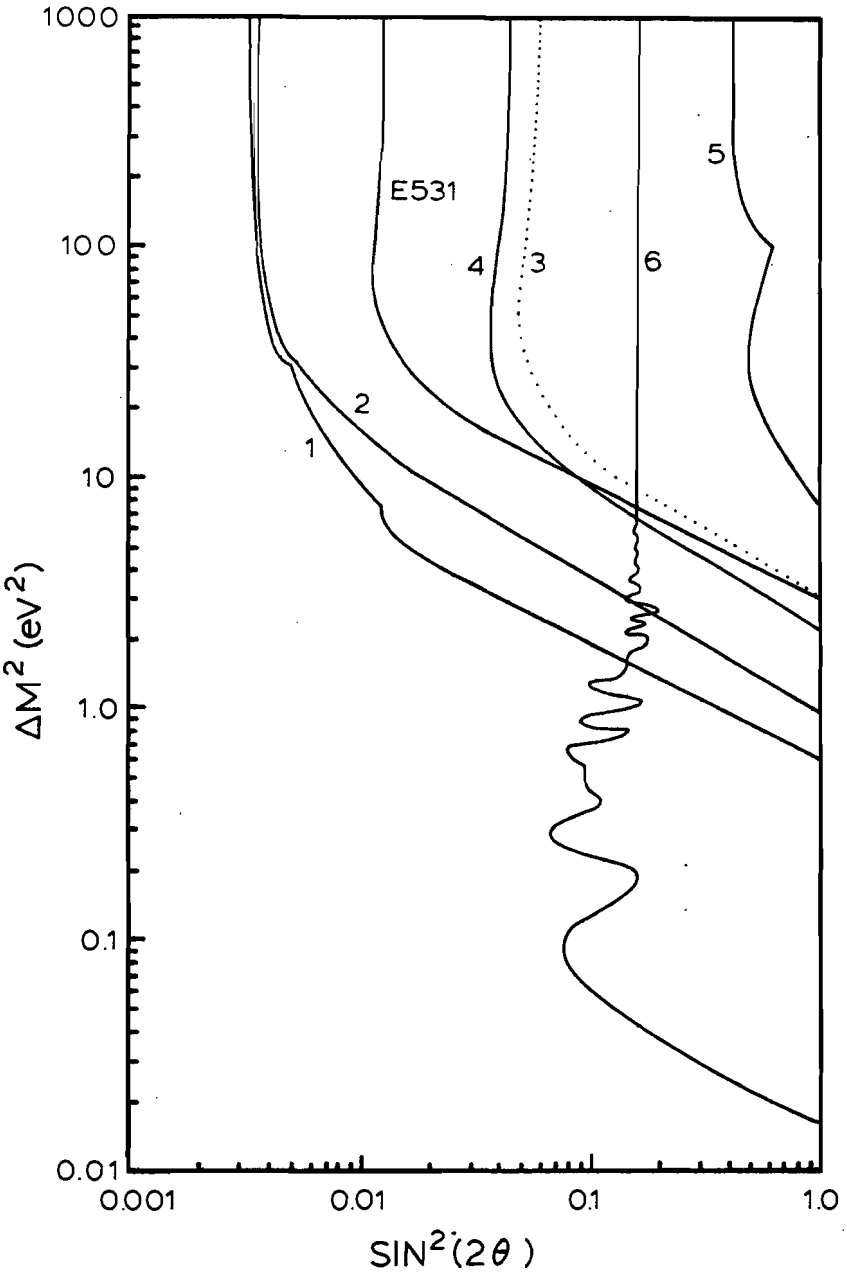

Figure 5-8: World limits (90% C.L.) to neutrino mixings.

1.	ν_μ-ν_e	2. $\bar{\nu}_\mu$-$\bar{\nu}_e$
E-531	ν_μ-ν_τ (this experiment)	4. $\bar{\nu}_\mu$-$\bar{\nu}_\tau$
5.	ν_e-ν_x	6. $\bar{\nu}_e$-$\bar{\nu}_x$

(This is an updated version of Fig. 1-5. Curve 3 is the previous limit to ν_μ-ν_τ mixing.)

References and Footnotes

[1] J.J.Aubert et al., Phys. Rev. Lett. 33 (1974) 1404.
J.-E.Augustin et al., Phys. Rev. Lett. 33 (1974) 1406.

[2] B.J.Bjorken and S.L.Glashow, Phys. Lett. 11 (1964) 255.
S.L.Glashow, J.Iliopoulos and L.Maiani, Phys. Rev. D2 (1970) 1285.

[3] M.L.Perl et al., Phys. Rev. Lett. 35 (1975) 1489.
M.L.Perl et al., Phys. Lett. 63B (1976) 466.
The tau lepton is reviewed by Martin L. Perl,
Ann. Rev. Nucl. Part. Sci. 30 (1980) 299.

[4] S.W.Herb et al., Phys. Rev. Lett. 39 (1977) 252.
W.R.Innes et al., Phys. Rev. Lett. 39 (1977) 1240.

[5] N.Ushida et al., Phys. Rev. Lett. 45 (1980) 1049.

[6] N.Ushida et al., Phys. Rev. Lett. 45 (1980) 1053.

[7] Michael Gutzwiller, Ph.D. thesis, The Ohio State University (1981), unpublished.

[8] Steve Errede, Ph.D. thesis, The Ohio State University (1981), unpublished.

[9] Hiroshi Shibuya, Ph.D. Thesis, Nagoya University (1982), unpublished.

[10] Toshio Hara, Ph.D. thesis,
Osaka City University (1982), unpublished.

[11] N.Ushida et al., Phys. Rev. Lett. 48 (1982) 844.

[12] Dale Pitman, Ph.D. thesis, University of Toronto (1983), unpublished.

[13] N.Ushida et al., New results for the lifetimes of the D^+, F^+, and Λ_c^+ particles, to be submitted to Phys. Rev. Lett.

[14] D.Allasia et al., Nucl. Phys. B176 (1980) 13, and references 7-11 therein.
D.S.Baranov et al., Phys. Lett. 26 (1977) 269; Yad. Fiz. 27 (1978) 362.
R.D.Ammar et al., Phys. Lett. 94B (1980) 118.

[15] E.G.Cazzoli et al., Phys. Rev. Lett. 34 (1975) 1125.
A.M.Cnops et al., Phys. Rev. Lett. 42 (1979) 197.
J.Blietschau et al., Phys. Lett. 86B (1979) 108.
M.Calicchio et al., Phys. Lett. 93B (1980) 521.
H.Grässler et al., Phys. Lett. 99B (1980) 159.
P.C.Bosetti et al., Phys. Lett. 109B (1982) 234.
See also Ref. 160.

[16] C.Baltay et al., Phys. Rev. Lett. 41 (1978) 73.
C.Baltay et al., Phys. Rev. Lett. 42 (1979) 1721.
T.Kitigaki et al., Phys. Rev. Lett. 45 (1980) 955.
T.Kitigaki et al., Phys. Rev. Lett. 48 (1980) 299.

[17] H.C.Ballagh et al., Phys. Lett. 89B (1980) 423.

[18] D.Son et al., Phys. Rev. Lett. 49 (1982) 1128.
P.Bosetti et al., Nucl. Phys. B209 (1982) 29.
H.Grassler et al., Nucl. Phys. B194 (1982) 1.
S.J.Barish et al., Phys. Rev. Lett. 45 (1980) 783.
V.V.Ammosov et al., Nucl. Phys. B177 (1981) 365.
Also Refs. 54 and 160.

[19] For reviews of dilepton data see Refs. 132 and 161;
see also Refs. 20, 123, 124, 122, 162, 163, 164, 165, 166.

[20] H.Abramowicz et al., CERN-EP/82-77 (1982), submitted to Zeitschrift für Physik.

[21] Haim Harari, "Quarks and Leptons", Phys.Reports 42 (1978) 235.

[22] W.Marciano and H.Pagels, "Quantum Chromodynamics", Phys.Reports 36 (1978) 137.

[23] O.W.Greenberg and C.A.Nelson, "Colour Models of Hadrons", Phys.Reports 3 (1972) 261.
O.W.Greenberg, "Quarks", Ann. Rev. Nucl. Part. Sci. 28 (1980) 327.

[24] A.Etkin et al., Phys. Rev. Lett. 49 (1982) 1620.
C.Edwards et al., Phys. Rev. Lett. 49 (1982) 259.
M.Chanowitz et al, Phys. Rev. Lett. 46 (1981) 981.
J.J.Coyne, P.M.Fishbane, and S.Meshkov, Phys. Lett. 91B (1980) 259.

[25] H.Fritzsch and P.Minkowski, "Quantum Flavordynamics", Phys.Reports 73 (1981) 67.

[26] Makoto Kobayashi and Toshihide Maskawa, Prog.Theor.Phys. 49 (1973) 652.

[27] Nicola Cabibbo, Phys. Rev. Lett. 10 (1963) 531.
See also Ref. 2.

[28] R.E.Shrock, S.B.Treiman, and L.-L.Wang, Phys. Rev. Lett. 42 (1979) 1589.

[29] There is one report of possible electron antineutrino oscillations: F.Reines, H.W.Sobel, and E.Pasierb, Phys. Rev. Lett. 45 (1980) 1307. This observation is in conflict with the limit of Ref. 39.

[30] V.A.Lubimov et al., Phys. Lett. 94B (1980) 266.

[31] T.Goldman and G.J.Stephenson Jr., Phys. Rev. D24 (1981) 236.

[32] J.Blietschau et al., Nucl. Phys. B133 (1978) 205.

[33] N.J.Baker et al., Phys. Rev. Lett. 47 (1981) 1576, and A.M.Cnops et al., Phys. Rev. Lett. 40 (1978) 144.

[34] O.Erriquez et al., Phys. Lett. 102B (1981) 73.

[35] N.Armenise et al., Phys. Lett. 100B (1981) 182.

[36] E.Bellotti et al., Lett. Nuovo Cim. 17 (1976) 533.

[37] A.E.Asratyan et al., Phys. Lett. 105B (1981) 301.

[38] H.Deden et al., Phys. Lett. 98B (1981) 310.

[39] J.L.Vuilleumier et al., Phys. Lett. 114B (1982) 298, and F.Boehm et al., Phys. Lett. 97B (1980) 310.

[40] These values are based on Ref. 109 and on the review of tau parameters of G.Flugge, Karlsruhe Preprint KfK 2995 (1980) and the experimental and theoretical references therein. See also [65].

[41] Published (non-zero) values are

MARK II	$(4.6\pm1.9)\times10^{-13}$s	G.J.Feldman et al., Phys. Rev. Lett. 48 (1982) 66;
MAC	$(4.9\pm2.0)\times10^{-13}$s	W.T.Ford et al., Phys. Rev. Lett. 49 (1982) 106;
CELLO	$(4.7\pm^{3.9}_{2.9})\times10^{-13}$s	H.-J.Behrend et al., Nucl. Phys. B211 (1983) 369.

Unpublished measurements are

TASSO	$(0.8\pm2.2)\times10^{-13}$s
MARK II	$(3.31\pm0.57\pm0.7)\times10^{-13}$s
MAC	$(4.1\pm1.1\pm1.2)\times10^{-13}$s

all reported by G.Kalmus, XXI International Conference on High Energy Physics, (Paris, July 1982).

[42] C.H.Llewellyn Smith, "Neutrino Reactions at Accelerator Energies", Phys.Reports 3 (1972) 261.

[43] Fermi motion effects in deep-inelastic lepton scattering from nuclei are discussed by A.Bodek and J.L.Ritchie, Phys. Rev. D23 (1981) 1070.

[44] The ocean quark content of the nucleon is $2(\bar{U}+\bar{D}+\bar{S})=0.26\pm0.03$, as calculated from the results of the CDHS(B) collaboration [20,176,175]; see also Refs. 45 and 178.

[45] A review of neutrino data on structure functions is given by A.Para, Rapporteur's talk in: Proceedings of the 1979 International Symposium on Lepton and Photon Interactions at High Energies, eds. T.B.W.Kirk and H.D.I.Abarbanel (Fermilab, USA, 1979) p.359.

[46] Average from results of Refs. 176 and 177; see also Ref. 45.

[47] Howard Georgi and H.David Politzer, Phys. Rev. D14 (1976) 1829. R.Barbieri, J.Ellis, M.K.Gaillard, and G.G.Ross, Nucl. PHys. B117 (1976) 50.

[48] (a) Bruce Campbell, Ph.D. thesis, McGill University, (1979), unpublished, and
(b) Y.Afek et al., Z.Phys. C6 (1980) 251.

[49] Thomas Gottschalk, Phys. Rev. D23 (1981) 56.

[50] Choy-Heng Lai, Phys. Rev. D18 (1978) 1422.

[51] I have calculated this S/D ratio from the results of Ref. 20.

[52] J.Bell et al., Phys. Rev. Lett. 41 (1978) 1008.
P.Allen et al., Nucl. Phys. B176 (1980) 269.

[53] J.Finjord and F.Ravndal, Phys. Lett. 58B (1975) 61.
R.E.Shrock and B.W.Lee, Phys. Rev. D13 (1976) 2539.
A.Amer et al., Phys. Lett. 81B (1979) 48.
C.Avilez et al., Phys. Rev. D17 (1978) 709.
C.Avilez and T.Kobayashi, Phys. Rev. D19 (1979) 3448.

[54] N.Armenise et al., Phys. Lett. 104B (1981) 409.

[55] M.K.Gaillard, S.A.Jackson, and D.V.Nanopoulos,
Nucl. Phys. B102 (1976) 326; B112 (1976) 545.

[56] See Pg.6-6 of Ref. 48a, also Ref. 47.

[57] J.J.Aubert et al., Phys. Lett. 110B (1982) 73.

[58] Calculated from rate given by H.Abramowicz et al.,
Phys. Lett. 109B (1982) 115.

[59] B.Andersson, G.Gustafson and T.Sjöstrand, Z.Physik C6 (1980) 235.
R.P.Feynman and R.D.Field, Nucl. Phys. B136 (1978) 1.

[60] B.Andersson and G.Gustafson, LUND Preprint LU TP 82-5 (May 1982).

[61] (a) A review of "Hadron Production in Lepton-Nucleon Scattering"
is given by P.Renton and W.S.C.Williams, Ann. Rev. Nucl.
Part. Sci. 31 (1981) 193.
(b) Tasso Collaboration: M.Althoff et al., DESY 82-070 (Oct. 1982),
submitted to Z. Phys. C; R.Brandelik et al., Phys. Lett.
105V (1981) 75 and 94B (1980) 91.
(c) V.V.Ammosov et al., Phys. Lett. 93B (1980) 210.
J.F.Martin et al., Phys. Rev. Lett. 40 (1978) 283.
W.F.Baker et al., Phys. Lett. 51B (1974) 303.
See Refs. 18, 160, and 99.

[62] (a) B.Andersson, G.Gustafson and T.Sjöstrand,
Nucl. Phys. B197 (1982) 45.
A.Bartl, H.Fraas and W.Majerotto, Phys. Rev. D26 (1982) 1061.
(b) Reference 59.

[63] W.J.Marciano and A.Sirlin, Phys. Rev. Lett. 46 (1981) 163.

[64] Quark Masses", J.Gasser and H.Leutwyler,
Phys. Reports 87 (1982) 77.

[65] Particle Data Group, "Review of Particle Properties",
Phys. Lett. 111B (April 1982).

[66] George H. Trilling, "Charmed Particles",
Phys.Reports 75 (1981) 57.

[67] George Kalmus, Rapporteur's talk at XXIth International
Conference on High Energy Physics (Paris, July 1982).

[68] R.E.Shrock and L.-L.Wang, Phys. Rev. Lett. 41 (1978) 1692.

[69] S.Pakvasa, S.F.Tuan, and J.J.Sakurai, Phys. Rev. D23 (1981) 2799.

[70] E.A.Paschos and U.Türke, Phys. Lett. 116B (1982) 360.

[71] L.J.Spencer et al., Phys. Rev. Lett. 47 (1981) 771.
A.Brody et al., Phys. Rev. Lett. 48 (1982) 1070.

[72] R.E.Shrock and M.B.Voloshin, Phys. Lett. 87B (1979) 375.

[73] JADE Collaboration: W.Bartel et al., Phys. Lett. 114B (1982) 71.

[74] Ref. 123,162,163,164,165,166,174.

[75] J.R.Sanford, Ann.Rev.Nucl.Sci. 26 (1976) 151.

[76] J.Grimson and S.Mori, Fermilab Technical Memo TM-824
(1978), unpublished.

[77] New England Nuclear, Pilot Chemicals Division, 36 Pleasant St.,
Waterton, Mass. 02172, U.S.A.

[78] RCA, Electronics Components, Harrison N.J. 07029, U.S.A.

[79] Perfection Mica Company, Magnetic Shield Division,
740 North Thomas Drive, Bensenville, Illinois, U.S.A.

[80] LeCroy Research Systems Corp., 700 South Main St., Spring Valley,
New York 10977, U.S.A.

[81] Amperex Electronic Corporation, Hicksville Division,
Hicksville, Long Island, N.Y., U.S.A.

[82] H.Hinterberger and R.Winston, Rev.Sci.Inst. 37 (1966) 1094.

[83] "Time-of-Flight Measurements" are reviewed by William B. Atwood,
SLAC-PUB-2620, presented at the 1980 SLAC Summer Institute,
Stanford, CA, USA.

[84] The "Status of Timing with Plastic Scintillator Detectors" is reviewed by M.Moszyński and B.Bengston, Nucl. Inst. and Meth. 158 (1979) 1.

[85] References 8 and 12 give more detailed descriptions of the drift chamber system; see also Dale Pitman, M.Sc. thesis, University of Toronto (1980), unpublished.

[86] The NIM standard for nuclear instrument modules, as developed by the NIM committee of the U.S. Atomic Energy Commision, is described in U.S. government document TID-20893.

[87] See [8] and [12]; the system is similar to that described in: W.Sippach, "Nevis Drift Chamber TDC System" and "8-Channel Time Recorder Module for Drift Chamber Readout System", Nevis Labs (1977), unpublished.

[88] Lead glass arrays are described in more detail by Roland Egloff, Ph.D. thesis, University of Toronto, 1979; (The lead glass blocks were purchased from Schott Optical Glass,Inc., Duryea, PA, USA, and Bourns,Inc., New Providence, NJ, USA.)

[89] A.Bodek, in: "Proceedings of the Calorimeter Workshop", ed. M.Atac (Fermilab, Batavia, USA, May 1975), p229.

[90] A.Grant, Nucl. Inst. and Meth. 131 (1975) 167.

[91] The CAMAC (Computer Automated Measurement And Control) standard, as developed by the NIM committee of the U.S. AEC and the ESONE committee of European Laboratories, is described in "CAMAC Tutorial Articles", U.S. government document TID-26618, and references therein.

[92] Data General Corp., Southboro, MA, USA.

[93] B.McLeod, M.Sc. thesis, University of Ottawa (1982), unpublished.

[94] V.L.Highland, Nucl. Inst. and Meth. 129 (1975) 497; 161 (1979) 171.

[95] C.F.Powell, P.H.Fowler, D.H.Perkins, "The Study of Elemaentary Particles by the Photographic Method", Pergamon Press, London, 1959.

[96] Walter H. Barkas, "Nuclear Research Emulsions", Academic Press, New York, 1963.

[97] K.Niu, Proceedings of the XXth International Conference on High Energy Physics (Madison, USA, 1980) vol. 1, p. 352.

[98] Ashigara Research Laboratories, Fuji Photo Film Co., Ltd., Japan.

[99] R.J.Stefanski and H.B.White, Fermilab Note FN-292 (1976), unpublished.

[100] The horn parameters are described in Ref. 76. The beam simulation is similar to that described in Refs. 76 and 101.

[101] S.Mori, Fermilab Technical Memo TM-888 (1979), unpublished.

[102] T.Kondo, Fermilab (now at KEK, Japan), personal communications.

[103] Jim Hanlon, Illinois Institute of Technology, private communication; see also, T.Kitigaki et al., Phys. Rev. Lett. 49 (1982) 98.

[104] Klaus Winter, Rapporteur's talk in: Proceedings of the 1979 International Symposium on Lepton and Photon Interactions at High Energies, eds. T.B.W.Kirk and H.D.I.Abarbanel (Fermilab, USA, 1979) p. 258.
T.Kafka et al., Phys. Rev. Lett. 48 (1982) 910.

[105] M.Gluck, E.Hoffmann, and E.Reya, Dortmund preprint DO-TH 80/13 (May 1980).

[106] Z.Koba, H.B.Nielsen, and P.Olesen, Nucl. Phys. B40 (1972) 317. KNO scaling is a prediction for the asymptotic limit, but it works quite well even at surprisingly low energies; see Ref. 170.

[107] E.V.Anzon et al., Yad. Fiz. 22 (1975) 736 (Sov. J. Nucl. Phys. 22 (1975) 380).

[108] The E-531 charm decay reconstruction, kinematic fitting, and charmed particle identification procedures are disscussed in more detail in Refs. 7, 8, 12.

[109] Particle Data Group, "Review of Particle Properties", Rev.Mod.Phys. 52,#2 (1980).

[110] A.G.Frodesen, O.Skjeggestad and H.Tofte, "Probability and Statistics in Particle Physics", Universitetsforlaget, 1979, p.225-229.

[111] C.Quigg and J.L.Rosner, Phys. Rev. D17 (1978) 239.

[112] Weighted average of rates from Refs. 113 and 137.

[113] R.H.Schindler et al., Phys. Rev. D24 (1981) 78;
R.H.Schindler, thesis, SLAC Report No. SLAC-219 (1979), unpublished.

[114] See, for example, G.Bunce., Nucl. Inst. and Meth. 172 (1980) 553.

[115] See Ref. 110, and for examples, Refs. 7,8, and 12.

[116] P.Allen et al., Nucl. Phys. B181 (1981) 385.
These data agree with results of Ref. 167; very recent νD_2 data [168] give $\langle n_{ch}\rangle=(0.05\pm0.06)+(1.43\pm0.02)\ln W^2$ for $W^2>3$GeV. Antineutrino data is similar [169].

[117] J.W.Chapman et al., Phys. Rev. Lett. 36 (1976) 124.

[118] The emulsion nuclei have 4% more d quarks than u quarks (see Table 2-1), so I have made a corresponding correction to the predictions of Campbell [48] which are calculated for an isoscalar target.

[119] E.Vella et al., Phys. Rev. Lett. 48 (1982) 1515.

[120] From the D^o lifetime (measured by E-531) and the theoretical semileptonic decay width [171,172], the semileptonic branching ratio is calculated to be $B.R.(D^o\rightarrow eX)=5\pm\frac{4}{3}\%$ [8]; direct measurements give values of $5.5\pm3.7\%$ [113] and $<4\%$ (95%C.L.) [173].

[121] The F^+ semileptonic branching ratio can be calculated to be $4\pm\frac{5}{4}\%$ [8] from the lifetime and simple theory, but F decays are not as simple as D decays, and branching ratios of as large as 15-20% have been predicted, (K.Shizuya, Phys. Lett. 105B (1981) 406.)

[122] N.Armenise et al., Phys. Lett. 86B (1979) 115.

[123] C.Baltay et al., Phys. Rev. Lett. 39 (1977) 62, and C.Baltay, in: Proceedings of the 1979 JINR-CERN School of Physics, September 1979, (Hungarian Academy of Sciences, Budapest, 1980) p. 72; see also Refs. 132 and 161.

[124] H.C.Ballagh et al., Phys. Rev. D21 (1980) 569.

[125] M.Holder et al. Phys. Lett. 74B (1978) 277.

[126] V.Efremenko et al., Phys. Lett. 88B (1979) 181.

[127] F.Buccella and L.Oliver, Nucl. Phys. B162 (1980) 237.

[128] R.D.Schamberger et al., Phys. Rev. D26 720.

[129] I use $\langle z_{beauty} \rangle \approx 0.87$, based on Table 1 of reference 140.

[130] M.S.Alam et al., Phys. Rev. Lett. 49 (1982) 357.

[131] J.Ellis, M.K.Gaillard, D.V.Nanopoulos, and S.Rudaz, Nucl. Phys. B131 (1977) 285.

[132] M.J.Murtagh, Rapporteur's talk in: Proceedings of the 1979 International Symposium on Lepton and Photon Interactions at High Energies, eds. T.B.W.Kirk and H.D.I.Abarbanel (Fermilab, USA, 1979) p. 291.

[133] R.M.Godbole and D.P.Roy, Phys. Rev. Lett. 48 (1982) 1711.

[134] Mahiko Suzuki, Phys. Lett. 71B (1977) 139.

[135] Campbell [48a] chooses $\beta=7$ based on Refs. 164, and 162b and 179, and this is in agreement with more recent data, e.g. $\beta=7\pm1$ from Ref. 149, see also Ref. 176.

[136] G.J.Feldman, in: Proceedings of 1977 Banff Summer Institute on Particles and Fields, eds. D.H.Boal and A.N.Kamal (Plenum, New York, 1978) p.75, and
G.Goldhaber et al., Phys. Lett. 69B (1977) 503.

[137] V.Vuillemin et al., Phys. Rev. Lett. 41 (1978) 1149.

[138] W.Buza et al., Phys. Rev. Lett. 34 (1975) 836, and references therein; see also Ref. 170.

[139] J.D.Bjorken, Phys. Rev. D17 (1978) 171.

[140] Jorge Dias de Deus, Nucl. Phys. B138 (1978) 465.

[141] J.M.Yelton et al., Phys. Rev. Lett. 49 (1982) 430.

[142] N.Schmitz, Rapporteur's talk in: Proceedings of the 1979 International Symposium on Lepton and Photon Interactions at High Energies, eds. T.B.W.Kirk and H.D.I.Abarbanel (Fermilab, USA, 1979) p.359.

[143] (a) Thomas A. DeGrand, Phys. Rev. D26 (1982) 3298.
(b) Reference 62a.

[144] (a) e^+e^- baryon production rates just above the Λ_c^+ production threshold are given by:
G.Abrams et al., Phys. Rev. Lett. 44 (1980) 10;
E.Vella et al., Phys. Rev. Lett. 48 (1982) 1515.
(b) The inferred e^+e^- charmed baryon rates of (a) should be compared to the D meson production data of:
P.A.Rapidis et al., Phys. Lett. 84B (1979) 507;
M.W.Coles et al., Phys. Rev. D26 (1982) 2190.
(c) e^+e^- baryon production rates much above the Λ_c^+ production threshold are given in Reference 61b.

[145] This curve is the sum of the down and strange curves in Fig. 5 of Ref. 48b.

[146] J.Ellis, M.K.Gaillard, D.V.Nanopoulos, and S.Rudaz, Nucl. Phys. B131 (1977) 285.
M.Gaillard and L.Maiani, Annecy-LAPP preprint LAPP-TH-09, 1979.
V.Barger, W.F.Long, and S.Pakvasa, J. Phys. G 5 (1979) L147.
S.-H.H.Tye, CLEO internal report CBX-81/9 (1981), unpublished.
Branko Gubering, Orsay Preprint LPTHE 82/5 (February 1982), unpublished.

[147] Columbia-Brookhaven collaboration, reported in Ref. 132.

[148] V.V.Ammosov et al., Phys. Lett. 106B (1981) 151.

[149] CHARM Collaboration: M.Jonker et al., Phys. Lett. 107B (1981) 241.

[150] This assumes a 10 μb F production cross section and B.R. $(F\to\tau\nu)\sim 3\%$.

[151] For a sample calculation of $d\sigma_\nu/dxdy$ for τ^- production, see K.Bongardt, Karlsruhe Preprint TKP 79-5 (1979); the E-531 ν_μ-τ^- coupling limit is 0.57% (instead of 0.63%) if calculated with the older structure function parameterization used by Bongardt. See also C.H.Albright and C.Jarlskog, Nucl. Phys. B84 (1975) 467.

[152] Since the completion of this analysis, new measurements of the tau kink branching ratio have been reported: 84±2% from CELLO (H.J.Behrend et al. Phys. Lett. 114B (1982) 282, and 86±2% from MARK II, C.A.Blocker et al., Phys. Rev. Lett. 49 (1982) 1369.

[153] S.M.Bilenky and B.Pontecorvo, Phys.Reports 41 (1978) 225.

[154] V.Barger, K.Whisnant, D.Cline, and R.J.N.Phillips, Phys. Lett. 93B (1980) 194.

[155] K.Bongardt, Karlsruhe preprint TKP79-5 (April 1979).

[156] V.Barger and R.J.N.Phillips, Nucl. Phys. B132 (1978) 249.

[157] M.Gluck and E.Reya, Nucl. Phys. B156 (1979) 456.

[158] A.J.Buras and K.J.F.Gaemers, Nucl. Phys. B132 (1978) 249.

[159] R.D.Field and R.P.Feynman, Phys. Rev. D15 (1977) 2590.

[160] P.Schreiner, Rapporteur's talk in: Proceedings of the 1979 International Symposium on Lepton and Photon Interactions at High Energies, eds. T.B.W.Kirk and H.D.I. Abarbanel (Fermilab, USA, 1979) p. 291.

[161] H.E.Fisk, Rapporteur's talk in: Proceedings of the 1981 International Symposium on Lepton and Photon Interactions at High Energies, ed. W.Pfeil (Physicalisches Institut, Universitat Bonn, 1981) p. 703.

[162] (a) A.Benvenuti et al., Phys. Rev. Lett. 34 (1975) 419; 35 (1975) 1199.
(b) A.Benvenuti et al., Phys. Rev. Lett. 41 (1978) 1204.

[163] B.C.Barish et al., Phys. Rev. Lett. 36 (1976) 939; 39 (1977) 981.

[164] M.Holder et al., Phys. Lett. 69B (1977) 377.

[165] J. Von Krogh et al., Phys. Rev. Lett. 36 (1976) 710; P.Bosetti et al., Phys. Rev. Lett. 38 (1977) 1248.

[166] H.Deden et al., Phys. Lett. 58B (1975) 361; J.Bleitschau et al., Phys. Lett. 60B (1976) 207.

[167] J.Bell et al., Phys. Rev. D19 (1979) 1.

[168] D.Zeiminska et al., Phys. Rev. D27 (1983) 47.

[169] M.Derrick et al., Phys. Rev. D17 (1978) 1.

[170] A review of experimental data for multiparticle production on nuclei is given by K.G.Gulamov, G.M.Chernov, and U.G.Gulyamov, Sov. J. Part. Nucl. 9 (1978) 226.

[171] M.K.Gaillard, B.W.Lee, and J.L.Rosner, Rev.Mod.Phys. 47 (1975) 277.

[172] G.Altarelli, N.Cabifbo, and L.Maiani, Nucl. Phys. B88, (1975) 285;
N.Cabibbo and L.Maiani, Phys.Lett 79B (1978) 109;
M.Suzuki, Nucl. Phys. B145 (1978) 420;
N.Cabibbo, G.Corbo, and L.Maiani, Nucl. Phys. B155 (1979) 93.

[173] W.Bacino et al., Phys. Rev. Lett. 45 (1979) 1073.

[174] P.C.Bosetti et al., Phys. Lett. 73B (1978) 380.

[175] J.G.H.deGroot et al., Zeit. fur Physik C1 (1979) 143.

[176] H.Abramowicz et al.: Neutrino and antineutrino charged-current inclusive scattering in iron in the energy range $20<E_\nu<300$ GeV, to be published in Z. Phys. C.; and Ref. 175.

[177] D.Allasia et al., Phys. Lett. 117B (1982) 262.

[178] M.Jonker et al., Phys. Lett. 102B (1981) 67.

[179] A.Benvenuti et al., 42 (1979) 149.

Appendix I: The E-531 Collaboration

N.Ushida
Aichi University of Education, Japan

T.Kondo
Fermi National Accelerator Laboratory, USA

G.Fujioka, H.Fukushima, Y.Homma, Y.Takahashi, S.Tatsumi,
Y.Tsuzuki and C.Yokoyama
Kobe University, Japan

S.Bahk, C.Kim, J.Park and J.Song
Korea University,, Korea

D.Bailey, S.Conetti, J.Fischer and J.Trischuk
McGill University, Canada

H.Fuchi, K.Hoshino, M.Miyanishi, K.Niu, K.Niwa, H.Shibuya and Y.Yanagisawa
Nagoya University, Japan

S.Errede, M.Gutzwiller, S.Kuramata, N.W.Reay, K.Reibel, T.A.Romanowski,
R.Sidwell and N.R.Stanton
Ohio State University, USA

K.Moriyama and H.Shibata
Okayama University, Japan

T.Hara, O.Kusumoto, Y.Noguchi and M.Teranaka
Osaka City University, Japan

H.Okabe and J.Yokota
Science Education Institute of Osaka Prefecture, Japan

J.Harnois, C.Hébért, J.Hébért, S.Lokanathan and B.McLeod
University of Ottawa, Canada

S.Tasaka
University of Tokyo, Japan

P.Davis, J.Martin, D.Pitman, J.D.Prentice, P.Sinervo and T.S.Yoon
University of Toronto, Canada

H.Kimura and Y.Maeda
Yokohama National University, Japan

Appendix II: Charm Events

This Appendix summarizes the characteristics of the E-531 charm decay candidate sample. Brief introductory remarks are given below; the event listings follow.

The value and Root-Mean-Square uncertainty of the parameters of each event are given in the form "value(uncertainty)".

Event is the E-531 Run-Record number of the event. Event 610-4088 is quasi-elastic Λ_c^+ production; the D^o-$\bar{D}^o$ charm pair is event 529-3013 and is at the bottom of the listings.

Particle is a brief code for the the type of charmed particle observed: D0 (for D^o), D0B ($\bar{D}^o$), D+ (D^+), D- (D^-), F+ (F^+), F- (F^-), L+ (Λ_c^+), C+ (ambiguous low momentum C^+ charmed particle decay candidates), and NB (neutral charmed baryon candidate).

Emulsion is a code that refers to the scanning group and emulsion module type: 1 is Osaka group (horizontal module), 2 is Kobe group (horizontal module), 3 is Ottawa group (horizontal module), 4 is Ottawa group (vertical module), and 5 is Nagoya group (vertical module).

NH, NS and ND are the number of heavily ionizing tracks from the primary neutrino interaction vertex, the number of shower tracks from the primary vertex, and the charged particle multiplicity of the charmed particle decay candidate.

Decay Length is the distance from the primary neutrino interaction vertex to the point of decay.

Weight is the charm event weight described in Sec. 3.12.2.

Fit is the number of constraints to the kinematic fit to the decay. 0-C is a calculation with zero constraints; 1-C and 3-C are fits with one and three constraints.

Decay Hypotheses are viable hypotheses for each decay. Only one decay hypothesis is given for identified decays. Secondary particles that

are underlined have been identified at the 90% confidence level; particles that are in brackets were not detected but their existence is inferred; particles that are not underlined and that are not in brackets were detected (observed) but not identified.

P_c, x'_c and y'_c are the momentum and slopes of the charmed particle candidate. ($x' \equiv \frac{dx}{dz}$ and $y' \equiv \frac{dy}{dz}$; z is defined by the neutrino beam direction, and x and y are horizontal and vertical axes.

E_H, P_μ, x'_μ and y'_μ are the total hadronic energy, primary muon momemtum, and slopes of the primary muon. Stars (***) indicate that no primary muon is identified in the event; an upper limit to the momentum of possible primary muon candidates is given.

E_ν, Q^2, and W (see Sec. 1.3) are the calculated total neutrino energy, square of the four-momentum transfer, and total mass of the hadronic system. x, ξ, and y (see Secs. 1.3 and 1.5.1) are the Bjorken x scaling variable, the slow rescaling variable for charm quark production, and the elasticity variable y. Except for E_ν and lower limits to y, values are not calculated for events in which no primary muon is identified.

Z and X_F (see Sec. 1.3) are the fragmentation variable and Feynman X; P_{out}, $P_\perp$, and ϕ_μ are the charmed particle momentum out of the ν-μ plane, the charmed particle momentum transverse to the calculated direction of the total hadronic system momentum, and the angle in the x-y plane between the charmed particle and the primary muon (see Sec. 4.13). Only Z can be calculated for events in which no primary muon is identified.

Event	Particle	Emulsion	NH	NS	ND	Decay Length (μm)	Weight	Fit
1. 476-4449	L+	4	20	12	3	27.2	1.13(0.07)	0-C
2. 478-2638	D0	5	1	3	6	126.0	1.50(0.17)	1-C
3. 486-6857	D0	5	1	4	4	256.0	1.55(0.18)	0-C
4. 493- 177	D0	5	0	3	2	324.0	1.53(0.17)	3-C
5. 493-1235	D+	2	3	4	3	2200.0	1.10(0.10)	3-C
6. 498-4985	L+	1	0	6	3	180.0	1.10(0.06)	3-C
7. 499-4713	L+	5	6	6	3	366.0	2.21(0.80)	1-C
8. 512-5761	D+	5	0	4	3	457.0	1.10(0.10)	3-C
9. 513-8010	D0B	5	0	5	4	27.0	1.50(0.17)	3-C
10. 518-4935	D0	5	0	2	2	116.0	1.70(0.19)	3-C
11. 522-2107	D+	1	14	4	3	13600.0	1.26(0.25)	0-C
12. 522-3061	D0	1	1	4	4	5480.0	1.78(0.20)	0-C
13. 527-3682	F-	2	7	5	3	670.0	1.08(0.06)	3-C
14. 529- 271	D+	5	0	5	1	2550.0	3.59(1.85)	0-C
15. 533-7152	D+	5	5	6	1	5350.0	3.38(1.68)	0-C
16. 546-1339	D+	2	1	9	3	2150.0	1.15(0.16)	0-C
17. 547-2197	D0	5	4	2	4	4060.0	1.66(0.19)	3-C
18. 547-3192	D+	1	1	11	3	185.0	1.10(0.11)	3-C
19. 547-3705	D0	5	0	3	4	748.0	1.56(0.18)	3-C
20. 549-4068	L+	5	4	8	3	20.6	1.21(0.10)	0-C
21. 556- 152	D0	5	3	2	4	41.0	1.58(0.18)	3-C
22. 567-2596	L+	2	6	6	1	175.0	2.16(0.78)	3-C
23. 577-5409	D0	5	6	7	2	67.0	1.53(0.17)	0-C
24. 580-4508	D-	5	2	4	3	2310.0	1.10(0.11)	0-C
25. 597-1851	F+	5	0	5	3	130.0	1.09(0.07)	3-C
26. 597-6914	D0	5	3	5	2	4370.0	1.77(0.20)	0-C
27. 598-1759	D+	5	1	2	3	1800.0	1.16(0.16)	3-C
28. 602-2032	L+	4	10	4	2	283.0	1.11(0.07)	0-C
29. 610-4088	L+	5	2	2	3	221.0	1.13(0.07)	3-C
30. 635-4949	NB	5	1	6	2	4390.0	1.75(0.90)	3-C
31. 638-5640	D0B	5	12	19	2	183.0	1.64(0.19)	3-C
32. 638-9417	F+	5	1	3	3	153.0	1.12(0.08)	3-C
33. 650-6003	L+	5	0	7	3	41.0	1.12(0.07)	3-C
34. 654-3711	D0	2	1	4	6	6.5	1.62(0.18)	1-C
35. 656-2631	D+	5	6	5	3	570.0	1.32(0.29)	3-C
36. 661-2729	D0	5	0	2	4	734.0	1.54(0.18)	3-C
37. 661-6517	D0	5	3	5	2	2650.0	1.70(0.19)	0-C
38. 663-7758	D+	5	0	6	3	13000.0	2.15(0.97)	0-C
39. 665-2113	C+	5	2	5	3	33.0	0.69(0.06)	0-C
40. 666-5294	D0	5	2	4	4	653.0	1.82(0.20)	3-C
41. 670- 12	C+	5	4	4	3	56.0	0.76(0.07)	0-C
42. 670-7870	D0B	5	0	7	2	187.0	1.47(0.17)	0-C
43. 671-2642	C+	5	7	4	3	2350.0	0.69(0.06)	0-C
44. 529-3013	D0	5	0	8	2	626.0	1.49(0.44)	3-C
45. 529-3013	D0B	5	0	8	2	3310.0	1.49(0.44)	3-C

	Event	Particle	Decay Hypotheses and Comments
1.	476-4449	L+	$\Lambda_c^+ \to p\underline{\pi}^+\underline{\pi}^-(K_L^o)$
2.	478-2638	DO	$D^o \to \underline{\pi}^-\pi^-\underline{\pi}^+\underline{\pi}^+K^-\pi^+\pi^o$; one γ from $\pi^o \to \gamma\gamma$ decay not seen
3.	486-6857	DO	$D^o \to K^-\pi^-\underline{\pi}^+\pi^+(\pi^o)$; from D^{*+}
4.	493- 177	DO	$D^o \to \bar{K}^o\pi^+\underline{\pi}^-$; $\bar{D}^o$ hypothesis possible
5.	493-1235	D+	$D^+ \to \pi^+\pi^+\pi^-K_L^o$, $F^+ \to \pi^+\pi^+K^-K_L^o$, $\Lambda_c^+ \to \pi^+\pi^+K^-n$; anti-charm hypotheses possible
6.	498-4985	L+	$\Lambda_c^+ \to \underline{\Lambda}^o\underline{\pi}^+\underline{\pi}^-\underline{\pi}^+$
7.	499-4713	L+	$\Lambda_c^+ \to \underline{\Sigma}^o\pi^+$; γ from $\Sigma^o \to \Lambda^o\gamma$ decay not seen
8.	512-5761	D+	$D^+ \to K^-\pi^+\pi^+\pi^o$, $F^+ \to K^-K^+\pi^+\pi^o$
9.	513-8010	DOB	$\bar{D}^o \to K^+\pi^+\underline{\pi}^-\underline{\pi}^-\pi^o$
10.	518-4935	DO	$D^o \to \pi^+K^-\pi^o\pi^o$; $\bar{D}^o$ hypothesis possible
11.	522-2107	D+	$D^+ \to \pi^+\underline{\pi}^+K^-(\pi^o)$, $F^+ \to K^+\underline{\pi}^+K^-(\pi^o)$, $\Lambda_c^+ \to p\underline{\pi}^+K^-(\pi^o)$
12.	522-3061	DO	$D^o \to \pi^-\pi^+\underline{\mu}^+K^-(\nu_\mu)$
13.	527-3682	F-	$F^- \to \underline{\pi}^+\underline{\pi}^-\pi^-\pi^o$
14.	529- 271	D+	$D^+ \to \pi^+\pi^o(K_L^o)$, $F^+ \to K^+K_L^o$, $F^+ \to K^+\pi^o(K_L^o)$
15.	533-7152	D+	$D^+ \to \pi^+\pi^o(K_L^o)$, $F^+ \to K^+(K_L^o)$
16.	546-1339	D+	$D^+ \to K^-\pi^+\underline{\mu}^+(\nu_\mu)$ $D^o \to \pi^+\pi^-\underline{\pi}^+K^-\pi^o$
17.	547-2197	DO	$D^o \to \pi^+\pi^-\underline{\pi}^+K^-\pi^o$
18.	547-3192	D+	$D^+ \to \pi^+K^-\pi^+$, $D^+ \to \pi^+K^-\pi^+\pi^o$, $F^+ \to \pi^+\pi^-\pi^+\pi^o$, $\Lambda_c^+ \to \pi^+\pi^+K^-(n)$; anti-charm hypotheses possible
19.	547-3705	DO	$D^o \to K^-\pi^+\underline{\pi}^+\pi^-$; from D^{*+}
20.	549-4068	L+	$\Lambda_c^+ \to \underline{p}K^-\underline{\pi}^+(\pi^o)$
21.	556- 152	DO	$D^o \to \pi^-K^-\underline{\pi}^+\underline{\pi}^+\pi^o$; from D^{*+}
22.	567-2596	L+	$\Lambda_c^+ \to \underline{p}K_L^o$
23.	577-5409	DO	$D^o \to \pi^+\underline{\pi}^-(\bar{K}^o)$; from D^{*+}
24.	580-4508	D-	$D^- \to \pi^+\underline{K}^+\underline{e}^-(\bar{\nu}_e)$
25.	597-1851	F+	$F^+ \to \underline{K}^-\underline{\pi}^+\underline{\pi}^+K_L^o$
26.	597-6914	DO	$D^o \to \underline{e}^+K^-(\nu_e)$

27. 598-1759 D+ $D^+ \to K^- K^+ \underline{\pi}^+ \pi^o$, $\Lambda_c^+ \to K^- p \underline{\pi}^+ \pi^o$, $D^+ \to \pi^- \pi^+ \underline{\pi}^+ (\bar{K}^o)$, $F^+ \to K^- \pi^+ \underline{\pi}^+ (\bar{K}^o)$, $F^+ \to K^- K^+ \pi^+ \pi^o (\pi^o)$

28. 602-2032 L+ $\Lambda_c^+ \to \underline{p} \pi^+ \pi^- (K_S^o)$

29. 610-4088 L+ $\Lambda_c^+ \to \underline{\Lambda}^o \underline{\pi}^+ \pi^- \pi^+$; quasi-elastic Λ_c^+ production

30. 635-4949 NB $NB \to \underline{p} \pi^- K_S^o$, $NB \to \underline{p} K^- K_S^o$; charmed neutral baryon candidate

31. 638-5640 DOB $\bar{D}^o \to \pi^- K^+ \pi^o \pi^o$; $D^{\pm}$ hypothesis possible

32. 638-9417 F+ $F^+ \to \underline{K}^+ K^- \pi^+ \pi^o$

33. 650-6003 L+ $\Lambda_c^+ \to \underline{\Lambda}^o \underline{\pi}^+ \pi^- \pi^+$

34. 654-3711 DO $D^o \to \pi^+ \underline{\pi}^+ K^- \pi^- \underline{\pi}^- \underline{\pi}^+$; decay length too short to measure parent angles; $\bar{D}^o$ hypothesis possible

35. 656-2631 D+ $D^+ \to \pi^+ K^- \pi^+ \pi^o$, $F^+ \to K^+ K^- \pi^+ \pi^o$, $\Lambda_c^+ \to p K^- \pi^+$

36. 661-2729 DO $D^o \to \underline{K}_S^o \underline{\pi}^+ \underline{\pi}^- \pi^o$ from D^{*+}; $\bar{D}^o$ hypothesis possible

37. 661-6517 DO $D^o \to K^- \underline{\mu}^+ (\nu_\mu)$

38. 663-7758 D+ $D^+ \to K^- \pi^+ \underline{e}^+ (\nu_e)$, $F^+ \to \pi^- \pi^+ \underline{e}^+ (\nu_e)$

39. 665-2113 C+ $D^+ \to \underline{\pi}^+ \underline{\pi}^- \underline{\pi}^+ (\bar{K}^o)$, $F^+ \to \underline{\pi}^+ \underline{\pi}^- \underline{\pi}^+ (\pi^o)$, $\Lambda_c^+ \to \underline{\pi}^+ \underline{\pi}^- \underline{\pi}^+ (\Lambda^o)$

40. 666-5294 DO $D^o \to K^- \pi^- \underline{\pi}^+ \pi^+$

41. 670- 12 C+ $\Lambda_c^+ \to \underline{p} K^+ \pi^- (\pi^o)$

42. 670-7870 DOB $\bar{D}^o \to K^+ \underline{\pi}^- (\pi^o)$; from D^{*-}

43. 671-2642 C+ $D^+ \underline{\pi}^+ \underline{\pi}^- \pi^+ (\bar{K}^o)$, $F^+ \to \underline{\pi}^+ \underline{\pi}^- K^+ (\bar{K}^o)$, $\Lambda_c^+ \to \underline{\pi}^+ \underline{\pi}^- \pi^+ (\Lambda^o)$

44. 529-3013 DO $D^o \to K^- \pi^+ \pi^o$; part of D^o-D0 pair

45. 529-3013 DOB $\bar{D}^o \to K^+ K^-$; part of D^o-$\bar{D}^o$ pair

Event	Particle	P_c (GeV/c)	x'_c	y'_c
1. 476-4449	L+	4.8(0.3)	0.100(0.018)	0.094(0.018)
2. 478-2638	D0	7.5(1.3)	0.133(0.005)	-0.024(0.005)
3. 486-6857	D0	12.9(0.5)	-0.015(0.002)	-0.040(0.002)
4. 493- 177	D0	11.2(0.2)	-0.031(0.005)	0.019(0.005)
5. 493-1235	D+	10.7(3.0)	-0.197(0.012)	-0.061(0.005)
6. 498-4985	L+	8.4(0.1)	-0.014(0.011)	0.132(0.005)
7. 499-4713	L+	4.2(0.1)	-0.165(0.004)	0.086(0.004)
8. 512-5761	D+	10.3(0.1)	0.026(0.004)	-0.028(0.004)
9. 513-8010	D0B	9.2(0.1)	-0.089(0.015)	-0.089(0.015)
10. 518-4935	D0	30.1(1.0)	-0.028(0.004)	0.042(0.004)
11. 522-2107	D+	27.0(5.0)	0.003(0.010)	0.122(0.005)
12. 522-3061	D0	47.0(3.0)	-0.016(0.008)	-0.054(0.004)
13. 527-3682	F-	12.3(0.3)	0.012(0.008)	-0.050(0.008)
14. 529- 271	D+	46.5(8.0)	-0.088(0.002)	0.003(0.002)
15. 533-7152	D+	38.0(3.0)	0.019(0.002)	0.010(0.002)
16. 546-1339	D+	16.7(2.9)	0.029(0.009)	-0.052(0.004)
17. 547-2197	D0	23.6(0.4)	0.032(0.002)	0.018(0.002)
18. 547-3192	D+	9.8(2.5)	-0.023(0.010)	-0.110(0.004)
19. 547-3705	D0	13.5(0.9)	0.092(0.003)	0.130(0.003)
20. 549-4068	L+	2.4(0.5)	-0.236(0.015)	0.025(0.015)
21. 556- 152	D0	15.4(0.3)	0.061(0.007)	-0.012(0.007)
22. 567-2596	L+	5.8(0.1)	0.096(0.003)	-0.010(0.003)
23. 577-5409	D0	11.3(0.5)	-0.040(0.003)	-0.021(0.003)
24. 580-4508	D-	9.7(1.0)	-0.003(0.002)	-0.049(0.002)
25. 597-1851	F+	9.3(0.4)	-0.105(0.018)	-0.002(0.013)
26. 597-6914	D0	46.3(2.8)	0.045(0.002)	0.036(0.002)
27. 598-1759	D+	17.4(0.3)	-0.097(0.003)	-0.045(0.003)
28. 602-2032	L+	6.3(0.1)	0.012(0.009)	-0.098(0.004)
29. 610-4088	L+	4.7(0.2)	0.236(0.007)	0.123(0.007)
30. 635-4949	NB	4.6(0.6)	0.158(0.002)	-0.118(0.002)
31. 638-5640	D0B	22.4(0.6)	-0.017(0.002)	0.020(0.002)
32. 638-9417	F+	5.9(0.1)	-0.002(0.001)	-0.213(0.001)
33. 650-6003	L+	5.7(0.0)	-0.167(0.050)	-0.038(0.050)
34. 654-3711	D0	19.2(0.3)	0.065(0.004)	-0.015(0.002)
35. 656-2631	D+	32.4(1.3)	0.015(0.002)	0.043(0.002)
36. 661-2729	D0	12.3(0.2)	0.070(0.002)	0.046(0.002)
37. 661-6517	D0	30.8(1.0)	0.022(0.003)	0.011(0.003)
38. 663-7758	D+	114.0(26.0)	-0.003(0.002)	-0.003(0.002)
39. 665-2113	C+	3.1(0.5)	0.018(0.012)	-0.019(0.012)
40. 666-5294	D0	55.0(2.0)	0.046(0.002)	0.009(0.002)
41. 670- 12	C+	2.4(0.2)	-0.021(0.002)	0.073(0.002)
42. 670-7870	D0B	6.8(0.2)	0.023(0.013)	0.011(0.003)
43. 671-2642	C+	3.1(1.1)	-0.122(0.003)	0.042(0.003)
44. 529-3013	D0	13.0(0.5)	-0.037(0.007)	-0.054(0.008)
45. 529-3013	D0B	48.0(2.0)	-0.011(0.002)	-0.019(0.004)

Event		E_H (GeV/c)
1. 476-4449	L+	23.4(5.8)
2. 478-2638	D0	8.8(1.5)
3. 486-6857	D0	22.0(4.6)
4. 493- 177	D0	30.7(8.3)
5. 493-1235	D+	41.0(7.5)
6. 498-4985	L+	10.0(4.0)
7. 499-4713	L+	21.0(5.0)
8. 512-5761	D+	16.2(1.4)
9. 513-8010	D0B	24.3(6.0)
10. 518-4935	D0	41.9(5.8)
11. 522-2107	D+	45.8(8.0)
12. 522-3061	D0	80.9(9.0)
13. 527-3682	F-	33.8(7.1)
14. 529- 271	D+	55.7(12.0)
15. 533-7152	D+	62.0(8.0)
16. 546-1339	D+	27.5(5.1)
17. 547-2197	D0	31.2(6.0)
18. 547-3192	D+	21.3(6.0)
19. 547-3705	D0	17.4(4.6)
20. 549-4068	L+	17.7(3.6)
21. 556- 152	D0	21.3(3.7)
22. 567-2596	L+	10.0(3.0)
23. 577-5409	D0	19.3(5.5)
24. 580-4508	D-	19.1(5.3)
25. 597-1851	F+	12.6(4.5)
26. 597-6914	D0	70.5(6.0)
27. 598-1759	D+	23.9(5.5)
28. 602-2032	L+	12.2(4.0)
29. 610-4088	L+	5.3(0.6)
30. 635-4949	NB	28.0(3.0)
31. 638-5640	D0B	54.1(8.3)
32. 638-9417	F+	14.6(1.5)
33. 650-6003	L+	9.4(3.0)
34. 654-3711	D0	46.9(6.5)
35. 656-2631	D+	46.5(7.5)
36. 661-2729	D0	18.0(4.0)
37. 661-6517	D0	46.1(6.9)
38. 663-7758	D+	131.0(46.0)
39. 665-2113	C+	10.0(4.0)
40. 666-5294	D0	131.0(14.0)
41. 670- 12	C+	6.5(2.5)
42. 670-7870	D0B	20.9(3.1)
43. 671-2642	C+	6.4(1.0)
44. 529-3013	D0	68.9(8.0)
45. 529-3013	D0B	68.9(8.0)

Event		P_μ (GeV/c)	x'_μ	y'_μ
1. 476-4449	L+	-51.5(13.3)	-0.046(0.004)	-0.033(0.004)
2. 478-2638	D0	-4.4(0.1)	-0.059(0.002)	-0.057(0.002)
3. 486-6857	D0	<2	******(*****)	******(*****)
4. 493- 177	D0	-17.1(1.5)	0.052(0.002)	-0.052(0.002)
5. 493-1235	D+	-7.0(0.3)	0.092(0.010)	0.065(0.004)
6. 498-4985	L+	-13.5(0.9)	0.044(0.009)	-0.062(0.004)
7. 499-4713	L+	-97.2(47.2)	0.001(0.008)	-0.015(0.003)
8. 512-5761	D+	-62.1(19.3)	0.000(0.002)	-0.012(0.002)
9. 513-8010	D0B	12.0(0.7)	0.043(0.002)	-0.013(0.002)
10. 518-4935	D0	-3.9(0.1)	0.260(0.005)	-0.203(0.005)
11. 522-2107	D+	-40.4(8.2)	-0.021(0.009)	-0.067(0.004)
12. 522-3061	D0	-58.8(17.3)	0.030(0.009)	0.062(0.004)
13. 527-3682	F-	36.8(6.8)	-0.012(0.008)	0.030(0.004)
14. 529- 271	D+	-44.5(9.9)	0.032(0.002)	0.045(0.002)
15. 533-7152	D+	-8.3(0.4)	-0.043(0.002)	0.049(0.002)
16. 546-1339	D+	-6.4(0.2)	-0.172(0.013)	0.216(0.006)
17. 547-2197	D0	-38.0(7.2)	-0.017(0.002)	-0.001(0.002)
18. 547-3192	D+	-15.0(1.1)	-0.002(0.009)	0.092(0.004)
19. 547-3705	D0	-96.4(46.5)	-0.026(0.002)	-0.026(0.002)
20. 549-4068	L+	-10.4(0.6)	0.066(0.002)	0.068(0.002)
21. 556- 152	D0	-9.8(0.5)	-0.163(0.003)	0.032(0.003)
22. 567-2596	L+	-5.5(0.2)	0.020(0.009)	0.089(0.004)
23. 577-5409	D0	-25.6(3.3)	0.063(0.002)	0.039(0.002)
24. 580-4508	D-	6.2(0.2)	0.046(0.004)	0.219(0.004)
25. 597-1851	F+	<4	******(*****)	******(*****)
26. 597-6914	D0	-47.4(11.2)	-0.100(0.003)	-0.069(0.003)
27. 598-1759	D+	-9.9(0.5)	0.160(0.003)	0.051(0.003)
28. 602-2032	L+	-18.8(1.8)	-0.009(0.008)	0.011(0.003)
29. 610-4088	L+	-7.4(0.3)	-0.118(0.003)	-0.110(0.003)
30. 635-4949	NB	-84.1(35.4)	-0.024(0.002)	0.044(0.002)
31. 638-5640	D0B	33.0(5.5)	0.049(0.002)	-0.067(0.002)
32. 638-9417	F+	-8.2(0.3)	0.046(0.004)	0.231(0.004)
33. 650-6003	L+	-13.7(0.9)	0.043(0.002)	-0.077(0.002)
34. 654-3711	D0	-4.3(0.1)	-0.398(0.016)	0.090(0.007)
35. 656-2631	D+	-126.0(79.4)	-0.030(0.002)	-0.042(0.002)
36. 661-2729	D0	-23.0(2.7)	-0.047(0.002)	-0.041(0.002)
37. 661-6517	D0	-18.6(1.7)	-0.091(0.002)	0.030(0.002)
38. 663-7758	D+	-108.0(58.3)	0.021(0.002)	-0.012(0.002)
39. 665-2113	C+	-24.4(3.0)	-0.021(0.002)	-0.035(0.002)
40. 666-5294	D0	-96.0(46.1)	-0.045(0.002)	-0.012(0.002)
41. 670- 12	C+	-4.7(0.1)	0.021(0.002)	-0.050(0.002)
42. 670-7870	D0B	39.1(7.7)	0.003(0.002)	0.013(0.002)
43. 671-2642	C+	-16.9(1.4)	0.025(0.002)	-0.061(0.002)
44. 529-3013	D0	<2	******(*****)	******(*****)
45. 529-3013	D0B	<2	******(*****)	******(*****)

Event		E_ν (GeV)	Q^2 (GeV/c)	W (GeV/c^2)
1. 476-4449	L+	74.0(14.5)	12.18(3.91)	5.6(0.9)
2. 478-2638	D0	12.3(1.5)	0.38(0.05)	3.9(0.4)
3. 486-6857	D0	22.9(5.0)	****(*****)	****(***)
4. 493- 177	D0	46.9(8.4)	4.34(0.96)	7.2(1.0)
5. 493-1235	D+	47.1(7.5)	4.20(0.65)	8.5(0.7)
6. 498-4985	L+	22.6(4.1)	1.76(0.37)	4.0(0.7)
7. 499-4713	L+	117.3(47.5)	2.58(2.61)	6.0(0.8)
8. 512-5761	D+	77.4(19.3)	0.69(0.66)	5.4(0.2)
9. 513-8010	D0B	35.4(6.0)	0.88(0.16)	6.6(0.8)
10. 518-4935	D0	44.9(5.8)	17.73(2.19)	7.7(0.5)
11. 522-2107	D+	85.3(11.4)	16.93(6.63)	8.3(0.9)
12. 522-3061	D0	138.8(19.5)	38.58(20.45)	10.6(1.3)
13. 527-3682	F-	69.7(9.8)	2.68(1.11)	7.7(0.9)
14. 529- 271	D+	99.3(15.6)	13.45(7.20)	9.5(1.1)
15. 533-7152	D+	69.4(8.0)	2.52(0.31)	10.6(0.7)
16. 546-1339	D+	33.0(5.1)	15.27(2.33)	6.0(0.6)
17. 547-2197	D0	68.3(9.4)	0.76(0.63)	7.5(0.6)
18. 547-3192	D+	35.4(6.1)	4.48(0.87)	5.9(0.8)
19. 547-3705	D0	112.9(46.7)	14.70(6.44)	4.1(1.1)
20. 549-4068	L+	27.2(3.6)	2.54(0.40)	5.5(0.6)
21. 556- 152	D0	30.2(3.7)	8.01(1.07)	5.6(0.5)
22. 567-2596	L+	14.6(3.0)	0.68(0.12)	4.1(0.5)
23. 577-5409	D0	44.0(6.4)	6.16(1.67)	5.4(0.7)
24. 580-4508	D-	24.4(5.3)	7.32(1.40)	5.3(0.7)
25. 597-1851	F+	15.8(6.1)	*****(*****)	****(***)
26. 597-6914	D0	117.0(12.7)	80.96(19.10)	7.0(1.3)
27. 598-1759	D+	32.9(5.5)	9.01(1.55)	5.9(0.6)
28. 602-2032	L+	30.1(4.4)	0.12(0.02)	4.7(0.7)
29. 610-4088	L+	11.8(0.7)	2.23(0.20)	2.6(0.2)
30. 635-4949	NB	111.2(35.5)	23.44(10.58)	5.3(1.1)
31. 638-5640	D0B	86.2(9.9)	19.51(6.07)	9.0(0.9)
32. 638-9417	F+	21.9(1.5)	9.57(0.82)	4.1(0.3)
33. 650-6003	L+	22.2(3.1)	2.35(0.44)	3.8(0.6)
34. 654-3711	D0	50.3(6.5)	32.16(4.54)	7.4(0.6)
35. 656-2631	D+	171.6(79.7)	57.48(29.56)	5.4(2.6)
36. 661-2729	D0	40.1(4.8)	3.58(0.84)	5.4(0.5)
37. 661-6517	D0	63.8(7.1)	10.85(1.74)	8.6(0.7)
38. 663-7758	D+	238.1(74.3)	15.05(11.76)	15.2(2.4)
39. 665-2113	C+	33.5(5.0)	1.36(0.38)	4.1(0.7)
40. 666-5294	D0	226.1(48.2)	47.01(48.05)	14.1(2.3)
41. 670- 12	C+	10.3(2.5)	0.16(0.04)	3.3(0.6)
42. 670-7870	D0B	59.1(8.3)	0.42(0.22)	6.2(0.5)
43. 671-2642	C+	22.4(1.8)	1.64(0.27)	3.1(0.3)
44. 529-3013	D0	68.0(8.0)	*****(*****)	****(***)
45. 529-3013	D0B	68.0(8.0)	*****(*****)	****(***)

Event		x	ξ	y
1. 476-4449	L+	0.29(0.08)	0.34(0.09)	0.30(0.06)
2. 478-2638	D0	0.03(0.00)	0.18(0.03)	0.64(0.04)
3. 486-6857	D0	****(****)	****(****)	>0.9
4. 493- 177	D0	0.08(0.01)	0.12(0.02)	0.64(0.07)
5. 493-1235	D+	0.06(0.00)	0.09(0.01)	0.85(0.03)
6. 498-4985	L+	0.10(0.02)	0.24(0.05)	0.40(0.08)
7. 499-4713	L+	0.07(0.06)	0.13(0.07)	0.17(0.06)
8. 512-5761	D+	0.02(0.02)	0.10(0.03)	0.20(0.05)
9. 513-8010	D0B	0.02(0.00)	0.07(0.02)	0.66(0.06)
10. 518-4935	D0	0.23(0.01)	0.26(0.01)	0.91(0.01)
11. 522-2107	D+	0.20(0.08)	0.23(0.08)	0.53(0.07)
12. 522-3061	D0	0.26(0.13)	0.27(0.13)	0.57(0.07)
13. 527-3682	F-	0.04(0.02)	0.08(0.02)	0.47(0.07)
14. 529- 271	D+	0.13(0.06)	0.15(0.06)	0.55(0.07)
15. 533-7152	D+	0.02(0.00)	0.04(0.00)	0.88(0.02)
16. 546-1339	D+	0.31(0.02)	0.35(0.02)	0.81(0.03)
17. 547-2197	D0	0.01(0.01)	0.05(0.01)	0.44(0.07)
18. 547-3192	D+	0.12(0.02)	0.18(0.04)	0.58(0.07)
19. 547-3705	D0	0.48(0.21)	0.55(0.22)	0.15(0.07)
20. 549-4068	L+	0.08(0.01)	0.15(0.03)	0.62(0.06)
21. 556- 152	D0	0.21(0.02)	0.27(0.02)	0.68(0.03)
22. 567-2596	L+	0.04(0.00)	0.17(0.03)	0.62(0.05)
23. 577-5409	D0	0.18(0.05)	0.24(0.05)	0.42(0.07)
24. 580-4508	D-	0.21(0.02)	0.28(0.03)	0.75(0.05)
25. 597-1851	F+	****(****)	****(****)	>0.7
26. 597-6914	D0	0.64(0.14)	0.65(0.14)	0.59(0.05)
27. 598-1759	D+	0.21(0.02)	0.26(0.02)	0.70(0.04)
28. 602-2032	L+	0.01(0.00)	0.11(0.03)	0.37(0.07)
29. 610-4088	L+	0.27(0.03)	0.55(0.07)	0.37(0.04)
30. 635-4949	NB	0.46(0.21)	0.51(0.21)	0.24(0.08)
31. 638-5640	D0B	0.20(0.06)	0.22(0.06)	0.62(0.06)
32. 638-9417	F+	0.37(0.03)	0.46(0.03)	0.62(0.03)
33. 650-6003	L+	0.15(0.02)	0.29(0.05)	0.38(0.07)
34. 654-3711	D0	0.37(0.01)	0.40(0.01)	0.91(0.01)
35. 656-2631	D+	0.67(0.36)	0.70(0.36)	0.27(0.12)
36. 661-2729	D0	0.11(0.03)	0.18(0.03)	0.43(0.05)
37. 661-6517	D0	0.13(0.02)	0.16(0.02)	0.70(0.04)
38. 663-7758	D+	0.06(0.04)	0.07(0.04)	0.55(0.11)
39. 665-2113	C+	0.08(0.03)	0.21(0.06)	0.27(0.07)
40. 666-5294	D0	0.19(0.20)	0.20(0.20)	0.58(0.11)
41. 670- 12	C+	0.01(0.00)	0.23(0.08)	0.54(0.08)
42. 670-7870	D0B	0.01(0.01)	0.07(0.01)	0.34(0.06)
43. 671-2642	C+	0.16(0.03)	0.38(0.05)	0.24(0.03)
44. 529-3013	D0	****(****)	****(****)	$\gtrsim$0.97
45. 529-3013	D0B	****(****)	****(****)	$\gtrsim$0.97

Event		Z	X_F
1. 476-4449	L+	0.24(0.07)	-0.66(0.13)
2. 478-2638	DO	0.99(0.22)	0.91(0.37)
3. 486-6857	DO	0.62(0.13)	****(****)
4. 493- 177	DO	0.38(0.12)	0.21(0.14)
5. 493-1235	D+	0.27(0.09)	-0.13(0.10)
6. 498-4985	L+	0.96(0.25)	0.75(0.36)
7. 499-4713	L+	0.24(0.08)	-0.60(0.10)
8. 512-5761	D+	0.69(0.06)	0.52(0.08)
9. 513-8010	DOB	0.40(0.13)	0.13(0.15)
10. 518-4935	DO	0.74(0.10)	0.68(0.11)
11. 522-2107	D+	0.60(0.13)	0.47(0.16)
12. 522-3061	DO	0.58(0.08)	0.53(0.10)
13. 527-3682	F-	0.38(0.10)	0.20(0.12)
14. 529- 271	D+	0.85(0.19)	0.67(0.20)
15. 533-7152	D+	0.62(0.10)	0.58(0.10)
16. 546-1339	D+	0.63(0.14)	0.52(0.18)
17. 547-2197	DO	0.78(0.12)	0.74(0.13)
18. 547-3192	D+	0.49(0.17)	0.28(0.24)
19. 547-3705	DO	0.83(0.16)	0.68(0.21)
20. 549-4068	L+	0.20(0.10)	-1.16(0.38)
21. 556- 152	DO	0.76(0.11)	0.69(0.14)
22. 567-2596	L+	0.69(0.15)	0.15(0.19)
23. 577-5409	DO	0.62(0.13)	0.45(0.14)
24. 580-4508	D-	0.54(0.15)	0.33(0.19)
25. 597-1851	F+	0.82(0.20)	****(****)
26. 597-6914	DO	0.65(0.07)	0.48(0.13)
27. 598-1759	D+	0.76(0.13)	0.68(0.17)
28. 602-2032	L+	0.60(0.17)	0.13(0.23)
29. 610-4088	L+	1.19(0.18)	*****(****)
30. 635-4949	NB	0.19(0.03)	-1.33(0.55)
31. 638-5640	DOB	0.42(0.08)	0.32(0.08)
32. 638-9417	F+	0.46(0.05)	-0.27(0.06)
33. 650-6003	L+	0.73(0.17)	-0.03(0.18)
34. 654-3711	DO	0.42(0.07)	0.27(0.09)
35. 656-2631	D+	0.71(0.10)	0.03(0.53)
36. 661-2729	DO	0.73(0.12)	0.64(0.16)
37. 661-6517	DO	0.67(0.10)	0.61(0.11)
38. 663-7758	D+	0.88(0.23)	0.85(0.23)
39. 665-2113	C+	0.42(0.14)	-0.55(0.22)
40. 666-5294	DO	0.42(0.05)	0.38(0.09)
41. 670- 12	C+	0.59(0.22)	-1.01(0.27)
42. 670-7870	DOB	0.35(0.06)	0.07(0.07)
43. 671-2642	C+	0.69(0.13)	-0.55(0.44)
44. 529-3013	DO	0.19(0.02)	*****(****)
45. 529-3013	DOB	0.71(0.08)	*****(****)

Event		P_{out} (GeV/c)	$P_{\perp}$ (GeV/c)	ϕ_{μ} (°)
1. 476-4449	L+	0.09(0.08)	0.09(0.18)	7.6(6.5)
2. 478-2638	D0	0.82(0.12)	0.86(0.13)	54.2(2.7)
3. 486-6857	D0	****(****)	****(****)	*****(****)
4. 493- 177	D0	0.10(0.05)	0.12(0.14)	13.5(7.7)
5. 493-1235	D+	0.67(0.24)	1.97(0.56)	18.0(3.8)
6. 498-4985	L+	0.54(0.13)	0.54(0.15)	29.3(7.7)
7. 499-4713	L+	0.66(0.19)	0.66(0.19)	58.7(25.8)
8. 512-5761	D+	0.27(0.06)	0.83(0.20)	137.1(9.8)
9. 513-8010	D0	1.01(0.14)	1.06(0.14)	61.8(7.5)
10. 518-4935	D0	0.47(0.12)	0.73(0.15)	18.1(4.5)
11. 522-2107	D+	0.90(0.45)	1.71(0.58)	16.0(7.9)
12. 522-3061	D0	0.43(0.39)	0.60(0.71)	9.3(8.8)
13. 527-3682	F-	0.09(0.13)	0.20(0.18)	8.3(12.1)
14. 529- 271	D+	3.40(0.48)	3.41(0.47)	56.5(2.6)
15. 533-7152	D+	0.79(0.09)	0.81(0.09)	76.5(4.8)
16. 546-1339	D+	0.16(0.10)	0.18(0.21)	9.4(6.6)
17. 547-2197	D0	0.38(0.09)	0.47(0.15)	26.0(6.6)
18. 547-3192	D+	0.25(0.15)	0.48(0.23)	13.1(7.1)
19. 547-3705	D0	0.36(0.12)	0.83(0.49)	9.7(3.0)
20. 549-4068	L+	0.44(0.24)	0.48(0.26)	51.9(3.8)
21. 556- 152	D0	0.00(0.11)	0.25(0.19)	0.0(6.4)
22. 567-2596	L+	0.55(0.02)	0.67(0.05)	96.7(5.8)
23. 577-5409	D0	0.04(0.03)	0.65(0.28)	4.1(3.4)
24. 580-4508	D-	0.07(0.02)	0.25(0.18)	8.4(2.5)
25. 597-1851	F+	****(****)	****(****)	*****(****)
26. 597-6914	D0	0.19(0.10)	1.03(0.58)	4.1(2.2)
27. 598-1759	D+	0.23(0.06)	0.65(0.23)	7.2(2.0)
28. 602-2032	L+	0.33(0.16)	0.50(0.07)	32.3(19.3)
29. 610-4088	L+	0.32(0.04)	0.32(0.10)	15.5(1.9)
30. 635-4949	NB	0.37(0.07)	0.39(0.16)	24.6(2.2)
31. 638-5640	D0	0.04(0.04)	0.56(0.31)	4.2(3.5)
32. 638-9417	F+	0.23(0.02)	0.48(0.09)	10.7(1.0)
33. 650-6003	L+	0.93(0.29)	1.06(0.27)	73.6(19.2)
34. 654-3711	D0	0.01(0.04)	0.60(0.16)	0.3(2.0)
35. 656-2631	D+	0.41(0.09)	3.17(1.76)	16.1(3.3)
36. 661-2729	D0	0.14(0.04)	0.14(0.19)	7.8(2.5)
37. 661-6517	D0	0.53(0.09)	0.86(0.20)	44.8(6.8)
38. 663-7758	D+	0.47(0.20)	2.21(0.88)	74.7(22.7)
39. 665-2113	C+	0.08(0.04)	0.37(0.12)	105.6(29.2)
40. 666-5294	D0	0.17(0.13)	0.71(0.68)	3.9(2.9)
41. 670- 12	C+	0.02(0.01)	0.07(0.04)	6.7(2.7)
42. 670-7870	D0	0.14(0.08)	0.32(0.08)	128.6(18.8)
43. 671-2642	C+	0.30(0.09)	0.46(0.12)	48.7(2.3)
44. 529-3013	D0	****(****)	****(****)	*****(****)
45. 529-3013	D0	****(****)	****(****)	*****(****)